Delft University of Technology

Relating Process Parameters to X-Core Properties through Experimental Testing and Modelling

Gaining an In-Depth Understanding of the X-Core Cure Process

M.P.J. Eversdijk

Relating Process Parameters to X-Core Properties through Experimental Testing and Modelling

Gaining an In-Depth Understanding of the X-Core Cure Process

by

M.P.J. Eversdijk

Student number: 4142705

Master of Science Thesis

Department of Aerospace Structures & Materials

Faculty of Aerospace Engineering - Delft University of Technology

In cooperation with Donkervoort Automobielen B.V.

August 22, 2017

Project duration:	November 1, 2016 – August 22, 2017	
Thesis committee:	Prof. dr. ir. R. Benedictus	TU Delft, Structural Integrity and Composites
	Dr. ir. J.M.J.F van Campen,	Supervisor, TU Delft, Aerospace Structures and Computational Mechanics
	Ing. R. Grooten,	Company Supervisor, Donkervoort Automobielen B.V.
	Ir. J. Sinke,	TU Delft, Structural Integrity and Composites

This report is subject to the cooperation agreement between the Delft University of Technology and Donkervoort Automobielen B.V.. It may not be published or redistributed without agreement of both parties within five years of the report publication date.

Preface

Performing my thesis research at Donkervoort has been a highly rewarding experience. It helped me to make the transition from student to being an engineer confident of being ready for the professional life. Experimenting with a novel material with such large potential to re-shape the manufacturing process of sandwich composites was very exiting and rewarding. Although some hours of sleep were lost in the completion of this project I feel like every effort was well worth it.

Without several people this thesis would not have been the way it is now. I would like to express my sincerest gratitude to Roel, who has dedicated so much of his time, knowledge and humor in guiding me through the research process. Furthermore, I would like to thank Julien for his support in helping me get the most out of my thesis project. Quintus and Stijn too deserve a mention and thank you for introducing me to the world of X-Core. Also, I would like to express my gratitude to Dennis who performed his thesis research in parallel to mine. I think our combined efforts made both achieve a higher level and having your company during the long months made it all the more enjoyable. I wish you best of luck in your future career. The technical staff at the DASML technical lab is also thanked for their help with the experimental work performed at the TUD. Finally, a thank you to my girlfriend Rosalieke with whom I could share the experience of completing an MSc. Thesis, your unconditional support has been invaluable to me.

I hope you enjoy reading.

M.P.J. Eversdijk
Lelystad, July 2017

Contents

Preface iii

List of Symbols ix

Abstract xi

1 Introduction 1

2 Relevant Literature 3

2.1 The Sandwich Concept . . . 3
2.1.1 Loading . . . 3
2.1.2 Types of Sandwich Cores . . . 4
2.2 Syntactic Foams. . . . 5
2.2.1 Density and Strength Dependencies . . . 5
2.3 Density Gradients and Functional Grading of Structural Foam Cores . . . 6
2.3.1 Density Gradients in Blown Structural Foam Cores . . . 6
2.3.2 Functional Grading of Syntactic Foams . . . 7
2.3.3 Determination of Density Gradients through X-Ray Tomography . . . 7
2.4 2D FDM Modelling of Thick Thermosetting Composites . . . 8
2.4.1 Example Models . . . 8
2.4.2 Resin Cure Kinetics . . . 10

3 X-Core Research and Development 11

3.1 The X-Core Concept . . . 11
3.2 Previous Research. . . . 12
3.2.1 J. Houwers (2013): Pure Expancel® Blends and Introducing a Thermosetting Binder . . . 12
3.2.2 F. Minde (2014): The Manufacturing Process and Methods of Lowering Density . . . 13
3.2.3 Q. Boegem and R.Santos (2015): Boundary Cases and Compressive Properties . . . 13
3.2.4 D.O. Berckmoes (2016): Integrally Heated Tooling . . . 14
3.2.5 S. Vial (2016): Relating Constituents to Material Properties . . . 14
3.3 Current Level of X-Core Technology. . . . 16
3.3.1 Floor Panels . . . 16
3.3.2 Door Window Frames . . . 16
3.4 Parallel Research Performed . . . 17

4 Optimal Mix Selection 19

4.1 Selection of Mixes of Interest . . . 19
4.2 Pre-cured Mixture Evaluation for Manufacturability . . . 20
4.2.1 Formability . . . 21
4.2.2 Manual pressure test. . . . 22
4.2.3 Stickiness . . . 23
4.2.4 Trade-off and Mix Selection for Compressive Testing . . . 23
4.3 Compressive Strength Tests . . . 23
4.3.1 Test Procedure . . . 24
4.3.2 Pressure Jack Drive Compliance . . . 25
4.3.3 Drive Compliance Validation. . . . 26
4.4 Final Mix Selection . . . 27

5 Tile Mould Design and Temperature Analysis 29

5.1 Tile Mould Design and Construction . . . 29
5.1.1 Design Overview. . . . 29
5.1.2 Sample Manufacturing. . . . 30

5.2 Tile Mould Surface Temperature Profiling 31
5.2.1 Test Setup and Sensors 31
5.2.2 Data Post-Processing 32
5.2.3 Test Series 32
5.2.4 Temperature Differences at Mould Surface 33
5.2.5 Temperature Overshoot 35
5.2.6 Temperature Distribution at T=85°C 36
5.2.7 Conclusions and Recommendations 37
5.3 Methods for Integrating a Highly Conductive Layer in Moulds 37
5.3.1 Discussion of Possible Methods 37
5.3.2 Trade-off 38
5.4 Copper Mesh Integration 39
5.4.1 Test Setup 39
5.4.2 Manufacturing of Copper Mesh Laminates 39
5.4.3 Temperature Distribution at Mould Surface using Copper Mesh 41
5.5 Conclusion 42

6 X-Core Pressure Generation 43
6.1 Evaluation of Previous Experiments 43
6.2 Factors Influencing X-Core Pressure Generation 45
6.2.1 DU Volume Fraction 45
6.2.2 Mix Composition 45
6.2.3 Temperature 46
6.2.4 Mould Filling 46
6.2.5 Mould Sealing 47
6.3 Controllable and Uncontrollable Factors 47
6.4 Alternate Method of Measuring Pressure using FlexiForce® Sensors 48
6.4.1 Test Method 48
6.4.2 Results 49
6.5 Oil Sensor Based Pressure Measurements 50
6.5.1 Design Overview 50
6.5.2 Sensors 51
6.5.3 Test Method 51
6.5.4 Results 51
6.5.5 Conclusion 53

7 Thermal Analysis of X-Core Curing Behaviour 55
7.1 Temperature Profiles in Various Thickness X-Core Samples 55
7.1.1 Test Plan 55
7.1.2 Test Setup 56
7.1.3 Data Collection and Post-Processing 57
7.1.4 Results 57
7.1.5 Density Gradients Through Local DU Expansion 60
7.1.6 Possible Effects of Temperature Overshoots 61
7.1.7 Conclusion and Initiators for Further Research 62
7.2 Test Plan for Proof of Concept 63
7.2.1 Dwell Cure Cycle Determination 63
7.2.2 Visual Inspection of Samples 65
7.2.3 Plan for Comparative Testing of Old and New Cure Cycle 66
7.2.4 Defining Density Gradients through X-Ray Tomography 67
7.2.5 Compression Tests Combined with DIC 69
7.3 Conclusions and Discussion 72

8 Numerical Modelling of the X-Core Cure Process 73
8.1 The Finite Difference Method . . . 73
8.1.1 Required Assumptions . . . 74
8.1.2 Derivation of the governing equations . . . 74
8.1.3 Solution method . . . 76
8.2 Mesh . . . 77
8.2.1 Central Nodes . . . 77
8.2.2 Boundary Nodes . . . 78
8.2.3 Boundary Conditions . . . 79
8.2.4 Initial Conditions . . . 79
8.3 Determination of Thermal Properties of X-Core. . . . 80
8.3.1 X-Core Constituent Material Properties . . . 80
8.4 Thermal Conductivity of X-Core . . . 81
8.4.1 Theoretical Models for the Effective Thermal Conductivity of Filled Composites. . . . 81
8.4.2 Effective Thermal Conductivity of Multiple Fillers . . . 83
8.4.3 Effective Thermal Conductivity of X-Core . . . 84
8.4.4 Validation of the Theoretical Model for X-Core Thermal Conductivity . . . 85
8.5 Specific Heat Capacity of X-Core . . . 86
8.5.1 Effective Specific Heat Capacity of Fillers . . . 87
8.5.2 Effective Specific Heat Capacity of X-Core . . . 87
8.5.3 Validation of the Theoretical Model for X-Core Specific Heat. . . . 88
8.6 Resin Cure Kinetics . . . 90
8.6.1 Theoretical Background . . . 90
8.6.2 Determining Resin Cure Kinetics through Differential Scanning Calorimetry . . . 91
8.6.3 Experimental Methodology and Apparatus . . . 91
8.6.4 Experimental results from Isothermal Scans and Post-Processing . . . 92
8.6.5 Computing Cure Kinetic Parameters from Experimental Data . . . 93
8.6.6 Integration of the Cure Kinetic Model into the Numerical Model. . . . 96
8.7 Model Verification . . . 97
8.7.1 Attaining the Analytical Solution Using Heisler Charts . . . 97
8.7.2 Numerical Solution Convergence . . . 98
8.8 Model Validation . . . 100
8.8.1 Validation Method . . . 100
8.8.2 Time Scaling . . . 101
8.8.3 Comparison of Experimental Data to Numerical Simulation . . . 101
8.8.4 Adjusting Thermal Interface Resistance . . . 102
8.8.5 Temperature Distribution Visualization . . . 104
8.9 Model Sensitivity to Thermal Conductivity and Specific Heat Capacity . . . 105
8.10 Degree of Cure Variation . . . 105
8.11 Case Study: Applying the Model for the Doorbeam Cure Cycle Design . . . 106
8.12 Conclusion . . . 109

9 Conclusion 111

10 Recommendations 113
10.1 Obtaining more Diffuse Temperature in Integrally Heated Moulds . . . 113
10.2 Pressure Setup Advances . . . 114
10.3 Density gradient research . . . 114
10.4 Further Validation and Implementation of the Numerical Model . . . 115

Bibliography 117

A Method of X-Core Sample Manufacturing 123

B NTC Calibration Data 125

C Calibration of FlexiForce® HT201 FSRs 127

D Overview of Design Choices of Oil Based X-Core Pressure Setup and Calibration 129
D.1 Design Choices and Justification . . . 129
D.2 Oil Pressure Sensor Calibration . . . 130
D.3 Test Procedure . . . 130

E Experimental Data for Density Determinations Using Archimedes Method 133
E.1 Density Determination of X-Ray Calibration Samples . . . 133
E.2 Density Determination for Density Gradient Tests . . . 134

F X-Ray Sample Preparation and Nanotom Calibration 139
F.1 X-Ray Sample Preparation . . . 139

G Isothermal DSC Methodology 141

H Specific Heat Capacity DSC Methodology 143

I Flow Chart of Numerical Model 145
I.1 Numerical Model Flow Chart . . . 145

J Heisler Charts 147

List of Symbols

Symbol	**Unit**	**Property**
α	-	Degree of cure
A	s^{-1}	Pre-exponential factor
Bi	-	Biot Number
C_p	J/kgK	Specific heat capacity
C_{p_b}	J/kgK	Binder specific heat capacity
C_{p_f}	J/kgK	Filler specific heat capacity
$C_{p_{eff}}$	J/kgK	Effective specific heat capacity
C_{p_g}	J/kgK	Microsphere gas specific heat capacity
$C_{p_{microsphere}}$	J/kgK	Microsphere effective specific heat capacity
C_{p_w}	J/kgK	Microsphere wall specific heat capacity
ϵ	-	Strain
E	MPa	Modulus
E_a	J/mol	Activation energy
$\Delta E_{element}$	J/m	Internal energy per unit length
Fo	-	Fourier number
θ	-	Dimensionless temperature ratio
m	kg	Mass
m_f	$-$	Mass fraction
k	s^{-1}	Rate constant
k_b	W/mK	Binder thermal conductivity
k_f	W/mK	Filler thermal conductivity
k_{eff}	W/mK	Effective thermal conductivity
k_g	W/mK	Microsphere gas thermal conductivity
$k_{microsphere}$	W/mK	Microsphere effective thermal conductivity
k_w	W/mK	Microsphere wall thermal conductivity
K_{int}	W/mK	Interface thermal conductivity
P	bar	Pressure
ρ	kg/m^3	Density
R	$J/molK$	Universal gas constant
R_{int}	m^2K/W	Thermal interface resistance
$\dot{q}$	W/m^3	Volumetric internal heat generation rate
$\dot{Q}$	W/m	Heat transfer rate
σ	MPa	Stress
σ_c	MPa	Compressive strength
$\sigma_{c_{norm}}$	MPa	Normalized compressive Strength
T	$^\circ C$	Temperature
v_f	-	Volume fraction
V	m^3	Volume

Abstract

X-Core is a novel core material that enables the one-shot manufacturing of complex shaped sandwich structures. The multi-phase syntactic foams consists of a thermosetting resin to which three types of microspheres are added. Altering the composition through variation of the constituents volume fractions allows the foam to be tailored to specific needs. Through using thermo-expandable microspheres the need for conventional methods for facesheet consolidation, like vacuum bagging or bladder moulding, is eliminated. This reduces labour costs by 54% while reducing the total costs by 64% [1]. The required pressure instead is generated through limiting the expansion of the microspheres in a closed mould. The current level of technology already allows implementation of the material and its corresponding manufacturing process in production ready components, however much is still unknown about why X-Core is successful in what it does and where its limitations lie. The current research provides more insight into the effect of the process parameters on the behaviour of X-Core and the relation to the properties of the final product.

Based on previous research an optimal combination of mix constituents was first selected. This X-Core mix assures maximal specific compressive strength combined with manufacturability at a density of $270 kg/m^3$.

To perform further research on X-Core under processing conditions similar to those used in the production of actual products, a new sample mould was designed and constructed. Surface temperature analysis of this mould revealed temperature differences as high as $28.5^\circ C$ over an area of 175x175mm. The temperature distribution was related to surface porosity and dry spots covering >40% of the carbon/epoxy facesheets. The concentrated introduction of heat of the carbon heating braids combined with the poorly conducting material in the mould lead to these temperature variations. Addition of aluminium at the mould surface and the integration of a copper mesh inside the mould laminate resulted in reductions of the temperature differences during a cure to 3.3 and $11^\circ C$ respectively, leading to improved prepreg surface with porosities around 2-6%.

The pressure generating effect of X-Core was also researched. There is reason to believe that the pressure generating properties of X-Core are related to many different parameters. A setup was designed and manufactured with the aim to evaluate these relations. The resulting setup enabled reliable testing of different conditions through elimination of variables. However, a major flaw related to thermal expansion differences made that no usable results were generated in this research.

Further research focused on the thermal behaviour of X-Core during its curing process. Previous experiences indicated that the exothermic reaction of the thermosetting resin combined with the insulating properties of the foam resulted in high temperature peaks in the products. In this research, temperatures as high as $167^\circ C$ were encountered. Applying a dwell in the cure cycle successfully lowered these temperatures to $119^\circ C$. Comparison of compressive properties of samples with either the 167 or $119^\circ C$ core temperatures did not provide reason to believe that materials properties are reduced through the higher core temperatures being reached during the curing process. However, density gradients in the foam were discovered and linked to the differential initiation of the microsphere expansion. A new cure cycle allowed the functional grading of the foam with 37% increased density at the edges. This way of tuning the material strength locally could have potential applications in creating higher specific flexural strength sandwich structures.

To enable evaluation of thermal behaviour of different X-Core mixes under various process parameters, a thermal model was set up which is able to predict the temperature distribution in rectangular geometries within $7^\circ C$. Theoretical models predict the thermal conductivity and specific heat capacity of a certain volume fraction combination and a cure kinetics are used to model the heat release of the thermoset resin. With the current accuracy the model allows the user to trial run several variations of a cure cycle to determine when temperature transitions occur and what maximal temperature will be reached. This limits the required temperature tests to a validation run with to determine if the required temperature behaviour is actually achieved.

1

Introduction

The first car ever to carry the Donkervoort name was introduced in 1978 and named the S7. Since that time Donkervoort Automobielen B.V., founded by Joop Donkervoort, has evolved with every new model. The latest, hand-build, ultra-light weight, sports car to roll out of the factory in Lelystad is the Donkervoort D8 GTO RS. With a body consisting for 90% out of carbon fibre reinforced composites, it truly is a modern piece of engineering. That Donkervoort Automobielen B.V. is more than just a car manufacturer was also proven with the introduction of the RS model. Along with the new car, a new technology named X-Core was introduced to the public for the first time.

X-Core is revolutionary as it enables one-shot manufacturing of lightweight, complex shaped, sandwich structures. The material classifies as a syntactic foam and expands when heated due to the presence of thermo-expandable microspheres. Placing the material in an integrally heated closed mould prohibits the expansion resulting in internal pressure generation. This pressure is used to consolidate fibre facings which replaces the classic methods involving vacuum or over-pressure. Development of this new material started in 2013 and is therefore still in its early stages. However, previous research has already led to the first successful parts being produced in 2016 which are integrated into the new RS model. The material and its process are not limited to Donkervoort as introducing the technology to other industries is already underway. Although the material provides promising results based on the current knowledge and technology, much is still unknown about why it is successful at what it does. The present research focuses on exploring the material and process further to develop a more complete comprehension of X-Core. The objective for this research is therefore:

To define the relationship between process parameters in a one-shot manufacturing process using X-Core and the properties of the final product.

Along with this objective, the aim is to provide a tool for engineers to predict the properties of various X-Core products and which helps to map the limitations and possibilities that the novel core material provides. All research was performed in a timeframe of nine months at location of Donkervoort Automobielen B.V.

To realize the set out objective and goal of the research it is split up into several topics of interest. All separate topic are interconnected and together aim to form a comprehensive overview on how X-Core behaves with respect to processing parameters. The report flow chart in figure 1.1 visually present the different research topics. The current report presents the performed research initiating with a review of relevant literature in chapter 2. The current level of technology of X-Core and the research that has led to this knowledge is discussed in chapter 3. The first phase of the current research starts with the determination of the optimal mix with respect to specific compressive properties and manufacturability based on previous research in chapter 4. The resulting X-Core composition is used for test performed in the subsequent chapters. The design of a new mould for manufacturing test specimens is presented in chapter 5 along with an evaluation of the surface temperature distribution of the used integrally heated mould technique. The resulting mould is used for the research towards the thermal behaviour of X-Core. Before proceeding with this, an effort to create a better understanding of the pressure generation of X-Core is discussed in chapter 6. Here the aim is to explore the possible relation between the temperature of X-Core during its process and the resulting pressure generated by the material. Unfortunately, determination of this relationship was not achieved in this research. Chapter 7 proceeds with a thermal study of X-Core in which the temperature distribution inside the material during a cure cycle is defined. The temperature history is then related to resulting material properties. Information attained here set the temperature bounds of interest for the pressure investigation in chapter 6. Lastly, a transient numerical model is set up in chapter 8 with which the temperature distribution during a cure cycle inside X-Core could be simulated. This model serves to predict thermally dependent properties of X-Core. Conclusions on the presented work are drawn in chapter 9 followed by recommendation for further research in chapter 10.

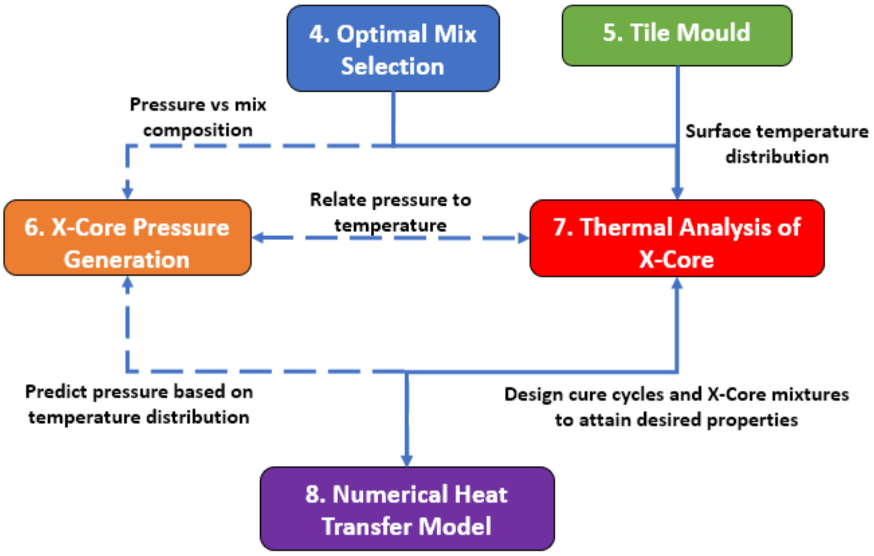
4. Optimal Mix Selection
5. Tile Mould
Pressure vs mix composition
Surface temperature distribution
Relate pressure to temperature
6. X-Core Pressure Generation
7. Thermal Analysis of X-Core
Predict pressure based on temperature distribution
Design cure cycles and X-Core mixtures to attain desired properties
8. Numerical Heat Transfer Model

Figure 1.1: Thesis main body flowchart showing interconnection between research topics

2

Relevant Literature

Before proceeding with the research performed in this thesis it is of order to first explore the relevant literature and present knowledge on the topics treated in the present report. X-Core can be classified as a sandwich core material. Therefore, the basic concept of sandwich structures is first defined followed by an overview of common core materials. A further specification of X-Core can be made as it belongs to the class of syntactic foams which are further discussed. Interesting properties with respect to density variations in in-situ foamed structural foam cores are then discussed. Lastly, as X-Core depends on a thermosetting matrix the theory of numerically modelling heat transfer in thick thermosetting composites is relevant and therefore touched upon.

2.1. The Sandwich Concept

The basic theory of sandwich structures comes down to enlarging the second moment of inertia of a structure with minimal added weight. This is performed through using a relatively light weight core material which induces a distance between the fibre reinforced facesheets. In this way, the flexural stiffness can be drastically increased with minimal increase in structural weight as indicated in figure 2.1.

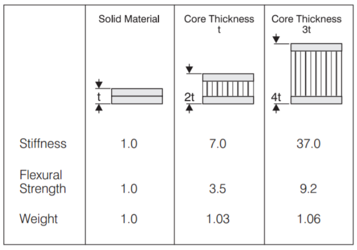

	Solid Material	Core Thickness t	Core Thickness 3t
	t	2t	4t
Stiffness	1.0	7.0	37.0
Flexural Strength	1.0	3.5	9.2
Weight	1.0	1.03	1.06

Figure 2.1: Relative stiffness, flexural strength and weight of sandwich structures compared to solid laminates [2]

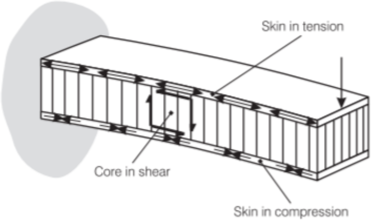

Figure 2.2: Schematic representation of a sandwich structures experiencing a bending load. Top skin in tension, bottom skin in compression and core carrying the shear loads [2]

2.1.1. Loading

The high bending stiffness of a sandwich structure springs from the high stiffness modulus (E) facesheets which are positioned away from the neutral axis to enlarge their second moment of inertia (I). Combined, this results in a high bending rigidity (EI). To position the facesheets away form the neutral axis in a dimensionally stable structure a core material is positioned between the facesheets. The main function of this core is to keep the facesheet in position relative to each other. The stiffness of the core is much smaller compared to that of the facesheet, so its contribution to the structural bending rigidity is often neglected. However, the strength of the structure does depend on the core materials strength. Under bending loading, the stresses in the structure are distributed according to figure 2.2. The top skin carries the tensile loading while the bottom skin is under compression. The core transfers the shear loads springing from the differences in deformation of the top and bottom skins. A high enough shear strength of the core material is therefore required to prevent core shear failure before other failure modes. A minimal shear stiffness of the core is also required to prevent excessive deflection of the structure under bending loads.

Furthermore, it is important to assure proper adhesion between the core material and facesheets in order to introduce the shear loads into the core. Good core to facesheet adhesion can be achieved in numerous ways depending on the core material used. Examples are the use of adhesive sheets between core and facesheet, adhesive pastes or co-infusion of the facesheets and core.

2.1.2. Types of Sandwich Cores

Various types of core material are commonly used and are shortly touched upon here. The type discussed are honeycomb, natural and foam cores.

Honeycomb

Used in high-end, weight critical applications in for instance the aerospace industry. Honeycomb cores rely on the parallel positioning of hexagon shaped cells which together achieve high specific buckling loads. Honeycombs are anisotropic of nature as the compressive strength is only present in the column direction. Bonding of honeycomb cores to facesheets can be performed through the use of adhesive sheets in a co-curing process or through use of adhesive pastes as shown in figure 2.3. Typical examples of honeycombs are Nomex$^{®}$ and aluminium cores.

Natural (Wood)

Nature also provides the world with suitable core materials. Balsa and cedar woods are two examples of this. The internal structure of elongated closed cells can be placed perpendicular to the facesheets to create a core similar to that of honeycombs. Light balsa cores have a density of $96kg/m^3$. Other properties include low thermal conductivity and acoustic insulation. Moisture sensitivity is however a major drawback of used natural materials as core.

Foam

A wide range of different foam types have been developed to fulfil the requirements of lightweight, strong core materials. Different precursors rely on a physical or chemical blowing agent which creates a structure of open or closed cells. Open cell foams are often more flexible but less suitable for structural application for which closed cell foams are preferred. The difference between the two is depicted in figure 2.4. A list of polymeric foam types and their properties is presented below along with a table of specific compressive, tensile and shear properties for comparative purposes in table 2.1.

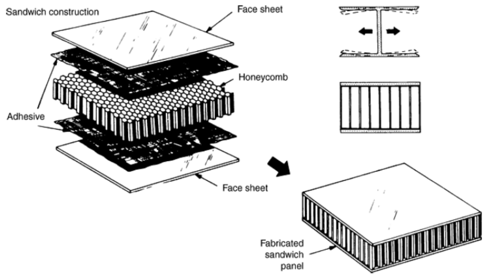

Figure 2.3: Schematic representation of a honeycomb sandwich core [3]

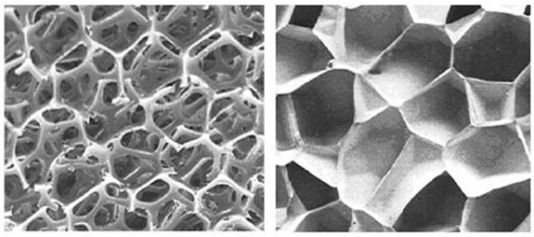

Figure 2.4: Comparison of the microstructure of open cell foam (left) and closed cell foam (right) [4]

PMI (Polymethacrylimide)

Highest specific strength and stiffness of all polymeric foam types in both shear, tension and compression. Closed cell structure of either thermoplastic or thermoset nature. Thermoformable to achieve lightly curved shapes. Applied in demanding fields as the aerospace industry. *Rohacell* is the main manufacturer of PMI foams in densities ranging from 75 to $205kg/^3$ and compressive strength between 1.5 to $9MPa$ [5].

PET (Polyethylene Terephthalate)

Consisting of either linear, thermoplastic or cross-linked, thermoset PET and either open or closed cell structures. Good compressive and tensile properties but lack in shear strength and stiffness. Used in a wide range of industries including aerospace, marine and transportation. Several large manufacturers produce this type of foam core including *AIREX*, *DIAB group* and *Armacell*.

SAN (Styrene Acrylonitrile)
Closed cell, thermoplastic foam with good impact properties and high thermal stability. Similar mechanical properties to PVC foams but allow larger degrees of thermoforming. *Gurit* is the main producer of SAN foams in densities ranging from 94 to 210kg/m^3 [6].

PVC (Polyvinylchloride)
Consisting of one of the most widely used plastics worldwide, PVC foams are available with a wide range of properties. These foams do not have as high thermal stability as PMI or PET but PVC foams do exhibit specific mechanical properties almost on par with those of PMI. Many different industries apply PVC foam and large manufacturers include *Gurit*, *DIAB group* and *AIREX*.

PU and Epoxy in-situ
Another group of structural foam cores is represented by the PU (Polyurethane) and epoxy in-situ foaming foams. These foams have the unique capability of having low viscosity in the pre-cured state allowing the foam to be poured into pre-forms. Blowing of the foam occurs in-situ, forming the foam to the mould cavity. Typical in-situ foams suffer from low mechanical properties and are therefore usually applied into low stress application such as insulation.

Syntactic Polymer
The last type of structural foams concern the microsphere filled polymers known as syntactic foams. As X-Core belongs to the class of syntactic foams this material type is further discussed in the next section.

Table 2.1: Comparison of specific mechanical properties of polymeric structural foams

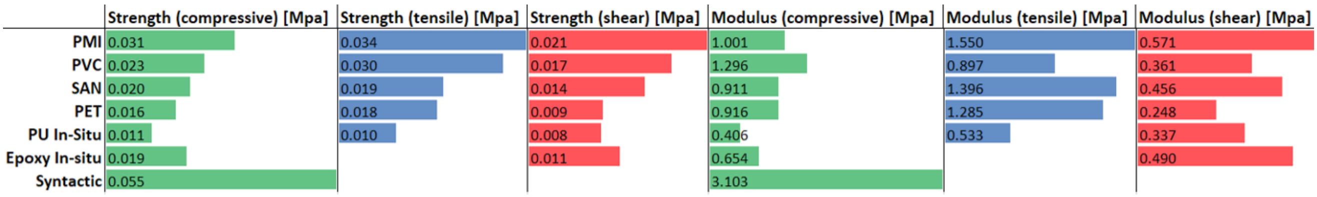

	Strength (compressive) [Mpa]	Strength (tensile) [Mpa]	Strength (shear) [Mpa]	Modulus (compressive) [Mpa]	Modulus (tensile) [Mpa]	Modulus (shear) [Mpa]
PMI	0.031	0.034	0.021	1.001	1.550	0.571
PVC	0.023	0.030	0.017	1.296	0.897	0.361
SAN	0.020	0.019	0.014	0.911	1.396	0.456
PET	0.016	0.018	0.009	0.916	1.285	0.248
PU In-Situ	0.011	0.010	0.008	0.406	0.533	0.337
Epoxy In-situ	0.019		0.011	0.654		0.490
Syntactic	0.055			3.103		

2.2. Syntactic Foams

These foams are characterized by the combination of microspheres with a polymeric matrix. Through adding different amounts or types of fillers to a polymer matrix the syntactic foams properties are highly tailorable. Common microfiller types consist of hollow spheres with either glass, polymeric, carbon, ceramic of metal walls. Matrix materials used are epoxy, phenolic, polyester of vinyl-ester resins. Due to the high hydrostatic strength of microspheres, syntactic foams often exhibit high compressive properties although tensile properties are often lacking.

2.2.1. Density and Strength Dependencies

The tailorability of syntactic foams is related to the used microspheres. Microsphere diameter, wall material, wall thickness and volume fraction inside the matrix can all be varied to achieve different bulk material properties.

Effect of Microsphere Diameter
A study by *d'Almeida* concentrated on the effect of microsphere diameter (45-210μm) on the compressive properties of syntactic foams with microsphere volume fractions between 25 and 55%. Results indicated that higher specific properties were attained when small diameter microspheres were used. Reason for this was believed to be the that larger diameter microspheres acts as an easier source for crack initiation [7].

Effect of Microsphere Wall Thickness
Gupta & Woldensenbet studied the effect of varying microsphere wall thickness while keeping the diameter of the spheres constant. Their study revealed that through alterations in wall thickness were more efficient in changing the density of syntactic foams compared to alteration in microsphere volume fractions [8]. This is clarified when looking at figure 2.5 where the change in compressive strength vs. density is plotted for two methods of density alteration. 'Present study' uses the variation of wall thickness whereas 'd'Almeida' uses the variation in microsphere diameter.

Effect of Microsphere Volume Fraction

Lastly, the most prominent way of influencing the density and mechanical properties of a syntactic foam is through controlling the volume fraction of microspheres in the composite. Numeral studies showed a strong dependency of mechanical properties of the microsphere volume fractions. Increasing the volume fraction from 30 to 60% caused a decrease in tensile strength with respect to the neat resin of between 60-80% [9] (see figure 2.6). Shear strength was found to decrease with 33% with an increase in microsphere fraction of 19.2% [10].

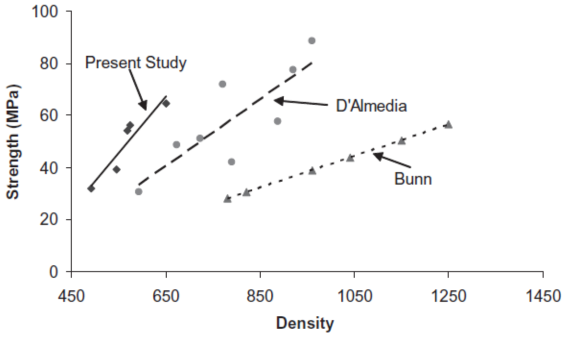

Figure 2.5: Compressive strength as function of syntactic foam density for different methods of density alteration [8]

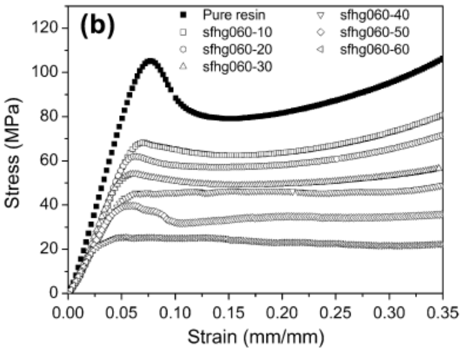

Figure 2.6: Effect of varying microsphere volume fraction from 0-60% on the compressive properties of a syntactic foam [11]

2.3. Density Gradients and Functional Grading of Structural Foam Cores

X-Core combines the material composition of a syntactic foam with the manufacturing process of an in-situ formed foam. It is therefore relevant to explore two density related variations occuring in both processes. First, density gradients occurring in in-situ foams are discussed after which the functional grading of syntactic foams is explored. Both variations in density offer possibilities with respect to creating more efficient structures through placing the material where it is needed.

2.3.1. Density Gradients in Blown Structural Foam Cores

When using a chemical blowing agent for the in-situ forming of foam density gradients may occur from the core to the edge of the foam. *Progelhof & Throne* reported on this when studying the density distribution of polypropylene foam samples. Figure 2.7 shown the density as function of thickness location were variations as large as 40% occur between the edge density and centre region density. The reason for this variation is illustrate in figure 2.8. Pore size of the foam is larger towards the centre region and densities towards the edges. This behaviour is possible related to the exothermic nature of the reaction causing the formation of the pores, which initiates in the centre of the foam leading to larger pores in this region [12].

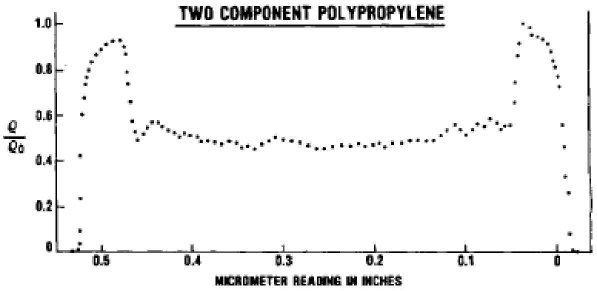

Figure 2.7: Normalized density profile of a polypropylene foam [13]

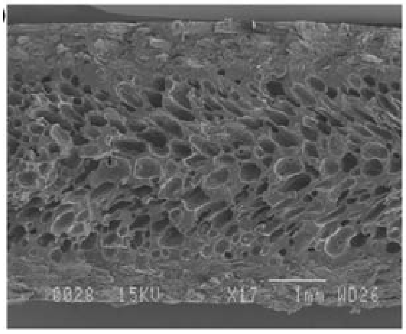

Figure 2.8: SEM image of chemically foamed polypropylene structural foam core material showing variation in pore size [12]

2.3.2. Functional Grading of Syntactic Foams

Purposely induced density gradients create functionally graded foams. Functional grading can help to position higher density, stronger, material in high stress locations of the structure. Other uses could be the more efficient absorption of energy in impact loading. An example of functional grading of syntactic foams (FGSF) was researched by *Doddamani et al.*. Trough layered co-curing of various volume fraction cenosphere filled epoxy based syntactic foams a three step density gradient was generated. This is illustrated in figure 2.9. Flexural and compressive testing of the FGSF showed an increase of 3-67% in the specific compressive modulus and increase of 34-87% in specific flexural strength [14]. The increase in specific strength can be attributed to the positioning of higher density material near the tensile side of the beam under flexure which *Gupta & Nagorny* already stated to have a positive effect on the tensile strength of syntactic foams [9]. Microscopic examination revealed that failure initiation in flexural loading occurred through crack initiation on the tensile side which propagates through the thickness to induce complete failure. *Doddamani et al.* concluded that appropriate use of FGSF can lead to materials with improved mechanical performance.

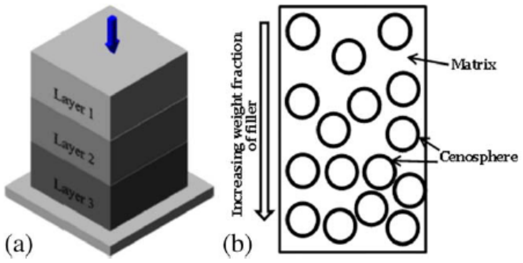

Figure 2.9: Schematic representation of FGSF structure with a difference in microsphere concentration over the thickness [14]

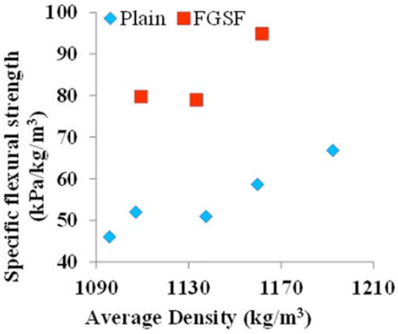

Figure 2.10: Specific flexural strength of FGSF compared to plain syntactic foams [14]

Another study by *Gupta & Woldensenbet* on the flexural properties of syntactic foams combined with glass fibre facesheets showed that all samples tested failed through fractures originating in the tensile side of the syntactic foam core [15] (see figure 2.11). This correlates with the relatively low tensile strength of syntactic foams compared to their compressive properties.

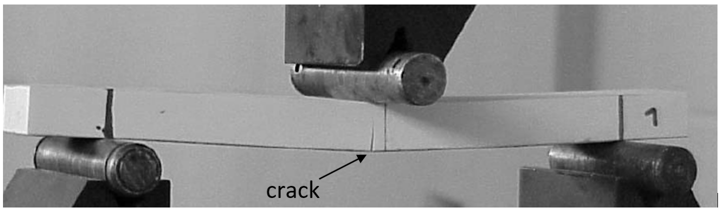

Figure 2.11: Crack appearing on the tensile side of a syntactic foam sandwich structure with glass fibre facings subjected to three point bending [15]

2.3.3. Determination of Density Gradients through X-Ray Tomography

Accurate determination of density gradients in material can be performed by making use of X-Ray tomography. The Beer-Lambert Law relates the attenuation of light to the properties of the material through which this light is travelling As the attenuation of the light depends on the linear attenuation coefficient (μ), which is dependent on the material density, it can be used to determine the relative density of different materials. The Beer-Lambert law is given as follows:

$$I = I_0 \exp(-\mu t) \tag{2.1}$$

In which I is the intensity of the transmitted x-rays, I_0 is the intensity of the incident x-rays, μ is the linear attenuation coefficient and t is the thickness of the material through which the x-rays have travelled

The linear attenuation coefficient can be further subdivided into two effects. Firstly, μ_p is the coefficient related to the photoelectric absorption and μ_c is the coefficient related to the Compton effect (e.g. the scattering of the x-rays). The Beer-Lambert law is then changed to the form:

$$I = I_0 \exp - (\mu_p + \mu_c) t \tag{2.2}$$

The value of the linear attenuation coefficient for a certain material is dependent on its density. For example:

$$\mu_{watervapor} < \mu_{water} \tag{2.3}$$

In water the probability of an x-ray photon hitting a water molecule is higher. Therefore the linear attenuation of coefficient will be larger. For a certain material, μ can be normalized w.r.t. the density to produce a value called the mass attenuation coefficient [16]. This attenuation/density ratio will be constant for a certain element or compound, continuing on the example of water this gives:

$$(\frac{\mu}{\rho})_{watervapor} = (\frac{\mu}{\rho})_{water} \tag{2.4}$$

If this coefficient is thus determined for a compound with known density it can be used to determine the density of another specimen of the same compound but of different density. In this way the grey-value of x-ray images, which is a direct result of the x-ray attenuation, can be used to determine the density variation in a specimen if an area of the specimen has a known density. An example of such an x-ray image of a polypropylene foam is shown in figure 2.8, based on this image the density profile presented in figure 2.7 was created. Absolute measures of density based on grey values can be attained through adding three samples of known density and equal thickness to the test specimen. A linear relationship between the grey value scale and absolute density can then be attained.

2.4. 2D FDM Modelling of Thick Thermosetting Composites

During the curing of thermosetting resin heat is generated through the exothermic nature of the reaction. In thick composite structures, this internal heat generation is slow to dissipate to the outer boundaries through conduction potentially leading to high core temperatures. These temperatures potentially cause material degradation. Furthermore, the large temperature gradients present in the material during a cure cycle can lead to variations in degree of cure locally. These variations lead to reduced product quality and material properties. Knowledge of these phenomena is relevant for industries like wind-energy where thick (>40mm) thermoset glass laminates are a common and high part performance is required. In order to understand the curing process in thick thermosetting composite parts, studies have been devoted to modelling the heat transfer process using two or three dimensional numerical modes. These models combine the principle of conservation of energy with cure kinetic models to predict temperature and degree of cure distributions under varying process conditions. Transient finite difference methods (FDM) are used to solve the partial differential equations discretized in both time and space.

2.4.1. Example Models

The results attained in two different studies aiming to model the curing of thick thermosetting composites are discussed in the following paragraphs.

Bogetti & Gillespie: Two-Dimensional Cure Simulations of Thick Thermosetting Composites

Bogetti & Gillespie constructed a model for the cure simulation of two-dimensional thick thermosetting composites [17]. Three geometries were analysed, consisting of a flat plate, right angle bend and ply-drop geometry. Both glass/polyester and graphite/epoxy composites were included using respective material properties of the materials. The effect of varying autoclave cure cycles, boundary conditions and material thicknesses were evaluated. Experimental results were generated for validation of the transient finite difference model. Excellent correlation of the simulation with the experimental results was found as shown in figure 2.13. Figure 2.12 shows the effect of various thickness glass/polyester laminate on the core temperature peak over time.

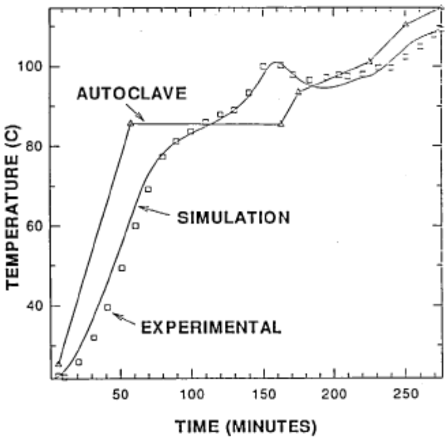

Figure 2.12: Comparison of simulation and experimental temperature over time in the core of a 25.4mm thick glass/polyester laminate [17]

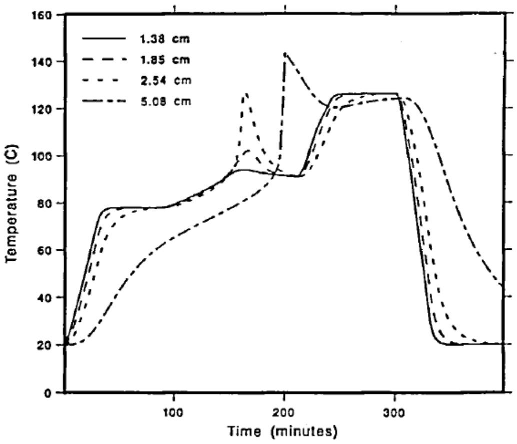

Figure 2.13: Variation of core temperature with different thickness of the glass/polyester laminates [17]

L. Shi: Heat Transfer in Thick Thermoset Composites

In the PhD. dissertation of Lei Shi performed at the Technical University of Delft another two dimensional model is constructed for the simulation of thick thermosetting composites [18]. A study towards the material properties of glass fibre epoxy composites is presented giving results for the density, thermal conductivity and heat capacity as well as cure kinetic parameters of the epoxy. Low thermal conductivity of the material coupled with the exothermic reaction of the thermosetting epoxy again was shown to generate significant temperature overshoots in the laminate. The Heat Transfer Module of COMSOL Multiphysics 4.4 with MATLAB was used for setting up the simulation. Experimental validation based on a vacuum infusion process was performed of which the results are presented in figure 2.14 for various thicknesses and in figure 2.15 for various cure temperatures. Differences between the experimental and simulation results were put down to the incremental resin introduction in the simulation compared to the continuous increase in resin fraction in reality.

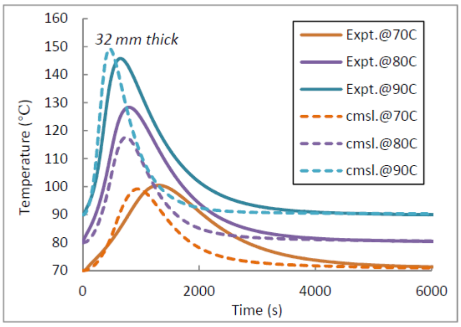

Figure 2.14: Comparison of experimental temperature data vs. simulation predictions for three different cure temperatures in a glass/epoxy composite [18]

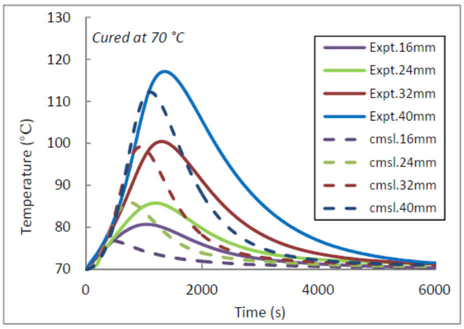

Figure 2.15: Comparison of experimental temperature data vs. simulation predictions for four different laminate thicknesses of a glass/epoxy composite [18]

2.4.2. Resin Cure Kinetics

Both studies discussed in the previous section used the theory of cure kinetic modelling in order to include the internal heat generation of the thermosetting resin in their respective numerical models. Cure kinetics describe the rate of reaction as a function of temperature and degree of cure of the resin. The theory uses the Arrhenius equation which is expressed as:

$$k = Ae^{-\frac{E}{RT}} \tag{2.5}$$

The activation energy, E, is the minimum energy molecules must accumulate to form a reaction product [19]. A is a pre-exponential factor which represents the amount of times molecules will collide in the way necessary to produce the required reaction. R is the gas constant at $8.314 J/molK$ and T presents the temperature in Kelvin. Both E and A can be defined for a certain reaction, allowing the prediction of the reaction rate constant k at various temperatures. The equation describes an exponential decay function in which $\frac{E}{RT}$ is the ratio of the activation energy (E) over the average kinetic energy (RT). A low activation temperature combined with a high temperature therefore results in high rate constants (k). A high activation energy at a low temperature results in a low rate constant.

The Arrhenius equation is included in a cure kinetic model which includes the degree of cure and reaction order to attain a measure of the reaction rate, $\frac{d\alpha}{dt}$, present under a certain temperature and degree of cure. In parallel to E and A, the reaction order are reaction specific and constant with temperature and degree of cure. Three common cure kinetic models are presented in table 2.2[18].

Table 2.2: Thee different cure kinetic models

Model	Equation
nth order	$\frac{d\alpha}{dt} = k(1-\alpha)^n$
Autocatalytic	$\frac{d\alpha}{dt} = k\alpha^m(1-\alpha)^n$
Autocatalytic + nth order	$\frac{d\alpha}{dt} = (k_1 + k_2\alpha^m)(1-\alpha)^n$

The nth order model represents a decaying reaction with the reaction rate being maximal at t=0. The autocatalytic reaction starts at zero reaction rate at time t=0 after which the reaction rate peaks and decays again. The combination of both reaction models results in the Autocatalytic + nth order model with non-zero initial reaction rate but with maximal rate of reaction after t=0. All three model are graphically illustrated in figure 2.16.

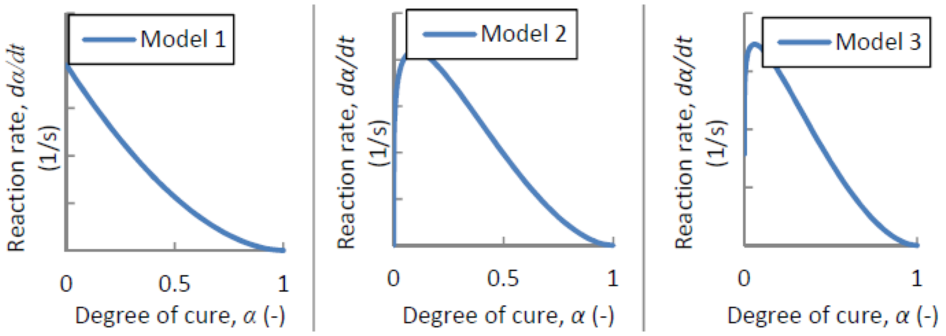

Figure 2.16: Visual respresentation of the different cure kinetic models. Model 1 = n$^t h$ order, Model 2 = Autocatalytic and Model 3 = Autocatalytic + nth order [18]

The parameters A, E, m and n for thermosetting resins can be attained through differential scanning calorimetry (DSC) experiments. Both isothermal and dynamics scanning methods are possible.

3

X-Core Research and Development

2013 marked the year in which the concept of X-Core was first actively researched. From this time onwards, the concept has developed into a novel core material with several unique properties. This chapter will first clarify what X-Core is and what makes it different. Afterwards, the research performed in previous studies is discussed.

3.1. The X-Core Concept

X-Core is a type of foam which is applied in combination with fibre reinforced facings to create so called sandwich structures. To consolidate and cure the facings, pressure and elevated temperatures are required. Classical consolidation methods depend on vacuum, mechanical pressure or bladder moulding to generate the required pressure. In the production of X-Core, none of these methods is required as internal pressure is generated in the material itself. The syntactic foam consists of a thermosetting matrix to which three types of micro-sized spheres are added of which each has its own function inside the composite. One of the microsphere types is essential to the pressure generation of the foam. DU Expancel® by *AkzoNobel* is a hollow thermoplastic polymeric microsphere with a gaseous blowing agent inside. Under elevated temperature the blowing agent, consisting of a hydrocarbon gas, start to expand. The thermoplastic resist this increase in pressure until the softening temperature of the shell material is reached. Sudden expansion of the microsphere occurs at this stage leading to a volume increase of around 40 times. Constraining this expansion through placing the microspheres in an enclosed mould will lead to an increase in pressure, this basic principle is used to consolidate the facesheets of the sandwich structure from the inside.

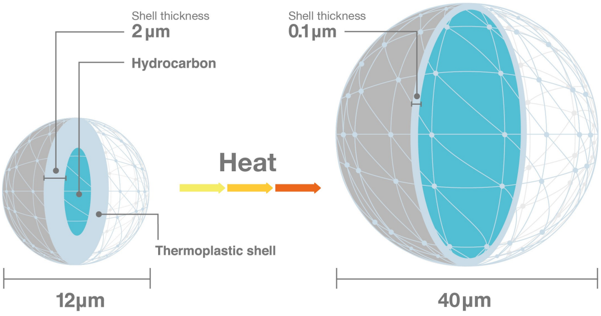

Figure 3.1: Expansion of a DU Expancel® microsphere

While the DU microspheres are in an expanded state, the thermosetting resin cures and vitrifies creating a dimensionally stable foam core. The other fillers in X-Core are added too further reduce the density of the material and, through varying the relative amounts, allow the tailoring of the materials properties.

3.2. Previous Research

The initiator to the development of X-Core was the need for a cost-effective core material capable of making complex shaped sandwich components. Lowering both material costs and production hours was the main objective. Current production of complex shaped sandwich components involve a two step process. The facings are first manufactured under vacuum in an oven. The second step involves the wrapping of a pre-shaped foam core of Divinycell H45 in glue films and placing it between the pre-cured facings. The assembly is then placed in a mould and cure again under vacuum. The 3D milled foam core is a main contributor to the material costs of a component. The two step process leads to many man hours, resulting in high labour costs of a product. A process that could reduce both these cost factors was therefore deemed necessary, which resulted in the research to what eventually would become X-Core.

3.2.1. J. Houwers (2013): Pure Expancel® Blends and Introducing a Thermosetting Binder

A first step in the research was taken by J. Houwers [1] during his internship Aiming for a lightweight core material which could produce the pressure required for the consolidation of the facesheets a mixture of two Expancel® was investigated. Samples were created with varying amounts of the expanding DU Expancel® combined with DE Expancel®. DE Expancel® is a pre-expanded variant of the Expancel® range available. This lightweight filler has a true density around $30 kg/m^3$ and is therefore ideally suited for the creation of lightweight products. Dimensional stability is achieved through the 'welding' together of the microspheres under elevated temperatures without requiring a binder material. A mixture of 7:1 DU/DE weight ratio was added to simple shaped mould. Resulting foams of similar composition to rubber bouncing balls. Increased amounts of DE added to the mould increased these properties slightly, but not to a satisfactory level to be applicable in sandwich structures. Increased amounts of DU revealed the potential extend of pressure generated in the mould as $3mm$ aluminum mould lids were deformed beyond yielding during a cure. Another issue brought to light in the research was the reheating of the cured material. A sample with facesheets in place was re-heated to $105°C$ resulting in the catastrophic failure of the product as depicted in figure 3.2.

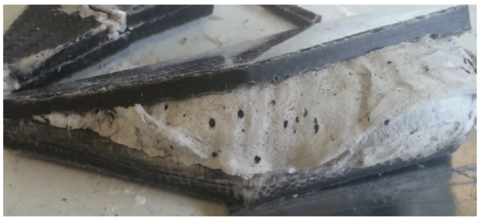

Figure 3.2: Result of the re-heating of a cured pure DU/DE Expancel blend sample with carbon fiber facesheet

This phenomenon led to the introduction of a thermosetting binder material. This binder in its cured state could resist the re-expansion of the microspheres and provide a dimensionally stable material under elevated temperatures. The introduction of the epoxy however led to a drastic increase in density of the foam from $\pm 30 kg/m^3$ to $450 kg/m^3$. The new mixtures however did result in several successful samples (figure 3.3a) and products (figure 3.3b) using the one-shot manufacturing process convincing *Donkervoort* to continue the research. Up-scaling of the material to create lightweight sandwich structures was however questionable due to the high core density and high surface porosities in the facesheets.

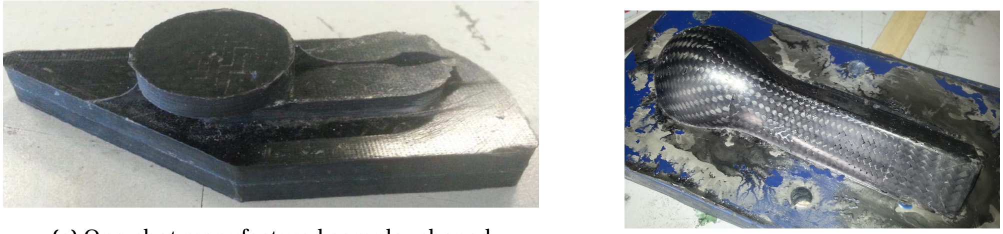

(a) One-shot manufactured complex shaped sandwich structure with carbon facesheets and X-Core core material

(b) Carbon fiber X-Core gearstick marking the first product produced with X-Core

Figure 3.3: The first successful complex shaped sample and product manufactured using the novel core material X-Core

3.2.2. F. Minde (2014): The Manufacturing Process and Methods of Lowering Density

F. Minde continued on the work of J.Houwers. Minde's objective was to define the new manufacturing process of the doorbeam of a Donkervoort D8 GTO, depicted in figure 3.4 as part of his MSc. thesis [20]. This component is complex shaped and is currently produced through the process explained in the introduction of this section. It therefore is an excellent proving case for the applicability of X-Core in actual components. *Minde* calculated that the use of X-Core and its on-shot production process could lead to labour cost reductions of 54% and total reduction in cost of 64%. Another part of the research aimed at reducing the density of X-Core, which now had a relatively high density binder material added to it. Several methods of lowering the density were applied with varying success:

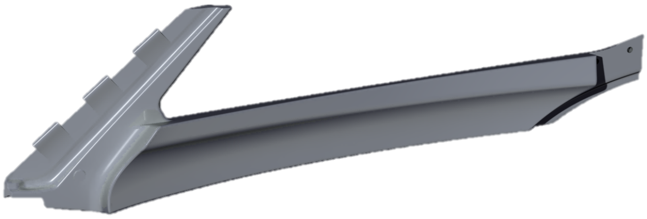

Figure 3.4: Passenger Side Doorbeam of a Donkervoort D8 GTO

- Adding Divinycell H45 cubes
  Trough addition of hand cut cubes of Divinycell H45 with a low density of $48kg/m^3$ the X-Core density was lowered. The laborious process of cutting the cubes did however lead to large increases in the labour costs.

- Adding Polystyrene Beads
  The addition of polystyrene beads replaced the H45 cubes. Beads of 2-5mm and 0.1-1mm in diameter were combined in an combination of 86% and 14% respectively to achieve optimal packing factors.

- Different combination of DU/DE
  The DU/DE mixing ratio was varied over 9 levels. A 30/50 ratio was chosen as optimal.

The polystyrene beads were later identified as being a weak link in the composite and a recommendation was made to search for a similar but stronger replacement filler.
The issue of the high surface porosity was addressed through evaluating several mitigation strategies. These consisted of curing the products under a vacuum, placing an additional layer of dry glass fibre between the mould surface as flow-medium, adding a PET foil barrier layer between the facing and X-Core and lastly testing different grades of DU Expancel®. The vacuum and dry fibre additives did not improve the surface porosity. The addition of a PET film barrier layer did significantly improve laminate quality but question arose on the quality of the core/facesheet interface integrity. Lastly, the combination of 031DU40 with 920DE80d30 Expancel® grades proved to be the most optimal with regard to surface quality in terms of porosity and discolourations

F.Minde also performed several temperature measurements which indicated that the exothermic reaction of the thermoset resin (SR8500/KTA317) created temperature overshoots up to 141°C. These temperature overshoots were linked to the cracking of the foam core in larger volume section of the door beam as depicted in figure 3.5. Furthermore, thermo-mechanical analysis was performed on several Expancel® grades. These tests showed that the onset of expansion of 031DU is very well defined at occurs at a temperature of 85°C. Moreover, the expansion of 031DU was dependent on temperature as shown in figure 3.6. An increase in temperature from 80 to 100°C leads to a defined increase in volume of the microsphere. No expansion of 920DE was identified up to 100°C.

3.2.3. Q. Boegem and R.Santos (2015): Boundary Cases and Compressive Properties

In 2015, two interns worked on further advancing the base of knowledge around X-Core. R.Santos developed a test setup on site at *Donkervoort* capable of determining the compressive properties of X-Core. Compressive test results were compared to tests performed according to ASTM standard revealing a difference of 5% in compressive strength and 45% in compressive stiffness. The setup was deemed adequate for the quick comparative testing of different X-Core varieties. Q.Boegem aimed to better understand the fundamental

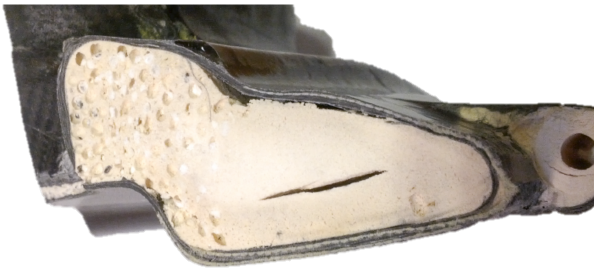

Figure 3.5: Cracking of X-Core observed in region with pure DE/DU resin blend linked to exothermic temperature peaks

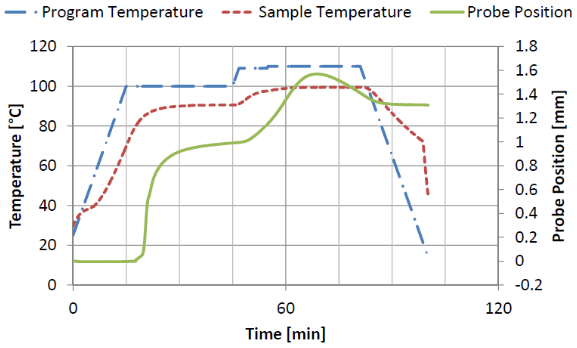

Figure 3.6: TMA analysis of the expansion of 031DU vs. temperature

properties of X-Core through performing large volume tests a wide variety of material compositions including pure Expancel® foams. High resin volumes were shown to lead to large voids in the foams. High DU contents were shown to lead to explosive behaviour of the composite during de-moulding.

3.2.4. D.O. Berckmoes (2016): Integrally Heated Tooling

D.O.Berckmoes performed his internship on the development of integrally heated tooling [21]. This research led to the current mould technology employed for the fabrication of X-Core sandwich structures. The concept comes down to the use of resistance heaters in the form of carbon fibre braids through which a current is sent. The resistance of the braid generates heat which is used to attain the desired temperatures of the mould. A thermocouple is placed near the mould surface and a proportional-integral (PI) controller is used to regulate the required current based on the difference between the desired temperature and the temperature read from the thermocouples. A software program provided by *Twenco CME B.V.* allows for the pre-programming of a cure cycle. The PI controller is connected to a windows computer running the software which allows for a high degree of temperature control. The complete setup is depicted in figure 3.7. The current method of heating the moulds is used for both the floor panel and door window frame components of the Donkervoort D8 GTO RS.

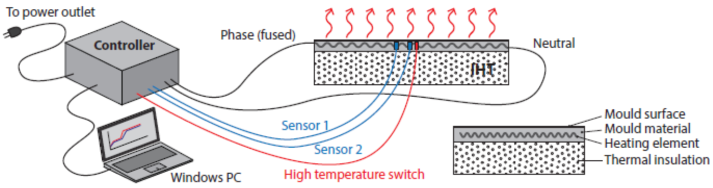

Figure 3.7: Schematic representation of the integrally heated tooling setup used for X-Core sandwich structure manufacturing at Donkervoort [21]

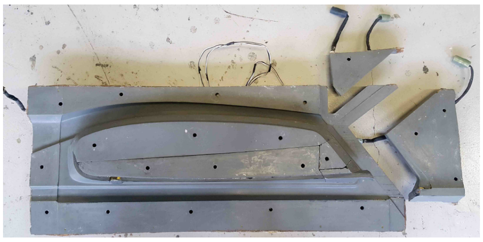

Figure 3.8: Integrally heated mould for the door window frame

3.2.5. S. Vial (2016): Relating Constituents to Material Properties

S.Vial focused on X-Core for his Master's thesis in 2016 [22]. His research brought forward knowledge on the dependence of X-Core material properties on the various constituents. The first phase consisted of replacing the polystyrene filler with hollow glass microspheres (HGM) under the name of Q-Cel 5028. This new filler provided higher compressive properties and higher thermal stability. The issue with the latent SR8500/KTA317 matrix was addressed through investigating a new epoxy based resin in combination with various hardener types. Epoxy resin under the name of Ancarez 4010® was combined with four different hardeners being UMX-144C, A2781, UMX-50F and UMX-157A. The potential high exothermic energies released during the cure of the thermosetting resin were recognized here and expected to be a potential issue as high temperatures could negatively effect the polymeric microspheres. Selection of the hardeners was based on temperature logging of fixed resin volume combined with rheology studies. Results are shown in figure 3.9. The UMX- 144C hardener was eventually selected because of its relatively low exothermic reaction

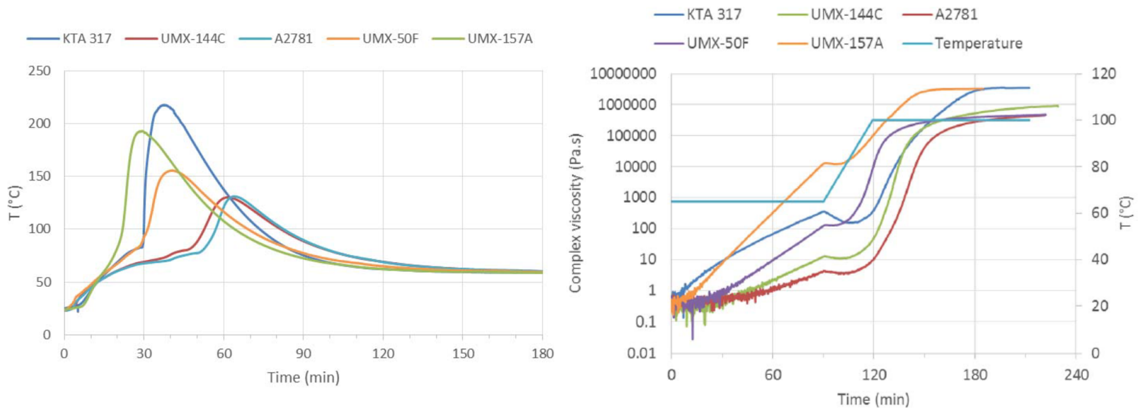

(a) Temperature logging of fixed weights of identical epoxy resin combined with different hardeners

(b) Complex viscosity during a cure cycle of epoxy with different type of hardeners

Figure 3.9: Temperature logging and complex viscosity measurements of different hardener types combined with epoxy

energy, slow reaction behaviour and optimal compressive properties compared to the other hardeners. Interestingly, compressive testing comparison of the slow reacting, low exothermic UMX-144C hardener and the faster reaction higher exothermic UMX-157A hardener revealed that the UMX-144C provided higher strength at higher resin volume fractions and higher modulus over the complete tested density range as indicated in figure 3.10.

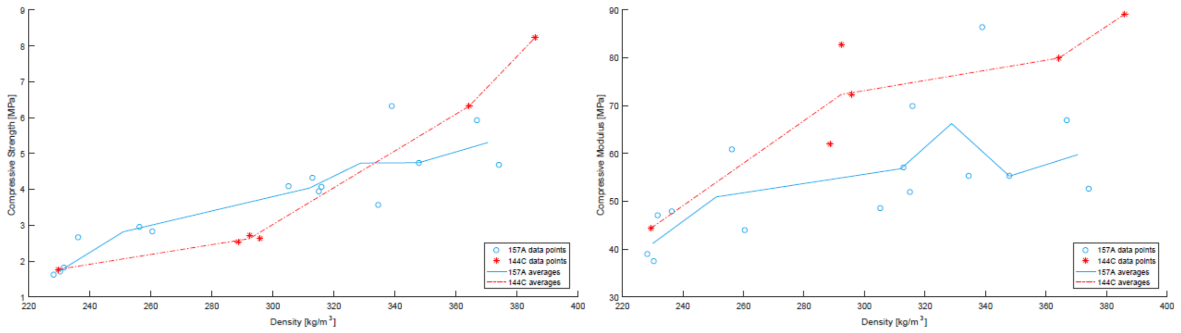

(a) Compressive strength over density

(b) Compressive modulus over density

Figure 3.10: Compressive properties comparison of two hardener types

The effect of an extending the cure cycle of 2 hours at 100°C with one hour was tested by comparing samples based on compressive strength. Consistent increase of the compressive strength was determined for the extended cure cycle.

A series of tests was also performed to determine the relationship between DU content and pressure generation of a mix. FlexiForce HT201 force resistive sensors were placed inside a metal mould with X-Core in place containing various amounts of DU microspheres. Equation 3.1 was presented to relate the DU content to the pressure generated by X-Core in bars. Chapter 6 discusses these measurements further.

$$P = 1.0653 + \phi_{DU} * 83.24 \tag{3.1}$$

Lastly, a designed experiment was set up to create a model for relating the volume fractions of the constituents to mix density and compressive properties. The resulting simplex model helps to identify which mixtures attain the highest compressive properties for a certain density as indicated in figure 3.11.

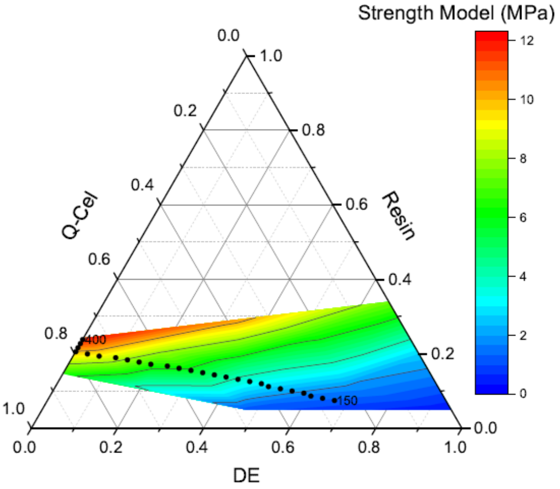

Figure 3.11: Simplex model showing the compressive strength attained for different volume fraction ratios at a constant 4% DU content. Block dots indicate the line of highest specific compressive strength.

During the time of S.Vial's research, two components of the Donkervoort D8 GTO were first manufactured using X-Core. The floor panels and door window frame used a $330 kg/m^3$ mix resulting in acceptable quality components which could be integrated into the cars.

3.3. Current Level of X-Core Technology

In the past four years, X-Core has evolved from mere concept to production ready product. Two parts of the current Donkervoort D8 GTO RS make use of the novel sandwich core and its one-shot manufacturing process, consisting of the floor panels and door window frames. Several other components of the GTO RS are also being converted to X-Core during and after this research.

3.3.1. Floor Panels

Simple geometry flat plates placed near the driver and passengers feet. $8mm$ thick with sharp 90° corners. X-Core is capable of pressing the fibres into these sharp corners to limit fibre bridging.

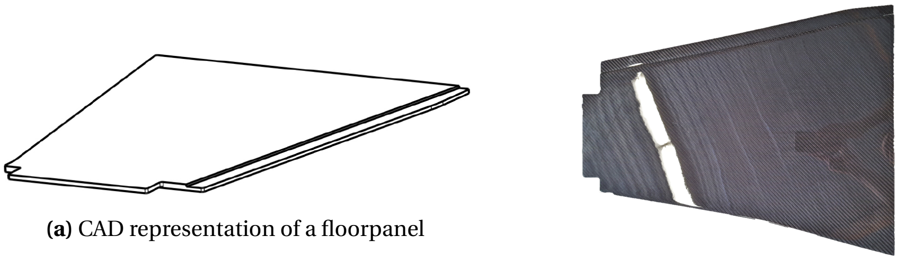

(a) CAD representation of a floorpanel

(b) Passenger side floorpanel

Figure 3.12: Pressure data attained in the research of S.Vial

3.3.2. Door Window Frames

Truly complex shaped product which showcases the capabilities of X-Core and its process. The door frames were designed specifically with X-Core in mind and are currently part of the production line at *Donkervoort* for production of the D8 GTO RS. A complex, eight piece, integrally heated mould is used for the one-shot production of this components shown in figure 3.8

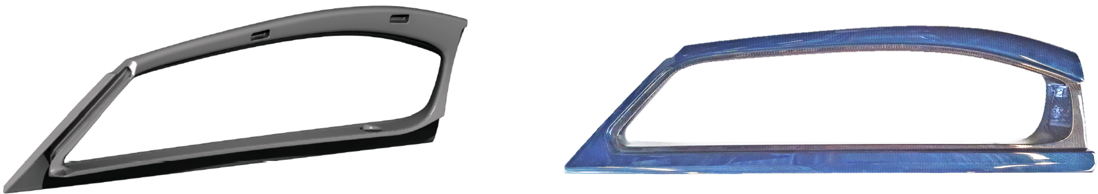

(a) CAD representation of a door window frame

(b) Driver side door window frame

Figure 3.13: Door window frame

3.4. Parallel Research Performed

In the time frame of this research, focusing on the behaviour of X-Core during the production process, two more concurrent studies are being executed at *Donkervoort*. D. Berckmoes is also devoting his MSc. thesis towards enlarging the body of knowledge around X-Core. His research focuses on relating process parameters and X-Core properties to the resulting facesheet porosity. Porosity in the form of pinholes and air inclusions are one of the issues currently still requiring post-processing of X-Core sandwich components. As a large amount of components on a Donkervoort D8 GTO RS consist of visual carbon fibre, e.g. the fibre weave remain visible and is only covered with blank lacquer, surface defects will remain visible to the naked eye. Sanding and filling of the pores currently takes up a significant amount of labour which leaves room for improvement. D. Berckmoes has developed a process window for the cure cycles leading to the best surface quality of the prepreg carbon fibre Furthermore, several mitigation strategies were explored to further optimize the surface quality.

Besides the research towards the carbon fibre surface quality another effort is made to develop lower density X-Core foams. For components without requirements on the structural strength very low density cores can be used. Currently, Divinycel H45 is applied in these parts with a density of only 48kg/m^3. In order to be competitive an X-Core mix with a density of 100kg/m^3 is under development. The lower door, indicated with the number 1 in figure 3.14 is used as a proof of concept component for this study. An integrally heated mould is being developed and build and prototypes using the low density X-Core variant are being produced and optimized. Lastly, the doorbeam (indicated with the number 2 in figure 3.14) is being prepared for the application of X-Core as well. This large volume, complex shaped component involves a hinge assembly where the one-shot capabilities of X-Core are really put to the test. The doorbeam currently applies the very low density H45 foam. Due to its large volume, X-Core densities currently developed lead to an unacceptably high component weight. Therefore, the combination of using a under-dimensioned low density foam core like H45 surrounded by a layer of higher density X-Core is investigated. This combination limits the increase in component weight and introduces the one-shot manufacturing process saving labour costs. To this extend, another integrally heated mould is also being developed for this part.

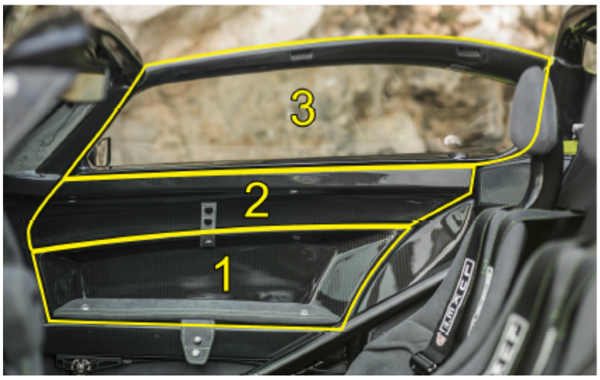

Figure 3.14: Complete door assembly inside the cockpit of the Donkervoort D8 GTO RS. Consisting of the lower door (1), doorbeam (2) and door window frame (3).

4

Optimal Mix Selection

As presented in chapter 2 the volume percentages of the mix constituents of X-Core can be altered to tailor the foam properties. For the research presented in this paper it is desired to limit the variability in the mixture to limit the amount of variables that have to be considered. Therefore, in this chapter an effort to select the most optimal mixture based on the current state of knowledge is presented. Several mixes will first be selected based upon their specific compressive strength. These mixes are then evaluated on several criteria concerning the manufacturing process. The compressive strength of the most promising mixture is then evaluated using a rudimentary test setup present at *Donkervoort*. Large deviations in the results were encountered which could be related to the setup drive compliance. This drive compliance was determined and validated after which the compressive strength results could be used to make the final mix selection.

4.1. Selection of Mixes of Interest

Research by S.Vial resulted in models that predict the density, compressive strength and compressive modulus for different mixtures with a 4% DU content. From these models, the mix composition providing the highest compressive strength at a certain density are defined. Figure 4.1 shows the simplex model representing the compressive strength. Each axis contains the volume fraction of one mixture component. Each point in the simplex thus presents a certain combination of these three mixture components which, combined with the 4% of DU, represent an X-Core type. The dotted line in the simplex present the mixtures with the highest compressive strength for a certain density in the range of 150-400kg/m^3.

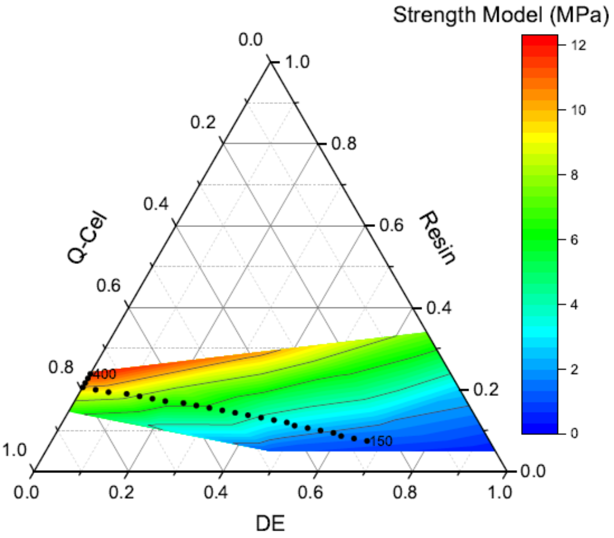

Figure 4.1: Simplex model predicting the compressive strength of X-Core mixtures with a constant 4% DU content. Dotted line indicates the mix compositions with the maximum strength at a given density between 150 and 400 kg/m^3 [22]

In creating lightweight components, materials with high specific properties are usually most interesting as these have the highest strength, stiffness or other property for a certain density. For the selection of the mixture to be used in the continued research the mix with optimal specific properties is thus preferred as *Donkervoort* is always aiming to lose weight on the car to increase its performance. This criterion narrows down the possible mixtures to those represented by the dotted line in figure 4.1.

Currently a mixture with a density of $330 kg/m^3$ is successfully applied in the construction of the floor panels and upper doors of the Donkervoort D8 GTO-RS. Therefore any X-Core compositions with a density above $330 kg/m^3$ are not of interest as they will only lead to an increased component weight. Previous experience with lower density mixtures ($<\pm 230 kg/m^3$) has shown that these become of a loose, dry and almost powdery composition before curing as not enough binder material is present to make the added microspheres stick together [22]. This is incompatible with the current manufacturing process described in section 3, which requires the uncured foam to be dimensionally stable in order to allow it to be moulded into the required shape. This lead to the decision too not consider mixtures with a density lower than $230 kg/m^3$.

The six mixtures between 230 and $330 kg/m^3$ with a $20 kg/m^3$ interval were selected from the line of optimal specific strength for evaluation. The corresponding composition of these mixtures is presented in table 4.1 along with the compressive strength (σ_c) predicted by the simplex model.

Table 4.1: Volume fractions of mixtures with optimal specific compressive strength

Density [kg/m^3]	**DU**	**DE**	**Resin**	**Q-Cel**	**σ_c [MPa]**
230	0.04	0.427	0.120	0.413	3.30
250	0.04	0.368	0.132	0.460	3.99
270	0.04	0.310	0.143	0.506	4.76
290	0.04	0.252	0.155	0.553	5.61
310	0.04	0.184	0.165	0.611	6.55
330	0.04	0.126	0.176	0.658	7.57

Looking at the predicted compressive strength values a wide variation is seen. Current sandwich structure components manufactured at *Donkervoort* employ either *Diab Divinycell® H45* foam with a compressive strength of $0.6 MPa$ [23] or *AIREX® C71.55* with a compressive strength of $0.95 MPa$ [24]. Therefore, even the 230 mix has a compressive strength far above the currently used foams and this property is therefore not a limiting factor in selecting the mixtures as the strength of current sandwich structure based components is adequate.

4.2. Pre-cured Mixture Evaluation for Manufacturability

The aim of this test is to define the lowest possible density mixture with optimal specific compressive strength which is still suitable for the currently applied manufacturing process. Suitability in this context concerns several properties of the mixture which together define the pre-cured foam. The properties on which the mixtures will be rated are presented below together with a description. A trade-off table is used to rank the mixtures and select the most interesting mix based on the criteria.

1. **Formability**

   How easy can the mix be shaped, deformed and placed inside moulds. Does it crumble into small parts or stick together as one mass? Evaluated by manually forming a ball of $\pm 10 cm$ in diameter and evaluating how well the material holds itself together.

2. **Manual pressure test**

   Manual pressure is applied to the formed balls. How many cracks appear and how easy can the mix be re-shaped? This represents the process of manually placing slabs of X-Core into a mould and pressing the foam into shape. Crumbling of the mixture while pressure is applied is unfavourable when placing the material into male parts of the mould. The balls were compressed by hand in about 10 seconds until a slab of $\pm 2 cm$ thickness remained.

3. **Stickiness**

   Does the mix stick to gloves? Less stick is preferred as it is easier to handle and place in the mould. Mixes with high binder content tent to adhere to gloves more readily than mixtures with lower amounts of binder. Nitrile gloves are used at *Donkervoort* and this property is therefore considered with respect to these types of gloves.

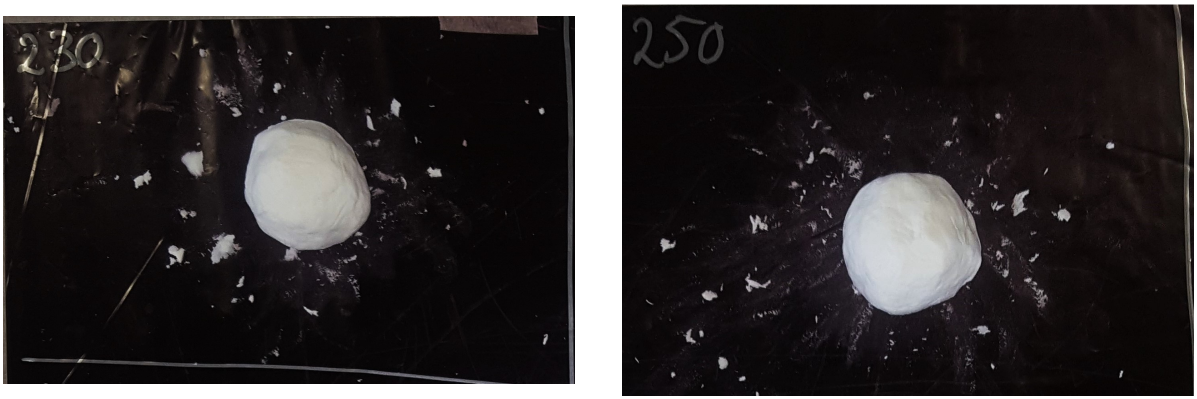

(a) 230kg/m^3 ball

(b) 250kg/m^3 ball

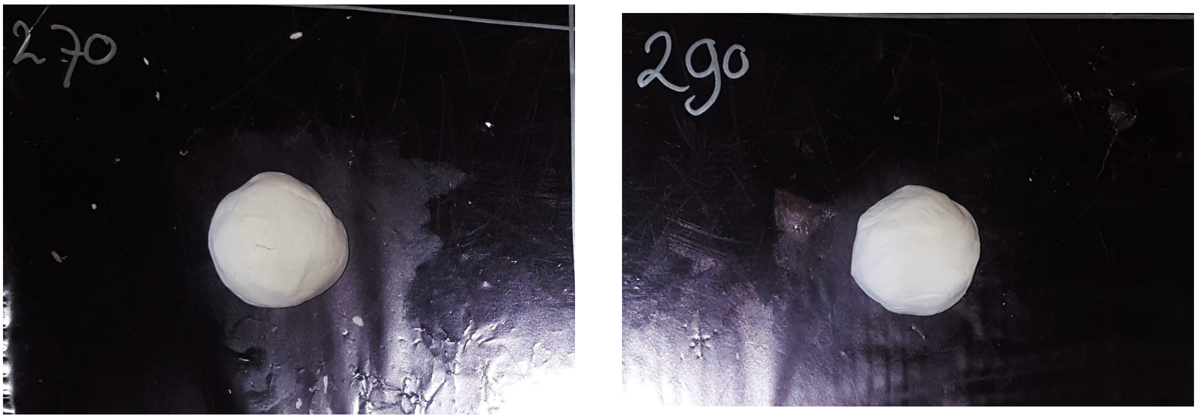

(c) 270kg/m^3 ball

(d) 290kg/m^3 ball

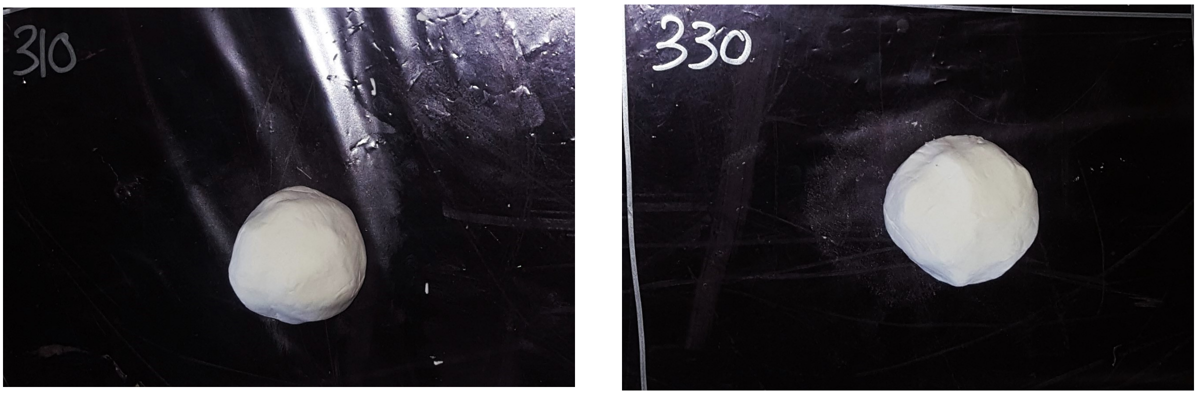

(e) 310kg/m^3 ball

(f) 330kg/m^3 ball

Figure 4.2: Balls shaped for formability test. Differences visible in residue separating from the main body

4.2.1. Formability

As described in section 4.2 balls, were shaped from the pre-cured X-Core variants and evaluated based on how easy the shapes were to form and how well these balls stayed together as one mass. Figure 4.2 shows the respective X-Core composition formed in a ball shape. 230 *(a)* and 250 *(b)* mixture balls show more residue compared to the 290 *(d)*, 310 *(e)* and 330 *f)* mixes. 270 *(c)* shows some residue but noticeably less compared to the two lighter mixes. An explanation for this is the lower resin content, see table 4.1, in the lower density mixes. The resin acts as a binder to make the microspheres stick together. Less binder material will therefore results in less 'glue' between the microspheres which can be the reason for pieces coming loose from the ball in the lighter mixes.

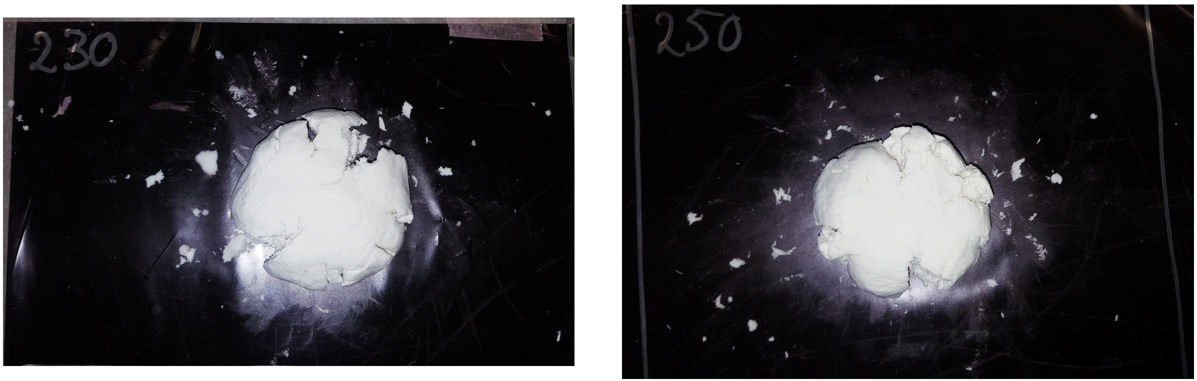

(a) 230kg/m^3 flattened ball

(b) 250kg/m^3 flattened ball

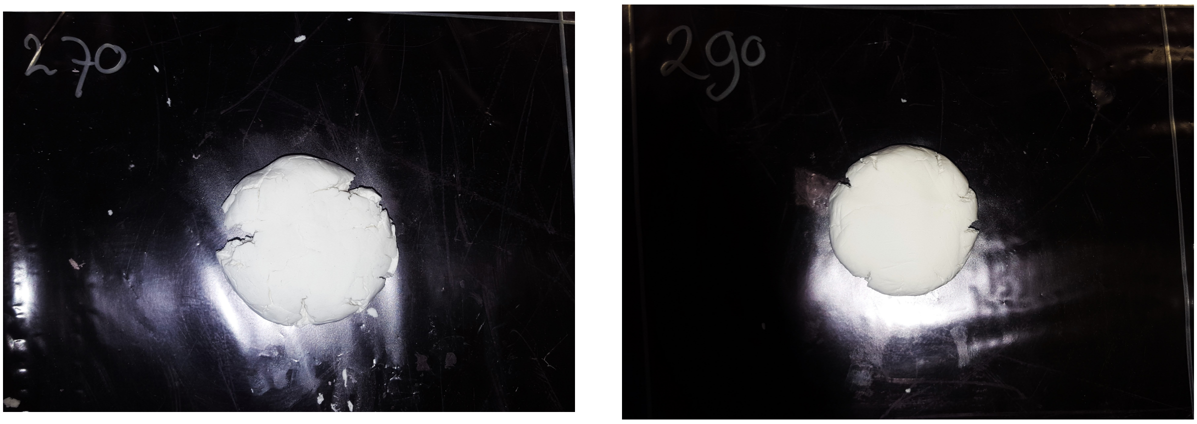

(c) 270kg/m^3 flattened ball

(d) 290kg/m^3 flattened ball

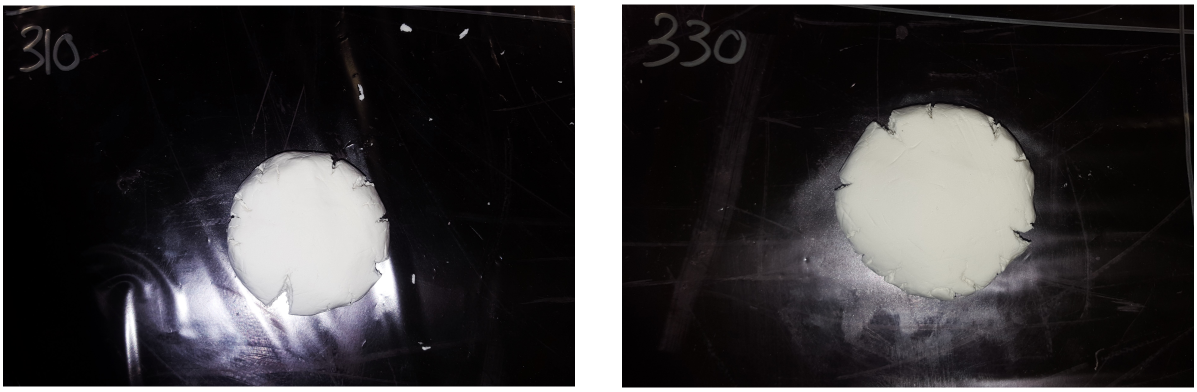

(e) 310kg/m^3 flattened ball

(f) 330kg/m^3 flattened ball

Figure 4.3: Balls flattened by manually applying pressure. Differences in the visible in the amount of cracking and material separating from the main body

4.2.2. Manual pressure test

The same balls created in section 4.2.1 for the formability test were pressed by slowly exerting pressure by hand until the height of the remaining slab was approximately 2cm. The level of cracking of the X-Core mass was evaluated. The 230 *(a)* sample shows the most severe cracking with a rupture running over nearly the complete diameter. The 250 *(b)* ball shows slightly less deformation but still large cracks are apparent. The cracks of sample 270 *(b)* are judged to be less severe compared to the lighter mixes. Comparing balls 290 *(d)*, 310 *(e)* and 330 *(f)* shows no significant differences but all three mixes do perform better compared to the 230 *(a)* and 250 *(b)* samples.

4.2.3. Stickiness

The amount of residue sticking to nitrile rubber gloves used by the composite department at *Donkervoort* while handling the mixtures was also evaluated. Mixes 230, 250 and 270 performed similar and no differences were noticed. Small amounts of X-Core stuck to the gloves but could easily be removed through rubbing the hand together. Mixes 290, 310 and 330 were noticeably more sticky compared to the other mixes. Large portions of the mix stuck to the gloves and were difficult to remove. This is undesirable as it means gloves will have to be exchanged multiple times during the manufacturing process when for instance the prepreg laminate requires adjustment. X-Core residue on the prepreg leads to white areas in the finished products, therefore contamination of the prepreg with X-Core needs to be prevented.

4.2.4. Trade-off and Mix Selection for Compressive Testing

Based on the three tests the respective mixtures were given points on a scale from 1-5, with one being the lowest score and five being the highest. The total points for each mix is the sum of the separate tests. This total score is then divided by the mix density, which results in a specific total score. The results are presented in table 4.2. The 270 and 290 mixes have the highest scores. Based on this, the 270 mix is selected as it attains the same score as the 290 mix at a lower density.

Table 4.2: Trade-off table for the selection of the optimal X-Core mixture composition

Criteria	**230**	**250**	**270**	**290**	**310**	**330**
Formability	2	3	4	5	5	5
Manual Pressure Test	1	2	3	5	5	5
Stickiness	4	4	4	2	2	2
Total Score	*7*	*8*	*11*	*12*	*12*	*12*
Specific Total Score	0.030	0.036	**0.041**	**0.041**	0.039	0.036

After evaluation, all six mixes were cured for 2 hours at 100°C in the metal mould shown in figure 4.4.

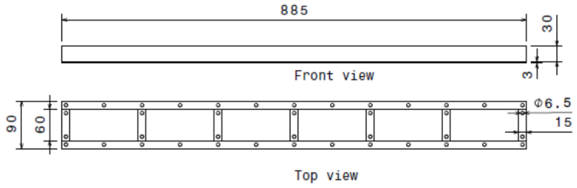

(a) Front and top view with dimensions in millimeters

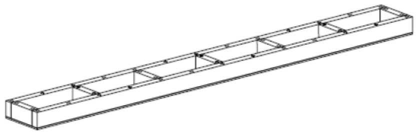

(b) Isometric view of the molds

Figure 4.4: Mold used to manufacture 130x60x30mm blocks of the six mix samples [22]

4.3. Compressive Strength Tests

To verify that the selected 270 mix indeed performs as predicted in terms of compressive strength it is subjected to mechanical testing. The manufacturing process used, considering mould filling and cure-cycle, is kept identical to that applied in the research of S.Vial in order to compare the outcome to the compressive strength predicted by this model [22]. To conduct the compression tests a setup present at *Donkervoort* is first used. This setup consists of a pressure jack, shown in figure 4.5, combined with a load cell based weighing balance and micrometer developed by R.Santos (2015) at *Donkervoort*. Although the setup does not conform to ASTM standards it allows for quick testing of samples to get an idea of the range in which the compressive strength falls. R.Santos concluded that results for compressive strength were 5% lower compared to tests conducted conform ASTM test standard D1621 on a Zwick 250kN bench.

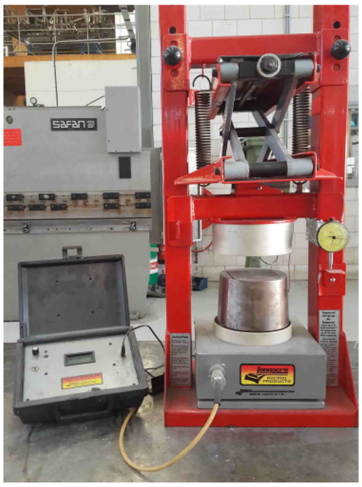

Figure 4.5: Pressure jack with load cell underneath and readout display combined with dial gauge micrometer [22]

4.3.1. Test Procedure

Six tests were conducted using the cured 270 mix sample block. The 130x60x30mm block was sectioned into 6 equal specimens of approximately 43x30x30mm. A pre-load between 0-10lbs was applied and the micrometer was zeroed at that point. Displacement steps of 0.25mm were used and the applied load was recorded after each increment. Compression was continued until at least 13% strain was reached. Strength values were taken at 10% strain after determination of the "zero-deformation" point through extrapolation of the steepest section of the curve to the horizontal axis as dictated by ASTM standard D1621 [25] for specimens showing no defined yield point before this strain level. Table 4.3 shows the results of the compressive tests. A large deviation of -29% is found compared to the expected strength from the simplex model. A possible explanation for this deviation is the drive compliance of the pressure jack, which has not been determined in previous research. Noticeable deflection of the jack arms was visible at high loads (>1000lbs). This could indicate that part of the deflection measured by the micrometer is actual deflection of the jack in stead of compression of the sample. Applying a drive compliance corrections leads to a shift of the stress strain curve to the left, this is depicted in figure 4.6. The stress values now correspond to a lower strain as part of the total strain is subtracted as the compliance contribution of the testing machine.

Table 4.3: Compressive strength results of the 270 mix tests conducted using the pressure jack

Sample	σ_c **[MPa]**
270.1	3.63
270.2	3.91
270.3	3.54
270.4	3.81
270.5	3.54
270.6	3.65
Average	3.68
Predicted	4.76
Difference	**-29%**

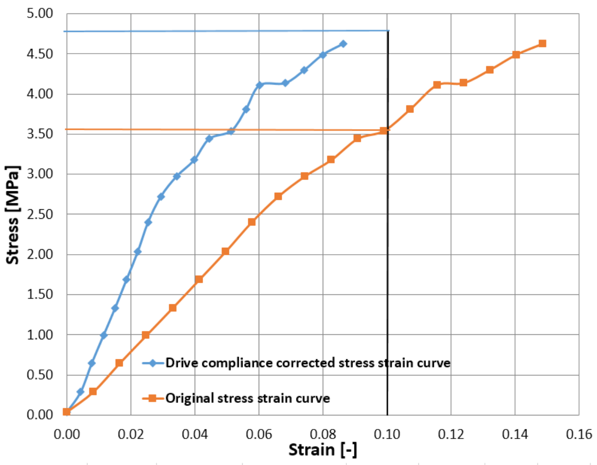

Figure 4.6: Comparison of stress strain curves with and without drive compliance correction

4.3.2. Pressure Jack Drive Compliance

To test this hypothesis, the 250 and 330 samples were also tested in compression using the exact same procedure. If drive compliance is the cause for the deviation then the total deviation should increase with increasing strength of the samples. The deflection of the jack increases with the applied loads so the error in the measured strain increases with the applied load as well. Higher loads are required to compress the higher density samples. The average strength value over six samples of the 250, 270 and 330 mixes are presented in table 4.4 along with the deviation from the simplex model predictions. A linear increase in the error is found with mix density leading to the conclusion that the drive compliance of the machine should be determined to correct for this deviation.

Table 4.4: Compressive strength test results and deviations from the simplex model predictions

Mixture	**250**	**270**	**330**
Average σ_c [MPa]	3.18	3.86	5.50
Predicted σ_c [MPa]	3.99	4.76	7.57
Difference	-25%	-29%	-38%

The drive compliance was determined by placing a relatively high stiffness solid block of steel in the pressure jack and consequently compressing this block. The deflection of the solid steel block is negligibly small for the loads applied assuring that the deflection read form the micrometer is purely related to the test setup. The deflections read from the zeroed micrometer are recorded up to a load of $2000 lbs$. The drive compliance is then attained by fitting a linear line (as strain is linearly dependent on stress according to Hooke's law) through the data, giving the amount of vertical displacement that should be contributed to the jack structure deflection in mm for a certain load in lbs, which is presented in figure 4.7.

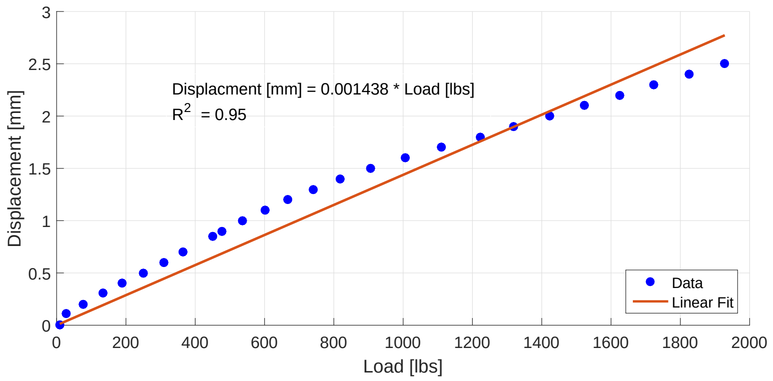

Figure 4.7: Comparison of stress strain curves with and without drive compliance correction

An example of the applied drive compliance on the test data was already presented in figure 4.6. A vertical line is drawn at 10% strain, where the failure load of the sample is determined. A relatively large shift in the data is present making it no longer possible to determine the failure load at 10% strain. New tests are needed which are continued to higher levels of strain to determine the failure load with the drive compliance correction applied.

4.3.3. Drive Compliance Validation

It was decided to manufacture a further two blocks of the 270 mix to compare the results of the *Donkervoort* jack setup to tests conducted according to ASTM standard D1621 [25] using a Zwick 250kN compression bench at the Delft University of Technology (DUT). From these two blocks four samples of 43x60x30mm were tested on the Zwick 250kN and another four samples of 43x30x30 were tested at *Donkervoort* using the pressure jack (see figure 4.8b).

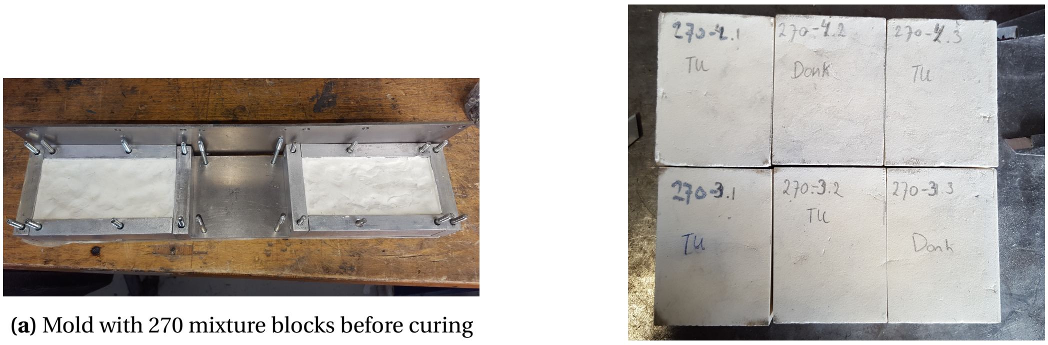

(a) Mold with 270 mixture blocks before curing

(b) Sectioned 270 mixture blocks with TU or Donk sample designation

Figure 4.8: Manufacturing and subsequent sectioning of the 270 mixture samples used for the compressive tests

Figure 4.9 shows the results of both test series. Sample *Donk 270-4.2.2* tested using the *Donkervoort* jack was discarded as a mistake was made during the recording of the data rendering it useless.

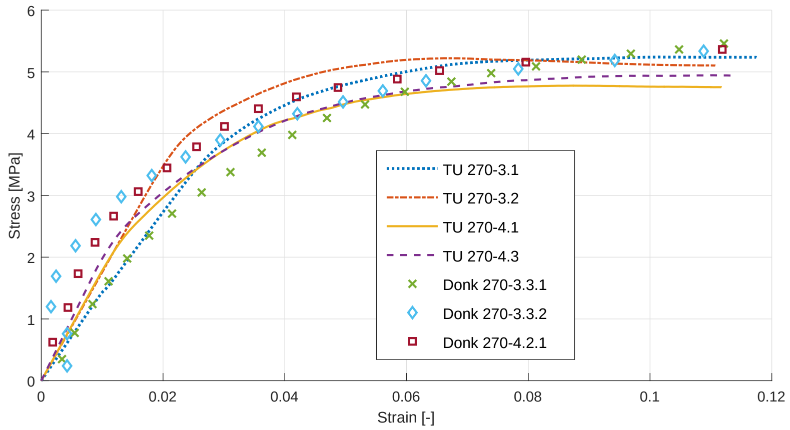

Figure 4.9: Stress strain curves of compression tests on 270 mix samples tested according to ASTM D1621 using the Zwick 250kN ($TU270-\#.\#$) and samples tested using the *Donkervoort* pressure jack ($Donk270-\#.\#.\#$)

Table 4.5 shows the extracted stress values at 10% strain for all samples. Furthermore, the density of every sample was attained. Five measurements were made with a caliper on each side of a sample from which the volume was attained. The samples were then weighed to the nearest 0.1g and the density was calculated. To compare the samples with the strength of the 270 mix according to the simplex model presented in section 4.1 the compressive strength of each sample was normalized to this density through applying equation 4.1.

$$\sigma_{c_{norm}} = \left(\frac{\sigma_c}{\rho}\right) * 270 \tag{4.1}$$

Table 4.5: Compressive strength results of both test series compared to the simplex model prediction

Sample	$\boldsymbol{\rho[kg/m^3]}$	$\boldsymbol{\sigma_c}$ **[MPa]**	$\boldsymbol{\sigma_{c_{norm}}}$ **[MPa]**	**Deviation [%] w.r.t. 4.76 MPa**
TU 270-3.1	285.84	5.24	4.95	3.97
TU 270-3.2	288.08	5.22	4.89	2.83
TU 270-4.1	274.22	4.78	4.70	-1.16
TU 270-4.3	275.71	4.94	4.83	1.58
Donk 270-3.3.1	286.06	5.28	4.98	4.64
Donk 270-3.3.2	280.39	5.18	4.99	4.78
Donk 270-4.2.1	279.28	5.36	5.18	8.93

Compressive strength of the samples tested with the Zwick 250kN bench are within 3.97% of the simplex model prediction of $4.76MPa$. The tests conducted at *Donkervoort* with the pressure jack are consistently higher than the model predictions. Samples *Donk 270-3.3.1* and *-3.3.2* differ by a maximal amount of $0.29MPa$ compared to the values attained on the Zwick 250kN. Sample *Donk 270-4.2.1* deviates more. Overall, the maximal difference with the simplex model prediction is 8.9% and the *Donkervoort* Jack predicts the strength of samples with a maximal difference of $0.48MPa$ compared to the Zwick 250kN. Applying the drive compliance correction has therefore reduced the error in the compressive strength prediction by 29-8.9 = 20.1%. Considering how basic the pressure jack is and how quickly it is able to produce these results makes it a very useful setup in attaining the compressive strengths of various X-Core mixtures, it is however necessary to take the drive compliance into account when performing these tests. For relative comparisons of different mixture types or initial determination of approximate strength values the setup at *Donkervoort* is adequate and therefore recommended if an uncertainty on the strength value of around 10% is acceptable. For more exact determinations of the strength values making use of a setup in accordance with ASTM D1621 is recommended.

4.4. Final Mix Selection

Based on the information presented, the $270kg/m^3$ mix was selected as base mixture on which further research will be conducted and is henceforth referred to as the "270-optimal mix" The selection of this mix provides potential weight savings compared to using the previous $330kg/m^3$ of $60g/L$ of X-Core. It is assured that the optimal combination of components is used to give the maximal compressive strength at this weight. Furthermore, the composition of the pre-cured foam has the characteristics required for the *Donkervoort* manufacturing process. The composition of the $270kg/m^3$ is presented again in table 4.6 in terms of pseudo-components. Which, in order to attain the real components fractions, need to be multiplied by (100-%DU). This assures an identical relative composition is always used for the resin, Q-Cel and DE constituents. DU levels can then be varied according to the required pressure generated by the mixture. This will be further discussed in chapter 6.

Table 4.6: Pseudo volume fractions of the "270-optimal mix"

Density [kg/m^3]	**DE**	**Resin**	**Q-Cel**
270	0.323	0.149	0.528

5

Tile Mould Design and Temperature Analysis

To create samples in a representative environment and process similar to the current production method applied at *Donkervoort* as introduced in chapter 2 a new mould was designed and manufactured. The choices which led to the final design of the mould and the evaluation of the temperature distribution on the mould surface are presented in this chapter. Furthermore, based on the results obtained in the evaluation of the temperature difference on the mould surface a new technique is evaluated to obtain a more even surface temperature which could be conveniently be integrated in the build process of the currently used integrally heated moulds.

5.1. Tile Mould Design and Construction

A parallel study conducted by D.O.Berckmoes [26] explored the effect of various process conditions on the quality of the carbon fibre facesheets. In function of this research, a mould was designed and constructed to produce square 175x175mm samples called 'tiles' with variable height from 5-80mm in 5mm increments. The mould is integrally heated through the use of carbon fibre heating elements in the form of braids. Section 3.2.4 gives a more detailed description and background of this technology used at *Donkervoort* for the production of X-Core sandwich structures.

5.1.1. Design Overview

Several requirements for the tile mould formed the basis of the resulting design. These requirements are:

1. Allow the manufacturing of variable thickness samples
2. Be insulated from the ambient atmosphere to prevent excessive heat losses
3. Minimize thermal mass to allow rapid heat up rates
4. Provide a uniform surface temperature distribution
5. Have minimal deflection of the mould surface (<0.5mm) under 10bar applied pressure

The resulting design choices are listed below with numbers in brackets referring to the labels in figure 5.1a showing a CAD model of the mould. With requirement 2 in mind the tile mould was designed to have 320x320mm lids which overlap the outside of the walls to allow insulation to be applied at a later stage if required (1). The lids are based on a sandwich panel construction using a Medium Density Fibre Board (MDF) as core material and a combination of glass/epoxy and carbon fibre/epoxy for the facesheets (2). The sandwich layup provides the required mould stiffness at a thickness of 26mm which was calculated by D.O.Berckmoes [26] to have deflection of 0.13mm at 10bar of pressure, satisfying requirement 5. Furthermore, the incorporation of a MDF core provides a layer of thermal insulation satisfying requirement 2. Stackable, 5mm thick, aluminium walls are used to provide the variation in height as required and allow a maximal stacking height of 80mm in 5mm increments (3). The high thermal conductivity of the aluminium walls aids in heating the sides of the specimens. Large pockets are cut in the aluminium walls to lower the thermal mass (requirement 3) and to limit transverse heat flows from the inside of the mould to the ambient air (4). Finally, 16 M8 bolts were used to close the mould.

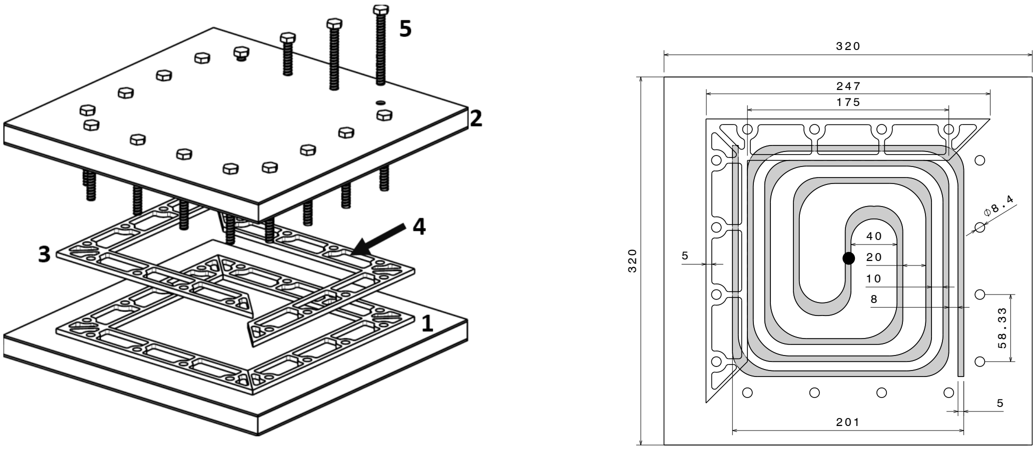

(a) Isometric view of tile mould; 1: Overlap of lids w.r.t. aluminium walls. 2: 26mm thick glass/carbon sandwich with MDF core, 3: Stackable 5mm aluminium walls, 4: Cutouts in aluminium walls limiting thermal mass, 5: Bolts used to close the mould.

(b) Heating tracing pattern and tile mould dimensioning

Figure 5.1: Tile mould isometric view (a) and corresponding heating tracing pattern (b)

Figure 5.1b presents a schematic drawing of a tile mould lid with the positioning of the carbon heating braid in gray. The braid pattern was chosen to provide an even temperature distribution at the mould surface. Reasoning behind this was that closer spacing of the braid near the edges would counteract the heat losses present in these areas as more area is exposed to the ambient atmosphere here. Spacing near the center of the mould is wider as less heat losses were expected to be present here. The thermocouples were positioned in the exact center of the mould indicated by the black dot in figure 5.1b.

5.1.2. Sample Manufacturing

The first experiments conducted in the tile mould using X-Core in combination with carbon fibre prepreg material resulted in poor quality facesheets. Large areas, in access of 10% of the area of the facesheet, consisted of dry spots where the fibres were not wetted. One such sample is depicted in figure 5.2. The sample has a thickness of 10mm and employed the 270-optimal mix, introduced in section 4, with a DU content of 4%. The cure-cycle consisted of a 1.5C/min heat-up rate followed by a hold at 110°C for 2 hours.

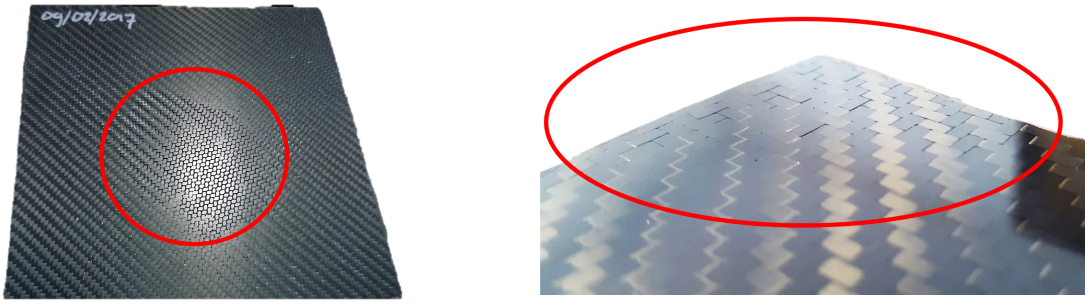

(a) Surface quality of a specimen manufactured in the tile mould

(b) Poor quality of the facesheet in the corners of a tile manufactured with tile mould

Figure 5.2: One of the first samples produced with the tile mould showing poor surface quality of the carbon fibre facesheets

Evaluation of particular areas in which poor quality regions appeared led to the hypothesis that temperature gradients at the mould surface might be the cause. The corners of the tile are surrounded by aluminium mould walls which could cause the temperature to be lower at this region due to heat losses.The wide heating tracing spacing depicted in figure 5.1b might result in too low temperatures in this region. Several more tiles of 10mm thickness with variations in heat up rate, dwell temperature and DU content were manufactured all resulting in similar surface qualities. It was therefore decided to investigate the temperature distribution of the tile mould to explore if this could be the cause of the poor surface quality of the samples.

5.2. Tile Mould Surface Temperature Profiling

The first sample manufactured using the tile mould showed dry areas at the corners and center of the sample covering around 40% of the total surface area. The location of the dry areas near the corners of the sample indicated that a temperature difference might be present at these locations due to insufficient insulation of the mould. To investigate this a test setup was devised to monitor the surface temperature distribution of the mould. Furthermore, this test setup was used to evaluate several methods aimed at providing a more even distribution of the surface temperature which allows better control of the process temperatures.

5.2.1. Test Setup and Sensors

To monitor the temperature distribution on the tile mould surface an array of temperature sensors is placed against the surface in a regular grid pattern. This allows the temperature data to be interpolated to create a surface plot of the temperature distribution at the mould surface.

Digital temperature sensors of the type DS18B20 by Maxim Integrated are used in this setup. An picture of such a sensor is shown in figure 5.3. These sensors have the advantage of requiring only one pin for communication with a microprocessor through a unique serial code, allowing multiple sensors to be read out using only one communication wire. The DS18B20 sensors have an operational range of -55 to +127.75°C with a rated accuracy of +-0.5°C [27]. The resolution can be programmed to temperature increments of 0.5, 0.25, 0.125 or 0.0625°C.

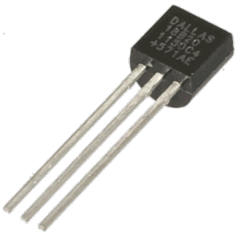

Figure 5.3: A DS18B20 digital thermosensor (Figure taken from www.domoticx.com)

Higher resolutions require longer conversion times per measurement ranging from 93.75ms for 0.5°C to 750ms at 0.0625°C. The minimal time increment required to read and log the temperature all sensor in an array is dictated by the sum of the time for conversion required by each separate sensor. The maximal heat up rate expected to be used is 3°C/min giving 0.05°C change in temperature per second, or 0.25°C/min per 5 seconds. Thirteen sensors will be applied in this setup. Therefore, an increment of 0.25°C is selected giving a conversion time of $13 * 187.5ms = 2.44s$. This allows to capture all changes in temperature with 0.25°C accuracy as the lowest possible sample rate is lower than the actual temperature change present in the mould. To limit the collection of unnecessary data the sampling rate was set at one reading every 5 seconds. More information on these sensors can be found in the datasheet provided by Maxim Integrated [27]. Thirteen DS18B20 sensors are combined and connected to an Arduino Nano® which handles the conversion of the data and provides a 5V power output and ground connection needed to power the sensors. A SD-card module is connected to the Arduino® for the collection of the temperature data into a textfile. The data can then be read out and analysed on a computer. The thirteen sensors are organized in a regular grid pattern as shown in figure 5.4a. In order to mimic the conditions of the actual process of curing X-Core inside the mould a 20mm high X-Core sample was cured with the sensors in place. The foam formed around the sensors leaving only the top area of each sensor exposed to the mould surface (figure 5.4b). The 20mm layer of X-Core also provides insulation from the opposite side of the mould to make sure that the tempera-

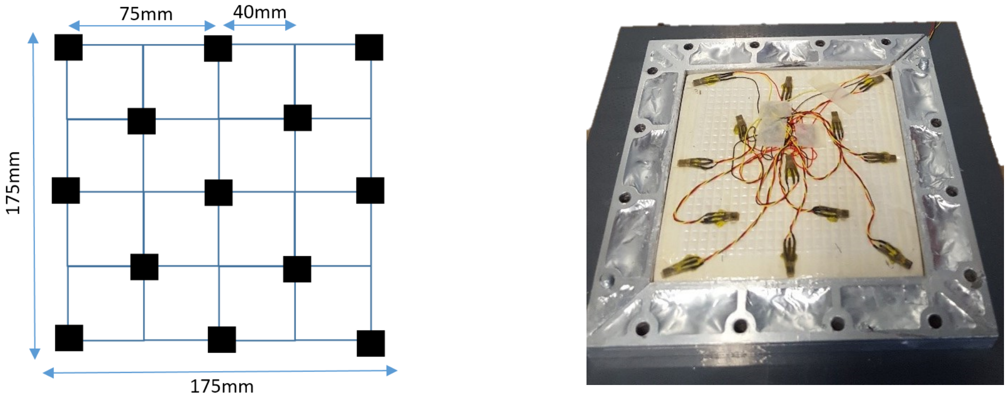

(a) Regular grid pattern used for temperature sensors

(b) Array of DS18B20 sensors placed in tile mould

Figure 5.4: Overview of the test setup used for determining the temperature distribution on the tile mould surface

ture distribution of the surface with the sensors is not influenced excessively by the other side of the mould. Additionally, the layer of X-Core limits the effects of convection currents influencing the temperature distribution which would otherwise also not be present in the actual process were X-Core is in direct contact with the mould surface.

5.2.2. Data Post-Processing

The data recorded during a test is stored on an SD-card and analysed on a personal computer. The data files consumed around 140kB per hour of data collection. Any values listed in the tables present in the next sections are those extracted from the actual sensors them selves and are not attained through data fitting. Surface temperature plots were created by using the 'griddata' function in MATLAB based on a 'v4' biharmonic spline fitting method. The sensors were not located at the exact edge of the tile mould, and therefore the corner and edge regions are purely based on the extrapolated data-fit. For this reason, the surface plots are only used to visualize the temperature distribution patterns and no conclusions are based on the values of the fitted data between the actual sensor locations.

The presence of electromagnetic waves generates by the alternating current in the heating braids caused some interference issues with the sensors. Some data samples showed erroneous values, being zero, negative or $\gg$127.75. However, as data was recorded for every 5 seconds it was possible to filter out these false readings in MATLAB through looping through the data and setting any false reading equal to that of the previous data point. Revision of the plotted data in figure 5.6 shows that this filter has no significant effect on the data trends as no plateau regions are visible indicating that large portions of time are dictated by erroneous readings.

5.2.3. Test Series

A series of tests was set up to discover the diffusivity of the temperature on the mould surface. For this, the top section of the tile mould was used which is identical to the bottom section as described in section 5.1.1. These test aim to provide a relative comparison of different mould setups as conditions are very specific to the used mould. Therefore, there is no preference for either the top or bottom side and the top side was thus selected for convenience. First, the distribution along the surface without any modifications was tested. After this, the mould was insulated using a band of breather cloth wrapped around the aluminium walls to prevent excessive heat loss through the sides of the highly conductive mould sides (see figure 5.5a). Furthermore, 6 layers of breather cloth were placed over the mould and 4 layers were laid under the mould. These layers insulate the mould from the relatively cold steel table which remains at room temperature during the measurements and prevent excessive heat loss at the top of the mould through convection.

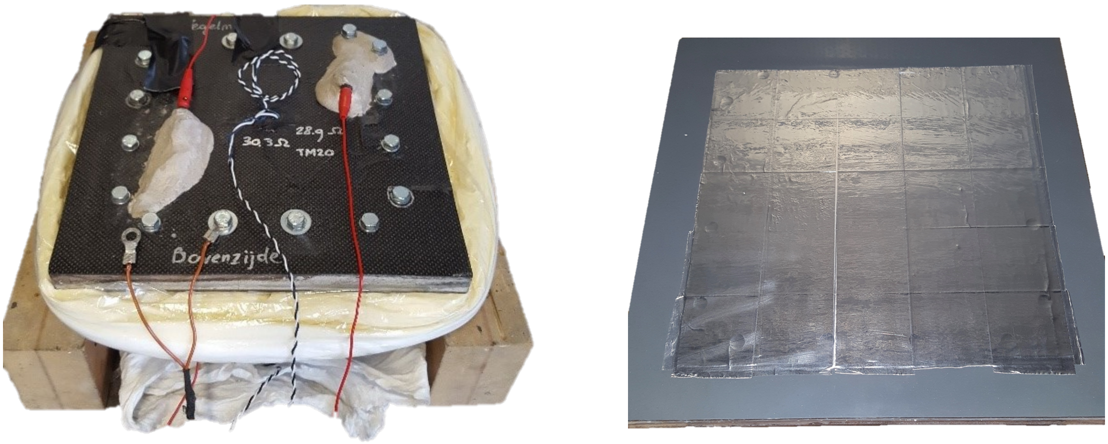

(a) Tile mould with breather cloth wrapped around the aluminium walls as insulation band (white)

(b) Aluminum tape applied to the tile mould surface

Figure 5.5: Depiction of the tile mould with the isolation band in place (a) and the aluminium tape placed on the tile mould surface (b)

Aluminium Surface

Furthermore, the effect of adding a layer of aluminium on the mould surface was investigated to explore if this would cause noticeable difference in the surface temperature distribution. The original mould surface consists of a gel coat which is a mix of epoxy resin with aluminium spherical particles which increase the strength and toughness of the surface. The thermal conductivity at room temperature of epoxy is $0.3W/mK$[28] compared to 200-220W/mK[29] for aluminium 6060. Therefore, the addition of aluminium can help to make the concentrated heat generated by the carbon braids more diffuse and lower the differences in temperature at the mould surface. To test this hypothesis, aluminium tape available at *Donkervoort* by *HPX* with a thickness of $0.075mm$ per layer was placed on the mould surface in either 1, 4 or 8 layers to create a layer of aluminium of 0.075, 0.3 and $0.6mm$ respectively (see figure 5.5b). Aluminium sheet material was used to create plates with a thicknesses of 1 and $1.5mm$. In total, seven different tests were conducted. The test variables of each test are listed in table 5.1.

Table 5.1: Tests conditions used to define the temperature distribution on the tile mould surface

Test	Isolation	$t_{alu}[mm]$
1	X	0
2	$\surd$	0
3	$\surd$	0.075
4	$\surd$	0.3
5	$\surd$	0.6
6	$\surd$	1.0
7	$\surd$	1.5

Test were conducted for 80 minutes capturing the ramp up to $110°C$ from room temperature, at $1.5°C/min$, which takes ± $60min$. A hold for $20min$ was employed to also capture the first part of the temperature hold at $110°C$. This was chosen as the X-Core expansion takes place during the ramp up when $85°C$ is exceeded (see chapter 6). Temperature differentials here can thus be of interest as local pressure differences could be linked to the varying quality of the facesheets. Furthermore, the overshoot encountered after the ramp up lead to a temperature peak. The differences in temperature are shown to be maximal during this peak as will be explained in the following paragraphs.

5.2.4. Temperature Differences at Mould Surface

For each measurement point the maximal and minimal temperatures are obtained over the 13 sensors. The difference between these values (ΔT) is recorded and presented in figure 5.6 for each mould setup. The maximal temperature differences that occurred during the duration of the tests (ΔT_{max}) are summarized in table 5.2 together with the temperature differences present when the mould reaches $85°C$ (ΔT_{85}). These values are compared to the baseline, for which test 2 is selected. This allows comparison between test 1 and test 2 on the effectiveness of the applied isolation and enables comparison between test 2 and tests 3-7 on the effect of the aluminium at the mould surface.

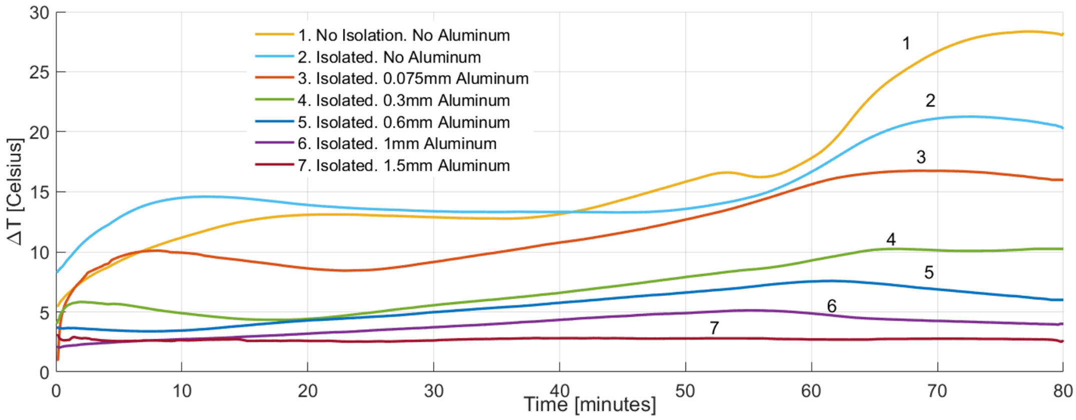

Figure 5.6: Maximal temperature difference (ΔT) between all sensors over time for tests 1-7

Table 5.2: Table with temperature differences at the mould surface when a point in the mould reaches 85°C; $\Delta\ T_{85}$ and the maximal overall temperature difference experienced during the complete test; ΔT_{max}. Both values are compared to test 2 and the % difference is listed.

Test	$\Delta T_{85} [^\circ C]$	diff. ΔT_{85} w.r.t. test 2	$\Delta T_{max} [^\circ C]$	diff. ΔT_{max} w.r.t. test 2
1	12.8	-3.8%	28.5	+31.0%
2	13.3	0.0%	21.5	0.0%
3	9.5	-28.6%	17.0	-20.9%
4	6.3	-52.6%	10.5	-51.1%
5	5.3	-60.2%	7.7	-64.2%
6	4.3	-67.7%	5.5	-74.4%
7	2.8	-79.0%	3.3	-83.7%

Looking at figure 5.6 and table 5.2 it is noted that without any modifications, the maximal difference, ΔT_{max}, in temperature on the mould surface is as high as 28.5°C for test 1. Considering the set-temperature of the mould being around 110°C, this is a significant difference. Adding the insulation lowers the difference to 21°C as heat loss around the mould, which gives rise to temperature gradients, is limited. Adding a layer of highly thermally conductive aluminium has a clear positive effect on the temperature distribution. Lowering the difference to 3.5°C with a thickness of 1.5mm aluminium. The temperature differences present in the mould when the first sensor reaches 85°C is referred to as ΔT_{85}. The first two tests show comparable values of approximately 13°C. Again, adding aluminium lowers the temperature delta. Only 1 layer of aluminium tape at 0.075mm thickness gives a reduction in ΔT_{85} of almost 29%. Increasing the thickness of the aluminium to 1.5mm further reduces the temperature difference to as little as 2.8°C. In section 5.2.6 the possible implications of these differences is further discussed.

The mentioned values are only valid for this exact mould setup, and may vary when different mould shapes and braid patterns are applied. However, the results do provide a good idea of the relative difference a certain layer of highly conductive material can have on the surface temperature distribution of a mould compared to the gelcoat surface.

Figure 5.7 gives the maximal temperature difference and temperature difference when the mould is 85°C against the thickness of the aluminium layer at the mould surface. An exponential function is fit to this data. The highest gains can be made in the first 0.6mm of aluminium. Afterwards, decreases in temperature delta's are reduced but still present. This plot indicates how effective even a few layers of aluminium tape on the mould surface are in creating a more diffuse surface temperature.

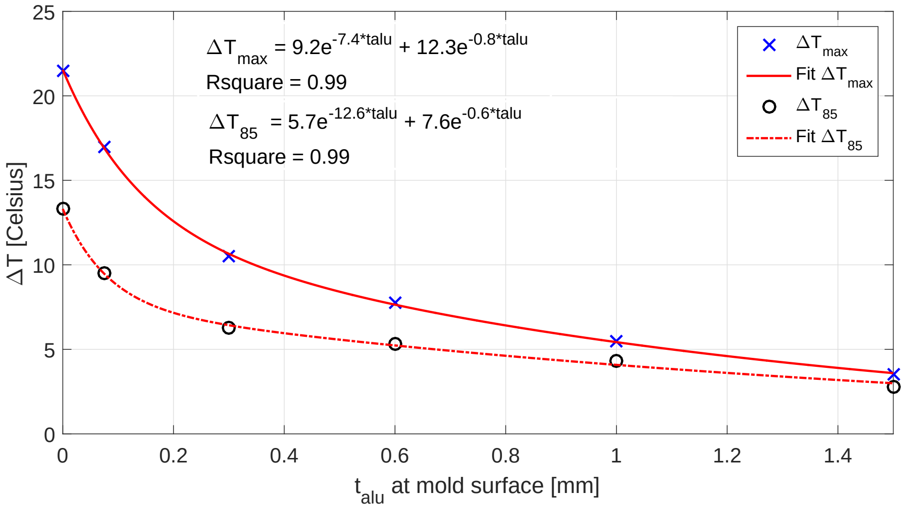

Figure 5.7: Maximal temperature differences, ΔT for a certain thickness of aluminium at the mould surface

5.2.5. Temperature Overshoot

Another effect of adding the aluminium layers was the lowering of temperature overshoot present at the mould surface. All tests had a temperature setpoint of $110^{\circ}C$, however test 1 showed an overshoot to above $127^{\circ}C$ (above the range of the DS18B21 sensor), the actual value is estimated to be between 132-$134^{\circ}C$. Adding the insulation limited the overshoot to $126^{\circ}C$, which is still $16^{\circ}C$ above the set-temperature. Subsequent addition of layers of aluminium lowered the overshoot significantly. $0.075mm$ aluminium already decrease the overshoot to only $118.7^{\circ}C$ and at $0.3mm$ or more the overshoot is nearly non-present. This is depicted in figure 5.8, along with the maximal temperatures present during the cure-cycle in the table 5.3.

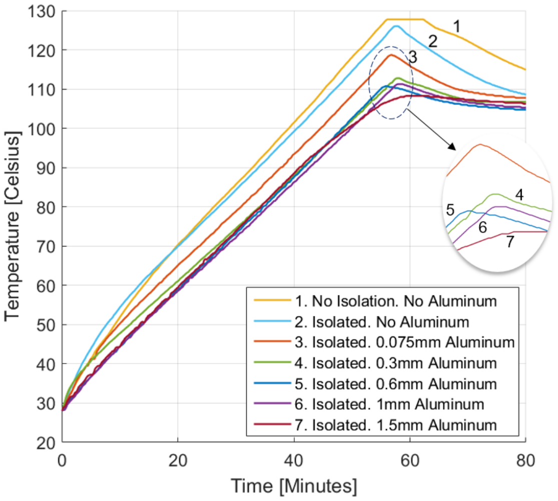

Figure 5.8: Maximal temperatures at the mould surface over time for tests 1-7. Test 1 influenced by temperature sensor limit of $127.75^{\circ}C$

Table 5.3: Maximal temperatures encountered at the mould surface during tests 1-7. Values for test 1 are estimates are sensor limit was exceeded

Test	T_{max} [$^{\circ}C$]	Diff. w.r.t $110^{\circ}C$
1	132-134	20.0%
2	126	14.5%
3	118.75	7.9%
4	112.75	2.5%
5	110.75	0.7%
6	111.25	1.1%
7	108.25	-1.6%

The explanation for this overshoot is found in the surface plots of the temperature distribution for the different tests. Figure 5.9 shows the surface temperature for test 1 and test 7 at the point when the maximal temperature is reached. Attention is called to the centre of the surface. This corresponds with the location of the thermocouple in the tile mould as discussed in section 5.1.1. It is clear that due to the large temperature gradients in the unaltered tile mould the exact centre of the surface has a lower temperature compared to the rest of the surface. Therefore, the software used to control the temperature reads a lower value than is actually present in the mould. Adding the layer of aluminium assures that the concentrated heat of the carbon braids is evenly spread out over the surface. The location of the thermocouple now has the same temperature as the surrounding area meaning the temperature read by the software is much closer to the actual mould temperature. Another solution can be sought in the placement of the thermocouples or the use of multiple thermocouples at different locations from which the readings can for example be averaged. This could reduce the temperature overshoot, but in itself would not change/improve the temperature differences present in the mould.

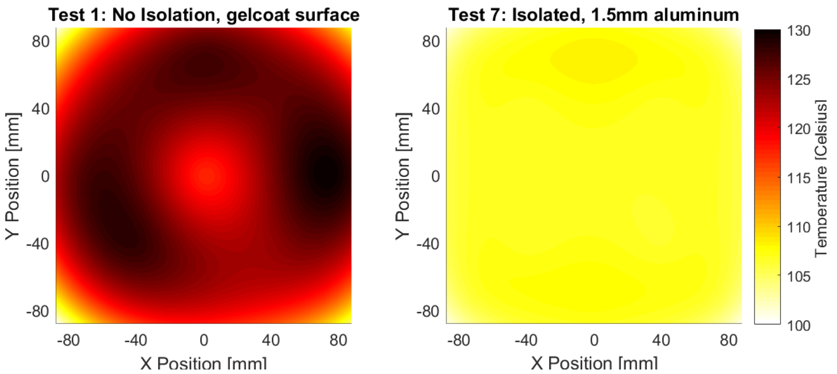

Figure 5.9: Surface temperature distribution at maximal temperature during cure-cycle for tests 1 and 7

5.2.6. Temperature Distribution at T=$85^{\circ}C$

The sample presented in the beginning of section 5.2 had higher void contents and dry areas in the centre and around the edges compared to the rest of the surface. A possible explanation is the temperature distribution in the mould at the initiation of expansion, when the surface reaches $85^{\circ}C$. Table 5.2 presented the magnitude of these differences at this temperature in the mould. S.Vial noted that the pressure generated by X-Core is not of a fluid type [22]. This implies that local pressure variations can occur when expansion differences are present. These differences could be present if the pressure generated by DU is dependent on temperature. This is expected as the expansion of DU is related to the expansion of the gas inside the microsphere of which the expansion increases with temperature. This will be further discussed in chapter 6. Local pressure differences on the facesheet combined with the effect of the temperature difference in itself could be related to the defects encountered in samples manufactured without aluminium and/or insulation present. Further support for this is given in figure 5.10. The 'cold-spots' are clearly visible for test 2 and are in the same location as the poor quality areas of the samples. Using aluminium at the mould surface is very effective in reducing the cold area in the centre which is basically not distinguishable any more for test 5. The cold areas in the corners are effectively reduced by using $1mm$ aluminium or more. Applying a $1mm$ aluminium plate and insulation led to large improvements in the laminate surface quality as shown in figure 5.11b.

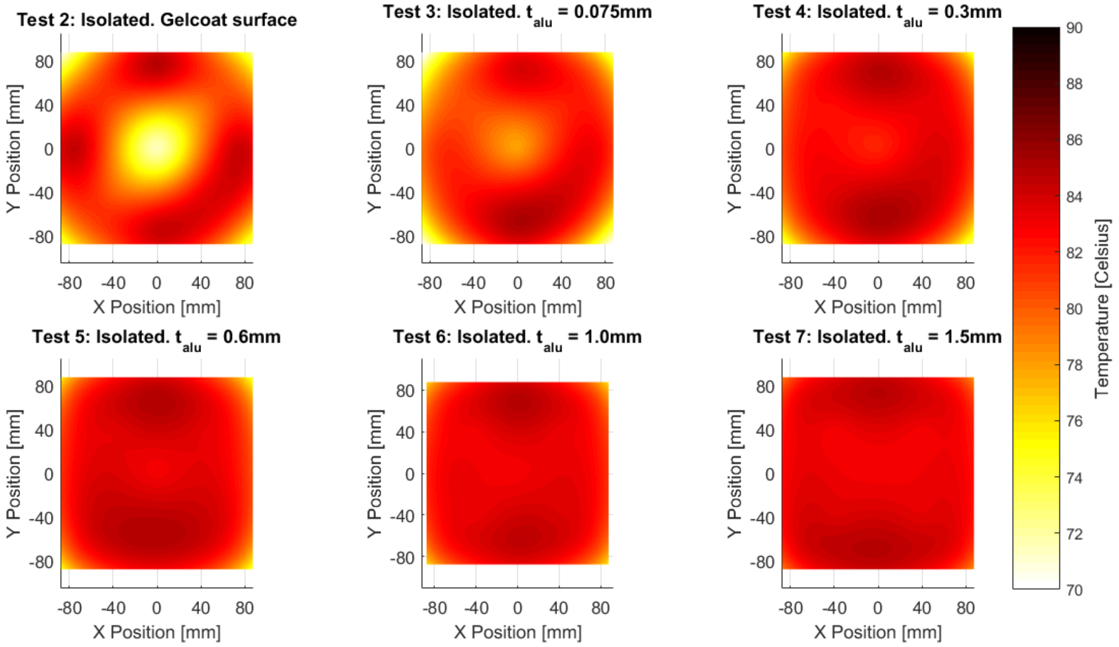

Figure 5.10: Surface temperature distribution when $85^{\circ}C$ is reached for tests 2-7

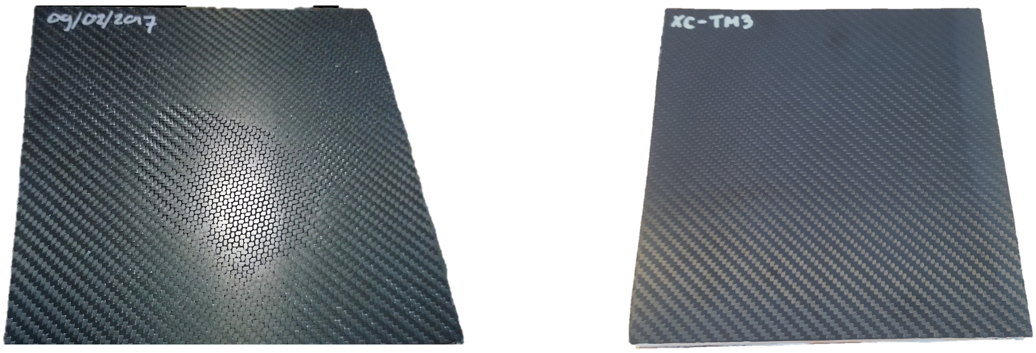

(a) Surface quality of tile manufactured with unaltered tile mould conform test 1

(b) Surface quality of tile manufactured with insulated and aluminium surface tile mould conform test 6

Figure 5.11: Comparison of tile mould sample surface quality related to temperature distributions according to test 1 (a) and test 6 (b)

5.2.7. Conclusions and Recommendations

The application of a layer of 0.3-1.5mm of aluminium lowered the maximal temperature difference from 28.5°C to 3.5°C showing that this is highly effective in providing a more controlled and even temperature distribution at the mould surface. Comparison of two samples showed that through lowering the maximal temperature difference at the surface and eliminating the cold-spots in the mould the distinct areas with high porosity and dry fibres were eliminated. Overall surface porosity was reduced from >40% to values around 2-6% [26].

The use of an aluminium plate between the original mould surface and the product can easily be applied when producing products with a large flat surface. However, the reason why X-Core is so attractive is the fact that it can be used to produce complex shaped sandwich constructions in one-shot. Complex shaped parts required complex shaped mould surfaces, which are not as easily covered with aluminium plate material. The currently used *HPX* aluminium tape is stiff and creases when applied on double curved surfaces. These creases will create defects in the products which counteracts the original purpose of applying the tape. For these reasons, other methods of improving the surface temperature distribution through applying a highly thermally conductive layer between the heating braid and the mould surface will be explored in the next section.

5.3. Methods for Integrating a Highly Conductive Layer in Moulds

Three methods to improve the surface temperature distribution of the moulds applied for the production of X-Core sandwich products at Donkervoort are compared in this section. Firstly, the initial method of applying layers of aluminium tape is re-evaluated. Then the possibility of using full metal moulds is explored. Lastly, the integration of a copper mesh inside the mould layup is discussed.

5.3.1. Discussion of Possible Methods

In this section, the three considered methods are shortly discussed and the dis/advantages of each method are listed.

Stretchable Aluminium tape

Aluminium tape can be applied to the existing mould surface in the amount of layers required to reach the desired thickness. The currently available aluminium tape by *HPX* is very stiff and has little elasticity although actual numbers are not provided by the manufacturer. Other types of aluminium tape are on the market which provide up to 3.5% of elongation like *3M™High Temperature Aluminium Foil Tape 433.* This product also has excellent high-temperature resistance up to 316°C which is far above the actual use temperature inside the moulds. The advantages and dis-advantages of this method are listed below:

+ Current tooling does not require replacement
+ Easily applicable and replaceable
+ Cheap
+ Careful layer thickness control
- Creases in the tape can lead to surface defects
- Unknown Durability
- Product dimensions decrease

Metal mould

Metal moulds are widely used in composite production for their superior surface quality and high stiffness. The moulds can be heated using an oven, autoclave, hot-press or oil bath/circulation. This mould type is however very costly to produce. The cost of an A-class surface finish milled aluminium mould can vary between €10,000 - €150,000 depending on size and complexity. These costs are acceptable when large volumes are produced, smearing the mould cost over many products. *Donkervoort* produces around 30-40 cars per year leading to high tooling costs per part. The advantages and dis-advantages of this method are:

+ Very low surface temperature differences
+ Durable
+ Very high quality surface finish (for class-A surface finish)
- Expensive compared to the material and labour costs of the resulting part
- Requires all new tooling
- Current heating method not applicable
- High thermal mass reduces ramp rates achievable
- Heavy tooling reduces process flexibility

Copper mesh

Integrating a layer of highly conductive material in the layup between the mould surface and heating braids is another possibility. This layer can provide a more diffuse heat input into the gelcoat mould surface. Copper mesh is already incorporated into the layup of aircraft as lightning protection. The thermal conductivity of copper is $403 W/mK$[30], twice that of aluminium and around 1000x that of epoxy. Many types of copper mesh are readily available and prices are in the range of those of carbon fibre prepregs. The advantages and dis-advantages of this method are listed below:

+ Can be integrated into the current mould production technique
+ Affordable at around the same price per m^2 as carbon fibre prepreg material
+ Does not affect the surface quality of the mould surface
- Unknown durability
- Unknown effectiveness

5.3.2. Trade-off

A trade-off is set up to evaluate which method is most interesting. The criteria are weighed on a scale of w = 1-5. The scores are given on a scale of 1-10. The motivation for the scores can be read in section 5.3.1. The considered criteria for *Donkervoort* are:

Durability: w = 2

How durable are the resulting moulds when applying the method? A weight of 2 is given to this criteria as *Donkervoort* produces a low volume of cars per year. Moulds are therefore used only around 80-100 times every year.

Ease of integration: w = 3

How easily can the method be implicated at *Donkervoort*. Does it require large adjustments to the current manufacturing process? This criteria is given a weight of 3. If significant improvement can be achieved it is acceptable to spend time into the integration of the method. Man power is limited however at the company, and a quickly implemented solution is therefore always preferred.

Effectiveness: w = 4

How effective is the method is creating a more diffuse surface temperature distribution compared to the gelcoat surface moulds? The main reason to apply the methods is to improve the surface temperature distribution, a weight of 4 is therefore attributed to this criterion.

Cost: w = 4

How large is the investment required to implement the method. *Donkervoort* is a relatively small company which is not directly capable of making large investments for developments. Cost is therefore an important parameter and is weighed at 4.

Surface quality: w = 4

How is the prepreg surface quality effected by the method? If the method negatively influences the surface quality of the products it will nullify the reason for implementing the method in the first place. Again, a weight of 4 is given to this criterion. Due to its ease of application and integration into the current moulds combined with the low cost the aluminium tape acquires the highest score. However, the difference with the copper mesh solution is small although several parameters, like the durability and effectiveness are not known and these values are therefore predictions. It is clear that the use of metal moulds has to be excluded. Already based on its cost and need to completely re-design the manufacturing process makes it an unrealistic option for a small company like *Donkervoort*. Based on the trade-off it was decided to explore the option of integrating a layer of copper mesh into the mould layup to be able to asses the durability and especially effectiveness of the method. This effort is described in the next section.

Table 5.4: Trade-off table for the comparison of the three methods of improving the mould surface temperature diffusivity

Criteria	w	Aluminum Tape	Metal Mould	Copper Mesh
Durability	2	3	10	5
Ease of integration	3	9	1	5
Effectiveness	4	7	9	5
Cost	4	9	1	8
Surface Quality	4	3	9	7
	Total score	109	99	105

5.4. Copper Mesh Integration

The combination of copper mesh with glass and/or carbon fibre in laminates is commonly used in the aviation industry as a means of lightning protection [31]. The high electrical conductivity of the copper helps to dissipate the energy peak of a lightning strike and therefore limit the damage to the underlying composite. A wide variety of copper meshes is available on the market, varying from plain woven strands to flattened, constant thickness meshes. Plain woven wire mesh is preferred as they can be draped around the complex shapes present in the current moulds (see figure 5.12).

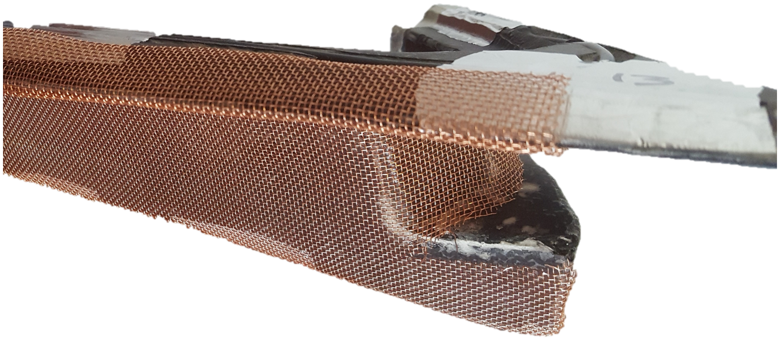

Figure 5.12: Plain woven copper mesh draped around a complex shaped section of a *Donkervoort* D8 GTO-RS upper door

Other possible permutations of the copper mesh are the wire thickness and mesh size. Thicker mesh wires will decrease the thermal resistance but will be more difficult combine with fibre reinforcements. The same holds for the mesh size, smaller mesh sizes mean more highly conductive material is present per area however this can also lead to the mesh being more difficult to integrate inside the laminate. In this phase, no statements can be made regarding the optimal combination of wire thickness and mesh size. The first goal is to test if the integration of a copper mesh actually has any positive influence on the temperature distribution and if the lamination of the mesh is viable. Therefore, it was chosen to use a plain weave mesh with a wire thickness of $0.35mm$ and a mesh size of $1mm$. This mesh was readily available for a price of €$65pm^2$ from *Kabel Zaandam B.V.*.

5.4.1. Test Setup

The effectiveness of the copper mesh in providing a more diffuse temperature distribution was analysed through use of the same setup as introduced in section 5.2.1. Three laminates were manufactured using either 1, 2 or 3 layer of copper mesh separated by layers of glass fibre and laminated into an epoxy matrix and will henceforth be referred to as CM1, CM2 and CM3. The laminates were cut to the same size as the aluminium sheets of $1/1.5mm$ and clamped between the tile mould lids and walls on both sides. Results will be compared to tests 2-7 from section 5.2.1 to see how effective the copper mesh is in distributing the concentrated heat form the heating tracing.

5.4.2. Manufacturing of Copper Mesh Laminates

A combination of 200g glass fibre (GF) chopped strand mats (CSM) and 40g GF veil were used in the layup. The GF veil is a very thin and light layer of glass. Each layer of copper mesh sandwiched between two veil layers. The aim of applying the veil layers is to get a better mechanical bond of the mesh and the glass fibre as the thin GF layer more easily penetrates the 1x1mm gaps of the mesh. 200g GF CSM mats were then placed over the GF veil to provide adequate reinforcement. Three laminates measuring 500 by $250mm$ were manufactured with either 1, 2 or 3 layers of copper mesh. The layups used are depicted below in figure 5.13. Sicomin SR1660/7820 temperature resistant epoxy resin was used as matrix.

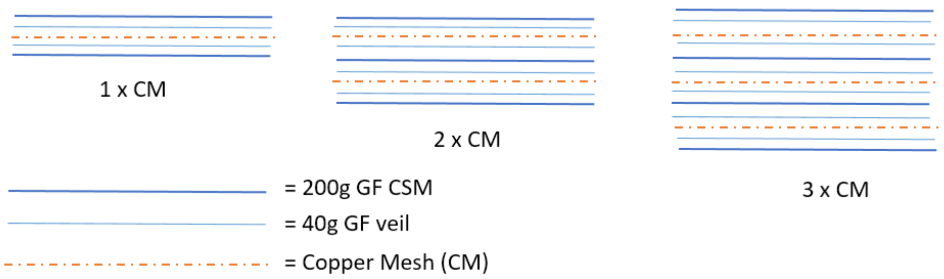

Figure 5.13: Layup sequence for the copper mesh / glass fibre laminates

A hand lay-up process was used for the manufacturing of the laminates. An aluminium plate was used as mould surface to which five layers of Frekote® 700-NC™ release agent were applied followed by one layer of Acmos release agent to ensure easy release of the large flat laminates.

Before starting the production, the copper meshes were de-greased thoroughly using brake-cleaner. Adequate wetting of every layer was ensured as it was expected that the copper mesh would consume a relatively large amount of resin in the 1x1mm mazes. The wet layups were covered with a layer of un-perforated release foil followed by a layer of breather cloth and vacuum bag. The laminates were then left to cure at room temperature for 24h followed by a post-cure in a large oven of 8h @ 60°C + 4h @ 90°C + 4h @ 120°C [32]. After the post-cure, the laminates were removed from the aluminium plate and trimmed to 250 by 250mm squares. Holes were drilled corresponding with the bolt placement of the tile mould. The finished plates are presented in figure 5.14.

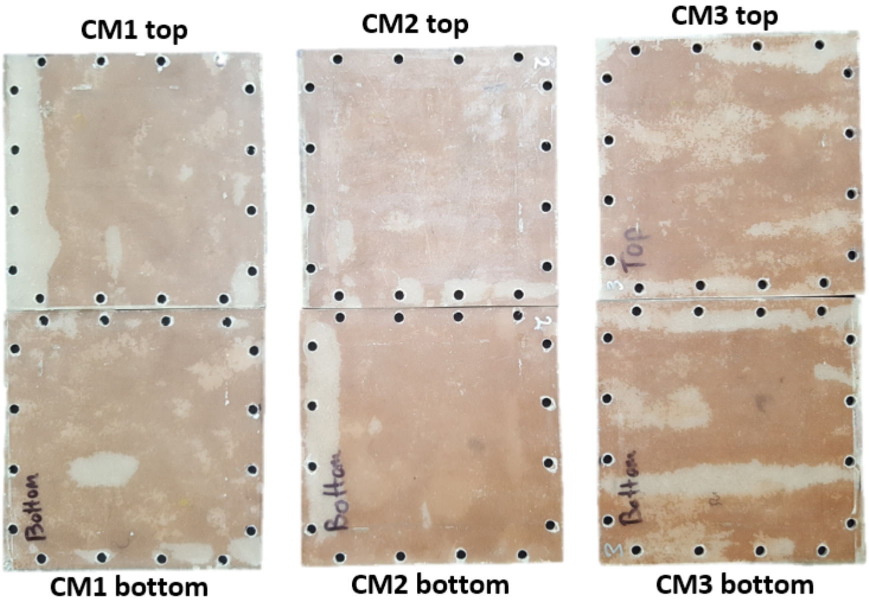

Figure 5.14: Copper Mesh plates CM1, CM2 and CM3 with top and bottom indication showing at which side of the mould the plate was positioned during the tests

Due to the use of non-perforated release film insufficient breathing was possible during the cure of the laminates, causing area's of trapped air to be present in the laminates visible in figure 5.14. The non-perforated release film was used to ensure that enough resin was kept in the laminate to wet the copper mesh. Air has a very low thermal conductivity (0.0263W/mK[30]) and can therefore negatively affect the effectiveness of the laminates in distributing the heat in the tile mould. Critical revision of the temperature results attained in the tests is therefore necessary to ensure that the voids do not have a significant effect on the results. The plate with the least voids of each respective laminate was placed on the sensor side of the mould and is indicated with 'top' in figure 5.14.

5.4.3. Temperature Distribution at Mould Surface using Copper Mesh

Three tests were conducted in total, one for each laminate. The setup was kept identical to that used for the determination of the surface temperature profiles in test 2-7 of section 5.2 including the isolation. A ramp of 1.5°C/min to 110°C was applied. The results are shown below in figure 5.15 compared against tests 3, 4 and 5 of the aluminium tests discussed in section 5.2.4. Again, temperature differences when the mould reaches 85°C (T_{85}) and maximal overall temperature differences (T_{max}) are listed in table 5.5. Looking at figure 5.15 it is noted that the temperature differences for the CM tests during the ramp up in the first 60 minutes closely follow test 4, which applied a $0.3mm$ thick layer of aluminium tape. Compared to the baseline represented by test 2 the maximal temperature difference is brought down to between 16 and 11°C. Interestingly, the ΔT during the ramp up phase is not significantly different for tests CM1, CM2 and CM3. All three CM laminates are able to halve the value of T_{85} to 6°C which is again comparable to test 4. Surface temperature distributions are plotted in figure 5.16 at the moment the mould reaches 85°C. These show that the differences between using 1, 2 or 3 layers of copper mesh are indeed very small.

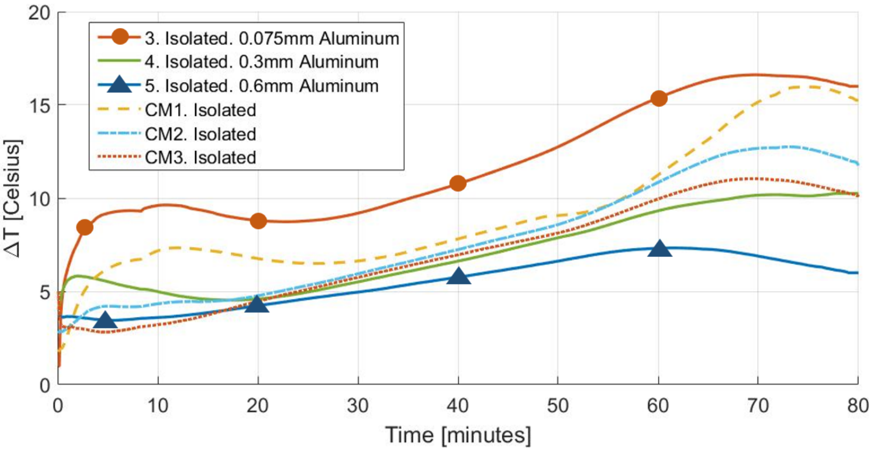

Figure 5.15: Max. temp. diff. (ΔT) between sensors vs time for copper mesh tests compared to tests 3, 4 and 5 from section 5.2

Table 5.5: Table with temperature differences at the mould surface when a point in the mould reaches 85°C; Δ T_{85} and the maximal overall temperature difference experienced during the complete test; ΔT_{max}. Both values are compared to test 2 and the % difference is listed.

Test	$\Delta T_{85}[°C]$	diff. ΔT_{85} w.r.t. test 2	$\Delta T_{max}[°C]$	diff. ΔT_{max} w.r.t. test 2
2	13.3	0.0%	21.5	0.0%
3	9.5	-28.6%	17.0	-20.9%
4	6.3	-52.6%	10.5	-51.1%
5	5.3	-60.2%	7.7	-64.2%
CM1	6.3	-52.6%	16.0	-25.6%
CM2	6.0	-54.9%	12.8	-40.5%
CM3	6.3	-52.6%	11.0	-48.8%

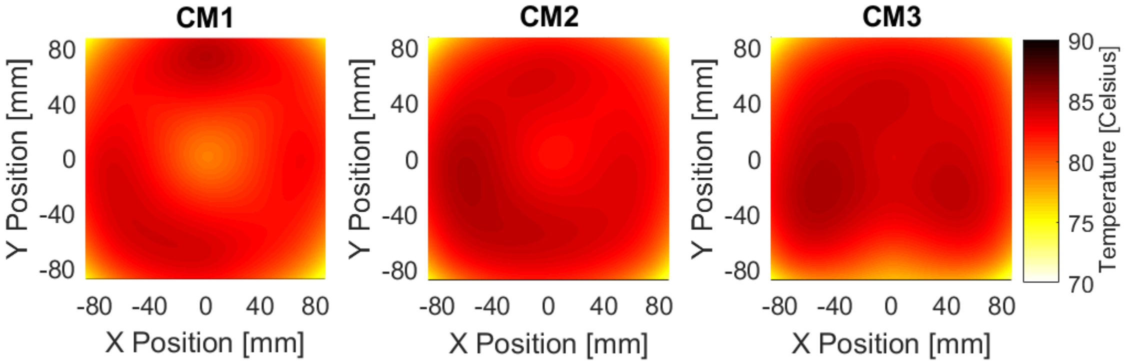

Figure 5.16: Surface temperature distribution when 85°C is reached for CM1, CM2 and CM3

The maximal temperatures experienced during the copper mesh tests are listed in table 5.6. Overshoots are comparable to those experienced in test 2 which did not employ a layer of aluminium. This results is surprising as the CM samples are effective in lowering the temperature differences at the mould surface but much less effective in lowering the temperature overshoot. This could be attributed to the fact that the layer(s) of highly conductive copper are separated from the mould surface by a layer of poorly thermally conductive glass/epoxy laminate. This creates a larger distance between the thermocouple and area of highly conductive material which could mean lower temperatures are read at the thermocouple than are actually present at the mould surface. However, this could be a result of the way the tests are set up rather than of the method it self. Further discussion and recommended solutions are discussed in chapter 10.

Table 5.6: Maximal temperatures at the mould surface over time for the CM samples compared to tests 3-5 from section 5.2.4

Test	$T_{max}[°C]$	Diff. w.r.t 110°C
3	118.75	+7.9%
4	112.75	+2.5%
5	110.75	+0.7%
CM1	128-130[a]	+16.4%
CM2	125.00	+13.6%
CM3	122.25	+11.1%

[a] Estimated value as sensor range is exceeded

Effect of Entrapped Air in Laminates

In figure 5.14 the presence of large areas of entrapped air in the CM laminates was shown. Comparing the plates labelled CM1 top, CM2 top and CM3 top to the surface temperature distribution in figure 5.16 no relation is seen between the locations of the entrapped air. It is therefore concluded that these areas of poorly conductive air do not have a significant effect on the surface temperature distribution.

5.5. Conclusion

It was shown that the copper mesh laminates indeed aid in the lowering of temperature differences present inside the tile mould. No significant benefit was seen of adding more than one layer of copper mesh. It was also noted that high temperature overshoots were still present during the cure-cycles for all laminates. This could however be related to the specific test setup which places the copper mesh laminates on top of the gel coat surface in stead of integrating them between the gel coat and heating braids. The temperature overshoots are therefore expected to decrease when the copper mesh is applied during the production of an actual mould in stead of later being applied to the surface. The used plain weave copper mesh was shown to quite easily shaped into complex forms. The manufactured samples did however show large areas of voids. These are related to the manufacturing process which applied non-perforated release film which limited the outflow of the air during the cure under vacuum. Lastly, the created laminates showed the tendency to delaminate between the mesh and glass fibre plies when flexed of machined even before being exposed to elevated temperatures. This could be related to the stiffness differences of the copper mesh and glass fibre layers or to the fact that the glass fibre is not adhering to the mesh enough. Overall, both the application of aluminium tape to the mould surface and the addition of a layer of copper mesh into the laminate between the braids and mould surface did prove promising in reduction of the temperature differences experienced at the mould surface during a cure-cycle. For flat plate moulds like the tile mould, the aluminium layer is most easily applied and is therefore also used for any samples produced in the tile mould in section 7. Recommendations for further research are presented in chapter 10.

6

X-Core Pressure Generation

In previous research several attempts have been made to determine the amount of pressure generated by X-Core. This is an important parameter of the material as the pressure is required to consolidate the facesheets. The research of D.O.Berckmoes indicated that there is a definite relationship between the volume fraction of DU and the surface porosity of samples [21]. Furthermore, X-Core is known to generate pressure capable of permanently deforming moulds. A good understanding of the pressure related properties of X-Core and how they can be influenced is therefore desired. This chapter presents an effort to generate this knowledge and build upon previous research performed on the topic. First, previous results are evaluated. Afterwards, a new setup is designed and build with the aim to generate more accurate and repeatable measurements.

6.1. Evaluation of Previous Experiments

Previous research aimed to determine the relationship between the pressure generated by X-Core to the DU volume content in a certain mixture [22]. Measurement were performed using the steel mould depicted in figure 4.4 placed inside an oven. Force resistive sensors (FSR) of the type FlexiForce® HT201 were selected based on their high temperature resistance, thin/flat geometry and easy readout using an Arduino®. The sensors were calibrated through the placing of three weights on the pressure sensitive area of the sensor and logging the signal produced by the sensor. The loads were selected to cover a pressure range between 3.8 and $11 bar$. A fixed temperature of $100°C$ and a constant 95% mould filling (of the net mould cavity) was used to perform 8 tests in a DU content range of 1-23%. One test was performed for every DU content. The test setup is shown in figure 6.1.

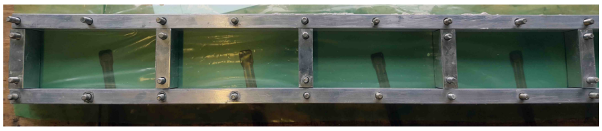

Figure 6.1: Placement of FSR sensors in mould covered by vacuum foil preventing sensor contamination [22]

The resulting data shown in figure 6.2 allowed for the determination of a linear relationship between DU content and pressure in equation 6.1.

$$P[bar] = 1.0653 + \phi_{DU} \cdot 83.24 \tag{6.1}$$

Several side notes are however required with these results. Firstly, repeatability of the experiments was not proven as only one measurement was performed per DU content. Revision of the raw data from the experiments points point to the need for this as interpreting the curves presented there is not straight forward. Several discrepancies are noted in the curve shapes presented in figure 6.3. Pressures were obtained by taking the maximal values of each curve. This however does not tell the full story. Some curves shown clear decreases in pressure after reaching their respective global maxima. Another curve present a distinct jump which was not discussed in the presentation of the results.

Furthermore, a test was performed where four FRS were placed besides each other in one sample. This test indicated that the location of the sensor in the mould has a significant effect on the pressure read for a

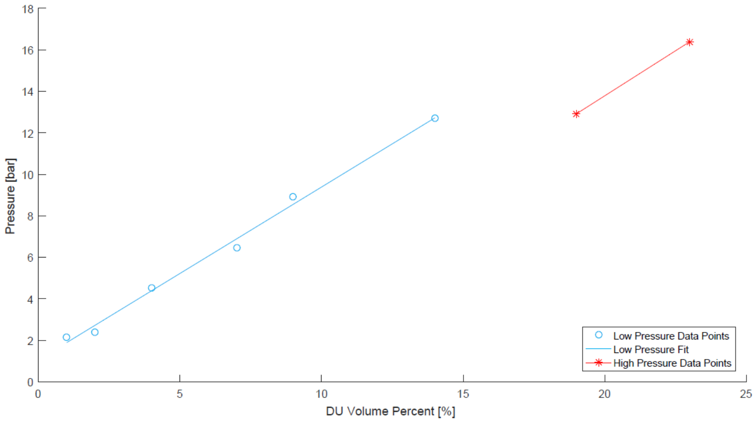

Figure 6.2: Placement of FSR sensors in mould covered by vacuum foil preventing sensor contamination [22]

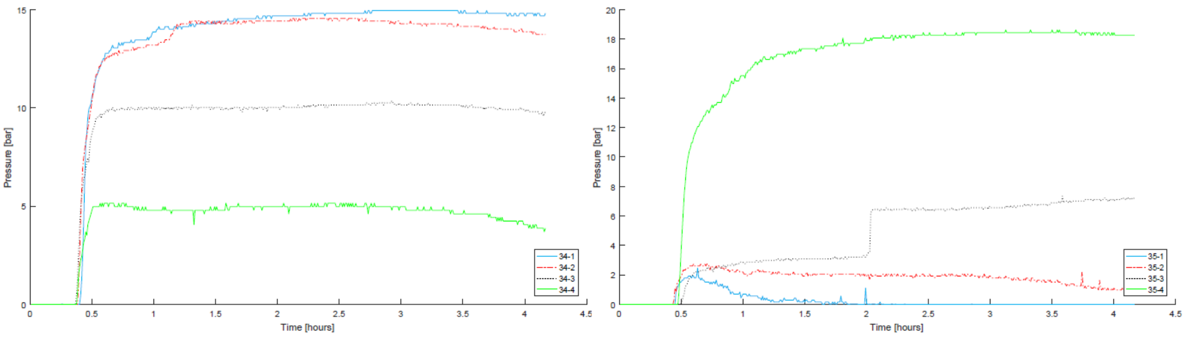

Figure 6.3: Raw pressure data used to obtain pressure data for DU contents varying between 1-23% [22]

certain mixtures. Figure 6.4 shows the test setup resulting in the pressure data shown in figure 6.5. Three sensors seem to give pressure readings within $1 bar$ of variation. The outer left sensor however (35-1) reads a $3 bar$ higher pressure. Conclusions were drawn that pressure generation is therefore not even, or fluid like.

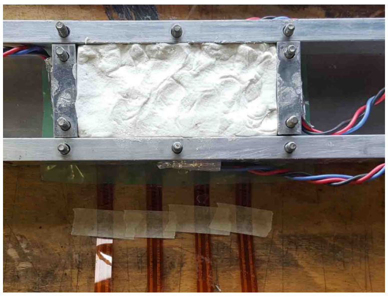

Figure 6.4: Four FSR sensors placed parallel in one mould cavity [22]

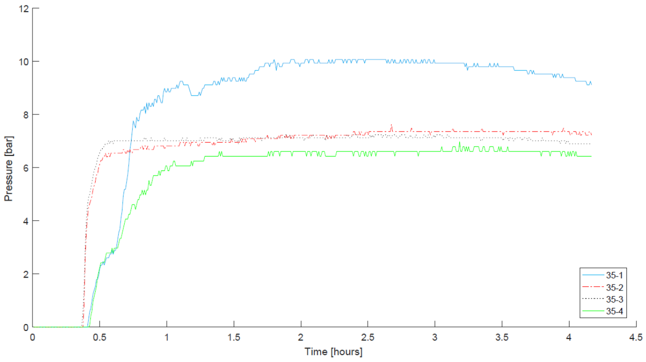

Figure 6.5: Pressure data obtained for four parallel placed sensors in one mould cavity [22]

Lastly, a discrepancy was discovered in the used microsphere density for Q-Cel. Calculations of DU volume fractions were based upon the Q-Cel true density, e.g. the density based on the volume and weight of one microsphere, of $0.25 g/cm^3$. Later on in the designed experiment a density of $0.16 g/cm^3$ was used for Q-Cel, which represents the materials bulk density. This bulk density should be used, as this represent the density based on the volume and weight of a large quantity (bulk) of microspheres, and this is how Q-Cel is used in X-Core. A correction therefore is required for equation 6.1. Using the actual weight fractions of the mixtures used in the pressure experiments allows for recalculation of the corrected volume fractions when using the correct, bulk, Q-Cel density. Table 6.1 presents an example of these calculations for mix 34-2 used in the pressure tests. The believed DU content of 9% changes to an actual DU content of 7.5% using the above-mentioned Q-Cel density correction. Applying these corrections to the complete range of mixtures used in the pressure tests allows adjustment of equation 6.1 to the new, corrected, pressure relationship presented in equation 6.2.

Table 6.1: Re-calculation of mix volume fractions based on corrected Q-Cel density. Shown mix proportions were used for test 34-3.

	Mix Proportions [g]	Incorrect Densities [g/cm^3]	Incorrect mL	Incorrect % Vol	Corrected Densities [g/cm^3]	Correct mL	Correct % Vol
Resin	58.20	1.15	50.61	20.7%	1.15	50.61	17.3%
DU	8.13	0.37	21.96	**9.0%**	0.37	21.96	**7.5%**
DE	1.20	0.014	85.72	35.1%	0.014	85.72	29.3%
Q-Cel	21.43	**0.25**	85.72	35.1%	**0.16**	133.93	45.8%

$$P[bar] = 1.0653 + \phi_{DU} \cdot 99.34 \tag{6.2}$$

Based on these findings, the validity of the results was put to question. Concluding that pressure is not generated evenly but using only one measurement location in following tests seems arbitrary if a variation of $3bar$ was shown over the mould cavity length. Moreover, other factors like temperature variations, mould filling and repeatability of measurements were note evaluated. Lastly, the FlexiForce® HT201 have a listed output change per degree Fahrenheit of 0.16%[33]. Over a temperature range of $80°C$ this produces a change in output of 23.2% which was not taken into account in the tests listed above. Before proceeding, an evaluation is made of which parameters are known or thought to have an influence on the pressure generating behaviour of X-Core. Afterwards, a new method of measuring pressure is proposed which aims to eliminate some of these variables.

6.2. Factors Influencing X-Core Pressure Generation

Multiple factors are known to or believed to influence the pressure generating properties of X-Core. These factors will be discussed in the following sections.

6.2.1. DU Volume Fraction

One thing that can be definitely concluded from the test presented in the previous section is that the pressure generated by X-Core is influenced by the amount of 031 DU Expancel®. Increased amounts of the expanding microspheres lead to higher pressure readings as more overall expansion/pressure generation takes place.

6.2.2. Mix Composition

The volume fractions in which the other components are combined can be another influencing factor. Q-Cel is a hollow glass microsphere (HGM) and has a compressive strength of $5MPa$, which should mean it can resist pressures up to $50bar$, collapse of Q-Cel is therefore not expected to occur under the functional pressure used in X-Core. DE Expancel® is a polymeric microsphere of unknown compressive strength. Polymeric microspheres generally have a lower compressive strength compared to HGM [34]. However, the presence of gas inside the DE microspheres will act as a reinforcing factor creating internal pressure in the microsphere. Collapse of DE microspheres under pressure is therefore not directly expected.

A factor which will vary between mixtures is the amount of interstitial voids [35]. Interstitial voids, or unreinforced voids are present when high volume fractions of spherical fillers are used compared to the amount of binder material added as shown in figure 6.6.

When the volume fraction of interstitial voids is larger than the volume fraction of binder interstitial voids will not be filled completely. The trimodal packing factor will dictate the optimal ratio of sphere sizes and volume fractions to achieve minimal voids between the spheres. This theory however is not considered when

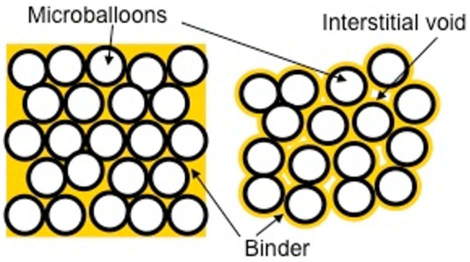

Figure 6.6: Schematic representation of interstitial voids in a microsphere filled composite

selecting X-Core mixing ratios. The voids could allow a certain degree of free-expansion of DU through filling of the voids. This in turn could affect the pressure generation between different mixes using the same volume fraction of DU.

6.2.3. Temperature

The dependency of the magnitude of pressure generated inside X-Core on temperature has never been verified. However, based on knowledge of the pressure generating component inside X-Core, being 031DU microspheres, a dependency on temperature is highly likely. Examining the expansion curve of 031DU Expancel® provided by *AkzoNobel* shows an increase in total expansion of a microsphere starting at 85°C and peaking around 125°C. A decrease in volume is then present from 125 to 200°C which is stated to be related to softening of the microsphere polymer wall and subsequent release of the internal gaseous blowing agent.

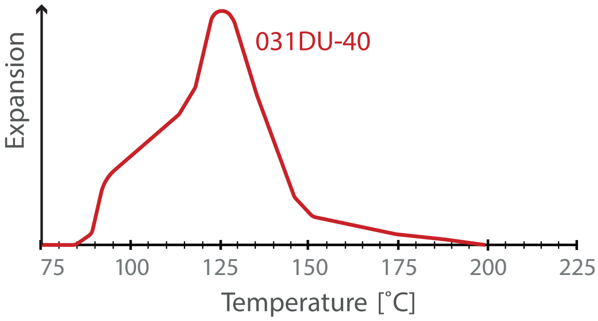

Figure 6.7: Relative volume change of 031DU Expancel® for a temperature range between 70 and 225°C [36]

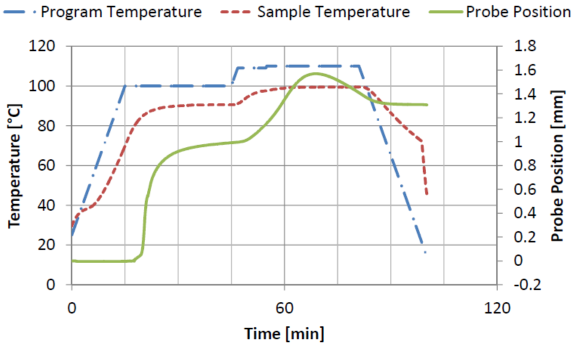

Figure 6.8: Thermo-mechanical analysis result for 031DU [20]

F.Minde [20] performed thermo-mechanical analysis (TMA) on 031DU. In these experiments, 031DU was placed inside a TMA instrument and the volume change of the materials was monitored under different temperature holds. Figure 6.8 shows one of the measurement results attained through using a temperature hold at 90 followed by a hold at 100°C. A clear increase in the expansion of DU is seen through the change in probe position. This indicates that the increase of gas pressure under increased temperatures leads to a physical increase in the DU volume. The hypothesis is therefore put forward that, when an X-Core mixture with a certain amount of DU is placed in a closed mould, different pressures will be generated depending on the temperature locally. Furthermore, temperatures >125°C could lead to decreases in pressure due to pressure loss occurring in the microspheres.

6.2.4. Mould Filling

The pressure generating capability of X-Core is based on limiting the free expansion of DU microspheres which results in an increase in pressure. Under-filling a mould would mean a certain degree of the expansion of DU is lost in the free-expansion required to fill the mould. D.O.Berckmoes [26] showed that the degree of filling of the mould cavity, several percent under or over filling, leads to a variation in surface porosity of around 4.5% to 0.1% in the prepreg facesheets. This could indicate that the net surface pressure was different between the degrees of filling. Therefore, it is not unlikely that the amount of pressure generated by a certain X-Core mixture is dependent on the degree of mould cavity filling.

6.2.5. Mould Sealing

Lastly, the effectiveness of the seal achieved in the mould filled with X-Core could be an influencing factor. Leakage is known to occur in the moulds used for the floorplates and door window frames. The metal mould used in the research of S.Vial also shows leakage, especially in the area where the FlexiForce® sensors are inserted. Leakage occurs in the form of resin outpouring or/and X-Core escaping in its low viscosity state. Leakage leads to a decrease in volume of X-Core in the mould, which makes the conclusions on pressure of the previous paragraph apply here as well.

6.3. Controllable and Uncontrollable Factors

The factors thought to, or known to affect the pressure generating properties of X-Core can al be influenced However, the amount of interstitial voids is inherent to a certain mixture and can therefore not be controlled directly (e.g. choosing a set volume fraction of interstitial voids). The effect of this factor can be measured indirectly through assessing various X-Core mixtures with identical DU contents. The other parameters are controllable variables which can be taken into account when aiming to model the pressure generating capabilities of X-Core. Requirements springing from these controllable variables are listed below:

1. **DU Volume Fraction**
   Simply influenced through adding a certain volume fraction of DU to a set of pseudo components (100% - V_{DU}). Current production uses a DU content between 0.8% and 4.5%. An upper limit of around 10% is though to be needed to prevent too high (>$8bar$) pressures occurring which can damage tooling based on the research of S.Vial.

2. **Temperature**
   031DU has a well defined onset of expansion temperature of $85°C$, meaning this is the lower limit of the temperature range of interest. Temperatures up to $167°C$ have been discovered in chapter 7 to occur in larger volumes of X-Core (175x80x$80mm$) and temperatures up to $130°C$ have been proven to occur in X-Core thicknesses of $30mm$. The range of temperatures of interest is therefore set between 85 and $170°C$.

3. **Mould Filling**
   D.O.Berckmoes has shown that under-filling of moulds of a few percent has a negative effect on the surface porosity [26]. Complete filling of the mould cavity is thus desired in X-Core sandwich products. Representable pressure measurements should therefore be conducted at this mould filling degree.

4. **Mould Sealing**
   The amount of leakage of resin of X-Core occurring varies widely per mould used. Defining the amount is however not straight forward and reproducing these conditions in a pressure test setup is even more questionable. Eventually, perfect mould sealing is always aimed for in designing and producing moulds. Therefore, performing pressure measurements without leakage is set as baseline.

The current method of measuring pressure in the metal mould (figure 4.4) depends on a small industrial oven present at *Donkervoort* for heating. This oven is limited to a temperature of $120°C$ and can therefore not satisfy the required temperature range up to $170°C$. Mould filling of 100% can be achieved in the metal mould but is challenging to achieve as a few mm of play are present in the mould walls at the bolt holes. Shifting of the walls can therefore lead to volume changes of the mould cavities. Controlling these variations is not possible in the current mould setup. Mould sealing is another issue with the metal mould. Inserting the FlexiForce® sensors with a thickness of $0.2mm$ leads to small gaps in the mould which lead to leakage. Furthermore, leakage also occurs through between the wall edges which do not create a perfect seal.

A new method of measuring pressure is therefore needed to be able to control the listed variables within the desired ranges.

6.4. Alternate Method of Measuring Pressure using FlexiForce® Sensors

A new method of measuring pressure is proposed here which aims to control the above-mentioned variables. To this end, the setup schematically shown in figure 6.9 was created. The setup uses a 20mm inner diameter round steel tube combined with steel plates functioning as lids.

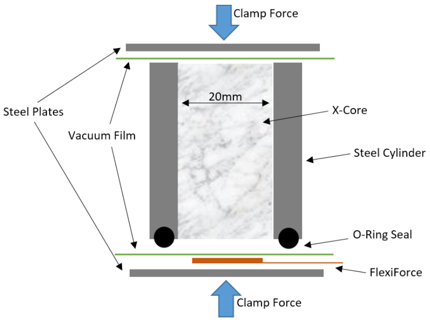

Figure 6.9: Schematic representation of the steel cilinder pressure setup

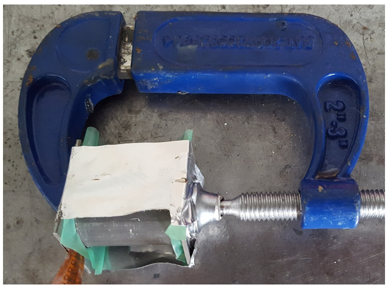

Figure 6.10: Steel cylinder clamped shut with sensor in place

This setup achieved control of the following variables trough:

1. **Temperature**
   The temperature range is extended through use of a simple, small, *Tefal* household oven with a maximal temperature of 200°C available at *Donkervoort*. A DS18B20 thermosensor was attached to the cylinders in order to log the actual temperature present during the tests.
2. **Mould Filling**
   The simple cylindrical mould geometry allows X-Core to be pushed through from one side while the other side is held shut. Excess X-Core is then carefully sliced off using a Stanley knife. This assures 100% mould filling every time.
3. **Mould Sealing**
   A rubber O-ring is placed inside a groove cut in the cylinder walls on one side. This O-ring assures the gap between the cylinder wall and the FlexiForce® sensor is closed when the cylinder is clamped shut. The groove was cut to a depth that assured that the steel wall, under compression, would touch the steel plates acting as lids. This assures no gap is present between X-Core and the mould lids before expansion. Two piece of vacuum film complete this simple setup, preventing contamination of the sensor by X-Core and assuring a good seal at the top side of the cylinder. The clamping force is provided by using a steel screw clamp as depicted in figure 6.10.

As four FlexiForce® sensors were available, four of these identical setups were constructed. This allows four measurements to be performed on one mixture batch in parallel under identical conditions. In this way, repeatability of measurements is easily achieved.

A re-calibration of the FlexiForce® sensors was performed and can be reviewed in Appendix C. A total of seven different weights were used covering a pressure range from 0-11bar. Non-linearity of the sensors was corrected for through fitting of a second order polynomial to the calibration data. Furthermore, the temperature drift was taken into account through applying a temperature correction factor of +0.29% per °C on the sensor output as dictate by the users manual [37]. This number was verified through placing a fixed weight on the sensors and subsequently heating them to 100°C. A drift in signal output of around +23% per °C was observed, verifying the number listed in the user manual. Data logging again was performed using an Arduino® Nano connected to an SD-card module with a 5s interval.

6.4.1. Test Method

Six batches of X-Core were individually prepared and tested with DU contents of 4, 7 and 10% respectively. Two batches were tested per DU content to take the influence of any weighing error occurring during mixing into account. The pseudo volume fractions of the 270-optimal mix, determined in chapter 4 were used to complete the mixture. To limit weighing inaccuracies cause by the 0.1g accurate scales, a large batch of 500ml of X-Core was prepared for every DU content. Four cylinders were prepared per mix batch and placed inside the small *Tefal* oven at room-temperature. Temperature was set to 110°C and tests were run for the duration of 40min.

6.4.2. Results

The resulting pressure in *bar* versus time is shown in figure 6.11 for the three DU levels analysed

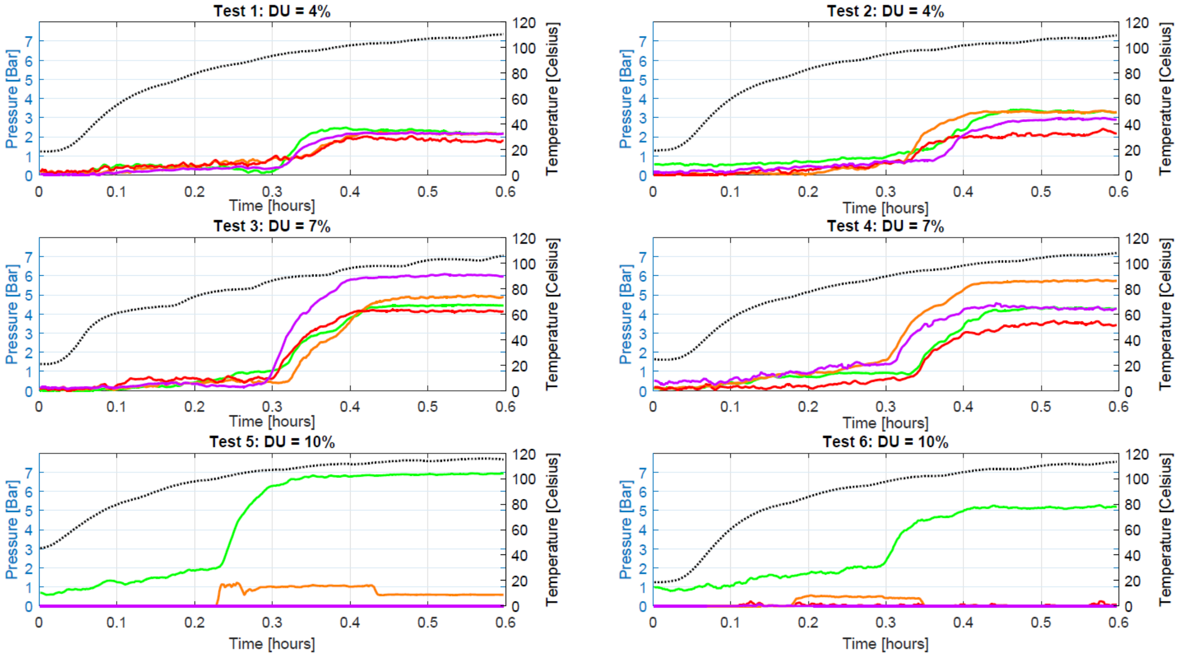

Figure 6.11: Pressure vs. time results of six tests performed with either 4, 7 or 10% DU in the 270-optimal mix. Temperature is represented by the dotted line.

As seen from figure 6.11 results still showed a significant amount of variation. The 4% DU tests showed pressures between 1.98 and 3.4*bar*. The 7% DU test showed even larger variations between 3.5 and 6.0*bar*. Lastly, the 10% DU cylinders had experienced pressures that exceeded the clamping force of the screw clamp, leading to leakage of X-Core and therefore three of the four sensors registered no pressure. The two successful measurements that were achieved gave a pressure of 6.9 and 5.2*bar* respectively. Colors of the lines are linked to one specific sensor. Looking at the data from tests 3 and 4 it can be seen that no relationship is present between the pressure measured and the sensor used. This indicates that possible faults in the calibration of the sensor in itself do not produce consequent low or high pressure readings. It was therefore concluded that the sensors themselves are not producing repeatable measurements. Revision of the sensor guidelines on numeral websites further strengthened this believe. These sources are in no way scientifically valid and are mere guidelines of resellers towards the application of FlexiForce® sensors. *Sparkfun.com* states: *"They're (FSR's) useful for sensing the presence of something, and the relative magnitude of that force, but they're not all that great at measuring weight."*. Furthermore, it is stated that the force accuracy ranges from 5% to 25% depending on consistency of the actuation and use calibration method. Lastly, the user is warned to not block the airvent which runs from the sensing area to the connecting pins in between the leads shown in figure 6.12 as this could lead to non-repeatable measurements [38]. The variation in the measurements using the cylinders is therefore attributed to the un-suitability of the used sensor type. Continuation of pressure measurements therefore requires the use of a more reliable sensor and setup as the current method shows pressure readings that overlap for 4% and 7% DU. Section 6.5 describes the second pressure setup design which was manufactured to solve these issues through using a different sensor.

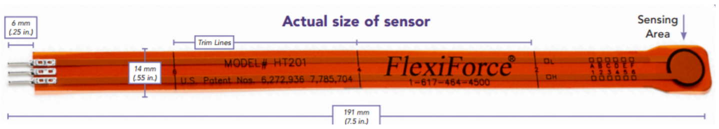

Figure 6.12: FlexiForce® HT201 FRS

6.5. Oil Sensor Based Pressure Measurements

A new idea is based upon separating the sensor from the high temperatures required to activate X-Core. In this way, highly sensitive sensors can be used without having issues with the allowable temperature range and related temperature drifts. Furthermore, the proposed setup allows constant 100% mould filling and sealing. Temperature control up to $170°C$ is again achieved through using the *Tefal* oven. With the proposed setup, the goal is to produce reproducible pressure tests with an accuracy of at least $0.2bar$. In this way, the effect of different temperatures and mix compositions on the pressure generated by X-Core can be defined.

6.5.1. Design Overview

The basic principle of the setup relates to that of an piston and cylinder of an engine. X-Core is contained in a sealed chamber in which the only moving part is the piston/driver. Through applying a small pre-load (max. $4lbs$) on X-Core no expansion is allowed as any increase in pressure is directly converted to an actuation force pushing on the driver. This driver is connected to a brake master cylinder which is set up as a closed system filled with brake oil. The resulting force on the master cylinder compresses the incompressible oil of which the increase in fluid pressure is read using an oil pressure sensor attached to the master cylinder. The oil containing master cylinder and sensor are positioned outside the hot oven which keeps these temperature sensitive parts within $10°C$ of room-temperature.

Figure 6.13 shows a CAD representations of the pressure setup along with a schematic indicating the different parts. A full review of the different parts in the setup along with the choices leading to their design is given in Appendix D.

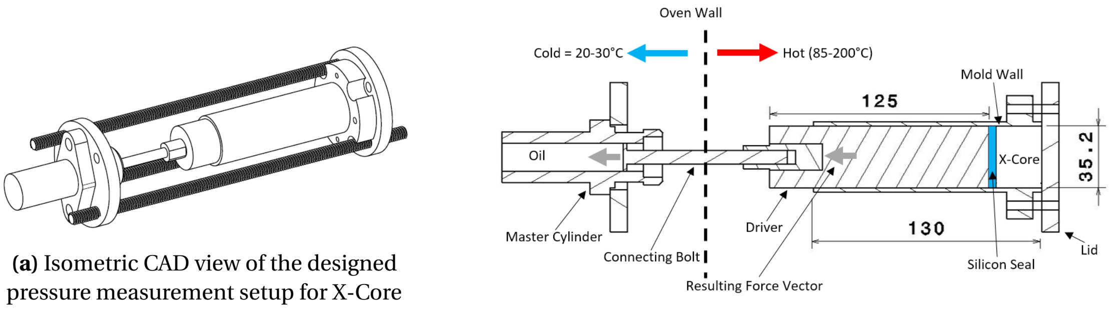

(a) Isometric CAD view of the designed pressure measurement setup for X-Core

(b) Side view cut-through of the pressure setup

Figure 6.13: CAD impression of the designed pressure measurement setup for X-Core

The resulting setup was build at *Donkervoort*. An Arduino® was wired to the pressure sensor and temperature sensor (not shown) programmed to read out the signals at $1Hz$. The data is written to an SD-card module allowing the resulting data to be read out in text format on a PC. More information on the used sensor is given in the next section.

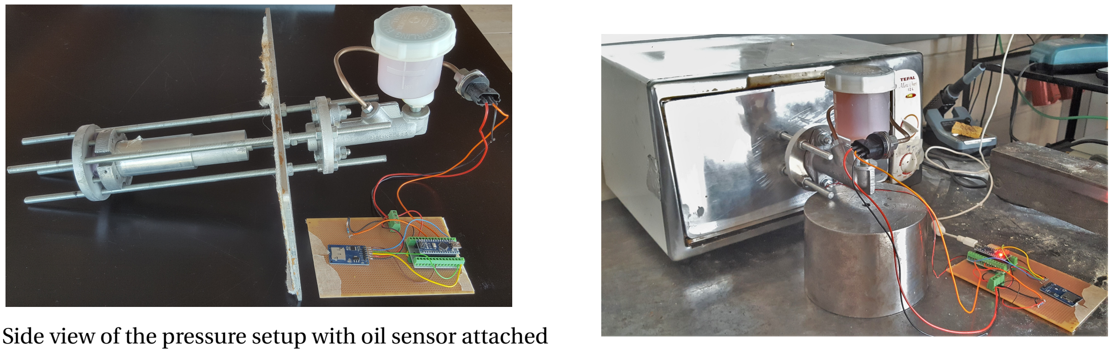

(a) Side view of the pressure setup with oil sensor attached to the master cylinder. Master cylinder and lid/mould wall fixed w.r.t. the oven wall. Bosch PSS-260 sensor connected to Arduino® logging data on an SD-card module

(b) Pressure setup inserted in *Tefal* oven. Stabilized by steel block.

Figure 6.14: Side view of the pressure setup along with the setup shown inserted into the oven as during experiments

6.5.2. Sensors

A *Bosch PSS-260* oil pressure sensor is used for reading the pressure generated in the oil of the master cylinder. This sensor has a measurement tolerance as percentage of the total force (FS) of 1%, e.g. $0.1 bar$ accuracy at $10 bar$ of pressure. It can be powered using the $5V$ output from an Arduino® Nano.

The sensors signal is read on an ADC port of the Arduino® at a rate of $1 Hz$. Translation of the logged signal to the actual pressure is achieved through the calibration procedure described in Appendix D.2. Based on a rmse of $2.38 lbs$ of the calibration, corresponding to $0.11 bar$ of X-Core pressure, the pressure readout accuracy of this setup is calculated as $0.11 + P_{X-Core} * 1\%$, which at $10 bar$ of X-Core pressure equals $0.21 bar$. This satisfies the $0.2 bar$ accuracy requirement stated at the beginning of this section. The resolution with a 12-bit ADC in the Arduino is calculated at $0.067 bar$ of X-Core pressure. Appendix D.2 explains these calculations in more detail. Lastly, accounting temperature drift is not required as the sensor and oil remain within $10°C$ of room-temperature because they are positioned outside the hot oven.

Figure 6.15: Bosch PSS-260 fluid pressure sensor [39]

An NTC thermistor is attached on the outside of the mould wall to attain the actual temperature of the mould during the experiments. Data from this sensor is also logged using the Arduino® Nano at a sampling rate of $1 Hz$.

6.5.3. Test Method

To test if the setup is functioning correctly and if realistic results are attained three DU content mixes are tested. A DU content of 7.5%, 5% and 2.5% were selected to be added to the pseudo components of the 270-optimal mix presented in chapter 4. In parallel to the procedure followed in section 6.4.1 a large batch of $500 ml$ X-Core was mixed for every test. An X-Core chamber depth of $50 mm$ was selected for these tests. A review of the full test procedure can be reviewed in Appendix D.3.

6.5.4. Results

The pressure results from the performed tests are shown in figure 6.16 along with the logged temperatures. This first run of tests revealed a major flaw to the setup. Performing tests at 7.5% and 5% initially seemed to give good results of pressures at 9.6 and $7.2 bar$ respectively. Afterwards, the 2.5% test was executed. This gave an unexpected pressure of $7.4 bar$. To assure that no weighing errors were made during mixing, the 2.5% was repeated, again resulting in pressure ranging around $7 bar$.

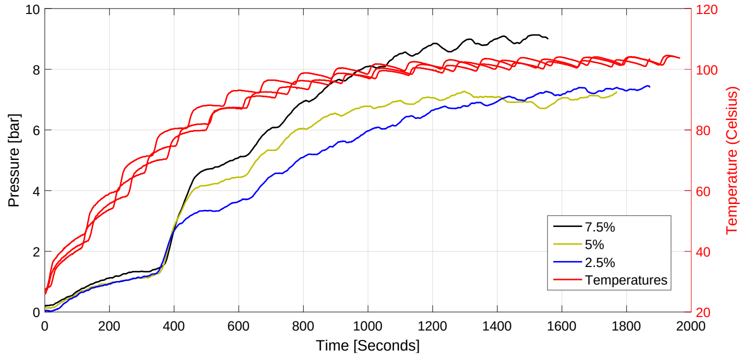

Figure 6.16: Pressure and temperature data against time for the performed tests with 2.5, 5 and 7.5% DU in the 270-optimal mix.

The cause for this measurement discrepancy is put down to thermal expansion differences present in the setup. A simple calculation is presented here which indicated that this is indeed most likely the reason for the similar pressure readouts for different DU contents. Long steel bolts were used to fix the lid with respect to the oven chamber. The steel bolts have a length of around $180 mm$ extending from the oven wall to the point where the lid attaches to the bolts with nuts. Steel has a thermal expansion coefficient of $12{\cdot}10^{-6} m/mK$ [40]. The driver is a $125 mm$ long piece of aluminium with a thermal expansion coefficient of around $24{\cdot}10^{-6} m/mK$[40]. Assuming a temperature change within the oven of $90°C$ we can calculate the thermal expansion of the driver and bolts as:

$$\Delta L_{driver} = 24 \cdot 10^{-6} \cdot 90 \cdot 0.15 = 0.324[mm] \tag{6.3}$$

$$\Delta L_{bolts} = 12 \cdot 10^{-6} \cdot 90 \cdot 0.18 = 0.199[mm] \tag{6.4}$$

The difference between the two expansions is then expressed as:

$$\Delta L = \Delta L_{driver} - \Delta L_{bolts} = 0.324 - 0.194 = 0.1296[mm] \tag{6.5}$$

Where the aluminium cylinder will thus expand by $0.1296mm$ more compared to the steel bolts. If it is assumed that this displacement is imposed on the X-Core sample inside we can calculate the strain present in this material.

$$\epsilon_{X-Core} = \frac{\Delta L}{L} = \frac{0.1296}{50} = 0.0026 \tag{6.6}$$

With a stiffness of around $200MPa$ of X-Core at $270kg/m^3$ the stress generated is $0.52MPa$.

$$\sigma = E \cdot \epsilon = 200 \cdot 0.0026 = 0.52[MPa] = 5.2[bar] \tag{6.7}$$

This would mean that around $5.2bar$ of pressure is generated purely due to expansion differences between the aluminium driver and steel bolts. Looking at figure 6.16 this is of the same order of magnitude as the pressures encountered in the experiments. The hypothesis was checked through running a 'blank' test, wherein the driver and silicon seal were pushed al the way though to the lid. A pre-load of 1-$4lbs$ was applied and the setup was again heated to 110°C. The result is shown in figure 6.17.

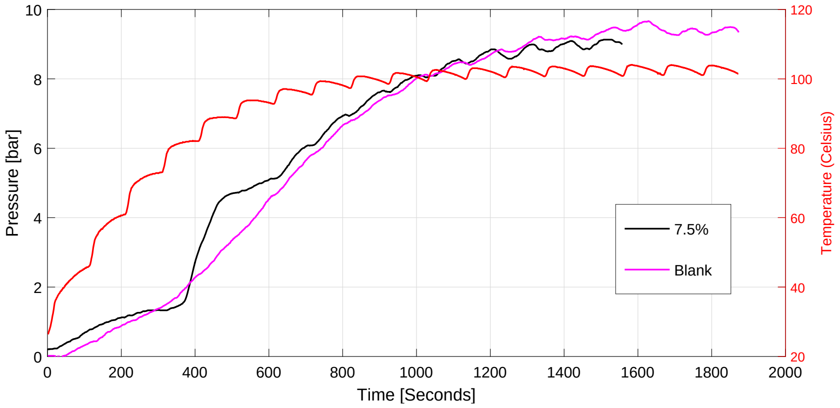

Figure 6.17: Comparison of 7.5% test and blank pressure.

It can be seen that a signal up to $9bar$ is generated without X-Core present in the chamber. The amount of measurement 'noise' is therefore in the same order of magnitude as the actual signal that is measured. Careful examination of the results through comparing the X-Core experiments with the blank in figure 6.17 shows some indication of what is happening during the experiments. Between 200 and $360s$ the pressure drops in relation to the blank test. This is attributed to the viscosity decrease of the resin, allowing the pre-load to ease of as X-Core 'settles', e.g. the mixture becomes viscous and microsphere packing can become more dense under load. A sharp increase in pressure in then noted around $360s$, linked to the expansion of 031DU microspheres around 85°C. The expansion takes place within $140s$ after which the pressure increase rate starts to follow the trend of the blank test again. The jump in pressure between 360 and $500s$ could therefore be related to the X-Core pressure generation, which for the three performed tests is:

Table 6.2: Pressure vs DU content for the measurements performed

%DU	Pressure [bar]
2.5%	2.1
5%	2.8
7.5%	3.2

This is however does not provide any more trustworthy measurements compared to the methods used previously as it is not known which portion of the pressure jump is related to the thermal expansion differences and which to the actual expansion of X-Core. This makes the setup in this configuration not usable for the accurate (± $0.2bar$) determination of the pressure generated in X-Core.

6.5.5. Conclusion

The designed pressure measuring setup based on an oil pressure sensor fulfils all the requirements that were set out. The setup has a high resolution of $0.067 bar$ and accuracy of at least $0.21 bar$ up to $10 bar$ of X-Core pressure. High temperature resistance of the complete setup is assured through positioning of the sensor and master cylinder outside the oven and using a silicon seal with thermal stability up to $200°C$. Temperatures up to $200°C$ can be simulated though use of a *Tefal* household oven and calibrated NTC thermistor. A perfect seal was achieved as no leakage was observed in any of the performed tests with X-Core. Constant complete mould filling is assured through initial overfilling and slicing of excess X-Core from the top of the mould. A controllable pre-load then assures that no free space of play is present between X-Core and the driver, creating constant initial conditions for every experiment.

The major flaw in the design concerns the differences in thermal expansion of the apparatus. This was shown to generate 'noise' of equal magnitude to that of the signal of interest. This makes the setup in its current configuration not ready for accurate determination of X-Core pressure generation. The setup does however fulfil all the other requirements and, with some alteration is believed to have the potential to deliver the desired knowledge on the dependence of X-Core pressure generation on the factors listed in section 6.3. Recommendations for future research and improvements of the current setup are discussed in chapter 10.

7

Thermal Analysis of X-Core Curing Behaviour

In this chapter, an investigation into the behaviour of X-Core with respect to temperature during a cure cycle will be presented. Previous research has indicated that the presence of the thermosetting resin can create exothermic energy peaks in X-Core during a cure. Samples showed cracks and ruptures which could be attributed to high temperature peaks. For this reason, a slow amine reacting hardener (Ancamide™ 3399) was selected which decreased the issues with the cracking of samples [22]. However, the actual magnitude of the temperature peaks was never quantified. Furthermore, only samples of $30mm$ thickness cured in an oven at $110°C$ were considered in selecting the slower reacting hardener. Components currently produced at *Donkervoort* are the floor plates and upper doors, which have maximal thicknesses of around $30mm$. At the time of this research, new products are under development which have thicknesses up to $80mm$. The expectation is that X-Core, being a foam, will have a low thermal conductivity. Combining this with higher thickness cross-sections can lead large variation in the temperature through the thickness with high temperature peaks occurring in the centre if internal heat generation is present. To investigate this, a test setup was devised capable of mapping the temperature distribution in thick (>$30mm$) X-Core samples cured in a mould representative of those used for the production of actual components. The information attained in these tests was used to design a new cure cycle which led to several interesting properties of the resulting X-Core samples.

7.1. Temperature Profiles in Various Thickness X-Core Samples

The first tests performed in this chapter aim to evaluate the temperature profiles in X-Core samples of various heights. This will help to evaluate several factors. Firstly, it is not known how fast the heat from the mould travels through X-Core to reach the core of the material. Foams are known to be good insulators which have low thermal conductivities. This could lead to large temperature gradients in the foam during the heat up phase possibly leading to material property differences through the thickness. Secondly, the exothermic reaction of the thermosetting resin used in X-Core is known to generate a certain amount of heat. How this internal heat generation effects the foams temperature during a cure cycle is not known. Temperature peaks could arise which could effect the material properties of the foam and defining these is therefore of interest.

7.1.1. Test Plan

To evaluate the effect of larger volume products on the temperature distribution inside X-Core during a cure, the temperature variation will be monitored internally during the manufacturing process of different thickness samples. The tile mould presented in chapter 5 is used for this as it allows thickness variations of 5-$80mm$ in $5mm$ increments and is therefore ideally suited for investigating temperature distributions at various sample heights. The choice of thicknesses and X-Core mixture to be investigated combined with the cure-cycle to be used and are explained in the following paragraphs.

Sample Thickness

The lower and upper boundary of the thicknesses to be investigated were determined by two factors. Firstly, the upper boundary is dictated by the maximal thickness present in the doorbeam of the Donkervoort D8-

GTO which is approximately 80mm and is currently being re-developed to be manufactured using X-Core. The lower boundary is dictated by several other factors. In order to be able to map the temperature distribution, several thermo-sensors need to be placed over the thickness. The used DS18B20 sensors have a minimal dimension of 4mm. Five sensors are used in the thickness direction to be able to map the variation in the thickness from the core to the edge with at least three data points. This leads to an absolute minimum thickness of 20mm, however sensors would then be in contact and no space remains for the wiring. Therefore, around 10mm extra is required to properly position the sensors and wiring. Because of this the lower bound is set at the maximal thickness previously researched by S.Vial, being 30mm. The third thickness was chosen at 55mm, halfway between the 30 and 80mm thickness.

X-Core Mix

The 270-optimal mix was selected as most interesting mix with respect to specific compressive strength at the end of chapter 4 and is therefore used for all test performed in this section. Caution is taken in choosing the DU content. High pressures could damage the temperature sensors and rather delicate solder buses where the wire are joint together. A DU content of 1% is therefore used for all tests in this section.

Cure Cycle and Mould Setup

The standard cure cycle currently used for the production is selected as baseline. This cycle employs a 1.5$°C/min$ ramp from room temperature to 110$°C$ where it is held for 2 hours. From the information gained in the surface temperature distribution investigation in section 5.2.4 it was chosen to perform all tests with 1.5mm aluminium sheets positioned on the top and bottom of the mould surface. This assures temperature variations over the entire tile mould surface to be within ±3$°C$ and that the actual mould temperature closely follows the programmed cure-cycle with no overshoot at the end of the ramp up.

7.1.2. Test Setup

The DS18B20 digital temperature sensors previously used for the determination of the tile mould surface temperature distribution (section 5.2.1) will be used again. In order to keep the sensors in predefined positions, metal grids with roughly 4x4mm maze size were cut to size of the tile mould cross-section, resulting of grids of 175x30, 175x55 and 175x80mm. The mazes in the grid allowed for easy fixation of the temperature sensors in the correct position using tacky tape. The heads of the sensors were positioned inside the mazes so that the temperature sensitive part of each sensor was in good contact with X-Core from both sides. A total of 15 sensors were arranged in a grid pattern shown in figure 7.1. The used pattern concentrates most sensors in the centre region of the grid where temperature peaks and gradients are expected to be most severe. A total of five datapoints are present in both the thickness and width direction, allowing integration of the data using MATLABs 'griddata' function. The fitted data is purely used for graphical presentation of temperature profiles and no actual temperature data from these fits is used for other purposes.

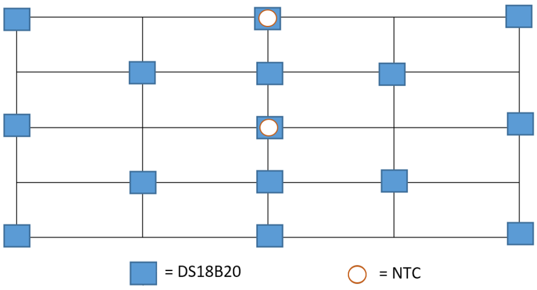

Figure 7.1: Grid pattern used for temperature sensor positioning. Squares indicate DS18B20 positions. Circles indicate placement of the NTC's later added to the setup

All sensors were soldered together combining the power, ground and signal wires into buses which eventually required only three wires to run outside the mould. The wires consist of PTFE (Teflon) sheaths which is temperature stable up to 200°. Soldered connections are covered in PTFE shrink tube to prevent short circuiting with the metal support mesh. The complete sensor grid is covered in vacuum bag material using double sided tape to assure easy release from the X-Core samples after curing. This allows the complete setup to be re-used multiple times. Both the bag and tape are again temperature resistant up to ±150°. The positioning

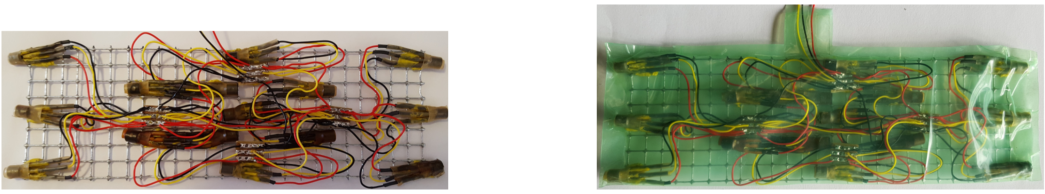

(a) DS18B20 sensors positioned on the 55mm grid with wiring present

(b) 55mm sensor grid covered in protective vacuum bag material. Three connection wire exiting at the top

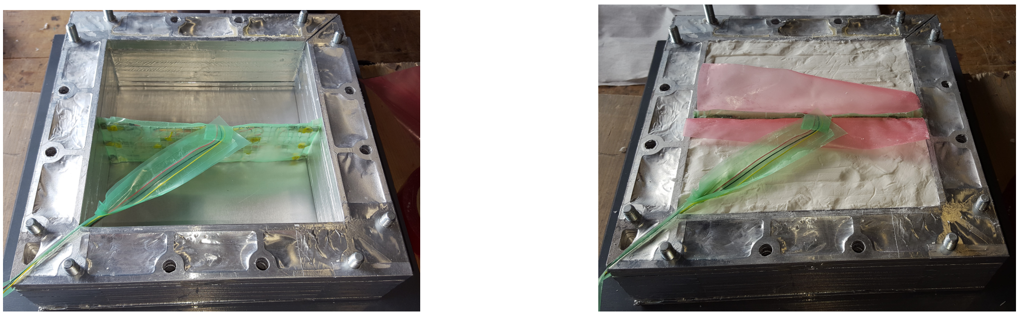

(c) Positioning of the sensor arrangement inside the mid plane of the tile mould

(d) X-Core placed inside the tile mould with temperature sensor grid in the midplane

Figure 7.2: Overview of the temperature sensor grid arrangement used for determining the temperature distribution in the midplane of X-Core samples at various heights

of the sensors on the grid, covering of the assembly in vacuum bag material and the placement of the sensors into the mould with and without X-Core in place are depicted in figure 7.2 for the 55mm high sample.

All tests are carried out with the sensor grid positioned in the midplane of the tile mould. The highest temperatures are expected in the absolute centre of the sample due to the exothermic heat generation of the resin cure and the insulating properties of foam. The midplane also acts as a plane of symmetry and is therefore the most logic place to perform the temperature measurements. Positioning of the grid in the diagonal symmetry plane of the mould was also considered. However, the boundary conditions here were expected to be influenced too much by the presence of the aluminium mould walls near the edges on both sides.

7.1.3. Data Collection and Post-Processing

Data collection was performed using an Arduino$^{\circledR}$ Nano combined with an SD-card module at a 5s measuring interval. The maximal accuracy of the 15 DS18B20 sensors can be set at 0.25°C for this interval. The post-processing of DS18B20 temperature data was previously treated in section 5.2.2, and the exact same procedure was applied in the processing of the data from the tests performed in this section.

7.1.4. Results

Results for the three tests revealed that temperature overshoots were more severe than expected. The temperature range of 127.75°C of the DS18B20 sensors was expected to be sufficient with the mould temperature programmed at 110°C. However, all three tests showed that the sensors in the centre section of the mould reached temperatures far higher than the upper limit of 127°C. Therefore, a different sensor is required to measure these temperatures. A negative temperature coefficient thermistor (NTC) was selected for its low cost of €1.50 per sensor, easy read-out using an Arduino$^{\circledR}$, small size (±1.5mm) and temperature range of -55-300°C. The NTC sensors were calibrated against a pre-calibrated PT100 sensor up to a temperature of 200°C. The calibration procedure and calibration curve are presented in Appendix B. The sensors have a rated accuracy of 3.1°C up to 200°C [41]. The 80, 55 and 30mm tests were repeated with the NTCs positioned at the same location as the central DS18B20 sensor as shown in figure 7.1. Data from the NTC sensors showed close correspondence with the DS18B20 sensors positioned at the same location up to the DS18B20 limit of 127.75°C. This assured that the calibration of the NTC was accurate. The maximal registered temperature by the NTC sensors at the core of the samples for the three heights are listed in table 7.1.

Table 7.1: Maximal temperatures in the centre of X-Core samples cured in the tile mould at various heights

Height [mm]	$T_{core}[°C]$
80	167
55	154
30	130

Remembering that the temperature at the mould surface is at $110°C$ gives temperature overshoots at the core of the samples of 57, 44 and $20°C$ respectively. The reason for the overshoot can be attributed to the exothermic reaction of the thermosetting resin used in X-Core. Even though the Ancarez® 4010 epoxy is combined with a relatively slow reacting Ancamide™ 3399 amine hardener [22], the heat generated by the reaction between the two components still results in large temperature increases in the central region of the X-Core samples compared to the mould temperature. The maximal temperature of $167°C$ reached in the $80mm$ thick X-Core block brought about questions on if this has any effect on the properties of the foam. Epoxy resin have a degradation temperatures at which the cured resin starts to fall apart into waste products. Discolouration of the resin indicates this phenomenon. To investigate this the produced blocks are sawed in half and lightly sanded. The cross-sections are depicted in figure 7.3.

Figure 7.3: Cross-sections of X-Core samples of 80 (top), 55 (middle) and $30mm$ (bottom) height. Discolouration visible relative to maximal temperatures present in the central region of the sample which reached 167, 154 and $130°C$ respectively.

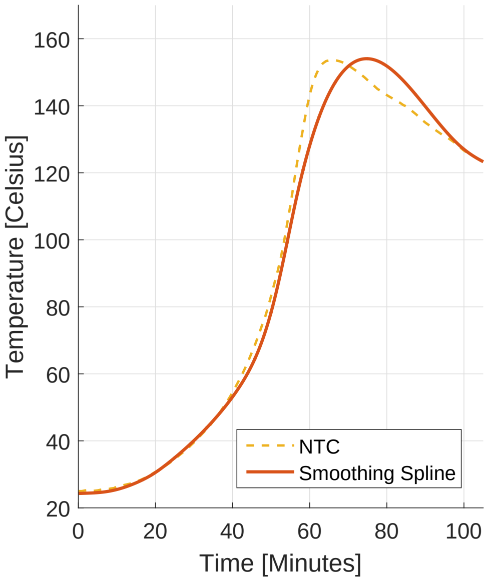

Figure 7.4: Fit smoothing spline for temperatures >$127°C$ compared to the NTC data for the $55mm$ sample central sensor

Darker regions are clearly visible in the $80mm$ sample. The $55mm$ sample also shows some discolouration but not as dark as the thicker $80mm$ sample. No discolouration is visible in the $30mm$ sample and its general colour is equal to that of the samples produced by S.Vial in his research [22]. This indicates that the discolouration is indeed related to the peak temperatures occurring in the sample core.

Further proof of this is found in the temperature data attained over all 15 sensors. As stated, the temperature exceeded the sensor limit for the DS18B20 sensors. However, using the acquired data from the NTC sensors, a curve can be fit over the region where the sensor limit is exceeded. Smoothing splines are ideally suited for this as they are not equation based but can be shaped using a shaping parameter. In this way, the shaping parameter can be adjusted until the maximal temperature corresponds to that of the NTC. Figure 7.4 illustrates this. The shaping parameter is tuned for the 80, 55 and $30mm$ tests such that the core temperature matches that of the NTC data. This tuned shaping parameter is then applied to the 14 other sensors present in the grid. In this way, the temperature trend of the DS18B20 sensor locations can be simulated allowing surface plots to be made for the complete cure cycle. The temperature data for all 15 sensors of each test is shown in figure 7.5. Exact representation of the NTC data was not achieved as a shift in the time at which the peak temperature occurred. This shift however is relatively equal for all sensor of a test. Therefore, the relative differences remain equal. This is deemed adequate enough for comparing the temperature distribution in the samples.

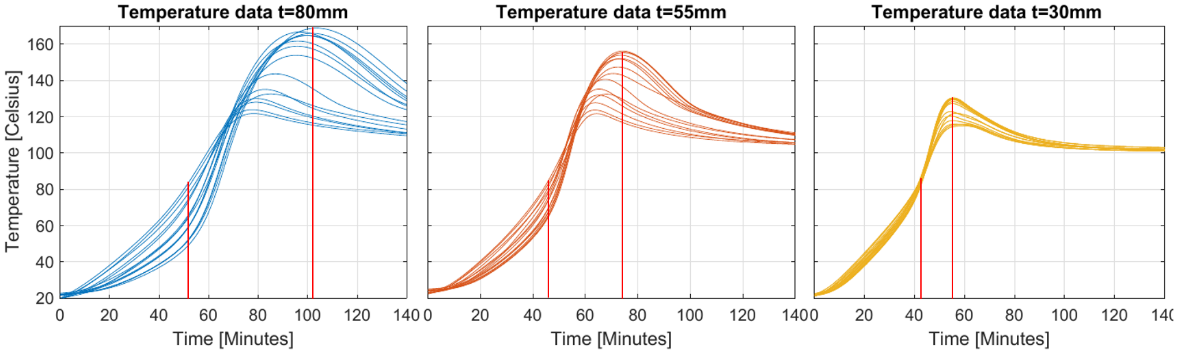

Figure 7.5: Temperature data from all 15 sensors for the 80, 55 and 30mm high samples. Showing the wide variation in temperatures between the sensors. Vertical lines correspond to temperature distribution plots in figures 7.6 through 7.8. Note: All data above 127.75°C is the results of a curve fit

Clearly visible are the large temperature variation between the sensors over the cross-section for the 80mm sample. This difference is much less in the 55 and 30mm sample. Figures 7.6 through 7.8 present the temperature distribution as a results of a 2D interpolation over the 15 sensors carried out in MATLAB using the 'griddata' function with a biharmonic spline interpolation method. Two plots are shown for all three heights, being the point in time where the first sensor reaches 85°C and the point in time where the maximal temperature is reached. These points in time are indicated with vertical lines in figure 7.5 for each height.

Looking at the surface temperature distribution plots in combination with figure 7.5 allows relation of the different lines for each sensor to their relative location. Clearly, in the 80mm sample large temperature gradients are present over the thickness. Interestingly, it is seen that the outer region of the sample reaches 85°C around 10min sooner than the core. When the outside reaches 85°C the core region is 50°C, giving a temperature difference of 30°C in 40mm of material. These differences are reduced in the 55mm samples, which still shown temperature gradients decreasing towards the core. At an edge temperature of 85°C the core of the 55mm sample is 65°C, reducing the temperature difference to 20°C. The 30mm sample hardly shows any temperature gradients when compared to the two thicker samples. A maximal difference of 5°C occurs here at the point when the sample reaches 85°C. At the peak temperature, this difference increases to 21°C. This large temperature gradients indicate that X-Core most likely has low thermal conductivity.

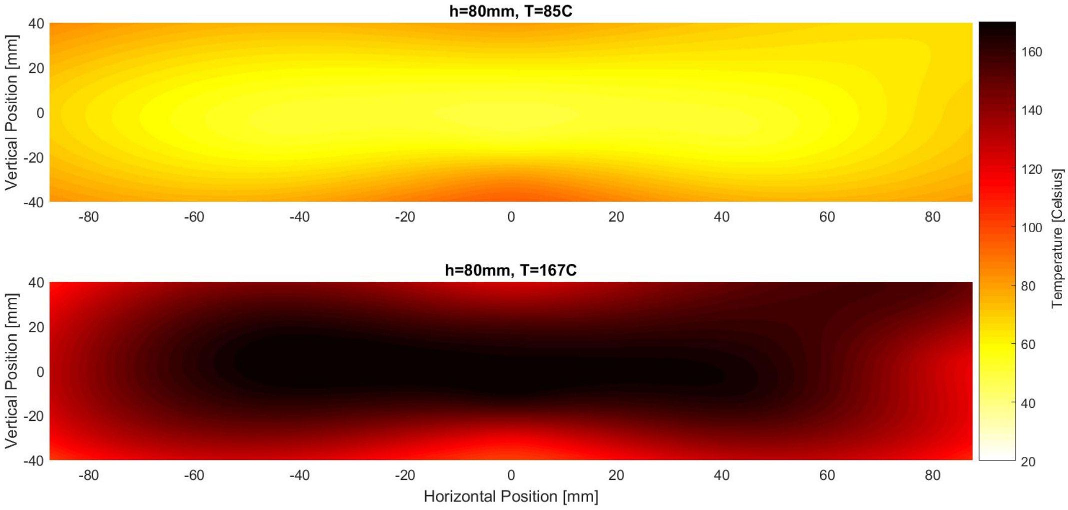

Figure 7.6: Temperature distribution in the 80mm sample when the temperature reaches 85°C (top) and when the max temperature is reached of 167°C (bottom)

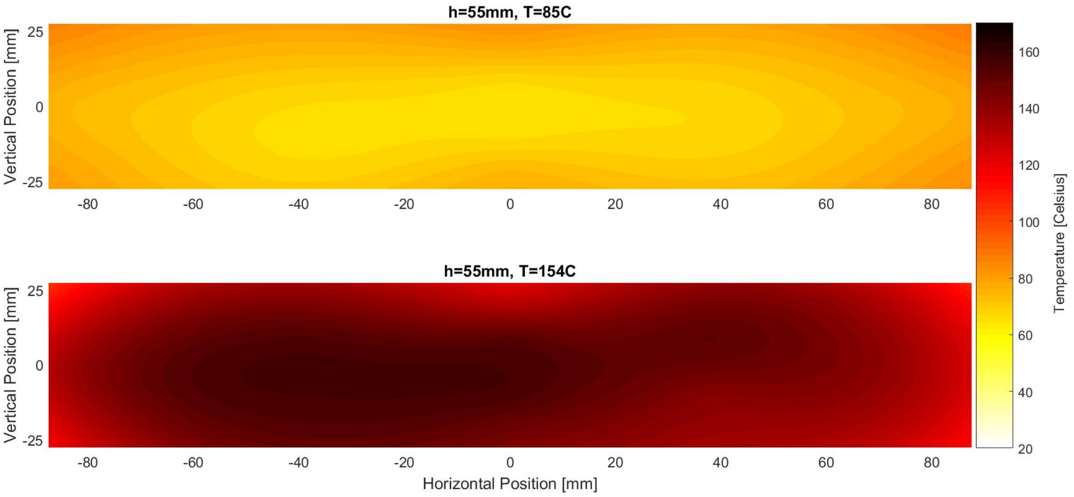

Figure 7.7: Temperature distribution in the 55mm sample when the temperature reaches 85°C (top) and when the max temperature is reached of 154°C (bottom)

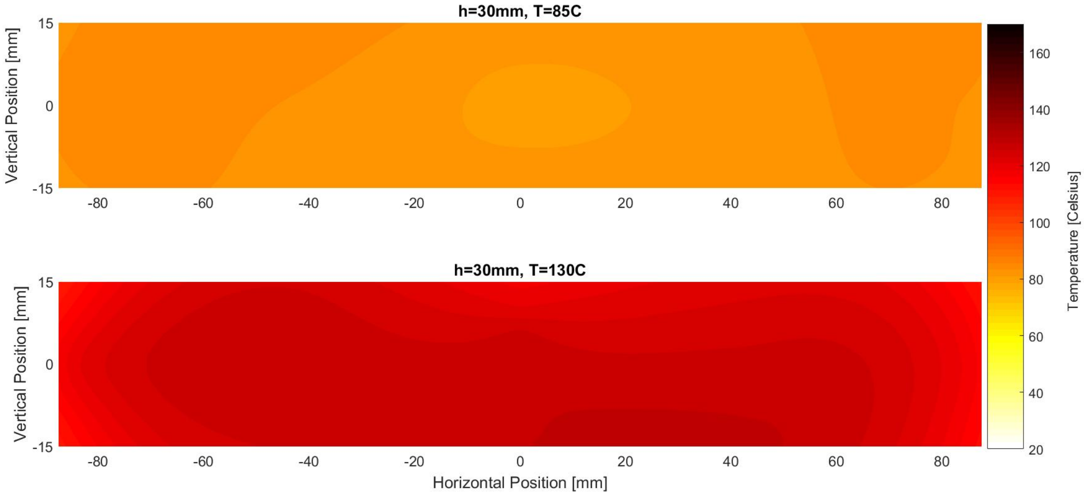

Figure 7.8: Temperature distribution in the 30mm sample when the temperature reaches 85°C (top) and when the max temperature is reached of 130°C (bottom)

7.1.5. Density Gradients Through Local DU Expansion

It is known that the DU components expands quite rapidly when 85°C is reached [22]. Having this expansions start at the surface and progressively moving towards the core could potentially results in density gradients through the thickness as material is gradually compressed from the inside out through the expansion of DU. Samples produced in the research of S.Vial, using the metal mould (figure 4.4) and oven with a cure cycle of $1.5°C/min$ to $110°C$, were used to test this theory. The Archimedes method of determining a materials density through displacement according to ASTM standard D792 [42] was used to this extend. The $30mm$ thick samples were sectioned vertically and horizontally thin slices of $\pm 10mm$ depth. Determining the individual density of each section through the thickness gives information on if any density differences are present. Five cured X-Core samples in a density range of 150-370kg/m^3 were tested. A full review of the results and sectioning approach is given in Appendix E.2. Figure 7.9 shows a summary of the results with density variation visible in both the vertical (left) and horizontal (right) directions of the sample. For three of the four tested samples the density near the edges was lower compared to the central region with differences as low as -11% compared to the average density. The gradient intensifies with increasing density. A switch occurs for sample S5, with a density of 370kg/m^3 and resin content of 24.5%. Density for this sample is higher at the edges by around 7-15%. Reason for this sudden change in density gradient could be attributed to the high resin content, which creates high heat generation in the centre of the specimen making this region reach 85°C before the edges do. All in all, results from these tests affirm the believe that the way in which X-Core is heated, from inside-out or outside-in, can result in density gradients through the differential expansion of DU. Based on these results, a method to control the density gradients is proposed and researched in section

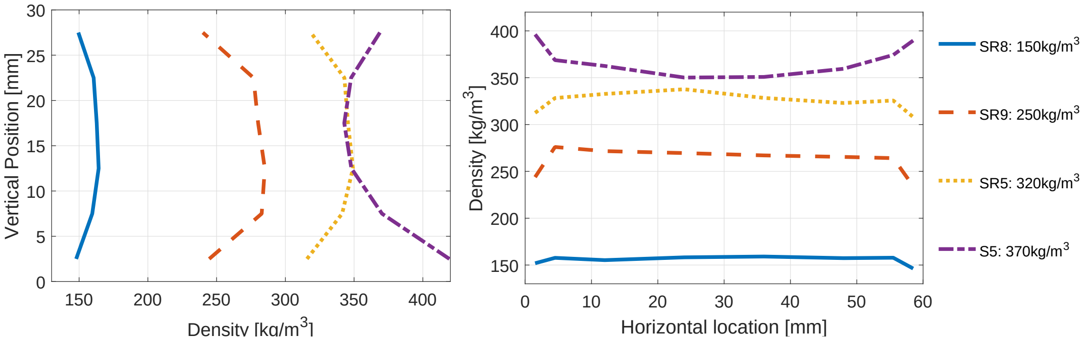

Figure 7.9: Density variation in vertical (left) and horizontal direction for four X-Core samples in the density range of 150-370kg/m^3

7.2. Creating functionally graded cores can be beneficial when designing sandwich structures for specific load cases. Higher densities are known to lead to give higher mechanical properties in syntactic foams. This topic was already addressed in the literature review in chapter 2 section 2.3.2. In flexure, high stresses tensile and compressive stresses occur near the facesheet/core interface. Literature shows that in flexure of syntactic foam sandwich structures, failure initiates on the tensile side of the structure [15]. Re-enforcing this regions through functional grading of the density could therefore aid in creating higher strength structures without net weight increase.

7.1.6. Possible Effects of Temperature Overshoots

To get a better understanding on if the discolouration in the core of the samples caused by the exothermic temperature peaks could be problematic, two experts were consulted. The manufacturer of the resin, *Airproducts*, stated that the discolouration of the epoxy is caused by the degradation of aminos inside the resin. The grade of discolouration seen is not excessive and is expected, according to *Airproducts*, to have no effect on the (mechanical-) properties of the epoxy resin. Long term (15-30 min) exposure to temperatures >200°C is expected to cause degradation of the resin system in terms of decreased mechanical properties, lower Tg and other chemical alterations due to the formation of non-functional waste products at elevated temperatures. Consultation with *Twenco CME B.V.* provided further information on the degree of discolouration which according to the expert was indeed a signal of degrading resin but not to the extend that it would surely effect the mechanical properties of the cure matrix.

Other possible issues of the high temperatures could be related to the DE and DU components inside X-Core. These polymeric microspheres are known to soften and expand under elevated temperatures. The expansion curve of 031DU is provided by *AkzoNobel* and is shown in figure 7.10.

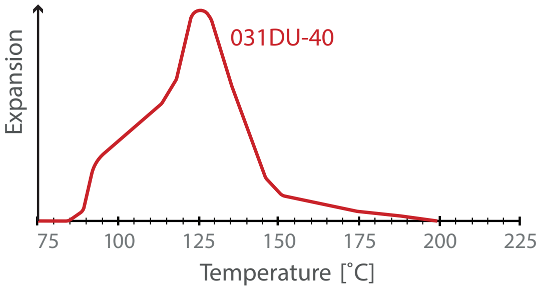

Figure 7.10: Expansion of DU 031-40 grade vs. temperature

Looking at the expansion vs. temperature behaviour of the 031-40 DU grade as used in X-Core shows that at temperature >125°C the degree of expansion reduces, indicating the escaping of the gas inside the microsphere. Expansion curves of the pre-expanded DE components are not available and where not provided by *AkzoNobel* when asked for. However, as they are still polymer based it is not unthinkable that these components are effected when exposed to temperatures around 160°C. Q-Cel is a borosilicate glass microsphere of which again no data with respect to thermal resistance is available. Glass however generally has a high thermal resistance and Q-Cel is therefore not though to be effected by the high temperatures.

All things considered no definite conclusion could be drawn on the fact if the temperature peaks experienced in the produced samples would lead to degraded properties of X-Core.

7.1.7. Conclusion and Initiators for Further Research

From the performed tests a clear relation is seen between the height of the sample and the core temperature. Temperature overshoots are maximal in the core of the 80mm sample at 57°C . The maximal temperature reached in the core of the 80mm is sample is 167°C. Consultation with experts provided reason to believe that these temperatures should not negatively influence typical epoxy-amine resin systems. However, making conclusions on the effects on the other components inside X-Core is not possible due to limited knowledge of the constituents thermal resistance. The polymeric microsphere could potentially suffer from the elevated temperatures which in turn could influence the mechanical properties of X-Core. Furthermore, it was indicated that in all three heights the edge region of the sample reaches the DU expansion temperature of 85°C first after which this front slowly progresses towards the core. In the 80mm sample, 10min separate the point at which the edge and core reach 85°C. There is reason to believe that this could potentially lead to density gradients through the thickness where lower densities are present at the edges and higher densities are present at the core as the sample compresses itself from the outside in. Testing of four samples indicated that density gradients were indeed present with a clear trend of decreasing density towards the edges for the foam with ρ<320kg/m^3. A higher density (370kg/m^3) sample with relatively high resin content of 24.5% showed inverse density gradients which could possible be attributed to heating of the sample from the inside out caused by the exothermic reaction of the resin. Controlling these density gradients could aid in making more efficient structures through local reinforcing of the core through increases in local density.

In the following section, a series of tests is proposed to answer the question on if there is an effect of the high temperatures on the properties of X-Core and if density gradients are indeed dependent on the way the sample is heated

7.2. Test Plan for Proof of Concept

From the results attained in the previous section, two regions of interest where highlighted. Firstly, it should be investigated if the high core temperatures have unfavourable effects on the mechanical properties of X-Core products. Secondly, the idea is brought forward to use the exothermic reaction and its effect on the core temperature to create controllable density gradients. If DU expansion can be steered to initiate at the core and progress towards the outer edge it could lead to an increasing density from the core towards the outer edges as material in gradually compressed against the edges of the mould. Increasing the facesheet/core interface strength potentially leads to higher strength sandwich structures. As the questions and hypothesis posed here are quite extensive and involve a lot of unknowns a series of tests is first required to test the viability of the ideas. *The following series of tests therefore act only as a proof of concept.* Several large steps are taken in order to explore if the hypotheses hold.

The following goals are set for the new test series:

1. Evaluate if the exothermic temperature peak of 167°C influences the mechanical properties of X-Core

2. Investigate if density gradients are present and if they are dependent on the location where X-Core reaches the DU expansion temperature of 85°C

To answer these questions the first objective is to find a method to lower the core temperature and have the core of the samples reach 85°C before the edges do.

Methods for Adjusting Temperature Profile

Using a slower reacting hardener with a lower exothermic energy could be one way to lower core-temperatures in large volume X-Core products. However, the dependency of the X-Core quality with respect to its internal and structure on the hardener type was shown in the research of S.Vial. The Ancamide™ 3399 hardener was selected from four different hardeners as it resulted in flawless X-Core samples [22] with higher mechanical properties compared to the other hardeners. Furthermore, goal 2 involves using the exothermic heat generation to create steerable density gradients which might not be possible is a slower reacting hardener is used. Initiating a search towards a new hardener with different properties is therefore not selected as method of lowering the core temperature as it is expected to lead to different issues with the X-Core composition which are not the topic of this research.

For the production of thick thermosetting composites in the wind industry long dwells (days) are applied to spread out the energy generation of the exothermic reaction and lower temperature gradients and temperature peaks in the laminate. This approach can also be applied to the cure cycle used in X-Core by applying a temperature dwell before ramping to a temperature of 110°C required for the curing of the prepreg facesheets. By having the exothermic energy peak occur at a lower mould temperatures the energy can more readily flow out of the central region of the product towards the cooler regions near the mould. This should lead to lower core temperatures. Furthermore, by correctly tuning the temperature of the dwell the exothermic energy could be used to heat the core of the sample beyond 85°C and initiate the expansion of DU in this region. Adding a dwell to the cure cycle could therefore satisfy both goals without requiring alteration of the X-Core material composition. This method is therefore selected and further explored in the following sections. The 80mm sample thickness is selected for these tests as it attained the highest core temperature and most severe temperature gradients.

7.2.1. Dwell Cure Cycle Determination

First, the required dwell temperature and duration have to be defined. This was performed through three dwell tests at different temperatures. The heat up rate of all temperature ramps is maintained at 1.5°C/min to limit the amount of variables that have to be considered. As this is not an optimization effort but merely a proof of concept, evaluating one variable is acceptable if this achieves goals 1 and 2. Altering the heat up rate is expected to also have an effect on the core temperature and temperature gradients, however the temperature of the dwell it self is expected to have more effect and is therefore preferred over adjusting the heat up rate.

The dwell temperature to be investigated are defined by an upper and lower bound. 80°C is set as upper bound, as 85°C should be reached at the core first. 50°C is set as lower bound as this is believed to be the onset of reaction temperature for the resin. Reviewing figure 7.5 for the 80mm thick sample shown a sharp increase in the temperature occurring around 50°C, indicating onset of the exothermic reaction at this point. 65°C is chosen as third dwell temperature as it lies halfway between the other to temperatures to be evaluated.

The exact same test setup as described in 7.1.2 was used again. The resulting temperature profiles are shown in figure 7.11 for the NTC sensors lying at the centre and top edge of the grid. All cure cycles consisted of a 1.5°C/min ramp from room temperature to the dwell temperature at which the mould was maintained for 2 hours. Table 7.2 summarizes the data of interest. The 80, 65 and 50°C dwells lowered the core temperature compared to the original cure cycle by 15, 24 and 48°C respectively. Temperature differences through the thickness are 42 and 43°C for the 80 and 65°C dwells and 33°C for the 50°C dwell. The point at which the core temperature exceeds the edge temperature is denoted by T_{switch} and should remain below 85°C to assure DU expansion is initiated at the core of the sample. This is achieved for the 65 and 50°C dwells. Time to peak (t_{peak}) values are also affected by the lower dwell temperatures, being 81, 98 and 113min for the respective dwell temperatures.

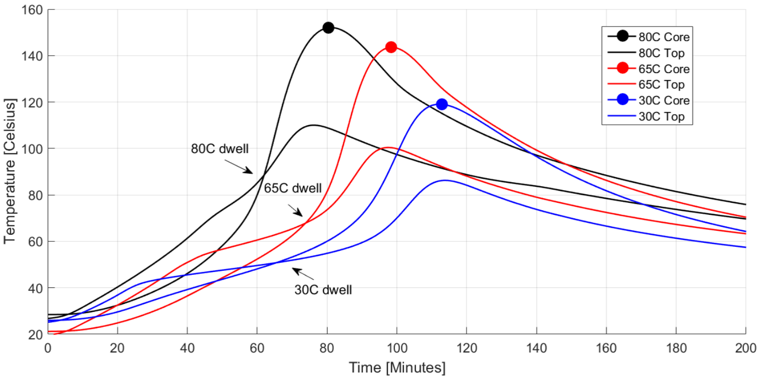

Figure 7.11: Temperature vs time for the three dwell temperatures of 80, 65 and 50°C. Core and top edge temperature attained with NTC thermistors on grid.

Table 7.2: Temperature data of interest extracted from figure 7.11 in °C

T_{dwell}	T_{core}	T_{top}	T_{switch}
80	152	110	89
65	144	100	68
50	119	86	51

Selecting Dwell Temperature and Cure Cycle Finalization

Based on the data attained for the three different dwell temperatures, the 50°C dwell was selected for further evaluation. This cycle lowers the peak temperature to 119°C reducing the overshoot to only 9°C. It also generates a temperature profile in which the core reaches 85°C before the edge as required for the investigation into the density gradients. What remains is to define the rest of the cure cycle, which should include a second ramp to 110°C for the prepreg facesheets present in the actual sandwich structures. In order to not increase the core temperature the second ramp should be initiated after the reaction exotherm is completed defined by t_{peak}, which is 113min for the 50°C dwell. In order to compare the effect on the mechanical properties of the new cure cycle to those of the original cure cycle it is important that both samples have similar degree of cure. This is achieved through using an estimate of the input energy during the cure cycle as E = Temperature[°C]*time[min]. The length of the dwell at 110°C for the new cure cycle is then adjusted such that the total E of the new cycle is identical to that of the original cure cycle. This resulted in a required dwell of 96min at 110°C for the new cure cycle. Both cure cycles are graphically visualized in figure 7.12. They are designated with the letter A for the original cure cycle and the letter B for the new cure cycle and will henceforth be referred to as such. Two samples were manufactured with the new cure cycle to verify that the ramp

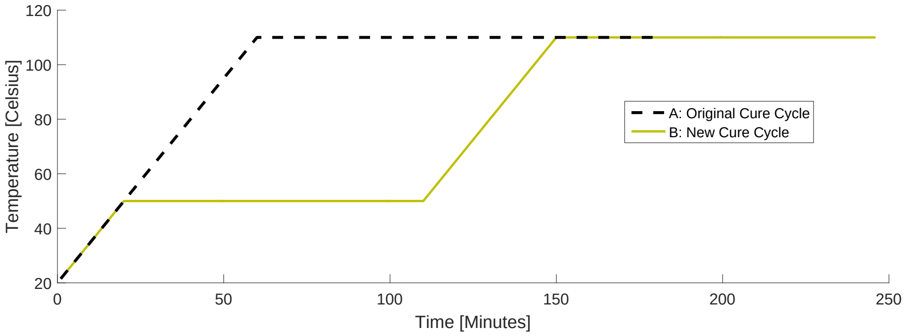

Figure 7.12: Original cure cycle with 1.5°C/min ramp to 110°C (A) and new cure cycle (B) with dwell at 50°C followed by ramp to 110°C with both ramps at 1.5°C/min

to 110°C does not effect the core temperature peak and to assure repeatability of the internal temperature distribution. The temperature results showed good repeatability within ±2°C as shown in figure 7.13 where the data from the initial 50°C dwell test is also included without the ramp to 110°C.

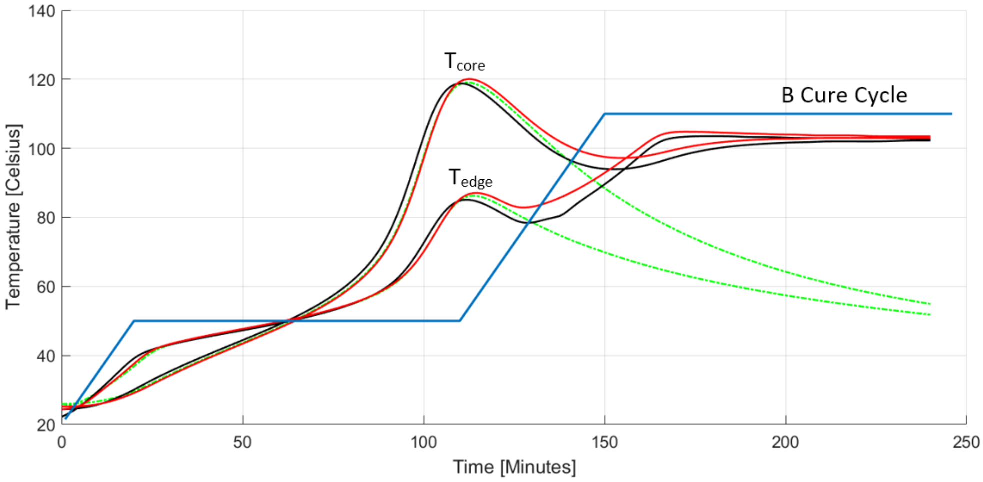

Figure 7.13: Repeatability of the temperature behaviour for three 50°C dwells. Solid lines correspond with cure cycle B. Dotted line corresponds with 50°C dwell from figure 7.11

The temperature distribution through the thickness when the core reaches 85°C for the new cure cycle is depicted in figure 7.14. This visualizes the way in which the central region of the sample reaches the DU expansion temperature first caused by the exothermic heat generation of the resin. This is the inverse of the behaviour seen in figure 7.6 where, for the same thickness but applying the original cure cycle, the edges of the sample reach the DU expansion temperature first.

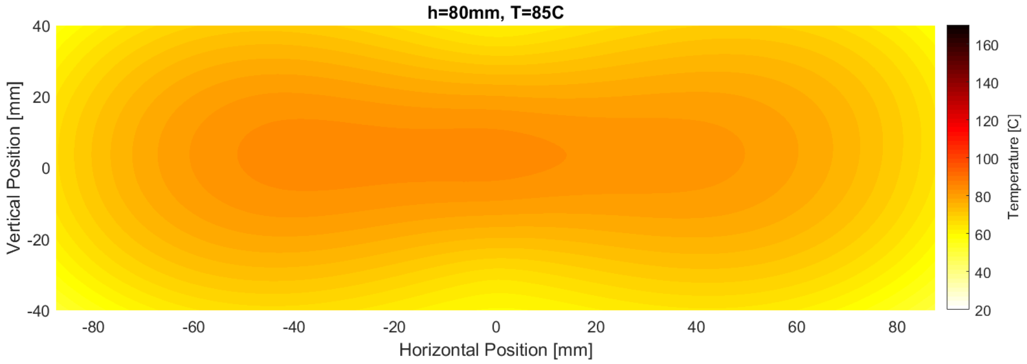

Figure 7.14: Temperature distribution of 80mm sample using B cure cycle when temperature reaches 85°C in the central region

7.2.2. Visual Inspection of Samples

Comparing the cross-section of both samples from both A and B series reveals several differences. The central region of the B sample clearly has less discolouration, attributed to the lower core temperatures during the cure-cycle. Consistency of the A sample shown numeral microcracks in the central region which could be indicative of damage related to the high core temperatures occurring there. A distinct darker region spanning the outer perimeter of the B samples is also visible. This region is thought to be related to higher resin contents locally, caused by the gradual expansion starting from the core of the sample and progressing outwards squeezing the resin to the edges of the sample. Some slabs showed microcracks appearing in the transition region as well possibly due residual stresses being present caused by the sharp change in material composition in this region. The sharp transition was unexpected and sections 7.2.4 and 7.2.5 will discuss the effects of this region in more detail.

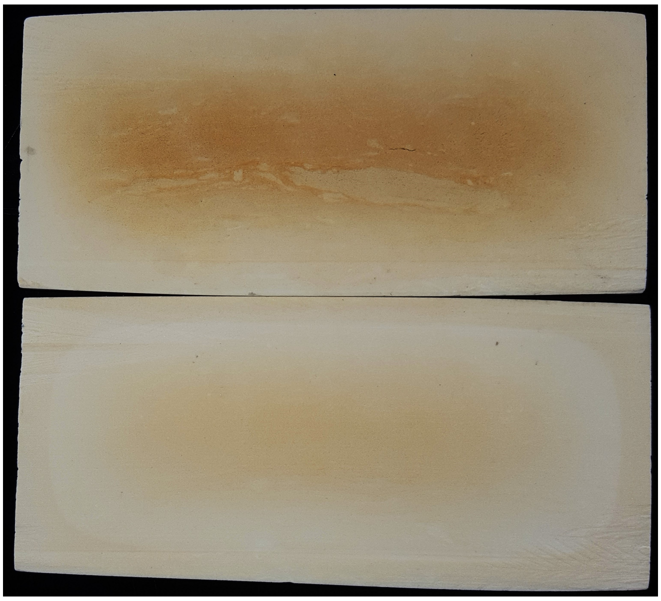

Figure 7.15: A series sample cross section (top). Discoloration visible with micro-cracks appearing in the high temperature region. Region of discolouration closely corresponding with temperature distribution shown in figure 7.6. B series sample cross section (bottom). Less discolouration visible in centre region compared to A sample linked to lower maximal core temperatures. Distinct darker region around the outer edges indicative of possible high resin concentrations

7.2.3. Plan for Comparative Testing of Old and New Cure Cycle

The new cure cycle allows for the realization of goals 1 and 2 set out in the beginning of this section. The new cycle both lowers the core temperature and in heated from the inside out. It can be compared to the original cure cycle to compare the effect of both the core temperature and possible differences in density gradients. The density gradients of these samples will be evaluated using X-Ray Tomography in section 7.2.4 and the compressive properties will be determined in section 7.2.5. Performing digital image correlation (DIC) in parallel to the compression tests will help to relate the density gradients to the failure behaviour of the samples. For these tests, a total of 12 samples are manufactured using the tile mould with $1.5mm$ aluminium sheets and insulation. Samples A1-A6 will be manufactured using the original cure cycle (A), samples B1-B6 use the new cure cycle (B). All samples are made using the 270 optimal mix defined at the end of chapter 4 with a 4% DU content. Of each series, two samples will be randomly selected for density gradient testing. The remaining four samples are tested in compression in combination with DIC.

Table 7.3: List of samples produced for the proof of concept tests on density gradients and compressive properties

Sample	Mix	% DU	Cure Cycle	Test
A1	270 optimal	4	A	X-Ray Tomography
A2	270 optimal	4	A	X-Ray Tomography
A3	270 optimal	4	A	Compression + DIC
A4	270 optimal	4	A	Compression + DIC
A5	270 optimal	4	A	Compression + DIC
A6	270 optimal	4	A	Compression + DIC
B1	270 optimal	4	B	X-Ray Tomography
B2	270 optimal	4	B	X-Ray Tomography
B3	270 optimal	4	B	Compression + DIC
B4	270 optimal	4	B	Compression + DIC
B5	270 optimal	4	B	Compression + DIC
B6	270 optimal	4	B	Compression + DIC

7.2.4. Defining Density Gradients through X-Ray Tomography

In chapter 2 the use of X-Ray tomography for the mapping of density gradients in structural foams was already introduced. X-Rays are transmitted from a source and travel through the object of interest after which they are caught by the detector. Part of the X-Ray beam is absorbed (attenuated) by the object. If the object has a constant thickness, the variation in the level of attenuation of the X-Rays is caused by the material composition only. If the object consists of one material type, the variation can be related to the local density of the material. Higher density areas will absorb more of the X-Rays, creating a lower intensity of the incident X-Rays on the detector at the location corresponding to the higher density area of the material. The resulting grey scale images can then be analysed in image processing software to attain knowledge of the location and of the relative density gradients. To relate the grey scale values to the absolute specimen density a calibration is required. This can be performed by scanning a minimum of three identical material composition samples with known constant density and identical thickness to the tested specimens.

Sampling Method

For the comparative research of the effects of the two cure cycles on the density distribution, six identical samples were created with each cure cycle in the tile mould at $80mm$ thickness. Two of these samples are randomly selected for the investigation of the density profiles of each cure cycle. These samples have to be sectioned into constant thickness slabs in order to be tested in the X-Ray tomograph. The method used to obtain the required slabs from the tile mould samples is described in Appendix F.

X-Ray Tomography Equipment and Procedure

A *Phoenix Nanotom* micro CT scanner was kindly made available for this research by Prof.dr.ir.E.Schlangen from the faculty of Geoscience & Engineering at the Delft University of Technology. The apparatus is depicted in Appendix F. The Nanotom was set to power of $90kV$, $260mA$ using a aperture time of $1500ms$ during which 20 images were attained and averaged to reduce the noise. Furthermore, three available X-Core specimens produced in previous research with known expected density were cut to the same thickness of the slabs to be scanned together with the slabs. By attaining the average gray scale values of these calibration specimens a relation between the gray scale and absolute density can be set up. The calibration procedure and results can be reviewed in Appendix F. The density of the calibration specimens was chosen to cover the expected density variations in the slabs. To assure accurate knowledge of the density of these sample the density of each calibration sample was determined using the Archimedes method according to ASTM standard D792 [42]. The resulting densities can be reviewed in Appendix E.1. Three images were required per slab to cover the complete height due to geometric limitations of the detector. The produced gray scale images were collected and imported into ImageJ where the Brightness/Contract was adjusted using identical setting for every image; min=132, max=165. The adjusted images were then imported into MATLAB for post-processing consisting of:

1. Attaining average greyscale value of calibration specimens and setting up calibration curve of absolute density vs greyscale value
2. Indicating area of interest consisting of left, right, top, and bottom boundaries
3. Attaining averaged greyscale values vs vertical location of the mid sections of the samples

Results

The X-Ray images of the middle and edge sections of two samples manufactured with either the A or B cure cycle are shown in figure 7.17. The other samples tested showed very similar patterns. Clearly visible is the sharp transition in density towards the edges of the B sample. The density of the A sample seems more evenly distributed. Clearly, the new cure cycle has been successful in increasing the density of the outer region of the block. However, the transition is very sharp. Reason for this is thought to be the transportation of resin towards the outside of the block during the gradual expansion of DU starting at the centre of the block and progressing towards the edges. Revision of the temperature trend at the edge in figure 7.13 shown that this region reaches the expansion temperature only shortly during the exothermic peak, decreasing below $85°C$ again until the ramp to $110°C$ raises the temperature again. This could indicate that expansion of DU in the edge region is limited and does little to prevent resin entering this region. A-samples also show slightly darker regions near the centre area compared to the edges. This difference is much less prominent however compared to the transition occurring in the B samples. Figure 7.16 shows the variation in density vs vertical location of the middle section of a slab of the A and B samples respectively. The lines represent the average density value attained over all the X-Ray analysed specimens for a certain cure cycle.

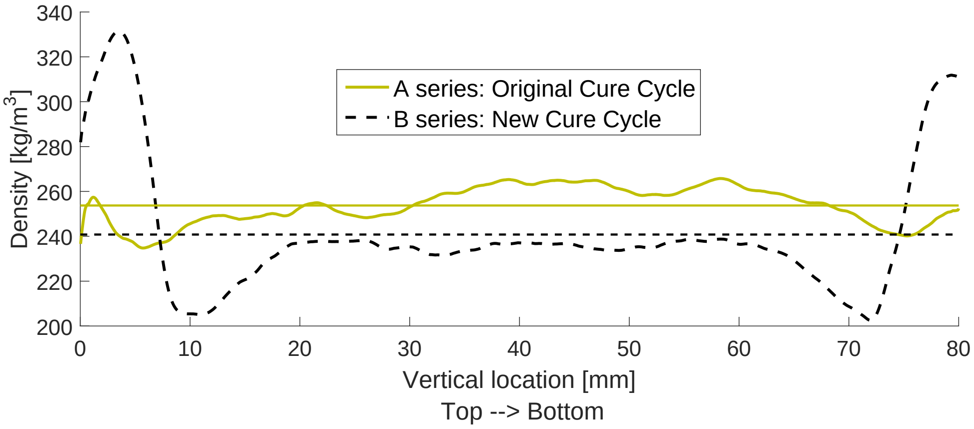

Figure 7.16: Averaged density gradients present in the original cure cycle samples (A) and the new cure cycle samples (B).

The average middle section density is indicated by the horizontal line and is $253.7 kg/m^3$ for the A series and $240.8 kg/m^3$ for the B series which have more high density material located around the sides not covered by the middle section (see figure 7.17b). The relation between the grey scale images presented in figure 7.17 is clearly visible. The density gradient of the original cure cycle samples shown a minimal density of $234.8 kg/m^3$ at the top edge region ($7mm$) and a maximal at the centre region of $265.8 kg/m^3$. This shown a decrease in density of -7.5% w.r.t. the average towards the edge of the slab which is in the same order of magnitude as the oven-cured samples analysed in section 7.1.5. The density at the edge of the new cure cycle samples reaches a maximum at the top edge ($5mm$) of $331.3 kg/m^3$. Moving towards the core of the sample the density decreases to $205.1 kg/m^3$ within $7mm$. Giving a maximal difference with the average density of +37.6% and -15.8%.

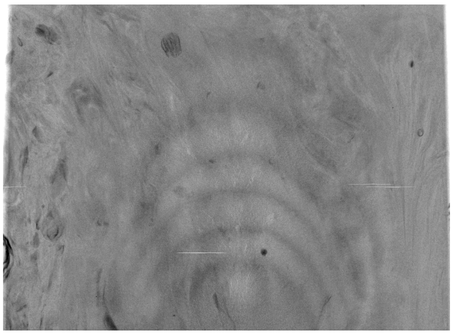

(a) Corner section of original cure cycle (A) sample

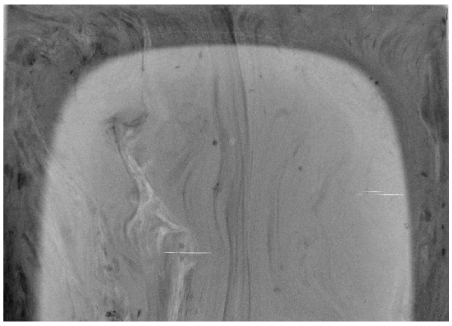

(b) Corner section of new cure cycle (B) sample

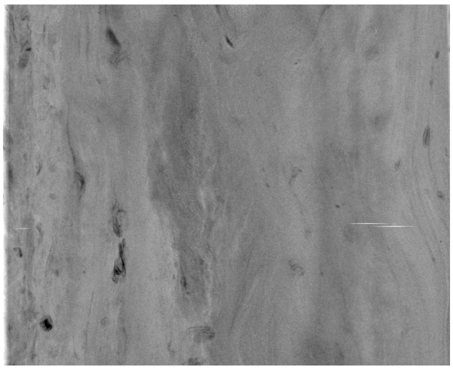

(c) Middle section of original cure cycle (A) sample

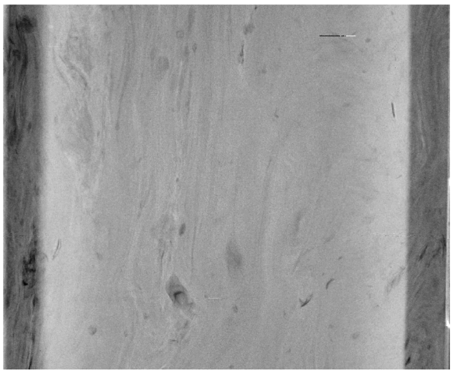

(d) Middle section of new cure cycle (B) sample

Figure 7.17: Post-processed X-Ray images of old (A) and new cure cycle (B) samples taken from the top and middle sections of two arbitrary samples. Gray scale values indicative of the density. Left side of the image is the top of the original block.

7.2.5. Compression Tests Combined with DIC

In order to find out if the density variations can also be linked to a variation in strength compression tests are executed on both cure cycle type samples. For each cure cycle four blocks were manufactured. These blocks are to be tested in compression combined with digital image correlation (DIC) which will provide information on the local strains present in the material during the compression. The presence of local strains are indicative of local failure of the material. Tracking the magnitude and location of the local strains therefore gives information on which region of the sample fails when and how. The compression test will be executed according to ASTM standard D1621 [25].

Specimen Preparation

The geometry of the samples is dictated by ASTM D1621 for square cross-section samples to be such that the height of the sample does not exceed the width. The height is fixed at 80mm as trimming of the blocks in this direction would mean losing the edges of the density gradients. To limit the effect of the boundary effects present in the samples as seen in figure 7.17b it was chosen to set the width of the square cross-section at the minimal allowed 80mm. The same procedure as used for the preparation of the X-Ray specimens (figure F.1) was used to attain constant width specimens with straight edges. The resulting cubes of 80x80x80mm were measured at three locations over every axis to attain the average cross-section area and height. One face of every sample was then painted evenly with white paint followed by a speckle pattern applied using black spray paint assuring proper contrast between the speckles and background as required for the DIC procedure.

Test Equipment and Procedure

A Zwick 250kN compression bench was used for the compressive testing of the samples. A Vic3D DIC measurement system was use consisting of two camera's, a light source and a data collection device connected to a PC. The complete setup is depicted in figure 7.18.

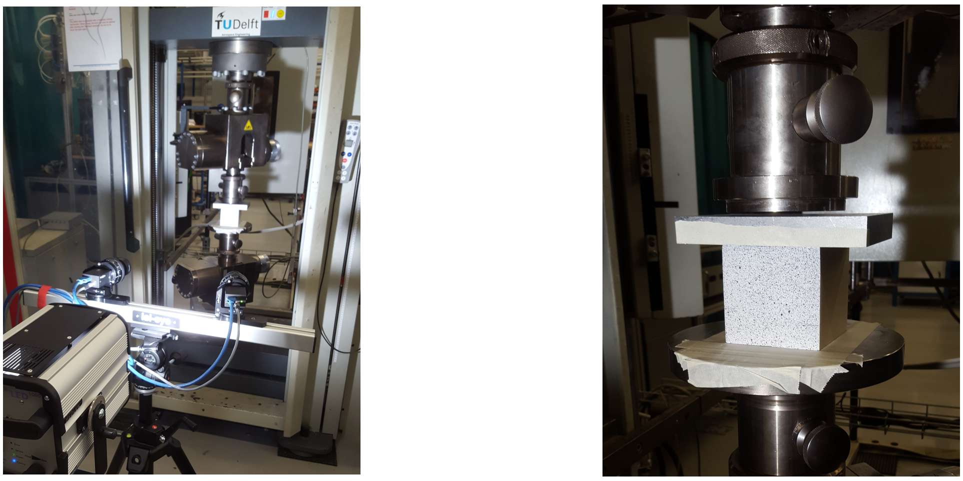

(a) DIC cameras and light source focused on the X-Core sample

(b) Speckled sample in Zwick 250kN bench, solid steel block placed on top to assure even stress distribution

Figure 7.18: Compression test setup combined with DIC equipment

A pre-load of 50N is applied at which point the test is initiated using a compression rate of 8mm/min. The tests are stopped when 13% deformation is reached. The complete compression test is recorded by the pre-calibrated DIC setup for every specimen at an imaging rate of 2Hz. This sampling rate assures an image is captured for every 0.067mm of vertical displacement.

Results

The attained stress vs. strain data is post-processed according to the steps pre-scribed in ASTM standard D1621. This consists of extrapolating the steepest straight part of the deflection curve to the zero-load axis to set the strain origin. 10% strain is then measured from this origin at which the stress is attained. This stress at 10% strain dictated the failure strength of the sample. The post-processed stress vs. strain data for the tested samples is shown in figure 7.19. All four samples of each cure cycle show very similar behaviour and failure strengths as shown in table 7.4. All samples show strain hardening without a defined yield point which correlates with the compressive behaviour noticed by S.Vial in his extensive study on X-Core compressive properties. The strain hardening can be attributed to the crushing and collapse of the microspheres [43]. The material of the sphere wall fills the cavity created by the microspheres collapse. Continued compression then densifies the residual material of the microsphere which act as a compact solid region and therefore has higher strength compared to the intact microsphere. On a macro-scale, this phenomenon leads to gradual strengthening of the material as the strain increases. The B samples manufactured using the new cure cycle have a 15% lower strength compared to the A series samples. The reason for this is found when inspecting the DIC data shown in figure 7.20.

Plotting the local strains in the compression direction (ϵ_{yy}) over the specimen cross section results in the images shown in figure 7.20. All specimens of either type A or B showed highly similar behaviour, and therefore two arbitrary samples of both sets (A3 and B5) are selected for reviewing. Re-visiting figure 7.16 shows that the failure behaviour is highly correlated to the local density variations. Sample A3 shows failure initiation, e.g. the point where local strains <-0.05 first appear, at the top surface of the specimen. Final failure is mostly dictated by local strains <-0.28 in the regions towards the edge of the sample. The central region shows small areas with ϵ_{yy}<0.06 but overall this region retains its integrity. This corresponds with the density gradient seen in figure 7.16 which revealed that A series samples have a 13% lower density at the edges compared to the central region. Looking at the ϵ_{yy} data for sample B5 shows clear initiation of failure in the region around $7mm$ away from the edge. Final failure is dominated by large local strains occurring in the same region. Compared to the final failure image of sample A3, the central region of B5 shows more local strain occurring indicative of material failure in this area. The edge region of the sample manufactured using the B cure cycle was shown to have a 30% higher density compared to the centre region. The local strains in this region are therefore also much lower compared to the rest of the specimen.

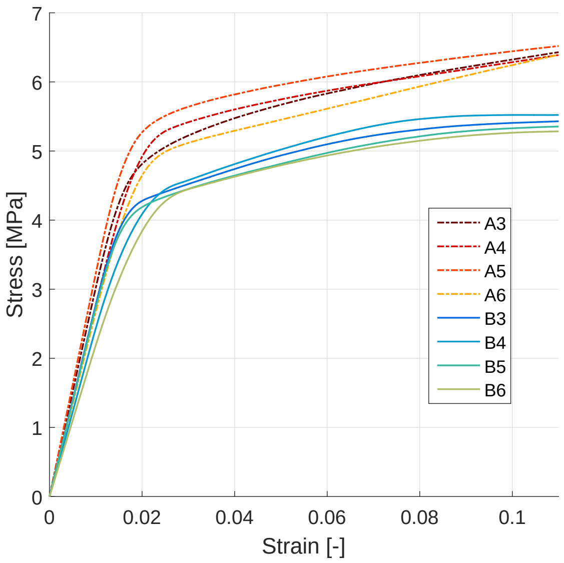

Figure 7.19: Stress vs. strain data of the original (A) and new (B) cure cycle samples

Table 7.4: Failure strength (σ_c) at 10% strain for the compression tested samples

Sample	**σ_c [MPa]**
A1	6.32
A2	6.29
A3	6.44
A4	6.24
Avg. A	**6.32**
B1	5.41
B2	5.52
B3	5.33
B4	5.26
Avg. B	**5.38**

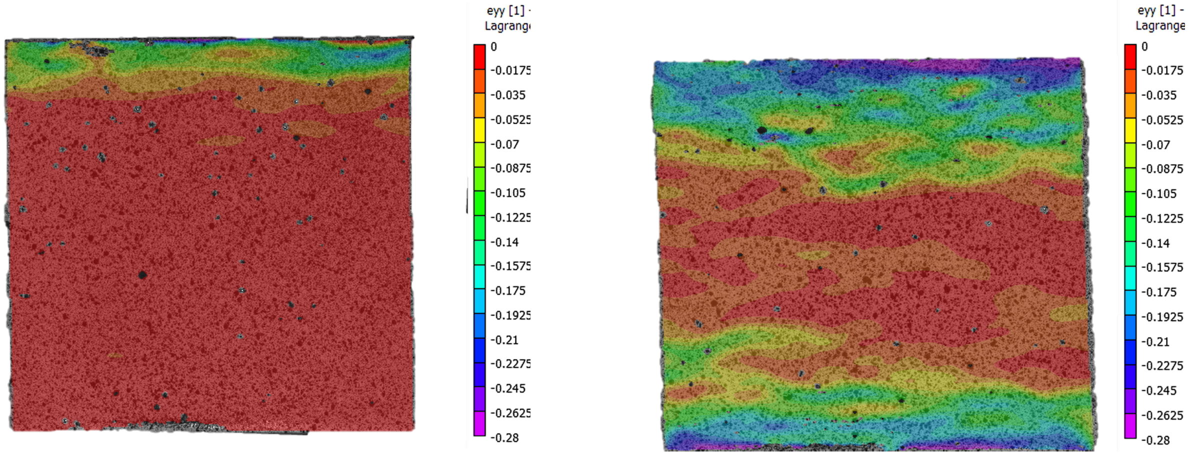

(a) Local strain in compression direction of sample A3 at failure initiation

(b) Local strain in compression direction of sample A3 at σ_c

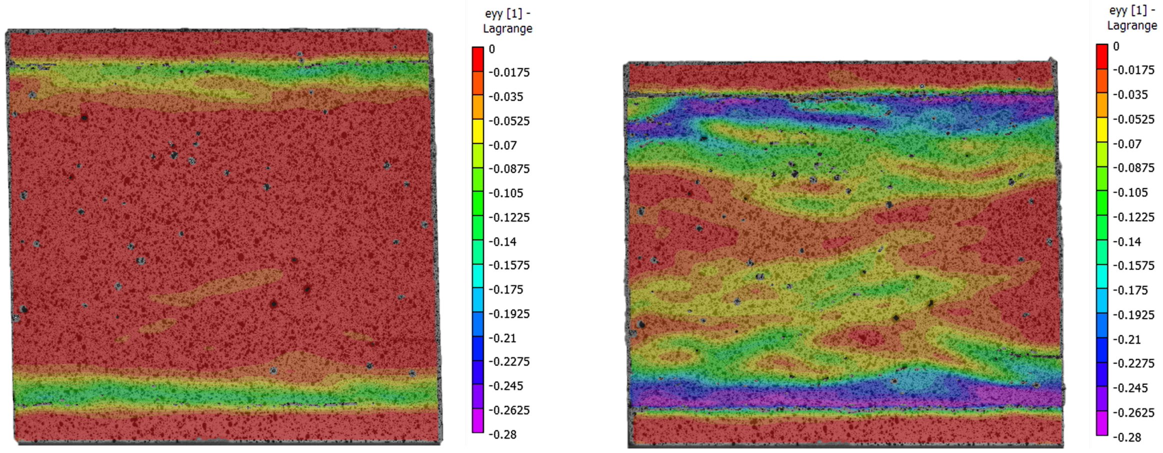

(c) Local strain in compression direction of sample B5 at initiation of failure

(d) Local strain in compression direction of sample B5 at σ_c

Figure 7.20: DIC results showing local strains in the test direction overlaid over the specimens undergoing compressive testing

7.3. Conclusions and Discussion

The present chapter has explored the temperature behaviour of X-Core during its cure inside a mould representative of current mould used for the production of X-Core components. An initial series of tests at various heights indicated that large temperature overshoots occurred with maximal temperatures reaching $167°C$ in an $80mm$ thick sample. Various degrees of discolouration of the samples occurred in relation to the maximal temperature reached in the centre region. The discolouration was found to be related to waste product produced through the degradation of the aminos inside the amine hardener. Consultation with experts provided no reason to believe that the extend of discolouration seen was reason for concern with respect to degrading properties of the resin. However, conclusions on the effect of the high temperatures on the other X-Core components were hard to make through limited availability of information on material properties. Furthermore, it was noticed that the DU expansion temperature of $85°C$ was reached on the outside edges of the samples first. This way of heating the sample was shown to be highly likely linked to density variations inside the products. The information obtained in this firs series of tests led to a proof of concept phase. Here, the effect of the high temperatures on the mechanical properties of the samples was evaluated as well as the theory that favourable density gradients could be imposed on the samples if the exothermic reaction of the resin was used to heat the centre region beyond $85°C$ before the edge region. A new cure cycle using a dwell at $50°C$ was set up. The new cure cycle lowered the core temperature with $48°C$ and caused the centre region to reach the DU expansion temperature first. Comparison of samples made with either the original (A) or new (B) cure cycle showing defined differences in density gradients. The original cure cycle sample produced relatively constant density through the thickness with 7.5% lower thickness towards the edges. The new cure cycle showed quite extreme density gradients with 37.5% increase in density near the edge regions. The variation in density was shown to be closely related to the local strength of the material. Compression test with DIC revealed that A-samples had a 15% higher compressive strength on average compared to the B-samples. Reason for this difference is the higher minimum density of A-samples compared to the minimum density of B-samples. Failure initiated towards the outer edges for the A-samples corresponding with the lower density in this region. B-samples failed in a region around $7mm$ away from the edges, again corresponding with the region with lowest density.

This second series of tests proved two things. Firstly, the compressive strength of X-Core is not noticeably effected by a temperature of $167°C$ occurring in the centre region during the cure cycle. Lowering this centre temperature to $119°C$ did not increase the compressive strength of the foam. Secondly, density gradients can indeed be controlled through initiating expansion of DU in the centre region instead of at the edges.

Past research on flexural loading of syntactic foam sandwich structures showed that failure in these structures initiates on the tensile side of the sandwich as indicated in section 2.3.2. Functional grading of the core to have higher density at the tensile side was shown to result in higher specific strength sandwich structures in flexural loading [14]. The initiation of expansion in the centre of X-Core provides this density gradient without requiring alterations of the material. The currently induced density gradient however shows a sharp transition and drop in density towards the centre, which leads to the question if this zone might become more critical in initiating failure. Another potential application of the new cure method could be the use of dry fibre facings combined with X-Core. Dry fibres are lower cost compared to prepreg fibre facings and are therefore interesting for the creation of low-cost sandwich composites. The resin squeezed out of X-Core during the expansion occurring from the inside out can then be used to impregnate the dry fibre facings. Chapter 10 provides a series of recommendations for further research based on the attained information in the performed tests.

Too facilitate further research towards these possible applications, a model is set up in the next chapter which aims to predict the temperature distribution and trends in X-Core during its cure. Without this tool, temperature tests have to be carried out for every alteration of the process or X-Core composition. With the tool, predictions can be made before doing experiments, limiting the amount of test required to attain the desired results.

8

Numerical Modelling of the X-Core Cure Process

In the previous chapter an investigation towards the thermal behaviour of X-Core during its cure was presented. It was proven that density gradients could be induced through adjusting the cure cycle. Recommendations for further research were also given as several applications for the technique of initiating DU expansion in the centre of the product were indicated. X-Core is not one material but a combination of different constituents which can vary in their volume fractions. Achieving the same temperature distribution when varying the X-Core composition is therefore not straight forward. Analytical models to predict the thermal properties of filled composites are present but no transient temperature solutions exist for materials with internal heat generation. Therefore, a numerical model is required to predict the effects of different X-Core mixtures and processing conditions on the thermal behaviour during a cure. As *Donkervoort* is not in possession of any thermal software capable of such simulation, an effort is made to set up a model which is independent of licensed software. MATLAB is used to set up a two-dimensional, transient finite difference method based heat conduction model with internal heat generation as the author is familiar with this programming language. The generated code however can easily be transcribed to open-source programming languages like Python™. The current chapter introduced the used finite differences method and explains how the thermal properties of various X-Core mixtures can be calculated. The resin cure kinetics are then experimentally defined and integrated into the model. The resulting model is verified against analytical solutions after which validation is performed through the comparison of the simulation with experimental results from chapter 7.

8.1. The Finite Difference Method

The method of finite differences uses a discretization of the medium of interest into smaller regions. Every region is assigned a reference point, or node, which together make up a nodal network or mesh. The temperature at the nodal point represent the average temperature of the region to which it is assigned. To further model the change of temperatures through time a transient analysis is required which applies a further discretization of time into time steps Δt. Differential equations can then be set up that govern the conservation of energy in the nodes. Solving the set of differential equations for all nodes gives the complete temperature distribution in the nodal network. Smaller time steps Δt increase the accuracy of the solution but require longer computational time. The same holds for the discretization in space where smaller elements will lead to closer approximation of the continuous exact solution. For solids and fluids at rest, the energy transferral from hotter to cooler regions is dictated by conduction [44]. Heat flows can be derived from the temperature gradients present inside the body. Therefore, knowing the temperature distribution inside a body as function of location and time allows for the heat flows to be determined from Fourier's law, relating the heat flow to temperature gradients. In this section, the derivation of the required governing equations are presented and subsequently related to the different nodes inside the nodal network.

8.1.1. Required Assumptions

In this analysis, X-Core will be treated as a homogeneous, isotropic solid with internal heat generation due to the exothermic reaction of the epoxy. *Homogeneity* is assumed as X-Core consists of mixture of different components on a micro-scale. The scale in this analysis is in terms of tens of mm's, therefore if it is assumed that the components are adequately mixed and evenly spread such that each volume segment of the body consists of a identical composition. Properties like specific heat capacity and thermal conductivity can therefore be assumed constant throughout the volume. The same holds for the assumption of *isotropy* inside the material, meaning that the conductivity in all direction is assumed equal.

Convection heat transfer inside the body through gas or fluid transport is assumed to not be present to prevent over-complication of the analysis. Support for this assumption comes from the fact that the pre-cured form of X-Core is of a dimensionally stable, foam like composition and is tightly packed inside the moulds Gases are present inside the hollow microspheres, but these are enclosed and can therefore not create convective currents outside the bounds of the microsphere. Interstitial voids can be present in mixtures with high microsphere contents but their contribution to the heat transfer is taken to be negligible compared to the effect of conduction. Resin flow might be present under elevated temperatures as the viscosity of the resin decreases at this stage before curing. Modelling these resin flows is essential in modelling the heat flow in processes like resin transfer moulding (RTM) which obviously involve significant resin flow. However, in this case the material is placed in an enclosed mould limiting the resin outflow to the outside environment.

Constant pressure is assumed throughout the analysis. Pressure differentials created by the temperature variation though the thickness could cause resin flows as indicated in chapter 7, however modelling these phenomena requires accurate knowledge of the resin viscosity and local pressures inside X-Core which are simply not available at this stage of the research. Furthermore, changes in pressure can have effect on the interfacial thermal resistance present at the boundaries but again too limited knowledge is available about the pressure generation against temperature of X-Core to account for this in the model. Therefore these phenomena are considered to be outside the scope of this analysis.

Radiative heat transfer is also not accounted for as X-Core is treated as a solid being in physical contact with a mould which is maintained at a prescribed temperature. Heat transfer through radiation at relatively low temperatures ($<150°C$) is therefore negligible with respect to the heat transfer occurring through conduction. Both the model by *Bogetti & Gillespie* and *Shi* introduced in section 2.4 use the same assumption.

Thermal material properties are assumed constant, being independent of time or temperature. This assumption is used to prevent over complication of the model based on too many assumptions. The large variety components inside X-Core will all behave differently under changing temperatures. Exploring all individual materials and there dependence on temperature is outside the scope of this research.

A *two-dimensional Cartesian coordinate system* is applied to analyse rectangular cross-sections of infinite length. This allows the model to be used to approximate the transient thermal behaviour of X-Core in products with various heights and widths in which the depth is $\gg$ width or height of the products. This is useful as most products consist of long slender beam type products such as the door sections and floor plates. The two-dimensional model assumes that no gradients in temperature in the depth direction are present and can be used when edge effects in the depth direction are minimal [17].

8.1.2. Derivation of the governing equations

Writing the governing equations in terms of conservation of energy of a control volume, in stead of purely as the distribution of the temperatures, around a nodal region is called the 'energy balance method'. It allows for the integration of internal heat generation and multiple materials in the model [45]. The energy balance equation for a differential control volume $V = \Delta x \Delta y$ inside the medium is given by:

[Heat transferred into volume element V through the surfaces during Δ t] + [Internal energy generation in volume element V during Δ t] = [Internal energy change in volume element V during Δ t]

Expressing this relation in terms of the actual variables gives:

$$\Delta t * \sum_{Allsides} \dot{Q} + \Delta t * \dot{q}_{int} = \Delta E_{element} \tag{8.1}$$

$\dot{Q}$ $[W/m]$ is the heat transfer rate between nodes, which for internal nodes is purely caused by conduction. At the boundaries, the heat transfer can also be caused by convection, heat flux and radiation [45] but these are neglected as stated in the assumptions.

In this analysis, the internal heat generation rate $\dot{q}_{int}[W/m^3]$ is caused by the exothermic reaction of the epoxy resin inside X-Core. This term will be further explored in section 8.6.2. For a volume element V this term is multiplied with the volume expressed as $\Delta x \Delta y$ to attain the heat generation rate per unit volume.

Lastly, the change in internal energy is equal to: $\Delta E_{element} = mC_p\Delta T = \rho C_p V\Delta T = \rho C_p \Delta x \Delta y \Delta T[J/m]$. Where $\rho[kg/m^3]$ is the material density, $C_p[J/kgK]$ is the material specific heat capacity and $\Delta T[K]$ is the change in temperature of the element.

Now re-writing equation 8.1 by dividing it by time step Δt gives

$$\sum_{Allsides} \dot{Q} + \dot{q}_{int}\Delta x \Delta y = \rho C_p \Delta x \Delta y \frac{\Delta T}{\Delta t} \tag{8.2}$$

How this equation is applied in the nodal network will be explained in the following paragraphs where a cell at a location m,n is taken as example. The heat flows, $\dot{Q}$, into/out of cell (m,n) are dependent on the temperature difference between the central node and an adjacent node together with the conductance, K, present between the cells. The heat flows per unit length (in depth direction) going into cell (m,n) through its four surfaces are shown in figure 8.1.

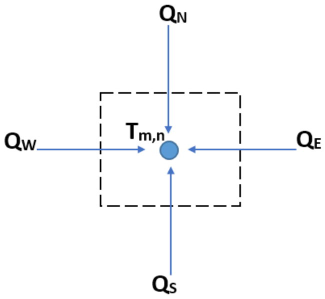

Figure 8.1: Heat flows into cell (m,n) from the neighbouring cells

The heat flows per unit length are denoted by $\dot{Q}_N$, $\dot{Q}_E$, $\dot{Q}_S$ and $\dot{Q}_W$ $[W/m]$and are calculated through:

$$\dot{Q}_N = K_{m,n+1/2}(T_{m,n+1} - T_{m,n}) \tag{8.3}$$

$$\dot{Q}_E = K_{m+1/2,n}(T_{m+1,n} - T_{m,n}) \tag{8.4}$$

$$\dot{Q}_S = K_{m,n-1/2}(T_{m,n-1} - T_{m,n}) \tag{8.5}$$

$$\dot{Q}_W = K_{m-1/2,n}(T_{m-1,n} - T_{m,n}) \tag{8.6}$$

Where a positive heat flow is established into cell (m,n) if the temperature of the neighboring cell is higher than the temperature of cell (m,n). This convention is maintained throughout the model.

Figure 8.2 shows the same central node with its four surrounding nodes. The thermal coupling between the nodes is dictated by the thermal conductances indicated by K [W/mK] [46]. The conductances are given per unit length in the direction perpendicular to the x,y-plane as required for a two-dimensional model. As example, the conductance between cells (m-1,n) and (m,n) is given by [46]:

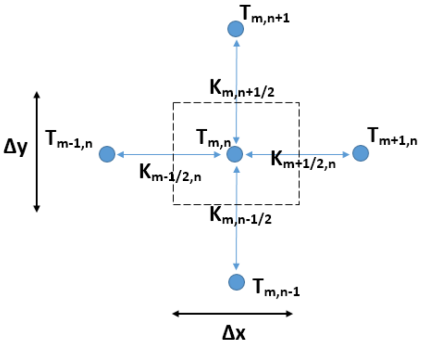

Figure 8.2: Thermal coupling through thermal conductances between cell (m,n) and its neighbors

$$K_{m-1/2,n} = \frac{\Delta y}{\frac{\Delta x}{2k_{x_{m-1,n}}} + \frac{\Delta x}{2k_{x_{m,n}}} + R_{m-1/2,n}} \tag{8.7}$$

Equation 8.7 applies the analogy of thermal resistance to that of electrical resistance and models the resistance/conductivity a set of resistors in series [40]. The conductance $K_{m-1/2,n}$ describes the ease of the heat flow through the left boundary of cell (m,n) per unit length (perp. to x,y-plane). $k_{x_{m,n}}$ $[W/mK]$ denotes the thermal conductivity in x-direction for cell (m,n), $k_{x_{m-1,n}}$ $[W/mK]$ denotes the thermal conductivity in x-direction for cell (m-1,n). If there is a further thermal contact resistance present at the boundary between cell (m-1,n) and (m,n) this is included in the $R_{m-1/2,n}$ term $[m^2K/W]$. Thermal contact resistance is related to surface roughness effects which reduce the effective contact between the two adjoining surfaces and therefore reduces the heat flow over the interface [40].

Equation 8.2 is now taken and the heat flows are inserted. Furthermore, ρ and C_p are combined into the volumetric heat capacity C $[J/m^3K]$ describing the energy required to cause a certain temperature change per unit volume. This results in:

$$\dot{Q}_N + \dot{Q}_E + \dot{Q}_S + \dot{Q}_W + \dot{q}_{int}\Delta x \Delta y = C \Delta x \Delta y \frac{\Delta T}{\Delta t} \tag{8.8}$$

This equation can be re-written to attain the temperature change for a time step Δt in the cell as $\Delta T = (T^{i+1} - T^i)$. In which superscript T^i denotes the temperature at the present time step and T^{i+1} is the new temperature at the next time step. Replacing ΔT in equation 8.8 and re-arranging gives:

$$T^{i+1} = T^i + \frac{\Delta t}{C \Delta x \Delta y}(\dot{Q}_N + \dot{Q}_E + \dot{Q}_S + \dot{Q}_W + \dot{q}_{int}\Delta x \Delta y) \tag{8.9}$$

Equation 8.9 is solved for all the nodes in the mesh while marching forward with time steps Δt. An explicit solution strategy is chosen here which will further be clarified in section 8.1.3.

8.1.3. Solution method

In setting up a transient finite difference method one has to choose how to calculate the temperatures at a certain time step t. The two most well-known solution strategies are the explicit and implicit methods. The explicit method uses the temperature at the previous time step (i) for the calculation of the heat flows and internal energy generation terms during the next time step $(i+1)$. The temperatures at time i are readily available and can therefore be calculated immediately without solving a set of simultaneous equations. The implicit method instead uses the unknown temperatures at the new time step $(i+1)$ for the calculation of the heat flows at that time step and therefore requires solving for all the nodal temperatures simultaneously. The explicit method is the most easily applied but has one big limitation compared to the implicit method. A limit has to be imposed on the time step Δt which dictates the maximal allowable step size required for the explicit method to be stable. For a two-dimensional transient heat conduction problem as present in this model the stability criterion is given by equation 8.10 [45].

$$\frac{\alpha \Delta t_{cr}}{l^2} <= \frac{1}{4} \tag{8.10}$$

Where α is the thermal diffusivity of a material calculated through $\alpha = \frac{k}{\rho C_p} [m^2/s]$ and $l = \Delta x = \Delta$ is the mesh size.

The implicit method does not have such limitations and is inherently stable for any time step size [45]. The implicit method however does require solving for all the nodal temperatures simultaneously, which makes it more complicated to implement into the MATLAB. Motivations for choosing the implicit method over the explicit method therefore are usually related to the required speed of the model. Implicit methods are more suitable for long (time-wise) analyses as they can apply are larger Δt to arrive at the solution quicker. However, *C. A. Long* already stated in 1999 that with the advances in computational speed the small time steps required for stability in the explicit method are no longer a limiting factor and this method is therefore preferred for its simplicity [30]. The explicit method is therefore applied in this model to limit the required complexity of the code. If shorter computation times are required later on, the option to adjust the model to apply an implicit solution method can always be chosen.

8.2. Mesh

To model the thermal behaviour in an infinitesimally long rectangular section of X-Core with height a and width b a two-dimensional mesh is set up which covers the area of interest to the analysis. M nodes subdivide the width b in sections with length Δx. N nodes are used to subdivide the height a in sections with length Δy. In this model square cells are used, setting $\Delta x = \Delta y$. Phantom nodes are used along the interface between the mould and X-Core which allow to model the heat transfer over the interface. The interface acts as an infinite heat source and is at a prescribed temperature T_∞ indicated as T_{mould}. A mesh of arbitrary length, width and nodal density is presented in figure 8.3. Relative locations of the nodes with respect to each other are indicated with m and n indices. Three type of nodes can be distinguished in the model; central nodes, edge nodes and corner nodes. For each node type, a different form of equation 8.9 is required as the heat flow terms ($\dot{Q}$) depend on the presence of a boundary in the surrounding region of the node or not. In the following sections, the nodal equations used for each type are presented.

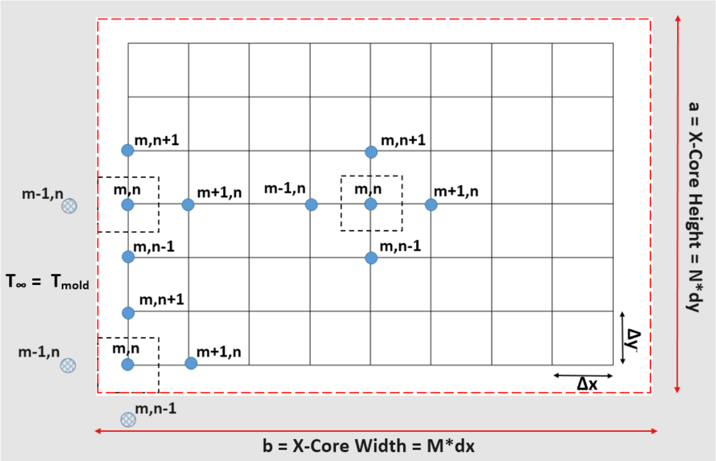

Figure 8.3: Representation of the used mesh to represent X-Core surrounded by an aluminium mould (grey area) with central and boundary nodes indicated

8.2.1. Central Nodes

Nodes of the central type cover the central region of the model. These nodes are present at locations $(2:M, 2:N)$. For these cells, no thermal resistance is present over the boundary, e.g. both cells are in perfect contact and of identical material composition, the R term in equation 8.7 is therefore set to zero. Furthermore, a square mesh is used; $\Delta x = \Delta y$. Lastly, the assumption of having an isotropic, homogeneous material dictates that the thermal conductivity is equal in all direction throughout the material e.g. $k_{x_{m-1,n}} = k_{x_{m,n}} = k_{eff}$. Equation 8.7 now reduces to the thermal conductivity of the material denoted by k_{eff} (equation 8.11) for X-Core (which will be derived in section 8.4.1).

$$K_{m-1/2,n} = \frac{\Delta y}{\frac{\Delta x}{2k_{x_{m-1,n}}} + \frac{\Delta x}{2k_{x_{m,n}}} + R_{m-1/2,n}} = \frac{\Delta x}{\frac{\Delta x}{k_{eff}} + 0} = k_{eff} \tag{8.11}$$

The equations for the heat flows from the surrounding nodes shown in figure 8.4 are given by equations 8.12 through 8.15.

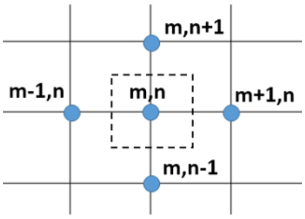

Figure 8.4: Central node

$$\dot{Q}_N = k_{eff}(T_{m,n+1} - T_{m,n}) \tag{8.12}$$

$$\dot{Q}_E = k_{eff}(T_{m+1,n} - T_{m,n}) \tag{8.13}$$

$$\dot{Q}_S = k_{eff}(T_{m,n-1} - T_{m,n}) \tag{8.14}$$

$$\dot{Q}_W = k_{eff}(T_{m-1,n} - T_{m,n}) \tag{8.15}$$

8.2.2. Boundary Nodes

At the boundary of the nodal network a special condition is required to dictate the heat transfer between the mould and X-Core. The experiments presented in chapter 7 were conducted in the tile mould. The boundary surrounding X-Core is made of aluminium. Therefore, it is required to deduce the heat flow over the interface between aluminium and X-Core which involves the thermal resistance R_{int} in equation 8.7 in the conductance term. Figure 8.5 depicts the case of a node in contact with the aluminium mould surface.

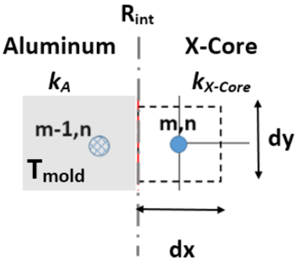

Figure 8.5: Interface between aluminium mould and X-Core present at the boundary nodes

The conductance K between node (m-1,n) and node (m,n) in figure 8.5 is given by equation 8.16 and henceforth referred to as the interface conductance K_{int}.

$$K_{m-1/2,n} = \frac{\Delta y}{\frac{\Delta x}{2k_{eff}} + \frac{\Delta x}{2k_{Aluminum}} + R_{int}} = K_{int} \tag{8.16}$$

In which the thermal conductivity of X-Core, k_{eff}, is defined in section 8.4.1. $k_{aluminium}$ is attained from literature to be between 237 and 240 $[W/mK]$ at T=200K and T=400K respectively [40]. A value of 239 $[W/mK]$ will be used in this analysis as the mould temperatures will vary between approximately 290 and 400K. The thermal resistance of the X-Core/Aluminium interface (R_{int}) is not known and has to be determined experimentally to acquire exact values. It will depend on how well X-Core is in physical contact with the aluminium mould surface on a micro-scale. Gaps between the mould and X-Core will lead to poorly conducting air filled areas which are the main contributor of the thermal resistance term [40]. A good estimation of the thermal resistance can be deduced from comparison between known values. For instance, the thermal resistance between epoxy and metallic wires was experimentally determined by *Chapelle et. all* to be within $0.3x10^{-5}$ and $1.6x10^{-5}$ $[m^2K/W]$ [47]. Looking at equation 8.16 and obtaining the approximate value of k_{eff} from section 8.4.1 to be around 0.12 $[W/mK]$ together with the mesh size of approximately 0.003m it can be seen that the first term in the denominator is around three orders larger compared to the second and third term if the values presented by *Chapelle et. all* are used. This indicates towards the minimal importance of the exact knowledge of the values for $k_{aluminium}$ and R_{int}. Therefore, a value of $1.6x10^{-5}$ for R_{int} is used in this analysis. Moreover, a low value of the inter-facial resistance is expected during the curing of X-Core in the mould as there is a liquid phase inside X-Core: the resin. Liquid phases can fill the gaps between the adjoining surfaces and are often applied in reducing thermal resistance between two rough surfaces [40]. After comparison of the model to experimental results the effect of R_{int} was re-evaluated due to its effect on the results. It will therefore be discussed in more detail in section 8.8.4.

Edge Nodes

Edge nodes are present along the top, bottom, left and right sides of the modelled region. These nodes are present at locations (1,2:N), (M,2:N), (2:M,1) and (2:M,N). The heat flow in the direction of the mould for every respective boundary (left, right, bottom and top) is dictated by the interface conductance term K_{int}. For the node on the left boundary shown in figure 8.6 the heat flows are:

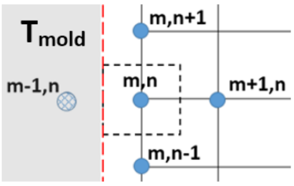

Figure 8.6: Edge node present along the left, right, top and bottom

$$\dot{Q}_N = k_{eff}(T_{m,n+1} - T_{m,n}) \tag{8.17}$$

$$\dot{Q}_E = k_{eff}(T_{m+1,n} - T_{m,n}) \tag{8.18}$$

$$\dot{Q}_S = k_{eff}(T_{m,n-1} - T_{m,n}) \tag{8.19}$$

$$\dot{Q}_W = K_{int}(T_{m-1,n} - T_{mould}) \tag{8.20}$$

Heat flows for the other edge nodes are deduced in a similar fashion. At the right boundary, K_{int} is used for $\dot{Q}_E$. At the bottom boundary this is done for $\dot{Q}_S$ and at the top boundary for $\dot{Q}_N$.

Corner Nodes

Lastly, four corner nodes complete the model. These nodes are present at the locations (1,1), (1,N), (M,1) and (M,N). At these nodes, two heat flows are dictated by the interface conductance K_{int}. Figure 8.7 shows the left bottom (1,1) corner node. The heat flows at this node are:

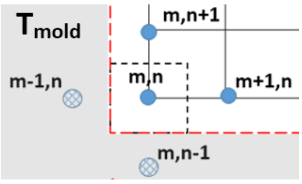

Figure 8.7: Corner node at the four corners of the nodal network

$$\dot{Q}_N = k_{eff}(T_{m,n+1} - T_{m,n}) \tag{8.21}$$
$$\dot{Q}_E = k_{eff}(T_{m+1,n} - T_{m,n}) \tag{8.22}$$
$$\dot{Q}_S = K_{int}(T_{m,n-1} - T_{mould}) \tag{8.23}$$
$$\dot{Q}_W = K_{int}(T_{m-1,n} - T_{mould}) \tag{8.24}$$

Again, the heat flow rates at the other corner nodes are deduced in an analogues fashion.

8.2.3. Boundary Conditions

For the modelling of curing X-Core inside a mould some specific boundary conditions are required. A PI controller is used to maintain a prescribed temperature at the mould surface. Therefore, the moulds used for manufacturing X-Core act as a boundary with prescribed temperature. The heat transfer from the mould surface to X-Core is described by a thermal resistance and conductance which was treated in section 8.2.2. The temperature of the mould is denoted by T_{mould} and is prescribed in the model for every time step to represent the cure-cycle that the user wants to use.

8.2.4. Initial Conditions

At time $t = 0$ two initial conditions are required to start the analyses. First, the initial temperatures at all the nodes should be entered. The temperature of the mould can be set different from that of the X-Core nodes. Evaluation of the experimental data acquired in chapter 7 showed that the temperature variation within X-Core at the start of the experiments was limited to $\pm 2°C$, and therefore a constant temperature is assumed over all the nodes that represent X-Core in the model. Furthermore, the initial degree of cure of the resin can be selected to be either zero or any value above zero. How this degree of cure is integrated into the model is further explained in section 8.6.1.

8.3. Determination of Thermal Properties of X-Core

In this section an effort is made to define theoretical models for both properties which allow the determination of the conductivity and specific heat for different X-Core compositions. These properties will be referred to as the effective thermal conductivity, denoted by k_{eff} and the effective specific heat denoted as $C_{p_{eff}}$ which represent the thermal properties of X-Core as a bulk material.

8.3.1. X-Core Constituent Material Properties

As a first step, the (thermal-)material properties of the constituents used in X-Core will be attained from literature. Table 8.1 lists the material properties of these materials at room temperature together with the literature source from which they were attained. The values presented in this table are used in the following section for the calculation of the thermal conductivities and specific heat capacities.

Resin

The resin/hardener combination used is the Ancarez® 4010 epoxy combined with an amine hardener named Ancamide™ 3399. Both are products manufactured by *Airproducts*. The density is $1150 kg/m^3$ [22], the values for thermal conductivity and specific heat capacity are attained from literature for similar resins based on epoxy-amine. A more thorough explanation for the specific heat capacity of epoxy-amine resins is given in section 8.5.

Microspheres

Three microsphere types are used in X-Core; Q-Cel® 5028, Expancel® 031 DU 40 and Expancel® 920 DE 80 d30. Q-Cel is a hollow glass microsphere (HGM) with a borosilicate glass wall [48] and air as internal gas. DU en DE Expancel® are polymeric microspheres. Exact material compositions of DE and DU are not provided *AkzoNobel* nor were they provided when asked for. However, careful revision of the material safety datasheets (MSDS) revealed hints to the material composition of the microspheres. The main weight fraction of the material is listed as a co-polymer of acrylonitrile and methacrylonitrile [49][50] which combined indicate the presence of polyacrylonitrile (PAN). Furthermore, the gas contained inside the microspheres is listed to be isobutane for DU [51] and isopentane for DE [50]. This information will be used in modelling the thermal conductivity of the DU and DE microspheres as well as for the prediction of the specific heat of these components.

Table 8.1: Densities (ρ), thermal conductivities (k), and specific heat capacities (C_p) of materials at room-temperature present inside X-Core attained from literature

Component	**Material**	$\rho [kg/m^3]$	**Source ρ**	**k [W/mK]**	**Source k**	$C_p [J/kgK]$	**Source C_p**
Binder	Epoxy-amine resin	1150	[22]	0.363	[52]	2217	[53][54][55]
Q-Cel wall	Borosilicate glass	2230	[56]	1.140	[56]	750	[56]
Q-Cel gas	Air	1.1614	[40]	0.024	[57]	1140	[40]
DE wall	PAN	1240	[58]	0.200	[59]	1300	[60]
DE gas	Isopentane	2.440	[57]	0.015	[57]	1680	[57]
DU wall	PAN	1240	[58]	0.200	[59]	1300	[60]
DU gas	Isobutane	3.212	[57]	0.015	[57]	1580	[57]

8.4. Thermal Conductivity of X-Core

Thermal conductivity describes the ease with which a material conducts heat. It has the unit of W/mK. Thermal conductivities are well defined for common materials, but not for filled composites like X-Core. In a filled composite, the thermal conductivity of the bulk material denoted by k_{eff} depends of the respective thermal conductivity of the components as well as on the geometrical build up of the components inside the composite. For filled composites theoretical models exist which aim to predict the effective thermal conductivity of the bulk material.

8.4.1. Theoretical Models for the Effective Thermal Conductivity of Filled Composites

Most theoretical models are able to provide very good estimates on the thermal conductivity of syntactic foams with low (<50%) volume fractions of microspheres. At higher contents, the microsphere shells will be in direct contact with one another, forming conductivity paths through which the conductivity can differ widely from a material with evenly dispersed non-contacting microspheres in a matrix. The volume fraction at which this phenomena occurs is also called the 'percolation threshold' [61] and is depicted in figure 8.8. The effect that this percolation threshold has is mainly dependent on how much the thermal conductivity of the microsphere walls differs from that of the binder material. For example, aluminium microspheres will cause a large increase in thermal conductivity at the percolation threshold as a continuous path of highly conductive aluminium is formed between the contacting microsphere walls. At lower volume fractions the heat has to travel through a layer of relatively much less conductive matrix material which limits the thermal conductivity of the filled composite. The two simplest theoretical models for particle filled composites are the series and parallel model. Figure 8.9 shows how both models behave in relation to the microsphere filler fraction indicated by φ. The series and parallel model describe the lower and upper bounds of k_{eff} for a certain microsphere filled composite [63] and use layers to represent the respective materials in the composite. The series model assumes the layer to be perpendicular to the heat flow, whilst the parallel model places them in parallel to the heat flow. Respective equations for both models are given in equations 8.25 and 8.26 [63] in which k_b *is the thermal conductivity of the binder,* k_f *that of the filler and* v_f *is the volume fraction of the filler in the composite.*

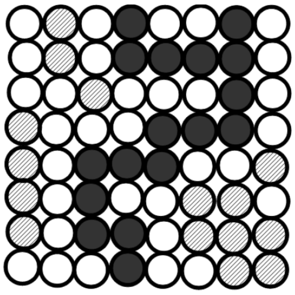

Figure 8.8: Representation of the percolation threshold where high-conductivity microspheres create a continuous conductive chain [62]

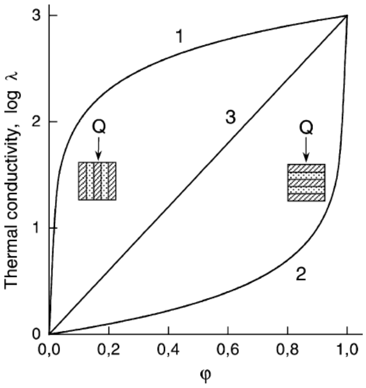

Figure 8.9: Relation between microsphere filler volume fraction (φ) and thermal conductivity based on the parallel (1) and series (2) model describing the upper and lower bounds of the effective thermal conductivity [63]

$$\boldsymbol{series}: k_{eff} = \frac{1}{((1-v_f)/k_b) + v_f/k_f} \tag{8.25}$$

$$\boldsymbol{parallel}: k_{eff} = (1-v_f)k_b + v_f k_f \tag{8.26}$$

These model are used to represent the lower and upper bound of k_{eff}. Other models have been proposed which give predictions that fall within these bounds. These models all use the *self-consistent field theory* which predict the macroscopic properties of a heterogeneous medium based on the properties and volume fractions of the individual constituents. This theory allow to determine k_{eff} if the thermal conductivities of the individual thermal conductivities are known [62].

Maxwell-Garnett model

Maxwell-Garnett relationship is one of the most recurrent models used for filled composites. *Zhu et. all* used this equation to predict the thermal conductivity of hollow glass microsphere filled syntactic foams based on an epoxy matrix with filler volume fractions up to 60%. The used HGM were of the type $K1$ and $K20$ manufactured by $3M^{\text{TM}}$ which have comparable true densities of 125 and 200 kg/cm^3 respectively to that of Q-Cel 5028 used in X-Core which has a true density of $290kg/m^3$. Experimental validation revealed good correspondence to experimental results as shown in figure 8.10. The researchers concluded that this equation can be used to predict the thermal conductivity of HGM filled composites at high volume fractions up to at least 60% [64]. It is described by:

$$k_{eff} = k_b \frac{k_f + 2k_b + 2v_f(k_f - k_b)}{k_f + 2k_b - v_f(k_f - k_b)} \tag{8.27}$$

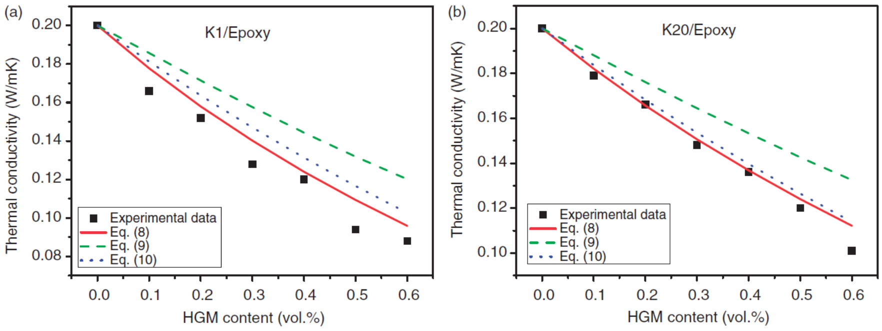

Figure 8.10: Comparison of experimental data of thermal conductivity in HGM filled epoxy composites with theoretical models [64]. Eq. (8) corresponds to the Maxwell-Garnett equation (eq: 8.27 and gives the closest matching results.)

Other models based on the self-consistent field theory exist but the majority of these methods are said to give inaccurate results above percolation threshold volume fractions [62]. However, as said this effect is mainly prominent when the filler material has a widely different conductivity compared to the matrix. *Zhu et. all* showed that the simple Maxwell-Garnett equation does indeed provide good estimations on thermal conductivity of high volume fraction HGM filled composites. Evaluating the thermal conductivities of the used components in X-Core will shed light on if this also holds for this novel core material. The reader is referred to table 8.1 at the start of this section where the thermal conductivities of all materials inside X-Core are listed.

For the values of the respective X-Core components it is noted that the thermal conductivities of the microsphere wall materials do not differ much to that of the binder material. The glass wall of Q-Cel deviates most at $1.140W/mK$ compared to that of neat epoxy at $0.363W/mK$. However, as stated in section 8.4.1 the Maxwell-Garnett model has been proven to be valid up to 60% of volume fraction of HGM. Looking at table 4.1 in chapter 4 it is noted that for the heaviest mix considered there the Q-Cel volume fraction is 65.8%. This slightly exceeds the validated of the Maxwell-Garnett model. S.Vial (2016) inspected the micro-structure of X-Core which showed the even dispersion of microspheres in the material (see figure 8.11).

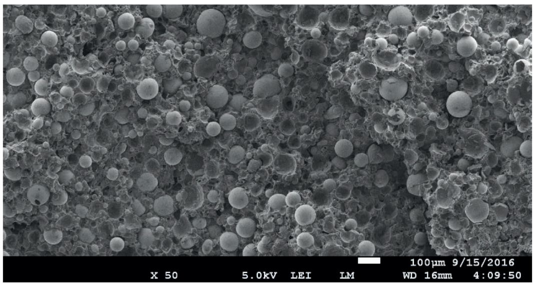

Figure 8.11: Scanning electron microscope image of X-Core, showing the even dispersion of the three microsphere types inside the foam [22]

This gives the author assurance that no percolation paths will be created between Q-Cel microsphere walls at high volume fractions leading to sudden changes in the thermal conductivity of X-Core deviating from the Maxwell-Garnett model. The issue is also not expected for high volume fractions of DE as the thermal conductivity of these walls is comparable to that of the epoxy.

8.4.2. Effective Thermal Conductivity of Multiple Fillers

Equation 8.27 is based upon the use of one type of filler. In X-Core, a mix of three different filler types are present. *D.Mishra* proposed a method of combining the thermal conductivity of multiple fillers through use of the relative volume fractions [52]. In this way, one term for the effective thermal conductivity of all the fillers combined is attained. This method will be applied in this study as well through equation 8.30. First, of a known X-Core mixture the volume fractions of the microspheres will be summed up, giving the total volume fraction for the fillers in the mixture:

$$v_{fill} = (v_{Q-Cel} + v_{DE} + v_{DU}) \tag{8.28}$$

Then the volume fraction of each component is taken relative to the total fraction through equation 8.29, in which Q-Cel is used as an example:

$$v_{Q-Cel} = \frac{v_{Q-Cel}}{v_{fill}} \tag{8.29}$$

The effective thermal conductivity of the combined fillers can then be calculated as:

$$k_f = k_{Q-Cel} v_{Q-Cel} + k_{DE} v_{DE} + k_{DU} v_{DU} \tag{8.30}$$

The separate thermal conductivities of each microsphere ($k_{Q-Cel}, k_{DE}, k_{DU}$) are determined using Hashin's equation (8.31 [65]) based on the thermal conductivity of the wall material (k_w), gas (k_g) and volume fraction of the gas (v_g) inside the microsphere.

$$k_{Microsphere} = k_w \left(1 + \frac{v_g}{\frac{k_w}{k_w - k_g} + \frac{v_g}{3}}\right) \tag{8.31}$$

Values for v_g were calculated from the known mean diameter of the microspheres combined with the true density and the densities of the gas and wall material which are all listed in table 8.2. E.g. the wall thickness required to attain the true density for a sphere with the given outside diameter based on the known densities was attained form which the internal volume of the microsphere could be calculated. The respective k_f values for each filler are listed in table 8.2 along with the used values for the microsphere diameters and true densities. The component DU poses another challenge to the model, as this component is known to expand and therefore change its v_g under elevated temperatures. Expansion is said to increase the volume of a DU sphere by around 37 times when un-restrained by the surrounding medium [22]. The effect of this change in v_g on the total effective thermal conductivity of the model will be evaluated by calculating k_{eff} for both the expanded and un-expanded state of the DU microsphere by setting the outer diameter and true density of the sphere to either one of the states. Both states are listed in table 8.2. As DU is surrounded by solid of viscous fluid phases in X-Core, the free-expansion of DU is inhibited leading to a pressure increase in stead of volume increase. The current analysis however evaluates the two boundary cases of un-expanded and fully expanded DU to evaluate its effect on the thermal conductivity and to see if modelling this change in composition is required.

Table 8.2: X-Core filler outside diameter and true density used to calculate the respective filler thermal conductivities k_{f_i}

Component	Mean outside diameter [μm]	True density [kg/m^3]	Source	k_{f_i} [W/mK]
Q-Cel 5028	75	290	[66]	0.126
920 DE 80 d30	70	30	[67]	0.0179
031 DU 40$_{unexpanded}$	13	120	[36]	0.0150
031 DU 40$_{expanded}$	40	3.2	[36]	0.0294

No experimental data or literature values are available to validate the thermal conductivities calculated for the DE and DU microspheres. Q-Cel thermal conductivity is also not available but can be compared to the thermal conductivity of similar hollow glass microspheres. Four types of HGM produced by $3M^{\text{TM}}$ are used in the research by 8.10 where values for the thermal conductivities are give and listed in table 8.3 along with the attained value for Q-Cel in the present model.

As seen from table 8.3 the thermal conductivity of Q-Cel 5028 lies between that of the microspheres designated as K20 and S38HS which is as expected as its density also falls within these two microspheres. This result gives the confidence that the model used provides realistic results for the microsphere thermal conductivities.

Table 8.3: Comparison between thermal conductivities of HGM from literature [64] and the value attained for Q-Cel 5028

Type of HGM	**True Density** $[kg/m^3]$	**Thermal Conductivity** $[W/mK]$
K1	125	0.064
K20	200	0.086
Q-Cel 5028	290	0.126
S38HS	380	0.137
S60HS	600	0.200

8.4.3. Effective Thermal Conductivity of X-Core

The required properties for determining the effective thermal conductivity of X-Core are now known. What remains is taking an X-Core mixture composition from which the volume fractions of the components are extracted. A MATLAB code was generated which allows the user to enter the mix composition, DU content and select if DU is in the expanded or unexpanded state. The program uses the values from literature presented in the previous paragraphs and calculates the effective thermal conductivity of X-Core based on the Maxwell-Garnett model. The '270-optimal mix', determined in chapter 4, is used here as an example. The pseudo volume fractions of this mix are repeated in table 8.4.

Table 8.4: Pseudo volume fractions of the "270-optimal mix"

Density [kg/m^3]	**DE**	**Resin**	**Q-Cel**
270	0.323	0.149	0.528

Comparison of Models and Sensitivity to DU Variations

With k_f, k_b and v_f determined, the effective thermal conductivity of X-Core can be calculated. Table 8.5 shows k_{eff} of the 270 optimal mix with DU contents varying between 1 and 10% in both the expanded and un-expanded state. The series, parallel and Maxwell-Garnett are compared.

Table 8.5: Comparison of series, parallel and Maxwell-Garnett model for the effective thermal conductivity of the X-Core 270 optimal mix with varying DU percentages in either the expanded or un-expanded state. *270-#* = DU %

	$k_{eff} [W/mK]$		
	Series	**Parallel**	**Maxwell-Garnett**
270-$1_{unexpanded}$	0.0443	0.125	0.116
270-$1_{expanded}$	0.0433	0.125	0.116
270-$5_{unexpanded}$	0.0427	0.121	0.112
270-$5_{expanded}$	0.0402	0.121	0.111
270-$10_{unexpanded}$	0.0415	0.116	0.107
270-$10_{expanded}$	0.0369	0.115	0.106

The series and parallel model give the lower and upper limit of the conductivity. The Maxwell-Garnett model should give value in between these two limits. Looking at the Maxwell-Garnett model, increasing the DU content from 1 to 10% gives a reduction of 8% in k_{eff}. The difference between the expanded and unexpanded DU state is smaller than 1% for the highest DU content. Conclusions on the importance of taking into account the variations in the DU component can be made in section 8.9 where the sensitivity of the model to changes in the thermal conductivity will be evaluated.

Evaluation of Effective Thermal Conductivities of Different Mixes

The change in thermal conductivity for different mix compositions is compared in table 8.6. The six mixes listed in table 4.1 are attained from chapter 4 which vary in density between 230 and $330 kg/m^3$. Furthermore, the lower bound of conductivity is attained through using a high DE content in mix 'HighDE'. This mix contrasts the '330opt' mix with high Q-Cel content. For all mixes the DU content is set at 4% in the unexpanded state.

Table 8.6: Effective thermal conductivities of the six optimal X-Core mixtures defined in chapter 4 along with high DE content mix to define lower boundary of conductivity.

X-Core Mix	DU	Resin	Q-Cel	DE	$k_{eff} [W/mK]$
HighDE	0.04	0.104	0.221	0.698	0.0669
230opt	0.04	0.125	0.430	0.382	0.0955
250opt	0.04	0.138	0.479	0.382	0.105
270opt	0.04	0.149	0.527	0.323	0.113
290opt	0.04	0.161	0.576	0.264	0.122
310opt	0.04	0.172	0.576	0.264	0.132
330opt	0.04	0.183	0.685	0.192	0.141

With a density reduction of $100 kg/m^3$ the thermal conductivity reduces from 0.141 to $0.0955 W/mK$. This presents change of 32% in the value of k_{eff}. Conclusions on the sensitivity of the numerical model to changes in the thermal conductivity of X-Core will be given in section 8.9.

8.4.4. Validation of the Theoretical Model for X-Core Thermal Conductivity

The proposed model provides values in the range of those presented in literature for similar syntactic foams [64]. However, as stated in the introduction X-Core is a unique material in its composition of three different microspheres and use of very high volume fractions of fillers. Experimental validation of the theoretical model is therefore required. Section 8.9 present a sensitivity study to define how much changes in k_{eff} effect the temperature distribution. In chapter 10 a recommendation is presented on how to proceed with experimental validation of the presented theoretical model.

8.5. Specific Heat Capacity of X-Core

The specific heat capacity of a substance is a measure of the energy required to raise a certain mass of the material with one degree in temperature. It is denoted by C_p and has the unit of J/kgK. In a filled composite like X-Core, the specific heat is a function of the C_p values of the separate components. X-Core does not have one fixed composition and therefore in order to use the numerical model for different mixtures it is desirable to be able to predict the specific heat of a wide variety of X-Core compositions. The specific heat of X-Core considered as a bulk material is then named the effective specific heat capacity denoted by $C_{p_{eff}}$ and can be applied under the assumption that X-Core is a homogeneous, isotropic material.

The rule of mixtures can be used to calculate the effective specific heat of a filled composite [68] based on the mass fractions (m_f) of the individual components present in the composite. Equation 8.32 describes the rule of mixtures applied to X-Core.

$$C_{p_{eff}} = C_{p_{binder}} m_{f_{binder}} + C_{p_{Q-Cel}} m_{f_{Q-Cel}} + C_{p_{DE}} m_{f_{DE}} + C_{p_{DU}} m_{f_{DU}} \tag{8.32}$$

An issue with the simple rule of mixture equation is that it is said to underestimate the values for the specific heat [68]. A slight adjustment to the equation was proposed to account for this, resulting in equation 8.33. Where A is a correction factor set at 0.2 for spherical particles [68], as present in X-Core. $m_{f_{filler}}$ is the total mass fraction of the fillers; $m_{f_{filler}} = m_{f_{Q-Cel}} + m_{f_{DE}} + m_{f_{DU}} = 1 - m_{f_{binder}}$. This model has successfully been applied in the prediction of the C_p for high volume fraction filled composites. Coefficients of fit were between 0.92 and 0.99 [68].

$$C_{p_{eff}} = [C_{p_{binder}} m_{f_{binder}} + C_{p_{Q-Cel}} m_{f_{Q-Cel}} + C_{p_{DE}} m_{f_{DE}} + C_{p_{DU}} m_{f_{DU}}] \cdot [1 + A \cdot m_{f_{binder}} m_{f_{filler}}] \tag{8.33}$$

The above mentioned equations require knowledge of the specific heat values of the materials present in X-Core. In the introduction of this section the material composition of the X-Core components was defined. Specific heat values for these materials at room temperature were attained from literature and are listed in table 8.1.

Specific Heat Capacity of Epoxy-Amine Resin

A note should be made on the specific heat capacity of the resin which undergoes a phase-transition during the cure. The variation of C_p for epoxy-amine combinations is known to drop by roughly 10% at the point of vitrification, e.g. the transition from liquid to solid of the resin. Up to this point, the specific heat is said not to be strongly influenced by cure temperature or degree of cure [54]. In this analysis, the main region of interest is during the curing reaction of the resin in which heat is released. The peak reaction rate, at which the heat release rate of the resin is maximal, occurs before the point of vitrification of the epoxy-amine. This is shown in figure 8.12 where the specific heat and heat flow of an epoxy-amine resin system is shown over time for an isothermal cure at 85°C.

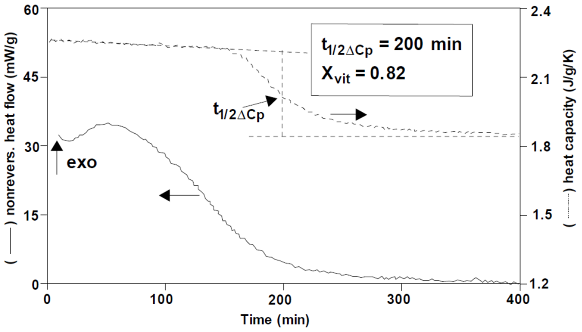

Figure 8.12: DSC heat flow and heat capacity for an epoxy-amine system cured isothermally at 85°C showing near constant C_p during the first ±170min followed by a reduction step in C_p during vitrification occurring at the end of the reaction. Figure taken from: [53]

Therefore, the specific heat of the resin will be assumed to be constant with time and temperature changes in this model. The effect of this assumption will be shown in section 8.9 to be acceptable. The specific heat for epoxy-amine resin systems as present in X-Core was attained from three separate publications for the pre-vitrification phase to be 2.00, 2.30 and 2.35 $[J/gK]$, the average of the three found values is used in this analysis.

8.5.1. Effective Specific Heat Capacity of Fillers

As a first step, the specific heat of the respective fillers ($C_{p_{Q-Cel}}, C_{p_{DE}}$ and $C_{p_{DU}}$) has to be determined. For this, the rule of mixtures can again be applied. The specific heat of a filler is calculated based on the mass fractions of the wall and internal gas of that filler:

$$C_{p_{microsphere}} = C_{p_{wall}} m_{f_{wall}} + C_{p_{gas}} m_{f_{gas}} \tag{8.34}$$

Knowledge of the true density and outer diameter is again used to solve for the volume fractions of the wall and gas from which the mass of each respective part is calculated using the density of the material. The attained values for the specific heat of the fillers are given in table 8.7.

Table 8.7: Calculated effective specific heat values for the filler present in X-Core

Filler	Effective Specific Heat [J/kgK]
Q-Cel 5028	750.9
031 DU 40	1309.5
920 DE 80 d30	1328.9

As expected, the effective specific heat of the fillers are mainly dependent on the specific heat of the wall material which account for the majority of the mass of a microsphere.

8.5.2. Effective Specific Heat Capacity of X-Core

With the values for the specific heat of the fillers and binder now determined it is possible to calculate the effective specific heat of an X-Core mixture. For this, the mass fractions of a mixture are first determined based on the volume fractions of the mixture to be analysed and the knowledge of the component densities. Equation 8.33 is then used to calculate the effective specific heat of the mix.

Effect of DU Content Variations

The effect of different DU contents is explored using the composition of the 270-optimal mix as listed in table 8.4 while varying the DU content from 1 to 10%. Increased DU contents lead to a decrease in the specific heat as the mass fraction of the resin becomes lower. The change is however quite limited as an increase in DU content of 9% in volume only gives a decrease in the specific heat of X-Core of 2.67%.

Table 8.8: Effect of varying DU contents on the specific heat of the 270-optimal X-Core mix. 270-# denoting the DU volume percentage.

X-Core Mix	$C_{p_{eff}}$ $[J/kgK]$
270-1	1798
270-5	1777
270-10	1750

The expansion of DU under elevated temperatures is not taken into account here, as this is a mere change in volume of the DU microspheres which generates an increase pressure in the closed mould. The total mass, or relative mass fractions do not change and therefore the specific heat of the bulk material remains the same.

Evaluation of Specific Heat of Different Mixes

To see the effect on the specific heat of using a variety of mix compositions three of the optimal mixes listed in chapter 4 are analysed with a DU content of 4% along a high DE content mix to contrast the ’330opt’ with Q-Cel content. The results are presented in table 8.9.

Table 8.9: Effective specific heat of the six optimal X-Core mixtures with 4% DU content

X-Core Mix	DU	Resin	Q-Cel	DE	$C_{p_{eff}}$ $[J/kgK]$
HighDE	0.04	0.104	0.221	0.698	1862
250opt	0.04	0.138	0.479	0.382	1784
290opt	0.04	0.161	0.576	0.264	1782
330opt	0.04	0.183	0.685	0.192	1774

The specific heat decreases with increasing density. The explanation for this is seen in the mix compositions. With increasing density, resin content increases causing an increase in the effective specific heat. At the same time however, the Q-Cel volume fraction is increased whilst the DE fraction is decreased. As seen from table 8.7 the specific heat of the glass Q-Cel spheres is less than half that of the DE spheres. Trading Q-Cel for DE therefore counteracts the increase of the specific heat caused by the increase in resin content. Specific heat therefore remains nearly constant with increasing density along the line of the optimal specific mixes defined in chapter 4.

8.5.3. Validation of the Theoretical Model for X-Core Specific Heat

In order to validate the model used to predict the specific heat of an X-Core mixture several DSC experiments were conducted in accordance with ASTM standard E1269 [69]. This test standard describes the determination of specific heat capacity by differential scanning calorimetry (DSC). Five cured X-Core samples manufactured in previous research were selected based on their wide variety in mix compositions. To determine the heat capacity of the cured samples the heat flow signal of the sample is compared to the signal of a calibrated standard with specified specific heat. Both signals are corrected by performing a base line correction using an empty sample pan. This empty pan run aids in filtering out the signal drift of the DSC apparatus. All three measurements are carried out using a *Perkin Elmer Sapphire DSC Standard 115V model* under identical conditions, using the same heating rate and starting temperature. Furthermore, it is important to use the exact same crucible for each test. A sapphire standard was used with a mass of $9.6mg$. The exact procedure used for the tests can be reviewed in Appendix H.

The specific heat of the test samples can be determined from the acquired DSC heat flow data using equation 8.35 [69].

$$C_{p_{sample}} = \frac{M_{sapphire}}{M_{sample}} * \frac{H_{empty}(T) - H_{sample}(T)}{H_{empty}(T) - H_{sapphire}(T)} \tag{8.35}$$

In which $M_{sapphire}$ and M_{sample} are the masses of the sapphire standard and sample respectively and $H_{sample}(T)$, $H_{empty}(T)$ and $H_{sapphire}(T)$ are the DSC heat flow measures at a certain temperature.

The mixture composition of the used cured samples is listed in table 8.10 along with the theoretical predictions of the specific heat capacity. Important to note here is that the samples were fully cured, as the author was not allowed to place uncured epoxy resin in the DSC apparatus as this is prohibited by the TU lab technicians to prevent contamination of the DSC chamber. Therefore, in the theoretical model the specific heat of the resin is set to the post vitrified value of $1850J/kgK$ (see figure 8.12).

Table 8.10: Volume fractions of samples used for the determination of the specific heat capacity through DSC along with predicted values based on the theoretical model using the C_p of the cured epoxy-amine resin

Sample	DU	Resin	Q-Cel	DE	Theoretical $C_{p_{eff}}$ $[J/kgK]$
SV1	0.04	0.102	0.354	0.504	1541.9
SV2	0.04	0.132	0.460	0.368	1545.6
SV3	0.04	0.160	0.577	0.223	1540.9
SV4	0.04	0.186	0.716	0.058	1527.9
SV5	0.04	0.228	0.732	0.0	1569.8

The results obtained after applying equation 8.35 to the DSC data are presented in figure 8.13. The results of sample SV2 had to be discarded as the wrong heat up rate was used during the experiment.

Comparing the experimental results with the predicted values listed in table 8.9 deviations are noted. The variation in C_p is much larger than predicted by the theoretical model. Sample SV3.1 is closest to the theoretical predictions. A possible explanation for these deviations was found in the weight variation and geometry of the samples. These parameters can influence the accuracy of the experimental results [54]. The sapphire standard used to calibrate the DSC is of a perfect flat disk geometry, making full contact with the DSC crucible bottom leading to few variations in heat transfer between the sensor of the DSC, the crucible and sapphire disk. The used samples however are of a powder like consistency similar to talc. Differences surface contact of the powder with the crucible can therefore lead to variations in heat transfer causing different readings in the DSC sensor. Furthermore, pressing the lid of the crucible down with more or less force also could cause a contact variation of the sample with the crucible bottom. This is illustrated in figure 8.14.

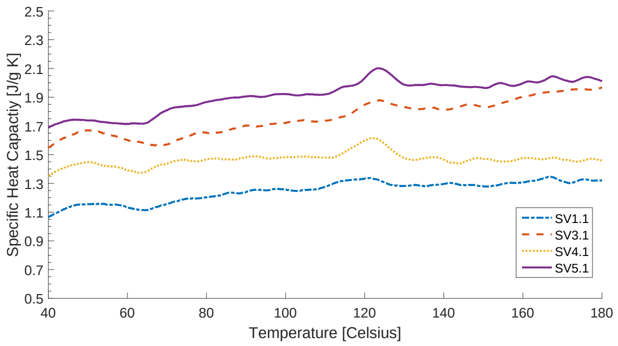

Figure 8.13: Experimentally determined specific heat capacity of four cured X-Core samples over a temperature range of 40-180°C

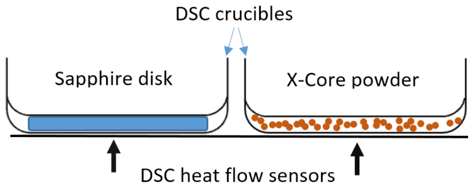

Figure 8.14: Schematic representation of the DSC chamber with the difference in surface contact of the sapphire standard disk and the X-Core powder samples

The weight of the samples could be another cause for variations. The optimal sample weight is achieved when the product of the sample weight and its specific heat is equal to that of the sapphire standard as [54].

$$m_{sample} C_{p_{sample}} = m_{sapphire} C_{p_{sapphire}} \tag{8.36}$$

Deviating from this was shown by *McHugh et all.* to lead to inconsistent results [54]. With $m_{sapphire}$ at $9.6mg$, its specific heat around $800J/kgK$ at room temperature [69] and a predicted heat capacity of the X-Core samples around $1550J/kgK$ the ideal sample weight is $4.9mg$. Sample weights of 4.5, 4.7, 4.9, 4.8 and $5.0mg$ were used for samples SV1, SV2, SV3, SV4 and SV5 respectively. Furthermore, a scale with an accuracy of maximally $0.1mg$ could be used which could lead to further inaccuracies in the determination of the sample weights. SV3 has the correct sample weight, and its experimental value for the heat capacity at is also closest to the theoretical prediction as shown in table 8.9. Sample SV1 has the largest deviation from the ideal sample weight which could explain its large deviation from the theoretical model as well.

All things considered, the results from the DSC tests are in the range of the values predicted with the theoretical model. However, validating the model based on these results is not possible as the deviations are quite significant. Several measurement variables could have cause these variations in the results and retesting the samples, performed by an experienced lab technician, is therefore advised.

As the thermal properties are assumed constant in the numerical model, the difference between the used constant theoretical values of specific heat capacity are compared with the average specific heat capacity values attained in the DSC experiments over the range of 40-160°C. This comparison is shown in table 8.11.

Table 8.11: Comparison of theoretical C_p values with experimentally attained values averaged over a temperature range of 40-160°C

X-Core Mix	**Theoretical $C_{p_{eff}}$ $[W/mK]$**	**Experimental Avg. [40-160°C]$C_{p_{eff}}$ $[W/mK]$**	**Difference [%]**
SV1	1541.9	1175	+31.2%
SV2	1545.6	-	-
SV3	1540.9	1653	-6.8%
SV4	1527.9	1391	+9.8%
SV5	1569.8	1864	-15.8%

A sensitivity study is presented in section 8.9 which will evaluate the significance of the deviation of the theoretical model with respect to the experimentally determined values of the specific heat capacity. Furthermore, chapter 10 present several ideas for improving on the used validation method.

8.6. Resin Cure Kinetics

The term $\dot{q}$ introduced in section 8.1.2 is related to the internal heat generation caused by the exothermic heat released during the curing of the epoxy-amine resin. This release of heat causes temperature increases inside the material when it cannot be dissipated out of the material fast enough. Temperature measurements performed in chapter 7 showed that for an $80mm$ high sample in the tile mould the temperatures in the core of the material can rise to as much as $57°C$ above the mould maximal temperature due to this release of heat being contained by X-Core.

Cure kinetics describe this release of heat of a thermosetting resin. Differential scanning calorimetry (DSC) has been extensively used to characterize the cure kinetics of a wide variety of resin systems. The information attained from the DSC experiments can be used to fit a certain kinetic model which describes the reaction rate of the resin system in a certain degree of cure and temperature. The resulting cure kinetic model can then be integrated into the transient numerical model to determine the release of heat at every stage of the simulation in a volume of material. The theoretical background of cure kinetic modelling is first presented in section 8.6.1 after which the experimental DSC measurements are discussed and the selected cure kinetic model is fit to the experimental data. At the end, the integration of the cure kinetic model into the numerical model is shown.

8.6.1. Theoretical Background

The basic assumption required to apply the DSC method to the curing of thermosetting polymers is that the rate of reaction ($d\alpha/dt$) is proportional to the measured heat flow (ϕ) as:

$$\frac{d\alpha}{dt} = \frac{\phi}{H_T} \tag{8.37}$$

In which H_T is the total heat of reaction, or reaction enthalpy. The degree of cure of the resin is described by α and varies from 0 (uncured) to 1 (fully cured). $H(t)$ is the total heat release up to time t.

$$\alpha = \frac{H(t)}{H_T} \tag{8.38}$$

The complex curing kinetics occurring inside the resin can then be described by a simple model which assumes that only one type of reaction is present [70]. The most simple model is the nth order model (equation 8.39). The nth order reaction model assumes the peak reaction rate to occur at t = 0, and therefore represent decaying reactions.

$$\frac{d\alpha}{dt} = k(1-\alpha)^n \tag{8.39}$$

In which k is the rate constant, described by the Arrhenius equation, which gives the dependence of the reaction rate on temperature:

$$k = Ae^{-\frac{E_A}{RT}} \tag{8.40}$$

A is a pre-exponential factor, E_A is the activation energy and R is the universal gas constant (8.3144621 $J/molK$) and T is the temperature in Kelvin. The pre-exponential factor A and activation energy E_A are fit to the DSC heat flow data and represent the type of reactions taking place and minimum energy for the reaction to occur respectively.

For epoxy-amine reactions, the reaction behaviour cannot be described by the nth order model as the peak rate of reaction occurs after t=0 [70]. This is also the case for the Ancarez® 4010 / Ancamide™ 3399 epoxy-amine resin used in X-Core as will be shown from the DSC results in section 8.6.4. The autocatalytic model is then used which applies two rate constants, $k1$ and $k2$, along with two reaction orders, m and n:

$$\frac{d\alpha}{dt} = (k_1 + k_2\alpha^m)(1-\alpha)^n \tag{8.41}$$

$k1$ represents the initial rate of reaction at t=0. Fitting this model to the experimental data obtained in the DSC experiments can be done in several ways. The numerical Ryan-Dutta method is often applied which uses the initial and maximum reaction rates to fit the kinetic model to the data. However, this model requires the assumption of the total reaction order ($m+n$) to be equal to 2. Graphical methods do not have these limitations but require a bit more work. *Kenny* [70] described a graphical-analytical method which requires no assumptions on the reaction order. This method has been used successfully in multiple other papers to model the reaction kinetics of epoxy-amine systems [71][72][73] and is therefore selected to be used in this analysis as well. The full procedure of fitting the autocatalytic model to the experimental DSC data is described in section 8.6.5.

8.6.2. Determining Resin Cure Kinetics through Differential Scanning Calorimetry

Differential scanning calorimetry (DSC) is used to measure the heat flow of thermosetting resin systems. A DSC consists of a heated chamber in which two sample pans, or crucibles are placed. Each crucible is heated at the same rate and two separate thermo-sensors measure the temperature of each crucible. The DSC measures the differences in heat flow required to maintain both crucibles at the same pre-described temperature, this difference is caused by the fact that one crucible is empty (the reference) and one identical crucible contains the sample. If the sample is a polymer with an exothermic reaction occurring the heat flow to this crucible will be lower as it in itself generates heat. This difference in heat flow can then be related to the heat of the reaction occurring for a certain sample weight of the polymer. Figure 8.15 shows a schematic of a heat flux DCS apparatus with the crucibles, heater and thermo-sensors indicated.

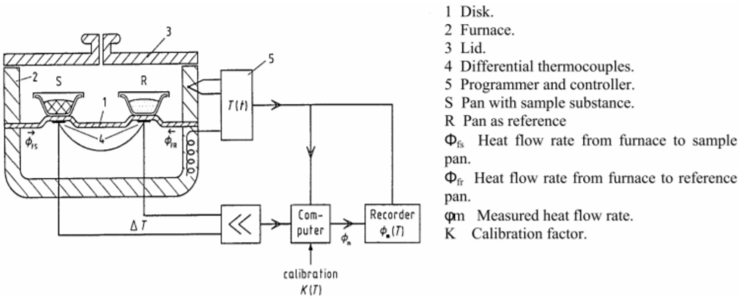
3
5
2
S
R
1
4
$\vec{\phi}_{FS}$
$\overleftarrow{\phi}_{FR}$
$T(t)$
ΔT
Com-
puter
Recorder
$\phi_m(T)$
ϕ_m
calibration
$K(T)$
1 Disk.
2 Furnace.
3 Lid.
4 Differential thermocouples.
5 Programmer and controller.
S Pan with sample substance.
R Pan as reference
Φ_{fs} Heat flow rate from furnace to sample pan.
Φ_{fr} Heat flow rate from furnace to reference pan.
φm Measured heat flow rate.
K Calibration factor.

Figure 8.15: Schematic representation of a DSC chamber with heat flux. Figure taken from: $polymerscience.physik.hu-berlin.de/docs/manuals/DSC.pdf$

8.6.3. Experimental Methodology and Apparatus

ASTM test method E2070 [74] describes the procedure for attaining the required kinetic parameters as described in section 8.6.1. The basic procedure consists of a a minimum of four isothermal experiments over a temperature range of approximately $10K$. Isothermal methods are most suitable for determining the cure kinetics of autocatalyzed systems [75]. They provide more accuracy compared to dynamic scanning methods but require more time to execute. Numeral papers and documents describe slight alterations to this method in order to attain the required results [76][77][75][70]. Variations on the ASTM E2070 method that are used consist of preheating the DSC chamber before inserting the specimen in stead of inserting the specimen in the chamber at ambient temperature and using a fast (20-40K/min) ramp to reach the isothermal temperature. Furthermore, a variation of either hermetically sealed or normal DSC pans are used depending on the expected behaviour of the resin (e.g. outgassing). The exact applied methodology for the isothermal DSC experiments in this study can be reviewed in detail Appendix G. Several important parts of the method are highlighted here.

- *A pre-heated DSC chamber was used to the isothermal temperature of the to be performed experiment.*
  Experiments starting at room temperature with a $20K/min$ ramp to the isothermal temperature showed poor results as most of the reaction took place within the ramp-up. Higher ramp rates were not possible for the used DSC apparatus.
- *The lid of the aluminium sample holders (crucibles) were perforated with a needle to allow pressure equalization inside the crucible.*
  The used DSC is not equipped with a pressurized DSC chamber. To assure equal pressure in the crucible and chamber a small (50-100μm) hole is therefore inserted into the lid of the crucible. TGA measurements performed beforehand indicated <2% of weight loss occurred over the used temperature range making it valid to used non-hermetically sealed crucibles as no significant weight loss of the sample occurs.
- *New batches of resin/hardener were mixed before every experiment.*
  To equalize and minimize the degree of resin/hardener pre-cure.

A pre-calibrated *Seiko Instruments Exstar 6000* heat flux DSC was used for performing the heat flow measurements. A total of seven isothermal experiments were conducted on the Ancarez® 4010 / Ancamide™ 3399 resin. Several pre-tests were performed to determine which temperature range is most suitable. ASTM E2070 prescribes performing at least four isothermal runs which should take between 15 and $100min$ to complete. Isothermal experiments were performed at 85 to $115°C$ at $5°C$ intervals.

8.6.4. Experimental results from Isothermal Scans and Post-Processing

The results attained from the isothermal DSC scans are imported into MATLAB and require some post-processing. From the seven tests, two had to be discarded. The 115°C isothermal run was stopped prematurely and the 100°C showed non-consistent behaviour with the other tests. As a minimum of four tests is enough to fit the cure-kinetic parameters, these two tests will not be used to prevent them interfering with the model fitting. The reader is referred to figure 8.16 as visualization of the steps taken in this paragraph. Firstly, a baseline heatflow needs to be established which corresponds to the heatflow recorded at the end of each test. At this stage, the reactivity of the sample is zero and the measured heatflow is therefore due to the DSC own signal. This baseline is constructed horizontally from the end of the reaction exotherm to the intersection with the exothermic heat flow at the initial phase of the test [74]. This baseline value is then subtracted form the heat flow data after which the area under de exothermic peak is integrated to obtain the total heat of reaction H_T in mJ. Using the respective total heat of reaction from each isothermal test, the reaction rate ($d\alpha/dt$) can be calculated by dividing the heatflow ($\phi(t)$) by H_T (equation 8.37). The fraction of reaction completed at time t ($\alpha(t)$) is calculated through integrating the heat flow up to time t and dividing it by H_T.

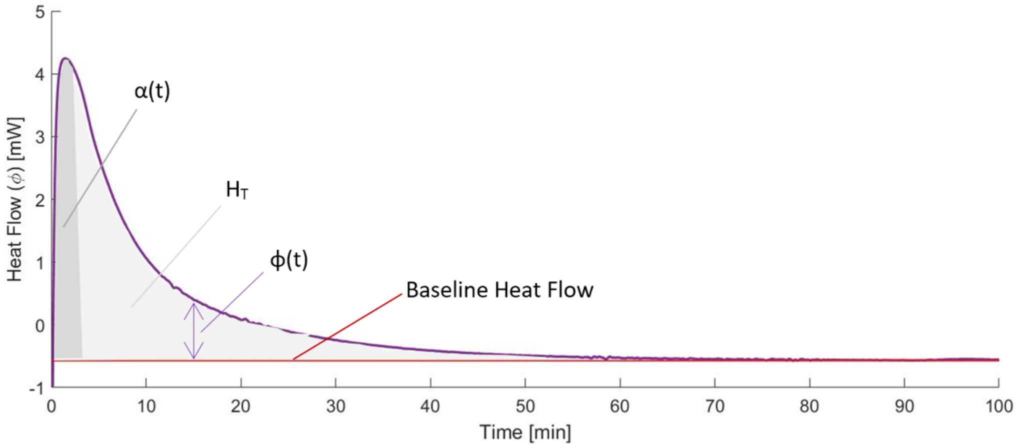

Figure 8.16: Example of raw heat flow data from isothermal DSC experiment. Post-processing steps shown are: Baseline construction, total heat flow calculation through integration (H_T), fraction of reaction completed at time t ($\alpha(t)$) and heat flow (ϕ) at time t

Performing these steps generates the required data for the fitting of the cure kinetic model being H_T, $\alpha(t)$ and $d\alpha/dt$. The reaction rates of the isothermal DSC tests over time are plotted in figure 8.17. Table 8.12 lists the total heat values (H_T) for the five different isothermal tests. The values are deemed close enough together to take the average of the five values to be used in the numerical model.

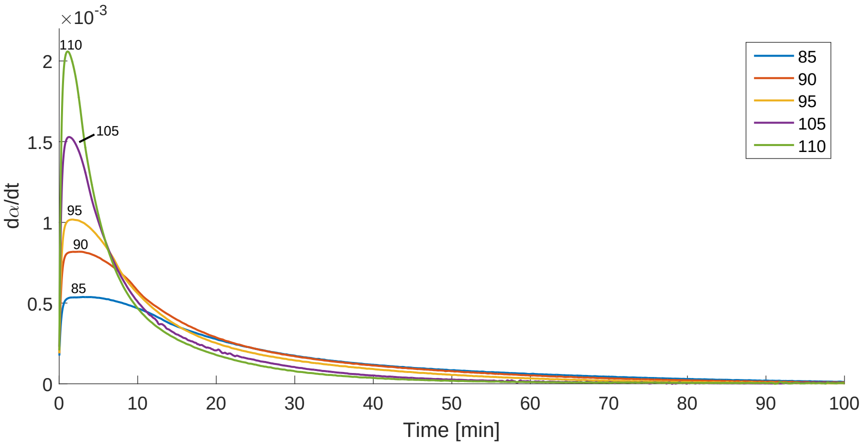

Figure 8.17: Reaction rate ($d\alpha/dt$) vs time of isothermal DSC experiment results for 85, 90, 95, 105 and 110 °C

Table 8.12: Total heat of reaction (H_T)

T_{iso} [°C]	H_T [J/g]
85	290.42
90	331.41
95	317.04
105	307.01
110	314.00
Avg.	311.98

8.6.5. Computing Cure Kinetic Parameters from Experimental Data

At the end of section 8.6.1 the graphical-analytical method by *Kenny* [70] was selected for attaining the cure kinetic parameters from the experimental DSC data. The data is presented in the previous section for five isothermal experiments conducted in the temperature range of 85-110°C. The procedure of *Kenny* requires the re-arranging of the autocatalytic equation in several ways to attain the different kinetic parameters step by step. The autocatalytic reaction model is described by:

$$\frac{d\alpha}{dt} = (k_1 + k_2\alpha^m)(1-\alpha)^n \tag{8.42}$$

$$k_1 = A_1 e^{-\frac{E_1}{RT}} \tag{8.43}$$

$$k_2 = A_2 e^{-\frac{E_2}{RT}} \tag{8.44}$$

The kinetic parameters to be obtained are:

- n = reaction order
- m = reaction order
- $k1$ = rate constant 1, consisting of:

  A_1 = pre-exponential factor 1

  E_1 = Activation energy 1
- $k2$ = rate constant 2, consisting of:

  A_2 = pre-exponential factor 2

  E_2 = Activation energy 2

First, the initial rate constant $k1$ is determined as simply being the reaction rate at the start of the reaction, $\alpha = 0$. A first guess for the reaction order n then is calculated by taking the logarithm of the autocatalytic equation 8.42 as:

$$\ln(d\alpha/dt) = \ln(k1 + k2\alpha^m) + n\ln(1-\alpha) \tag{8.45}$$

$\ln(d\alpha/dt)$ is now plotted against $\ln(1-\alpha)$ in figure 8.18 for an isothermal experiment. Inspection of equation 8.45 shows that when $\alpha -> 1$ the slope of the linear line is the reaction order n. Fitting a linear regression line to this part and extracting the slope gives the value for the initial approximation of n for the separate isothermal experiments.

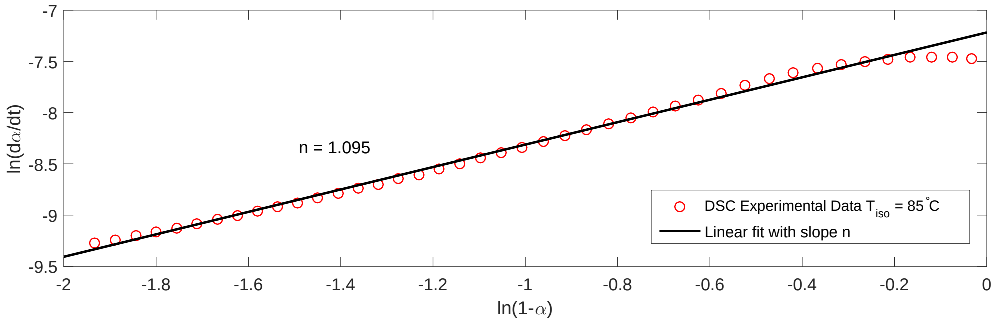

Figure 8.18: Plot of $\ln(1-\alpha)$ vs $\ln(d\alpha/dt)$ for isothermal experiment T$_{iso}$=85°C showing the linear regression line with slope n

Using the acquired values for $k1$ and n for every isothermal experiment, the reaction order m and rate constant $k2$ can now be determined. First, equation 8.42 is re-arranged again into the form:

$$\ln([(d\alpha/dt)/(1-\alpha^n)] - k1) = \ln(k2) + m\ln(\alpha) \tag{8.46}$$

Now, plotting $\ln([(d\alpha/dt)/(1-\alpha^n)] - k1)$ vs $\ln(\alpha)$ allows the calculation of m and $ln(k2)$ as the slope and zero intercept of the linear part of the plot. This is illustrated in figure 8.19. Figure 8.19 and the linear fit used to determine m and $ln(k2)$ requires some extra explanation as it might look somewhat arbitrary at first. The deviation from the linear behaviour observed between $ln(\alpha)$ = -5 and -1 has two explanations. The initial period of the cure, up to $\alpha = 0.007$ ($ln(\alpha)$ = -5) deviates form the linear behaviour due to the time required for the DSC to equilibrate after insertion of the sample. This period should therefore not be considered in fitting the linear regression [71]. The last part of the cure for $ln(\alpha)$>-1 is influenced by the vitrification of the

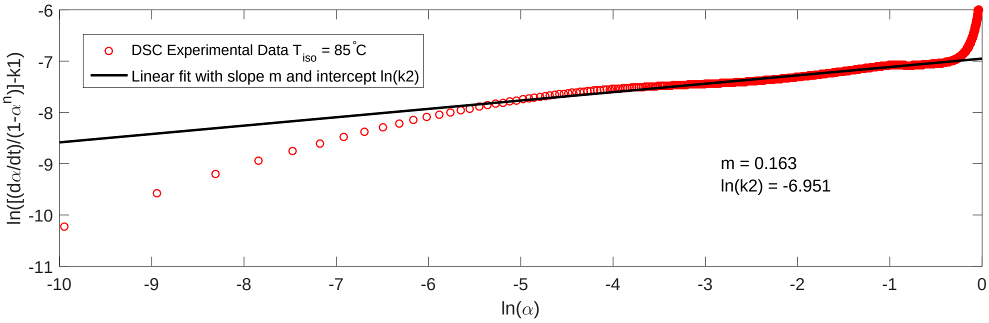

Figure 8.19: Plot of $\ln(\alpha)$ vs $\ln([(d\alpha/dt)/(1-\alpha^n)]-k1)$ for isothermal experiment T_{iso}=85°C showing the linear regression line with slope m and intercept $ln(k2)$

epoxy-amine resin. This causes a difference in the thermal properties of the sample, like the specific heat (see section 8.5), and influences the heat flow measurements made by the DSC. This region should therefore also not be considered in fitting the linear regression line [71]. Similar issues were observed in the other studies applying the *Kenny* [70] method and all applied similar mitigation strategies resulting in successful kinetic models.

Initial values for the required parameters n, m, $k1$ and $k2$ are now determined. The procedure however involves using these fist guess parameters to update the fit. This creates an iterative procedure in which the values for $k1$, m and $k2$ are used to update the estimate for n which in turn is used to calculate new values for m and $k2$. Again, equation 8.42 is re-arranged to allow this procedure:

$$\ln((d\alpha/dt)/(k2\alpha^m + k1)) = n\ln(1-\alpha) \tag{8.47}$$

The results of this equation can be plotted as $\ln(1-\alpha)$ vs $\ln((d\alpha/dt)/(k2\alpha^m + k1))$ where the slope will give the updated value for n. This value is then used in equation 8.46 to attain new values for m and $ln(k2)$. This procedure is repeated until all three parameters converge (change <1%). Five iterations were required to achieve convergence. The results from each iteration per parameter for every isothermal test are shown in figure 8.20.

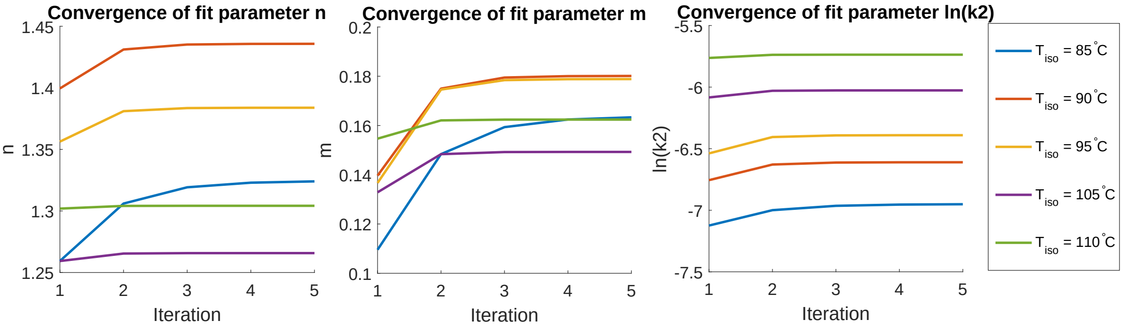

Figure 8.20: Convergence plots of kinetic parameters n, m and $ln(k2)$ for five iterations for all isothermal DSC experiments

The activation energies (E) and pre-exponential factor A can now be calculated by taking the logarithm of the Arrhenius equation (eq. 8.40) as:

$$ln(k) = ln(A) - \frac{E}{RT} \tag{8.48}$$

Plotting the $ln(k1)$ and $ln(k2)$ against $1/T$ gives the classical Arrhenius plots which should present a straight line if the assumption of Arrhenius reaction behaviour is correct. This implies that the cure mechanism is not changing with temperature, e.g. the reaction orders are constant with temperature. This allows taking the average of the n and m values found for the different isothermal experiments to represent the kinetic reaction behaviour. The Arrhenius plots for $k1$ and $k2$ are presented in figure 8.21.

Looking at figure 8.21 it is observed that a linear regression line present a very good fit to the five isothermal data points for $ln(k2)$. This confirms the Arrhenius behaviour of the Ancarez® 4010 / Ancamide™ 3399

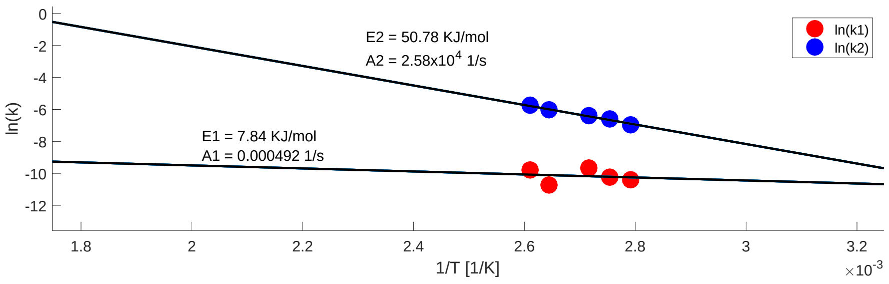

Figure 8.21: Arrhenius plots showing temperature dependence of rate constants $k1$ and $k2$. Values for activation energy (E) and pre-exponential factors (A) attained from linear regression fit slope and y-axis intercept respectively

epoxy-amine resin system. The $ln(k1)$ points show slightly more variation which can be due to these points be extracted from the initial period in the DSC experiment where some stabilization effects might still be present. The values for the activation energies (E) and pre-exponential factors (A) are attained from the slope and y-axis intercept of the linear regression lines respectively. All cure kinetic parameters have now been determined and are listed in table 8.13.

Table 8.13: Kinetic parameters of the autocatalytic model for Ancarez® 4010 / Ancamide™ 3399

Parameter	Value	Unit
n	1.342	[-]
m	0.167	[-]
E1	7.84	KJ/mol
E2	50.78	KJ/mol
A1	0.00049	1/s
A2	25814.94	1/s

Comparison of Model Predictions with Experimental Results from DSC Isothermal Measurements

The cure kinetic parameters listed in table 8.13 can now be used to reproduce the experimental isothermal DSC data to evaluate the correctness of fit of the autocatalytic model. This is presented in figure 8.22 for the reaction rate against time.

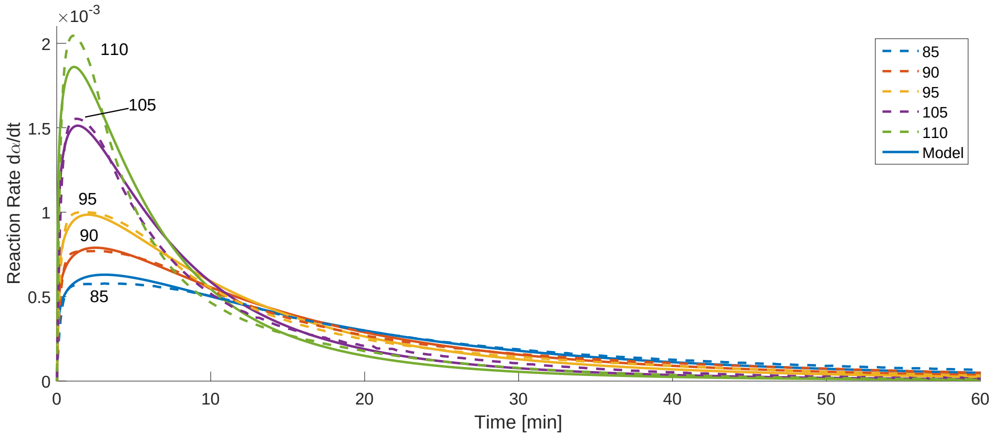

Figure 8.22: Reaction rate $d\alpha/dt$ vs time for the experimental DSC isothermal tests (solid lines) compared with the autocatalytic model (dashed lines) with parameters from table 8.13

The model, represented by the solid lines, predict the cure kinetic behaviour very well for the 90, 95 and 105°C isothermal tests. The 85 and 110°C lines deviate slightly more, however the fit is still of equal quality to these observed in literature. This shows that the autocatalytic model fit using the graphical-analytical method of *Kenny* [70] successfully predicts the behaviour of the Ancarez® 4010 / Ancamide™ 3399 resin system and can be integrated into the numerical model with the parameters listed in table 8.13.

8.6.6. Integration of the Cure Kinetic Model into the Numerical Model

As introduced in section 8.1.2 the exothermic heat generated during the cure of the resin is integrated into the energy balance equation by adding the term $\dot{q}$.

$$T^{i+1} = T^{i} + \frac{\Delta t}{C\Delta x\Delta y}(\dot{Q}_N + \dot{Q}_E + \dot{Q}_S + \dot{Q}_W + \boldsymbol{\dot{q}_{int}}\Delta x\Delta y) \tag{8.49}$$

$\dot{q}$ represents the heat generation rate of the resin during time step Δt. To calculate this in the transient finite difference model the autocatalytic model is used. At each time step, the temperature (T) and degree of cure (α) of a unit volume ($\Delta x\Delta y$) for the previous time step are used and plugged into the autocatalytic model to obtain the reaction rate ($d\alpha/dt$) for that specific temperature and degree of cure.

$$\frac{d\alpha}{dt} = (k_1 + k_2\alpha^m)(1-\alpha)^n \tag{8.50}$$

$$k_1 = A_1 e^{-\frac{E_1}{RT}} \tag{8.51}$$

$$k_2 = A_2 e^{-\frac{E_2}{RT}} \tag{8.52}$$

The heat generation rate during the time step is then calculated by:

$$\dot{q}^i = V_{f_{resin}}\rho_{resin}H_T(\frac{d\alpha}{dt})^i[W/m^3] \tag{8.53}$$

Where $V_{f_{resin}}$ denotes the volume fraction of resin is an element which is simply the volume fraction of resin used in the X-Core mixture. ρ_{resin} represents the resin density which is attained from *Airproducts* to be $1150kg/m^3$, and is used to calculate the mass of resin present in an element. The total heat H_T of the reaction was determined to be $311.97J/g$, which multiplied with the reaction rate $d\alpha/dt$ gives the amount of energy in J/g released in the volume element. When multiplied with the time step Δt and volume of the element $\Delta x\Delta y$ this term attains the unit of $[J/m]$, denoting the total heat release due to the resin exothermic reaction over the time step.

The degree of cure (α) for every element is tracked through:

$$\alpha^{i+1} = \alpha^i + \Delta t(\frac{d\alpha}{dt})^i \tag{8.54}$$

Where i is the current time and $i+1$ is the time after the current time step Δt.

8.7. Model Verification

The model created can be verified to function correctly trough comparison with an analytical solution which is known to be valid for certain simplified cases. The procedure followed here is similar to that performed by *Bogetty & Gillespie* for their model of two-dimensional curing of thick thermosetting composites [17] and is also advised as a method of assuring model correctness in: [40]. No analytical, exact solutions are present for two-dimensional, transient temperature cases where internal heat generation is present. Model verification will therefore be performed with the internal heat generation term $\dot{q}$=0. By employing insulated boundary conditions at the side of a two-dimensional model it can be compared to analytical one-dimensional transient temperature solutions [17]. The solutions are available in the form of Heisler charts, which provide a graphical analysis tool with which transient heat transfer solution can be obtained for an infinitely long plane wall with thickness $2L$. One set of charts give the temperature in the midplane of the wall at any time in the transient process. Another set of charts can then be used to relate this midplane temperature to any temperature away form the midplane [78]. The reader is referred to Appendix J for revision of both charts. In this section, only the used method and results will be presented. The analytical results will be used to conduct a convergence study on both time step and mesh size.

8.7.1. Attaining the Analytical Solution Using Heisler Charts

The procedure for using the Heisler charts is as follows. First, the Biot number and Fourier numbers need to be determined based on the material properties and geometry. These two dimensionless parameters are given by equations 8.55 and 8.56 respectively.

$$Bi = \frac{hL}{k} \tag{8.55}$$

$$Fo = \frac{\alpha t}{L^2} \tag{8.56}$$

In equation 8.55, h is the convection coefficient $[W/m^2K]$, L is the half wall thickness $[m]$ and k is the thermal conductivity $[W/mK]$. For equation 8.56 α is the thermal diffusivity given by equation 8.57, t is the time in seconds and L again is the beam half thickness. The validity of the Heisler charts is limited to $Fo > 0.2$ [78].

$$\alpha = \frac{k}{\rho C_p} \tag{8.57}$$

With these parameters the value for θ can then be determined from the Heisler charts by graphical analysis. θ relates the temperature at the boundary to the temperature at the midplane of the plane wall through:

$$\theta = \frac{T - T_\infty}{T_i - T_\infty} \tag{8.58}$$

In which T is the new temperature, T_i is the initial temperature of the material and T_∞ is the temperature of the surrounding medium. After the temperature at the midplane is determined at a time step, it can be related to any temperature away from the midplane using a seconds set of Heisler charts. The way in which the distance from the midplane is expressed in shown in figure 8.23a. Locations at $\frac{x}{L}$ =0.4, 0.6, 0.8 and 0.9 are selected in this analysis. For each location, a value of θ_x is read from the graph, which relates the midplane temperature (T_0) to the temperature at the location away from the midplane (T_x) through equation 8.59.

$$\theta_x = \frac{T_x - T_\infty}{T_0 - T_\infty} \tag{8.59}$$

For X-Core, convection coefficients (h) are not known but though imposing a sudden change in surface temperature of the material it self allows a unique case to be used in the Heisler charts where the Biot number is set to zero [78]. This eliminate the need for the convection coefficient to be known. Prescribed temperatures are then applied to the top and bottom edges of the material, replacing T_∞ by the imposed surface temperature T_s. This leaves only the Fourier number to be determined at a desired time interval after which the corresponding value for θ can be read from the Heisler chart for the line corresponding with $Bi = 0$.
The following X-Core material properties where used to generate the verification data as they match closely with the values attained for the mixes in section 8.3:

- $k = 0.12\ W/mK$
- $\rho = 270\ kg/m^3$
- $C_p = 1700\ J/kgK$

A beam thickness of $2L = 30mm$ was used to generate the verification data from both the Heisler charts and the numerical model. An initial temperature of $T_i = 0°C$ was used with a directly implied surface temperature at the top and bottom of $T_s = 30°C$. Solutions from the Heisler charts were attained using $200s$ time increments in the Fourier equation up to a maximum of $2000s$. The combination of this thickness and time step means the Fourier number just exceed 0.2 as required for validity of the Heisler charts in the first time step t = $200s$.

8.7.2. Numerical Solution Convergence

The rectangular geometry of the mesh is used to represent the plane wall. At the left and right boundary an insulation boundary condition is used. This implies that no heatflow will leave or enter through that boundary, effectively setting the heat flow $Q_W = 0$ at the left edge and corner nodes and setting Q_E=0 at the right edge and corner nodes. The immediate change in surface temperature is simulated by setting the initial temperature at the top and bottom edge nodes to $T_s = 30°C$. The rest of the nodes have an initial temperature of $T_i = 0°C$. The minimal time step required for stability of the numerical model was shown in section 8.1.3 to be dictated by:

$$\frac{\alpha \Delta t_{cr}}{l^2} <= \frac{1}{4} \tag{8.60}$$

This however does not imply convergence, therefore a convergence study on the time step is initiated. Altering the time step also influences the choice of mesh size. Therefore, both quantities need to be evaluated simultaneously to discover which combination is required in order to converge to the exact analytical solution. The starting point of the time step is that required for a stable solution dictated by equation 8.1.3. For this, an initial mesh size is required as input for l. A minimal required initial mesh size of $10mm$ is chosen as this provides three nodes through the thickness. After attaining the solution for this combination of time step and mesh size, the time step is halved and a new solution is attained for the same mesh size. This procedure is continued until the time step is $\frac{1}{64}\Delta t_{cr}$. At that point, the mesh size is halved and the new time step required for stability is determined from 8.60. For the new mesh size, the time step is again stepwise reduced up to $\frac{1}{64}\Delta t_{cr}$. This procedure is repeated up to a mesh size of $1.25mm$. This procedure is visualized in figure 8.23b for the mesh size of $10mm$.

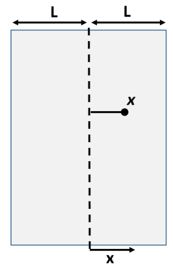

(a) Definition of the location away from the mid-plane $\frac{x}{L}$

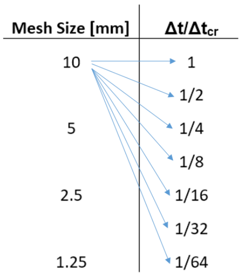

(b) Visualization of convergence procedure. Selection of a mesh size and consecutive reduction of the critical time step by factors of 2.

The solution for all 28 combinations of mesh size and time steps are compared to the exact analytical solution at the four location through the thickness for $t = [200{:}200{:}2000]\,s$ and the error is tracked. The change in the error for every mesh and time step refinement is also recorded. As the analytical method was attained graphic-analytical, an error margin of ±2% is deemed acceptable for the numerical solution. Furthermore, the solution is said to be converged when a further reduction in time step of mesh size leads to a change in the solution <1%. It was noted that the solutions at t=$200s$.

Maximal absolute errors encountered for nine combinations starting at a mesh size of $5mm$ and time step of $\frac{1}{8}\Delta t_{cr}$ are listed in table 8.14.

Table 8.14: Absolute error of numerical model w.r.t. exact analytical solution for different mesh sizes and time steps

	$\Delta t/\Delta t_{cr}$		
Mesh Size [mm]	1/8	1/16	1/32
5	12.43%	10.83%	10.03%
2.5	4.91%	3.67%	3.13%
1.25	2.73%	**1.90**%	1.79%

From table 8.14 it is seen that a mesh size of at least $0.125mm$ is required to attain a solution within 2% of the analytical. At this mesh size, a time step of $\frac{1}{16}\Delta t_{cr}$ gives a maximal error of 1.90%. Further reduction of time step leads to a decrease of only 0.11% in the solution error, therefore the solution is converged at $\frac{1}{16}\Delta t_{cr}$. Further reduction of mesh size is not required as the solution is within the accepted limits. Figure 8.24 shows the comparison of the numerical to the exact analytical solution for this mesh size and time step. For the numerical model, the verified mesh size of $1.25mm$ will be used combined with a time step of $\frac{1}{16}\Delta t_{cr}$.

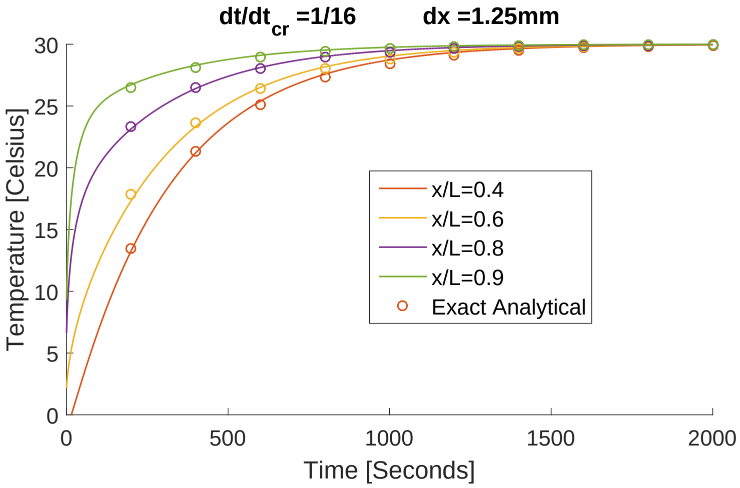

Figure 8.24: Converged numerical solution using mesh size = $1.25mm$ and time step $\frac{1}{16}\Delta t_{cr}$

Verification of the cure kinetic model embedded in the numerical model is not performed due to lack of comparative data, however comparison of the numerical results with the experimental data generated in chapter 7 should provide a good idea about the accuracy of the overall model including the internal heat generation term. This validation process is presented in section 8.8.

8.8. Model Validation

The experimental data obtained in chapter 7 is used for the validation of the numerical model created in this chapter. Before presenting these results it is important to remember the original goal that was set out to accomplish at the start of this chapter. The model was set up to predict the temperature behaviour of X-Core during a cure cycle in order to facilitate research towards functional grading and temperature overshoots. The most significant data points to this extend are:

- **Maximal temperature at centre (T_{Centre}) and edge (T_{Edge})**
  The maximal temperature occurring in the centre of the sample to evaluate if issues may arise with X-Core degradation and pressure behaviour. The experimental range of this value is between ± 170°C and 110°C. A maximal deviation of 10°C is considered acceptable to give the user a good idea in which range he/she is operating with the used combination of parameters.

- **Transition temperature (T_{Trans})**
  The point at which the centre temperature exceeds the edge temperature. Transitions above 85°C mean the onset temperature of expansion for 031DU is reached at the edges first, linked to density gradients with lower density at the edges. Transitions below 85°C mean the expansion temperature is reached at the core first, leading to increased density at the edges. A maximal deviation of 5°C is considered acceptable as the transition point as just exceeding or overshooting the 85°C point could lead to non-desirable density gradients.

- **Time to peak (t_{peak})**
  Time after cure cycle initiation at which the peak temperature occurs. Has significance as it will indicate at which temperature further heating of the mould will not lead to increases in core temperature any more This helps the user to tune cure cycles of which an example is provided in section 8.10. A maximal window of $10min$ is deemed acceptable as the total cure cycle time is around $120min$.

8.8.1. Validation Method

As stated, the validation will be performed using the data obtained in the tests from chapter 7. This data includes a variation in height between 30 to $80mm$ and a variation in dwell temperature from 50 to 110°C using the 270-optimal mix with 1% DU content. Validation data is not yet available for different X-Core mixtures and different ramp-rates. The six tests with which the validation data is performed are listed in table 8.15 along with the thermal conductivity and specific heat capacity obtained using the theoretical models presented in section 8.3 for the used X-Core variant.

Table 8.15: Specification of Validation Tests and X-Core Mix Properties

X-Core mix	$k_{eff}[W/mK]$	$C_{p_{eff}}[J/kgK]$
270-optimal, 1% DU	0.116	1798

Test	**Height [mm]**	**Dwell Temp. [°C]**
H80-T110	80	110
H55-T110	55	110
H30-T110	30	110
H80-T80	80	80
H80-T65	80	65
H80-T50	80	50

The centre temperature is achieved through logging the temperature of the centre node in the numerical mesh. The edge temperature is taken to correspond with the node between 92.5 and 87.5% of the total height as slight variations in positioning of the sensor in the mesh can have occurred. Initial temperatures of the mould and X-Core were set to the experimental initial temperatures. X-Core initial temperature was taken as the average of the sensor values at the start of the test. The verified mesh size and time step attained in section 8.7 were used for all validation simulations being: $\Delta x = \Delta y = 1.25mm$ and $\Delta t = \frac{1}{16}\frac{\Delta t}{\Delta t_{cr}}$. Validation data was generated for $140min$ of simulation time and compared to the central and edge NTC sensors as indicated in figure 7.1.

8.8.2. Time Scaling

After evaluating the initial results of the simulation data a discrepancy was noticed with respect to the time. The simulation consistently produced time to peak t_{peak} values between 5 to 15min shorter than the experimental validation data. The deviation increases with reduced dwell temperatures from 5min at 110°C to 15min at 50°C. This trend is believed to be related to the cure kinetic model fit presented in figure 8.22. A trend is visible in the model to increasingly under-estimate the reaction rate at higher temperatures (>95°C) and increasingly overestimate the reaction rate at lower temperatures (<90°C). This can be related to the increased deviation in t_{peak} values towards lower temperatures as the kinetic model will overestimate the reactivity in this temperature region, therefore resulting in a completed reaction of the epoxy-amine in a shorter time period hence underestimating the t_{peak}. Time scaling is therefore applied to mitigate this deviation in the results. A time scaling between 0.9 and 0.8 was required to have corresponding time to peak values for all tests. The time scaling is simply applied through dividing the time stamp for each data point by the time scaling factor (t_{scale}).

$$t_{new} = \frac{t_{unscaled}}{t_{scale}} \tag{8.61}$$

The used time scaling is presented above the figures in te next section. A time scaling of 0.85 is advised when using the model to attain t_{peak} values within 10min of the actual value. This uncertainty of 10min is of significance when deciding when to initiate the second dwell in four step cure cycles.

8.8.3. Comparison of Experimental Data to Numerical Simulation

Figure 8.25 shows the comparison of the simulation data with the experimental data for all six tests. Table 8.16 presents the comparison of the three significant temperature points being the centre peak temperature (T_{max}), transition temperature T_{trans} and edge peak temperature T_{edge}.

Table 8.16: Comparison of simulation results to experimental data for three significant temperature points. R_{int}=1.16e-5m^2K/W

	$T_{Centre}[°C]$			$T_{Edge}[°C]$			$T_{Trans}[°C]$		
Test	**Sim.**	**Exp.**	**Error**	**Sim.**	**Exp.**	**Error**	**Sim.**	**Exp.**	**Error**
H80-T110	165	167	-2	136	143	-6	120	140	-20
H55-T110	152	155	-3	126	132	-6	98	122	-24
H30-T110	117	130	-13	113	122	-9	76	95	-19
H80-T80	156	152	4	102	108	-6	89	87	2
H80-T65	141	144	-3	88	100	-12	71	66	5
H80-T50	113	123	-10	74	84	-10	54	51	3

T_{Centre} temperatures correspond within 4°C with the experimental data, with the exception of H30-T110 and H80-T50 which deviate by -13°C and -10°C. T_{Edge} values consistently underestimated with a maximal deviation of -12°C. The values for T_{Trans} deviate up to -24°C for the 110°C dwells and with 5°C for the other tests. According to the criteria set at the start of this section the results of T_{Centre} are acceptable except for H30-T110 and H80-T50. T_{Edge} values deviate too much for test H80-T65. All three dwell tests at 110°C deviate beyond 5°C for T_{Switch} and again do not meet the set out requirement.

The constantly under prediction of T_{Edge} along with the T_{Centre} H30-T110 deviation can be related to the assumption on the thermal interface resistance (R_{int}) of the interface determined in section 8.2.2. A value of 1.6e-5m^2K/W is taken here, according to neat epoxy/metal wire experimental data. Increasing the thermal resistance at the interface naturally leads to an increase in X-Core temperature at the edges as the heat escapes less readily through the mould boundary. The effect of this is more pronounced in lower thickness cores as the boundary is positioned closed to the edge region. An increase in thermal interface resistance of the X-Core/aluminium interface compared to neat epoxy/metal wire interface is in the line of expectations. The next section will go into this in more detail and a new value for R_{int} is propose along with the new results.

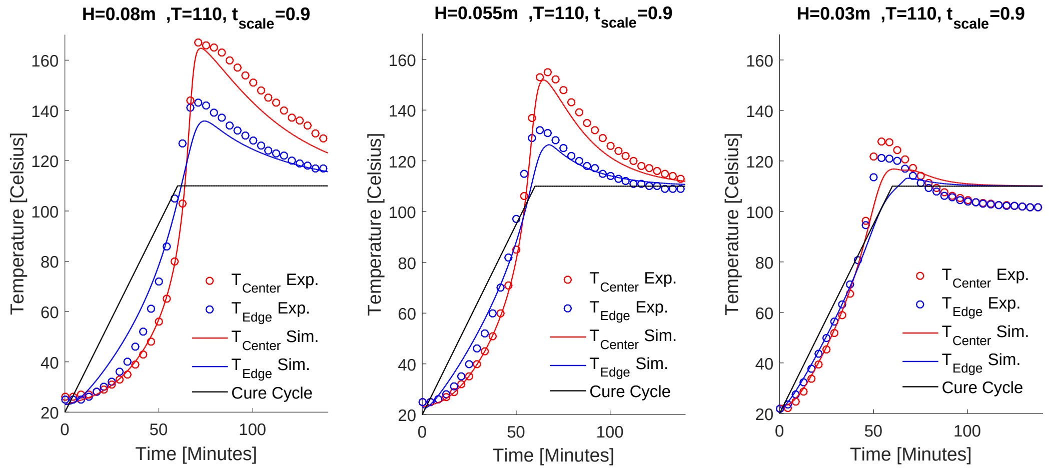

(a) H80-T110 **(b)** H55-T110 **(c)** H30-T110

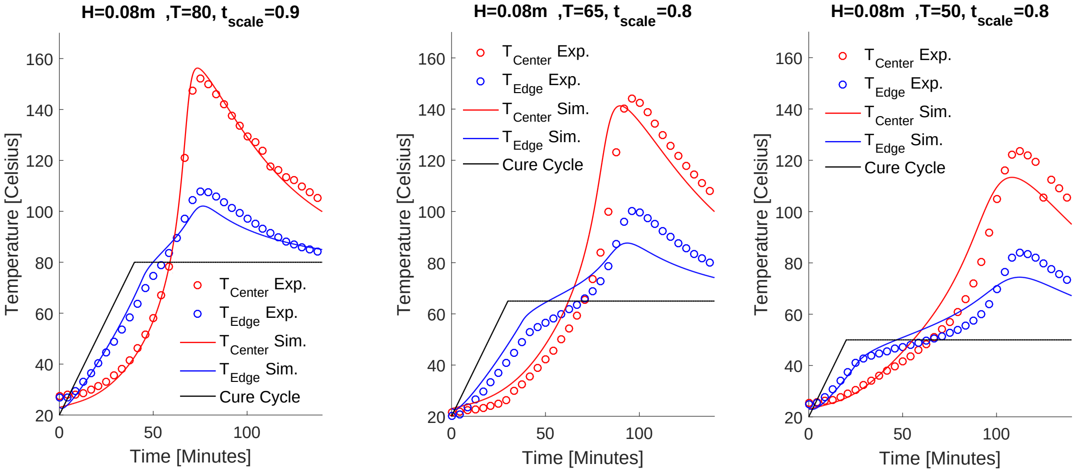

(d) H80-T80 **(e)** H80-T65 **(f)** H80-T50

Figure 8.25: Comparison of experimental data to numerical simulation data at centre and edge of tile mould samples for various dwell temperatures. R_{int}=1.16e-5 m^2K/W

8.8.4. Adjusting Thermal Interface Resistance

Thermal interface resistance was briefly discussed in section 8.2.2 but is reviewed in this section in more depth. The resistance is caused by imperfect contact of two adjoining surfaces, leading to decreased heat transfer through conduction [40]. This is illustrated in figure 8.26. One can imagine a similar phenomenon occurring between the aluminium mould walls and X-Core. X-Core has a large volume of microspheres embedded in an epoxy matrix, placing spheres against a flat surface gives poor surface contact hence leading to the expectation that the thermal interface resistance is higher compared to the initial assumption based on a neat epoxy/metal wire interface. Neat epoxy is a viscous fluid which is likely to have better surface contact with a metal surface compared to a microsphere filled epoxy. The value of 1.6e-5m^2K/W is therefore

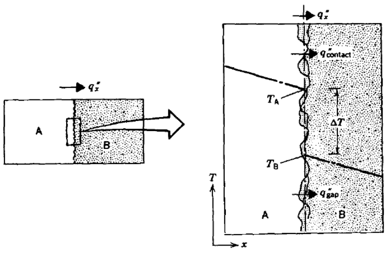

Figure 8.26: Schematic representation of two contacting surfaces with heat transfer being reduced to the imperfect contact due to surface roughness resulting in a thermal interface resistance [79]

taken as lower bound of the thermal interface resistance, as it represents a type of best case scenario for a metal/epoxy interface. The upper bound is derived from a research on insulation materials in contact with a steel pipe [79]. For a steel pipe encased in either fibreglass or calcium silicate insulation thermal interface resistances of 0.37 and 0.18m^2K/W were determined between the steel pipe and the insulation layer. Considering that both insulation materials are solids, compared to the viscous state of X-Core with fluid resin inside, these values are taken as upper bounds. The fluid resin in X-Core can fill gaps between the surfaces, which compared to a solid insulation material, should lead to a higher total contact area.

A new thermal interface resistance was selected through varying the value between the lower and upper bounds of 1.6e-5m^2K/W and 0.37m^2K/W and comparing the simulation data with the test data from the 30mm high sample. Adjusting the thermal interface resistance to 0.03m^2K/W leads to better fitting results as shown in figure 8.27c. The new value was also applied to the other validation data sets, resulting in improved edge temperature results while giving little change in the centre temperature. The new validation data is presented in figure 8.27. Table 8.17 gives the updated errors.

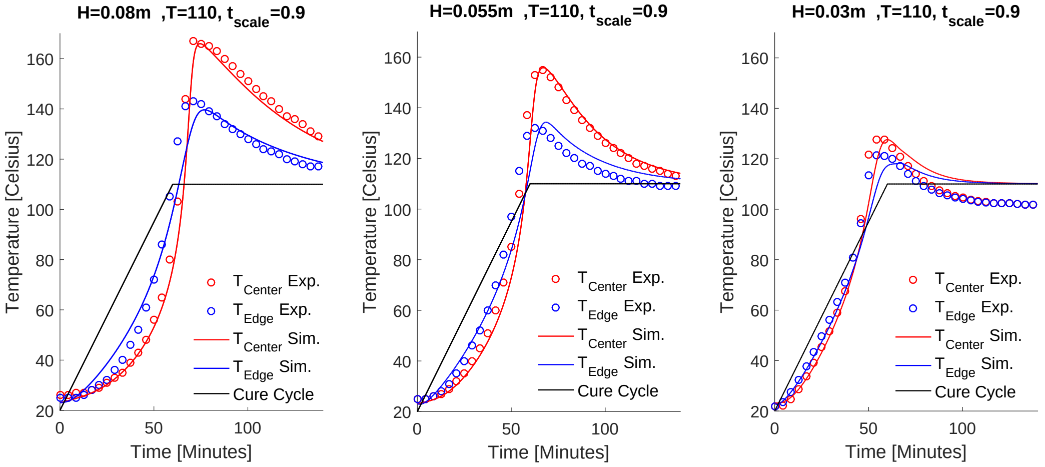

(a) H80-T110 **(b)** H55-T110 **(c)** H30-T110

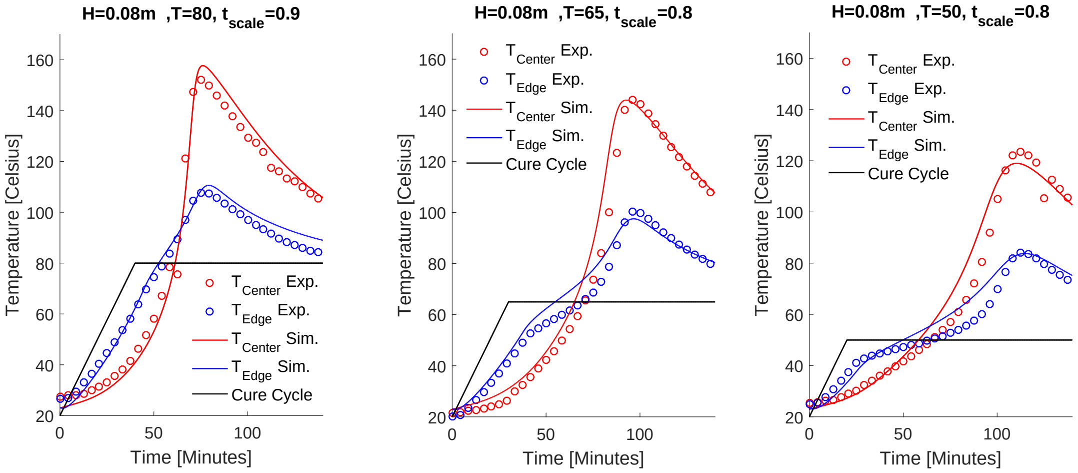

(d) H80-T80 **(e)** H80-T65 **(f)** H80-T50

Figure 8.27: Comparison of experimental data to numerical simulation data at centre and edge of tile mould samples for various dwell temperatures. R_{int}=0.03 m^2K/W

Visual comparison of the new plots presented in figure 8.27 for R_{int}=0.03m^2K/W to the previous plots shown in figure 8.25 for R_{int}=1.16e-5m^2K/W show the better agreement of the simulation data to the experimental data. Table 8.17 present the new error values. The maximal error at T_{Centre} is reduced from 13 to 5°C. The T_{Edge} error is reduced from 12 to 4°C. Both datapoints now fall within the set acceptable bound of 10°C. The error at T_{Trans} is also reduced with 8°C but the maximal error of 16°C still lies outside the acceptable bounds of 5°C for the 110°C dwells. The lower temperature dwells, aimed at positioning T_{switch} below 85°C

do predict the switch within 7°C. This still exceeds the desired accuracy bound by 2°C. This overall decrease in error for the updated value of R_{int} shows that this factor is indeed likely cause for the initial discrepancies found in the model. However, the large change in the model due to the variation of this parameter also indicated the importance of accurate knowledge of the value, especially when analysing core heights <55mm. Section 10.4 will discuss the significance of this parameter along with other uncertainties in more detail.

Table 8.17: Comparison of simulation results to experimental data for three significant temperature points. R_{int}=0.03m^2K/W

	T_{Centre}[°C]			T_{Edge}[°C]			T_{Trans}[°C]		
Test	**Sim.**	**Exp.**	**Error**	**Sim.**	**Exp.**	**Error**	**Sim.**	**Exp.**	**Error**
H80-T110	166	167	-1	140	143	-3	124	140	-16
H55-T110	156	155	1	134	132	2	106	122	-16
H30-T110	128	130	-2	118	122	-4	81	95	-14
H80-T80	157	152	5	111	108	3	94	87	7
H80-T65	144	144	0	98	100	-2	73	66	6
H80-T50	119	124	-5	84	84	0	55	51	4

8.8.5. Temperature Distribution Visualization

Figures 8.28a and 8.28b show the midplane temperature distribution of X-Core at the point when 85°C is reached for test H80-T50. Comparison of these figures shows the similarities of the simulation to the experimental temperature distribution. Highest heat release occurs around (-40,0) and (40,0) corresponding to the combined heat input of the mould surface from both the top and bottom side and the left or right side respectively. This comparison speaks for the physical validity of the model as temperature distribution correspond with those of the experimentally determined distributions.

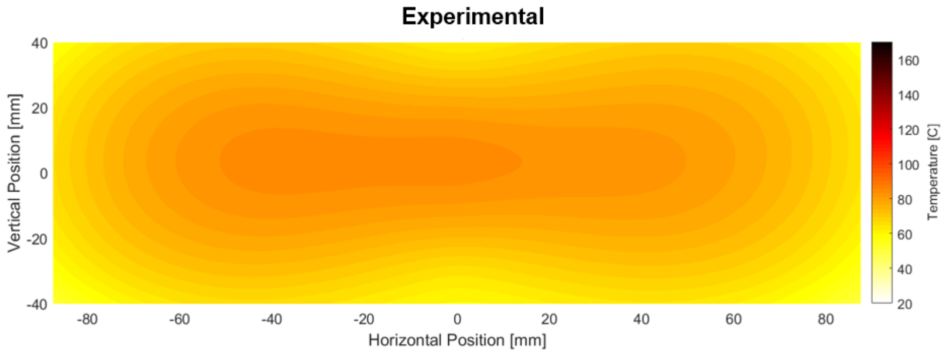

(a) Experimental data

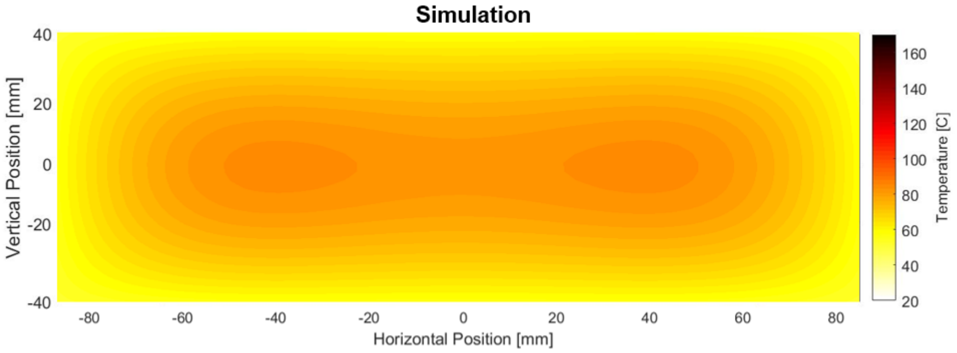

(b) Simulation data

Figure 8.28: Comparison of midplane temperature distribution of experimental and simulation data for 80mm thick X-Core at 50°C dwell. Snapshot taken when T=85°C

8.9. Model Sensitivity to Thermal Conductivity and Specific Heat Capacity

In order to evaluate how accurately the thermal conductivity and specific heat capacity need to be determined a sensitivity study is performed. To evaluate how sensitive the model is to changes in thermal conductivity and specific heat capacity only these values will be varied over the range presented in tables 8.6 and 8.9. These tables present the k_{eff} and $C_{p_{eff}}$ values for mixes varying from high Q-Cel to high DE (>60%) content. The range for k_{eff} from 0.0669 to $0.141 W/mK$ and $C_{p_{eff}}$ ranges from 1862 to $1774 J/kgK$. The results are shown in figures 8.29a and 8.29b for a $55mm$ high core with density of $270kg/m^3$.

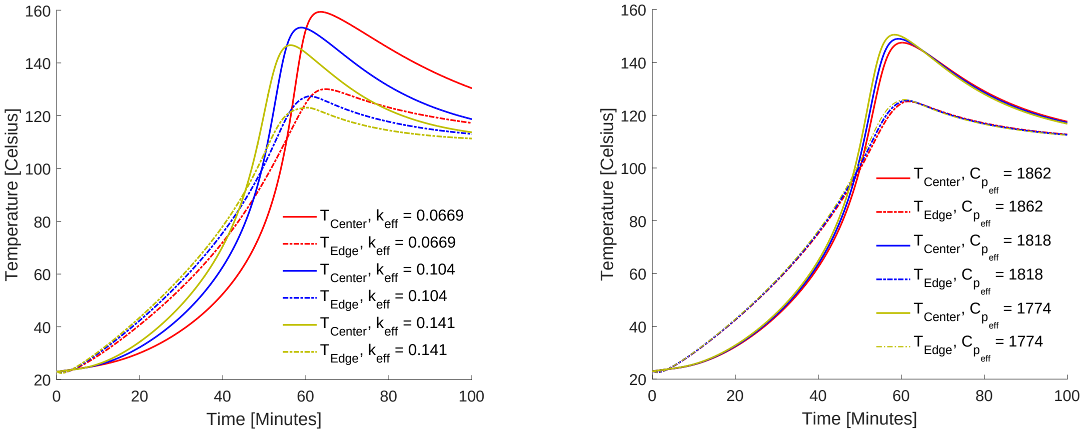

(a) Temperature at centre and edge for three different values of k_{eff} **(b)** Temperature at centre and edge for three different values of $C_{p_{eff}}$

Figure 8.29: Sensitivity study of the model on changes in k_{eff} and $C_{p_{eff}}$ within the expected window

Table 8.18: Sensitivity of centre peak temperature to variation in k_{eff} and $C_{p_{eff}}$

$k_{eff}[W/mK]$	$T_{Centre}[°C]$	$C_{p_{eff}}[J/kgK]$	$T_{Centre}[°C]$
0.0669	159.4	1862	150.5
0.104	153.4	1818	148.9
0.141	147.7	1774	147.5

As can be seen from figure 8.29 the variation in temperatures is higher in the window of expected k_{eff} values compared to the variation seen for changes in $C_{p_{eff}}$. To attain an accuracy of $5°C$ with respect to the thermal conductivity the value needs to be determined within $0.03W/mK$. To attain an accuracy of $5°C$ with respect to specific heat capacity this value needs to be determine within $143J/kgK$. Further recommendations on which methods are best suited for validation of these X-Core parameter will be given in chapter 10.

8.10. Degree of Cure Variation

Another aspect of the model is the information it provides on the degree of cure throughout the mesh. Microcracks were noticed in the centre regions of the $80mm$ high samples cure with a ramp of $1.5°/minC$ to $110°C$ (see figure 7.15). These defaults could be related to the large temperature gradients that occur in the model. These variations in temperature over time at different location of the sample lead to differences in degree of cure (α) of the thermosetting matrix. The model can provide information on the nodal degree of cure over time. An example is presented below which shows what can be achieved through using this information. Identical inputs are used for two simulations, in which only the cure cycle is altered. The degree of cure difference ($\Delta\alpha$) is monitored through extracting the maximal and minimal degrees of cure present at any time in the model. First, the A-cure cycle is used consisting of a straight $1.5°C/min$ ramp to $110°C$ followed by a hold at this temperature. This cycle is compared to a cure cycle employing a $1.5°C/min$ ramp to $50°C$ followed by a dwell for $40min$, afterwards the second ramp uses a $1.5°C/min$ rate to reach the final cure temperature of $110°C$. Figure 8.30 shown both the temperature and $\Delta\alpha$ trends for both cure cycles. Cure cycle B lowers the temperature overshoot and decreases the temperature difference between the edge and centre of the mould through carefully timing the second ramp. This reduces the maximal $\Delta\alpha$ from 0.48 for the A cycle to 0.25 for the B cycle. Employing cure cycles with a carefully timed dwell can therefore be used to limit degree of cure differences leading to potentially higher quality cores.

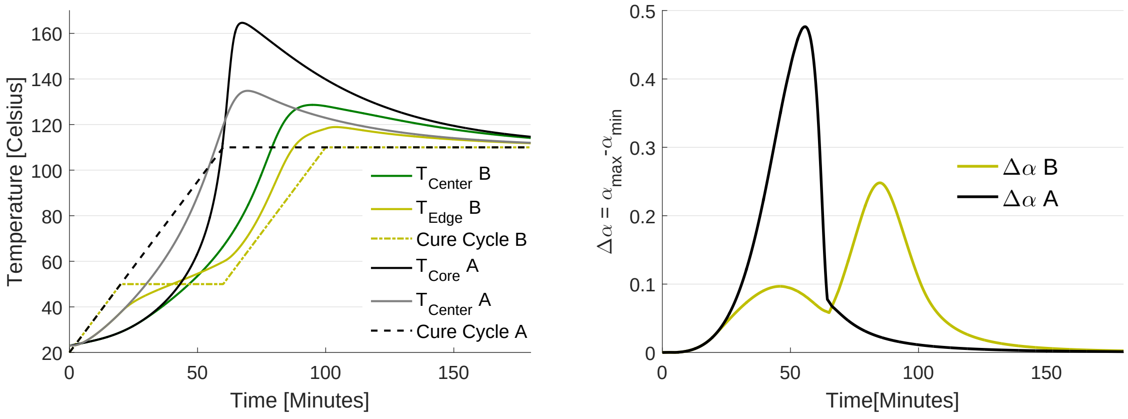

(a) Temperature trend for A and B cure cycles **(b)** $\Delta\alpha$ trend over time for cure cycle A and B

Figure 8.30: Comparison of a straight ramp to 110°C cure cycle (A) to a cure cycle employing a timed dwell at 50°C (B). Effects on temperature and degree of cure distribution presented.

8.11. Case Study: Applying the Model for the Doorbeam Cure Cycle Design

An example of how to constructed model can be applied in a real world design case is presented in this section. A case study is proposed in which the door beam is used as the to be manufactured part. This part consists of a long, $1.0m$, beam member with relatively constant cross section. The cross section of the middle section is indicated in figure 8.31 and can be represented by rectangle of $110x45mm$.

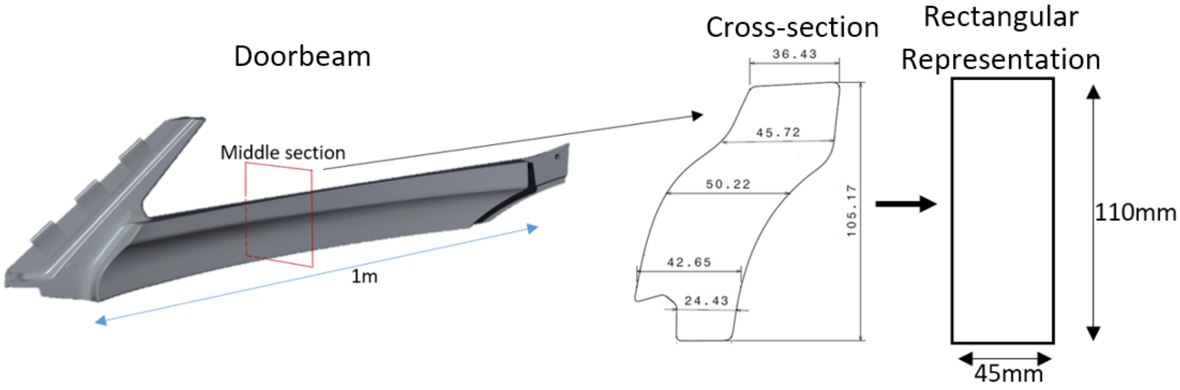

Figure 8.31: Doorbeam with cross-sectional view and rectangular representation used for the simulation

Requirements

Several hypothetical requirements are set on the properties of the final product:

1. X-Core density of $175kg/m^3$
2. 4% DU content
3. Maximal core temperature of 125°C to prevent DU collapse
4. $T_{switch} < 85°C$ to have an increased density towards the edges
5. Limit degree of cure-variations during the cure-cycle
6. Full cure ($\alpha > 0.99$) reached in complete cross-section

Mix Properties

The simplex model of S.Vial is used to determine the (pseudo-)volume fraction required to have the highest possible compressive strength for a mix with $175 kg/m^3$ density. The resulting mix composition is given in table 8.19 and will be referred to as '175-optimal'. The thermal conductivity and specific heat capacity resulting from these volume fractions can be determined using the theoretical models presented in section 8.3 where a 4% DU content is applied. Table 8.20 gives these values. The last mix property required is the real volume fraction of the resin in the X-Core mix. At 4% DU content and a pseudo volume fraction of 9.02% for the resin the real resin volume fraction is $0.0902 * (100 - 4) = 0.0866$.

Table 8.19: Pseudo volume fractions of a $175 kg/m^3$ mix with maximal compressive strength

Density [kg/m^3]	**DE**	**Resin**	**Q-Cel**	$\sigma_c[MPa]$
175-optimal	0.596	0.0902	0.314	1.81

Table 8.20: Specification of Validation Tests and X-Core Mix Properties

X-Core mix	$k_{eff}[W/mK]$	$C_{p_{eff}}[J/kgK]$
175-optimal, 4% DU	0.0735	1760.7

Cure Cycle Tuning

As a baseline cure cycle, the example is again used of a ramp from room temperature to $110°C$ at $1.5°C/min$. The temperature profile of this initial cycle is visible in figures 8.32a and 8.32a where the recommended time scaling factor of t_{scale}=0.85 is used. This first try gives a peak temperature of $138°C$ after $68min$ and switch temperature around $95°C$. This violates requirements 3 and 4 which dictate a maximal temperature of $125°C$ and $T_{switch} < 85°C$.

In order to satisfy these requirements alterations to the cure cycle can be tried. Two options will be evaluated here and there resulting temperature profiles compared consisting of:

Reduced heat-up rate

Reducing the heat-up rate (R) can help reduce temperature gradients though the thickness and spread out the heat release of the resin more over time. For the reduced heat-up rate a value of $1.0°C/min$ is used in stead of the original $1.5°C/min$. This reduced the peak temperature in the centre to $118°C$ with T_{switch} around $75°C$.

Intermediate Dwell

The addition of a dwell below the final cure temperature of $110°C$, required for the curing of the prepreg facesheets, was already shown in chapter 7 to be an effective method of lowering peak temperatures and switch temperatures. Setting the intermediate dwell at $70°C$ for a duration of $15min$ was found to give satisfactory results as the peak temperature now becomes $115°C$ and $T_{switch} = 74°C$. Both options therefore satisfy requirements 3 and 4. Figure 8.32 shows the temperature profiles of both options compared against the results from the initial cure cycle.

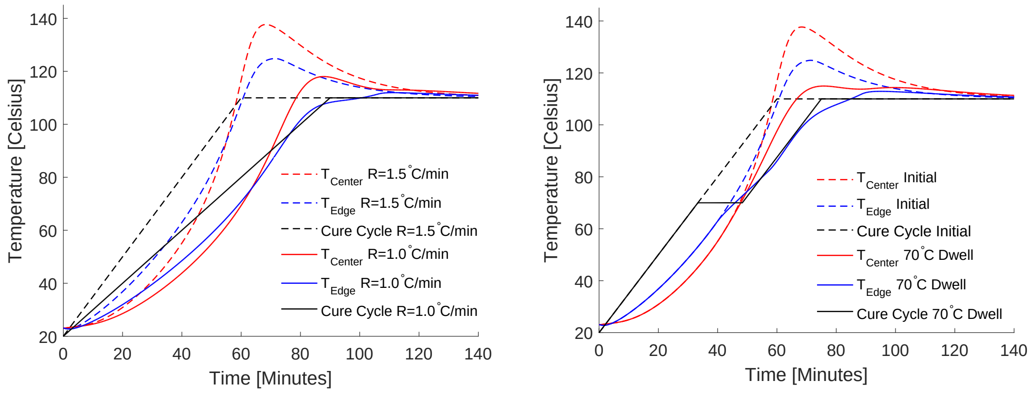

(a) Comparing initial, $1.5°C/min$, cure cycle to a reduced heat-up rate cure cycle at $1.0°C/min$

(b) Comparing initial cure cycle to cure cycle with an intermediate dwell at $70°C$ for $15min$

Figure 8.32: Comparison of the reduced heat-up rate and intermediate dwell as methods to reduce core temperature and lower T_{switch}

Choosing between the two cure strategies can be done though evaluating requirements 5 through 7. The point in time at which the cross-section reaches a full cure, e.g. $\alpha = 1$ dictates the complete duration of the cure-cycle. Lastly, tracking the degree of cure variation as done in section 8.10 gives information on which strategy results in the most evenly cure X-Core product. Figure 8.33a shown the degree of cure differences in the cross-section throughout the cure cycle. The lower heat-up rate cure cycle has a maximal $\Delta\alpha$ of 13.7% against 17.2% and 17.8% for the other cure cycles. The total time required for the minimal degree of cure throughout the cross-section to exceed 0.99 is taken as end-point of the cure. The initial cure cycle reached this point after $105min$, the intermediate dwell cure cycle requires $119min$ and the lower heat up rate strategy extend the cycle time to $130min$. The lower heat-up rate therefore is therefore preferred when looking at the degree of cure difference during the cure-cycle in the cross-section. This cycle does require $11min$ extra to complete compared to the dwelled cure cycle. Furthermore, in the research of D.O. Berckmoes [26] it was discovered that a reduction in surface porosity of up to 44% is possible when reducing the heat-up rate from 1.5 to $1.0°C/min$. Therefore, the engineer can conclude from this analysis that a cure cycle involving a heat-up rate of $1.0°C/min$ to $110°C$ followed by a dwell at $110°C$ for $40min$ has a high chance of leading to a doorbeam with higher density at the edges, a maximal temperature occurring in the centre of $118°C$, degree of cure variation below 14% and 99% cure of the cross-section after $130min$ of cure duration.

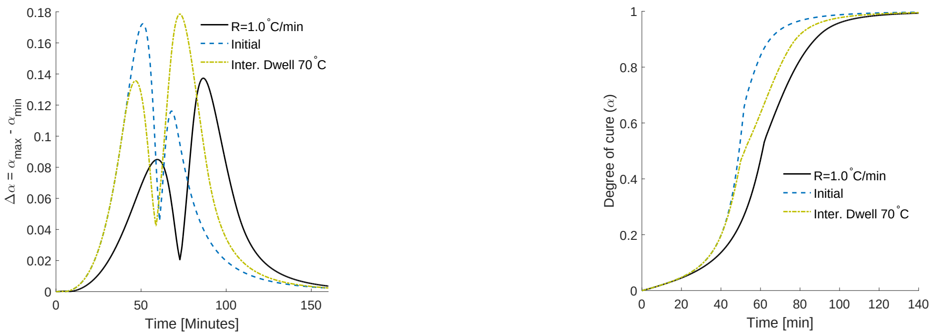

(a) $\Delta\alpha$ vs. time for the three cure cycles evaluated in this section

(b) Minimal degree of cure α present in the cross-section over time for the three cure cycles being compared

Figure 8.33: Comparison of the three cure cycles based on degree of cure variation and minimal degree of cure over time

Comparison with Previous Prototypes

Lastly, it is interesting to compare the discolouration seen in a prototype of the doorbeam manufactured in previous research. Here, a $330kg/m^3$ mixture was used with a basic $1.5°C/min$ heat-up rate to $110°C$. Looking at figure 8.34 this cure cycle combined with the geometry and 330 mixture gives a maximal temperature in the core of $146°C$. The degree of discolouration is comparable to a sample created in the tile mould which has a known core temperature of $154°C$ as visible in figure 8.35. Through lowering the heat-up rate to $1.0°C/min$ this temperature is predicted by the simulation to be reduced to $125°C$ and the switch temperature descends below $85°C$. Again, this shows how the model can be applied to determine proper cure-cycles beforehand for actual products created at *Donkervoort*.

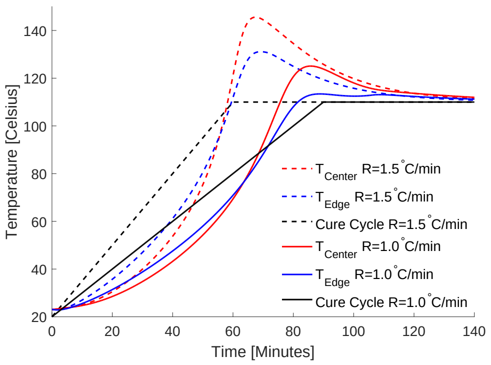

Figure 8.34: Comparison of temperature profiles with a $330kg/m^3$ mix in the doorbeam section for two different cure cycles

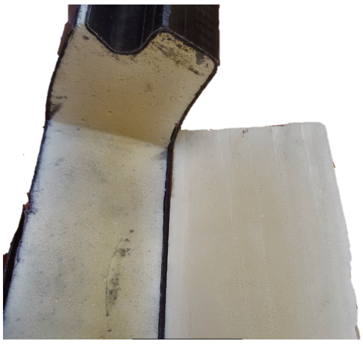

Figure 8.35: Comparison of discoloration seen in a prototype doorbeam (left) with $146°C$ predicted core-temperature to a tile mould sample (right) with $154°C$ core-temperature

8.12. Conclusion

A transient finite difference method has been set up to solve the energy balance equation for a system with internal heat generation. A rectangular mesh is used where the energy transportation over the boundaries is dictated by the thermal resistance of the interface. Theoretical models have been set up to predict the thermal conductivity and specific heat capacity of X-Core. The internal heat generation of the thermosetting binder was experimentally determined and modelled using the theory of cure kinetics. The combination of these parameters along with the input of a cure cycle results in information on the temperature and degree of cure as function of time and position. The model was validated based on experimental results attained in chapter 7 for heights between 30 and $80mm$ and dwell temperatures between 50 and $110°C$. Maximal temperatures occurring in the centre could be predicted within $5°C$, the edge temperatures within $4°C$ and the transition temperatures for the dwell test within $7°C$. Time scaling was required to attain corresponding time to peak values with the experimental results, attributed to the deviations occurring in the cure kinetic model fit. A time scaling factor of 0.85 was determined to deliver time to peak values within $10min$ of the experimentally determined values. The complete code was written in MATLAB without being dependent on any MATLAB specific functions, this allow for the code to be easily transferred to open-source software such as Python™ making the model usable without software licensing. With the current accuracy the model allows the user to trial run several variations of a cure cycle to determine when temperature transitions occur and what maximal temperature will be reached. This limits the required temperature tests to a validation run with to determine if the required temperature behaviour is actually achieved. Increasing the accuracy of the model is believed to be possible through experimental testing of X-Core thermal conductivity and thermal interface resistance. Recommendations on how to perform such experiments are presented in chapter 10 along with other recommendations for further improvement and implication of the presented model.

9

Conclusion

The research presented in this report has focused on adding to the body of knowledge of X-Core in exploring the effect of various process parameters on the properties of the material. The novel core material classifies as a syntactic foam as it consists of microspheres added to a resinous binder material. X-Core is unique in its way of using thermo-expandable microspheres which, under elevated temperatures, increase in volume. Through placing X-Core in an integrally heated closed mould the expansion of DU is limited leading to an increase in the internal pressure in the mould. This phenomenon is used in consolidating the carbon fibre facesheets, resulting in a one-shot manufacturing process capable of making complex shaped sandwich structures. The addition of a thermosetting resin which cures after DU expansion means X-Core remains in its expanded state after the product cools to room-temperature and is released from the mould. Introducing thermosetting resin into a medium with poor thermal conductivity can lead to high core temperatures due to heat release of the exothermic epoxy-amine curing reaction. Analysing the effect of this heat release during the curing of X-Core has been extensively investigated in the present research. Before starting with this phase of the research, several other topics were addressed.

Based on previous research of S.Vial a new mix was selected named the ’270-optimal mix’. This combination of constituents assures that the optimal specific compressive strength is attained for this X-Core density. Reducing the density further was shown to lead to undesirable properties of the pre-cured mass as it becomes dimensionally unstable. The 270-optimal mix formed the base for the rest of the research performed towards the thermal behaviour of X-Core during its cure.

Further foundation for the research was laid in the design and construction of the Tile Mould. This mould was created to be able to manufacture samples under similar process conditions as present in the current production method. During initial tests performed in the mould the sample quality was deemed unacceptable as dry spots and porosity covered around 40% of the carbon fibre facesheets area. This initiated an investigation towards the surface temperature distribution present in the mould. Differences in temperature at the surface as high as $28.5°C$ were discovered as well as temperature overshoots up to $134°C$ compared to the control temperature of $110°C$. Visualizing the temperature distribution helped to link the regions with poor surface quality to the variation in surface temperatures. Addition of aluminium at the mould surface drastically increased the diffusivity of the temperature. $1.5mm$ of aluminium reduced the temperature differences over the complete mould to $3.3°C$ and eradicated the problem with the temperature overshoots. This resulted in improved surface quality of carbon fibre prepreg facesheets to porosity levels around 2-6%. Applying a $1.5mm$ layer of aluminium in complex shaped tooling is however not convenient. Therefore, methods for improving the temperature distribution in complex shaped moulds were investigated. The addition of a layer of copper mesh laminated inside glass fibre epoxy was shown to be as effective as adding $0.3mm$ of aluminium on the mould surface, reducing the temperature difference to about $6°C$ during the ramp up.

A side step was made to the pressure generating property of X-Core. Previous research on this topic presented a relationship linking pressure generation of X-Core purely to the fraction of DU added to the mix. It is expected however that more factors will influence the magnitude of the pressure generated in a certain mix. To investigate this, a new pressure setup was designed and manufactured. The new setup allowed for the elimination of variation in degree of filling and mould sealing and had the aim to evaluate the pressure generation of X-Core for different mixes and at temperatures between 85 and 170$^\circ C$. A major flaw prohibited completion of this research however, as thermal expansion differences in the setup led to unexpectedly high pressure being generated by the setup it self even without X-Core present. No conclusions could therefore be drawn on the pressure dependency of X-Core on mix and temperature variations.

Using the manufactured tile mould a thermal analysis of 270-optimal X-Core mix was performed . Different heights of X-Core samples between 30 and 80mm led to core temperatures varying between 130 and 167$^\circ C$ at a mould temperature of 110$^\circ C$. These high temperature overshoots could not be linked to a reduction of X-Core compressive properties. What was discovered is that the way in which the temperature is increased through the thickness is related to density gradients in the cured foam. A dwell at 50$^\circ C$ was used to activate the exothermic reaction of the thermosetting resin to let the centre of the sample reach the DU expansion temperature of 85$^\circ C$ first. This led to a functionally graded core with 37% higher density at edges with respect to the average cross-sectional density. These density gradients are expected to be usable in creating higher specific flexural strength X-Core sandwich structures.

As the properties of X-Core vary widely with the used volume fraction combination of constituents it is hard to extrapolate the attained knowledge in the thermal analysis of X-Core using the 270-optimal mix to other mix types. The tailorability of X-Core is one of the materials strengths and limiting the knowledge to only one X-Core mix is therefore not desired. To this extend a tool was created with which engineers can predict the thermal behaviour of a wide variety of X-Core types under various curing conditions. The tool is based upon a two-dimensional finite difference method. This method is used to solve the partial differential equation of conservation of energy along with internal heat generation. Theoretical models were used to predict the thermal conductivity and specific heat capacity of X-Core based on its volume fractions and a cure kinetic model was used to model the energy release of the resin. Validation of the model through comparison with experimental data showed that the it successfully predicts maximal temperatures occurring at the sample centre within 5$^\circ C$ and edge temperatures within 4$^\circ C$. The point at which the core temperature starts exceeding the edge temperature is significant as this dictates the resulting density gradients, these transition points were predicted within 7$^\circ C$ for dwells at 80, 65 and 50$^\circ C$ respectively.

The research objective has been realized within a nine month project through inducing functional density gradients in X-Core by varying the used cure cycle. The aim to provide a tool to predict X-Core properties has also been realized in the construction of the numerical model with which the thermal behaviour of X-Core can be predicted.

10

Recommendations

The current chapter will discuss the recommendations that have sprung from the performed research in this report. These subjects are, in the authors opinion, the way forward when building upon the results obtained in this report. The recommendations are ordered per chapter starting with methods to obtain more diffuse tooling surfaces, then the pressure setup is discussed followed by advice on proceeding with research towards functional grading of X-Core. Lastly, the numerical model is discussed and possibilities for increasing its accuracy are presented.

10.1. Obtaining more Diffuse Temperature in Integrally Heated Moulds

Chapter 5 presented a research towards the mould surface temperature distribution in carbon braid integrally heated tooling. Large temperature differences were found over the surface and several solutions for attaining a more diffuse temperature distribution were explored. The following recommendations are given for future research and implementation of the proposed solutions.

For flat plate moulds like the tile mould, an aluminium layer is most easily applied and is therefore also advised for any flat geometry moulds. Scaling the proposed methods to larger, more complex shaped moulds is still to be researched. For quick assessment on if the improved surface temperature distribution does lead to better products it is advised to explore the use of more stretchable aluminium tapes. Between 1 and 4 layers of $0.075mm$ thickness, should lead to a significant reduction in temperature delta's. A trade-off to be made however is if a reduction in the product dimensions of between 0.075 and $0.3mm$ is allowable and if the surface quality of the product is not negatively effected by the possible seams and creases of the aluminium tape. Applying only one layer of copper mesh does provide an interesting solution and the author therefore advices *Donkervoort* to further research this method in the future. Investigating the use of thinner, wider maze meshes is advised to see if this effect can be reduced and to evaluate if the tendency to delaminate will be an issue in the actual moulds. A vacuum infusion method could provide a possible solution to the large amounts of voids in the copper mesh mazes as it pulls out the air more thoroughly with the infusion of the resin. Other manufacturing processes might also be experimented with to produce higher quality laminates compared to hand lamination. The copper mesh laminates were not successful in limiting the temperature overshoot present at the end of the ramp. However, this is thought to be related to the specific test method used as the sensor is located too far away from the copper mesh. Laminating the copper mesh as close to the sensor is therefore advised is the technology is to be applied in actual moulds. Other methods of applying a layer of highly conductive material inside the moulds might also be explored. Conductive copper paints or the use of sputter disposition of metals can be options worth considering. Lastly, the temperature overshoots might be limited through using multiple thermocouples distributed over the mould surface to limit the chance of placing the only sensor in a cold or hot-spot in the mould leading to large deviations of the software temperature with respect to the the average mould temperature.

10.2. Pressure Setup Advances

In chapter 6 a new pressure setup based on a brake master cylinder and oil pressure sensor was designed and tested. Although the setup did fulfil all set requirements, a major flaw was discovered leading to unsatisfactory results. Differences in thermal expansion led to pressure readings of the same order of magnitude as the expansion of X-Core itself. Several mitigation strategies are presented here which could provide a solution to this issue.

Use of materials with lower coefficient of thermal expansion (CTE)
Using materials like Invar with low CTE values around $1.2x10^{-6}K^{-1}$ compared to that of steel ($\pm\ 12x10^{-6}K^{-1}$) and aluminium ($\pm\ 23x10^{-6}K^{-1}$). This decreases the expansion difference, therefore lowering the pressure signal generated by thermal expansion of the setup.

Alternative method for heating of X-Core
Only X-Core actually requires a raised temperature. Providing a more direct heat input into the X-Core chamber in stead of heating the complete setup could limit the effects of thermal expansion differences. Applying a spiral heater to the mould wall could be considered.

Balancing out thermal expansion
Through carefully balancing the lengths of the bolts and driver and using different materials to compensate for the differences in expansions could *in theory* provide zero net difference in thermal expansion.

Once a usable setup has been attained the advice is to focus on the variation of X-Core pressure in a variety of mixes and under various temperatures. The magnitude of pressure generation is expected to be related to the applied temperature. If a relation between the two can be set up, this knowledge can be used in parallel with the presented numerical model to more accurately predict the pressure generated in X-Core. The numerical model can provide information on the expected temperature distribution which can then be linked to the overall expected expansion of DU to predict the net pressure in the volume.

10.3. Density gradient research

Based on the attained results in chapter 7 more research is advised to explore the full possibilities of the inducing of density gradients in X-Core. A range of flexural tests could be performed to see if an increase in strength can indeed be achieved through positioning higher density material at the edges of the core. Another series of tests using various cure cycles should aim to control the density gradient in different ways. The sharp density transition seen in the B-samples could possibly be smoothed out through using a slightly higher dwell-temperature to assure DU expansion also occurs during the exothermic peak at the edges. This could prevent excessive amounts of resin entering the edge region. Dry fibre tests could also be performed to see if the fibres can actually be impregnated using the resin from X-Core. Another interesting feature could be too use the differential heating of two locations of the mould to initiate expansion at specified locations. An example could be to first heat the top side of the tile mould, followed by the bottom side. One sided density gradients could then possibly be induced from top to bottom.

10.4. Further Validation and Implementation of the Numerical Model

The numerical model in its current configuration is capable of predicting centre temperatures for various X-Core heights and dwell temperatures within $5°C$, edge temperatures within $4°C$ and for dwell temperature up to $80°C$ can predict the transition temperature of the centre temperature exceeding the edge temperature within $7°C$. Comments on validity when changing X-Core mixes and ramp-rates can not be made, as no experimental data has been generated with these variables. The same test setup as used in the generation of the presented experimental data can however be applied to also generate experimental data for validation on these parameters. Further additions are however recommended and are listed in the following paragraphs:

Thermal Conductivity of X-Core

The thermal conductivity was shown to have a significant effect on the temperature distribution in the model in section 8.9. To limit deviations in the temperatures within $5°C$ and accuracy of k_{eff} of $0.03 W/mK$ is required. Determining k_{eff} of X-Core is therefore advised to be performed according to ASTM methods to obtain the required accuracy, several different methods are available. ASTM standard E1225 describes the method of using a Guarded Heat Flow meter as a method of determining the thermal conductivity of solids [80]. This method was also applied by *Zhu et all.* to successfully determine the thermal conductivity of high volume fraction filled composites [64]. Another widely accepted method is the Laser-flash methods described in ASTM standard E1461 [81] which can determine the conductivity based on the measured thermal diffusivity if knowledge of the materials density and specific heat is present. Unfortunately, none of the setups listed in these standards were available to the author. Therefore, a recommendation is made to evaluate the thermal conductivity experimentally with either of these methods in future research. Until validation of the model is achieved, the user is advised to exhibit caution with mixtures consisting of very high (>70%) volume fraction of one component, especially for Q-Cel. The mentioned percolation paths could make the thermal conductivity deviate from the model predictions.

Specific Heat Capacity of X-Core

Section 8.9 showed that variation in the specific heat capacity of X-Core within the expected bound only lead to a temperature variation of around $4°C$. Determination of $C_{p_{eff}}$ within $143 J/kgK$ therefore already gives an temperature uncertainty of $5°C$. Therefore, highly accurate experimental validation should be given less priority compared to k_{eff}. If it is decided to validate the theoretical model, the author advices to test the specific heat capacity of the constituents separately first as repeatable measurements with identical materials lead to higher certainty of the result. This should validate the specific heat capacity values used for the fillers. ASTM standard E1269 is advised but caution should be exhibited with assuring that thermal resistance between the calibration standard and the powdery constituents is comparable. Using hermetically sealed containers of which the lid is clamped on the sample could assure better surface contact of the powder to the crucible.

Thermal Interface Resistance between X-Core and Mould

Adjusting the thermal interface was shown to have significant impact on the temperature distribution especially for low height ($30mm$) Cores. This factor therefore requires experimental determination. The current model uses an aluminium contact surface of the mould with the product. If other mould materials are used such as gel-coats (aluminium filled epoxy) the thermal interface resistance is expected to be different and again experimental testing is required. ASTM standard D5470 describes several possible test methods for testing of interfacial thermal resistance, furthermore the reader is advised to read the following paper presenting a comparison of test methods for thermal interface resistance testing: [82].

Integration of Fibre Reinforced Facing at Model Boundary

The current model is used to show that the proposed approach indeed produces reasonably accurate predictions of the temperature behaviour of X-Core during its cure. However, the presence of fibre reinforced facing is not evaluated as validation was performed against experimental results without facesheets present. Thermal conductivity and specific heat capacity data of carbon and glass-epoxy composites is widely available in literature. Integrating these layers therefore possible through placing a series of nodes at the boundary between X-Core and the mould surface with material properties corresponding to the facesheet material. Again, the thermal interface resistance between the new mould/facesheet interface should be determined or attained from literature. Refining the mesh near the boundary can also be performed to account for the low thickness of the facesheets.

Bibliography

[1] J. Houwers. Expanderende sandwichkernen. Internship report, Academic Life Science, Engineering & Design. Saxion Enchede, 2013.

[2] *HexWeb Honeycomb sandwich design technology*. Hexcel Composites, 2000. URL `http://www.hexcel.com/resources/datasheets/brochure-data-sheets/honeycomb_sandwich_design_technology.pdf`. AGU 075B.

[3] Jim Kindinger. Lightweight structural cores. In *ASM Handbook Volume 21: Composites*. ASM international Materials Park, OH, USA, Ohio, 2001.

[4] SprayFoamInsulationPhoenix.net. Types of spray foam insulation. `http://sprayfoaminsulationphoenix.net/types-of-spray-foam-insulation`. Accessed: 5-12-2016.

[5] *ROHACELL WIND-F*. Evonik Industries AG, March 2016. URL `http://www.rohacell.com/product/rohacell/en/products-services/rohacell-wind-f/pages/default.aspx`.

[6] *Gurit Corecell T*. Gurit, 2016. URL `http://www.gurit.com/files/documents/guritcorecell-tv12pdf.pdf`. Gurit Corecell T-12-0916.

[7] An analysis of the effect of the diameters of glass microspheres on the mechanical behavior of glass-microsphere/epoxy-matrix composites. *Composites Science and Technology*, 59(14):2087 – 2091, 1999.

[8] Nikhil Gupta and Eyassu Woldesenbet. Microballoon wall thickness effects on properties of syntactic foams. *Journal of Cellular Plastics*, 40(6):461–480, 2004.

[9] Nikhil Gupta and Ruslan Nagorny. Tensile properties of glass microballoon-epoxy resin syntactic foams. *Journal of Applied Polymer Science*, 102(2):1254–1261, 2006.

[10] Ravi Shankar and S Sankaran. Short-beam three-point bend tests in syntactic foams. part ii: Effect of microballoons content on shear strength. *Journal of Applied Polymer Science*, 98(2):680–686, 2005.

[11] Quasi-static uni-axial compression behaviour of hollow glass microspheres/epoxy based syntactic foams. *Materials & Design*, 32(8–9):4152 – 4163, 2011.

[12] A Mechraoui, B Riedl, and Denis Rodrigue. Mechanical properties of polypropylene structural foams with fibre-reinforced skins. *Journal of Cellular Plastics*, pages 115–132, 2011.

[13] RC Progelhof and JL Throne. Young's modulus of uniform density thermoplastic foam. *Polymer Engineering & Science*, 19(7):493–499, 1979.

[14] Mrityunjay Doddamani, Vasanth Chakravarthy Shunmugasamy, Nikhil Gupta, HB Vijayakumar, et al. Compressive and flexural properties of functionally graded fly ash cenosphere–epoxy resin syntactic foams. *Polymer Composites*, 36(4):685–693, 2015.

[15] Nikhil Gupta and Eyassu Woldesenbet. Characterization of flexural properties of syntactic foam core sandwich composites and effect of density variation. *Journal of composite materials*, 39(24):2197–2212, 2005.

[16] Jerrold T Bushberg and John M Boone. *The Essential Physics of Medical Imaging*. Lippincott Williams & Wilkins, 2011.

[17] Travis A Bogetti and John W Gillespie Jr. Two-dimensional cure simulation of thick thermosetting composites. *Journal of Composite Materials*, 25(3):239–273, 1991.

[18] Lei Shi. *Heat Transfer in the Thick Thermoset Composites*. PhD thesis, Delft University of Technology, 2016.

[19] LibreTexts: Chemistry. Arrhenius equation. `https://chem.libretexts.org/Core/Physical_and_Theoretical_Chemistry/Kinetics/Modeling_Reaction_Kinetics/Temperature_Dependence_of_Reaction_Rates/The_Arrhenius_Law/Arrhenius_Equation`. Accessed: 17-6-2017.

[20] F. Minde. One-shot manufacturing of complex sandwich structures. a new process for donkervoort automobielen b.v. Master's thesis, Delft University of Technology, 2014.

[21] D.O. Berckmoes. Integrally heated tooling for composite manufacturing at Donkervoort Automobielen. Internship report, Delft University of Technology, 2016.

[22] S. Vial. Development of a novel core material for one-shot manufacturing. Master's thesis, Delft University of Technology, 2016.

[23] *Divinycell H.* DIAB Group, February 2016. URL `http://www.diabgroup.com/en-GB/Products-and-services/Core-Material/Divinycell-H`. H Feb 2016 rev16 SI.

[24] *Airex C71.* 3A Composites, 2011. URL `http://www.airexbaltekbanova.com/airex-c71-high-temperature-foam.html`. GM-TDS-107.

[25] ASTM D1621-16. Standard Method for Compressive Properties of Rigid Cellular Plastics. Standard, ASTM International, West Conshohocken, USA, November 2016.

[26] D.O. Berckmoes. The effect of X-core foam processing on the surface defects in carbon fiber-epoxy sandwich composites. Master's thesis, Delft University of Technology, 2017. Unpublished.

[27] *DS18B20. Programmable Resolution 1-Wire Digital Thermometer.* Maxim Integrated, 2015. URL `https://datasheets.maximintegrated.com/en/ds/DS18B20.pdf`. 19-7487.

[28] Wonho Kim, Jong-Woo Bae, Il-Dong Choi, and Yong-Seog Kim. Thermally conductive emc (epoxy molding compound) for microelectronic encapsulation. *Polymer Engineering & Science*, 39(4):756–766, 1999.

[29] *Alloy Data Sheet EN AW-6060.* Nedal Aluminium, 2005. URL `https://www.nedal.com/wp-content/uploads/2016/11/Nedal-alloy-Datasheet-EN-AW-6060.pdf`. EN AW-6060.

[30] Christopher Long. *Essential Heat Transfer.* Longman, 1999.

[31] Jennifer A. Segui. Lightning protection for aircraft structures. `www.aerospacemanufacturinganddesign.com`. Accessed: 21-5-2017.

[32] *Technical Datasheet: SR 1660 Heat resistant epoxy systems.* Sicomin, 2014. URL `http://www.sicomin.com/datasheets/product-pdf41.pdf`. SR1660.

[33] *FlexiForce Sensors User Manual.* Tekscan, 2009. URL `https://www.tekscan.com/resources/articles-research/flexiforce-user-manual`. Rev G.

[34] Yi-Jen Huang, Chia-Hao Wang, Yu-Lin Huang, Gangjian Guo, and Steven R Nutt. Enhancing specific strength and stiffness of phenolic microsphere syntactic foams through carbon fiber reinforcement. *Polymer Composites*, 31(2):256–262, 2010.

[35] Krishan K. Chawla Gary Gladysz. The space between: Voids in heat shield protecting orion spacecraft. `http://scitechconnect.elsevier.com/the-space-between-voids-in-heat-shield-protecting-orion-spacecraft/`. Accessed: 18-11-2016.

[36] *Product Specification for Expancel microspheres.* AkzoNobel, 2014. URL `https://www.akzonobel.com/expancel/system/Images/AkzoNobel_Expancel_DU_product_specification_tcm65-59186.pdf`. 2014.12.

[37] SensorWiki.org. Force-sensitive resistor (fsr). `http://sensorwiki.org/doku.php/sensors/force-sensitive_resistor`, 2011. Online; accessed 12 December 2016.

[38] *FSR Force Sensing Resistor Integration Guide and Evaluation Parts Catalog.* Interlink Electronics. URL `https://www.sparkfun.com/datasheets/Sensors/Pressure/fsrguide.pdf`. 90-45632 Rev. D.

[39] *Pressure Sensor Fluid PSS-260.* Bosch, 2016. URL `http://www.bosch-motorsport.de/media/catalog_resources/Pressure_Sensor_Fluid_PSS-260_Datasheet_51_en_2781159307pdf.pdf`. 2781159307|en, V2.

[40] Theodore L Bergman, Frank P Incropera, David P DeWitt, and Adrienne S Lavine. *Fundamentals of heat and mass transfer.* John Wiley & Sons, 2011.

[41] *Datasheet NTC G650/100k/+.* EPCOS, 2001. URL `http://www.farnell.com/datasheets/102485.pdf?_ga=2.222443538.865997100.1496920489-1616029141.1496920489`. FBL1A/d.

[42] ASTM D792 - 13. Standard test methods for density and specific gravity (relative density) of plastics by displacement. Standard, ASTM International, West Conshohocken, USA, November 2013.

[43] N Gupta, E Woldesenbet, S Sankaran, et al. Studies on compressive failure features in syntactic foam material. *Journal of Materials Science*, 36(18):4485–4491, 2001.

[44] M Necati Ozisik. *Heat conduction.* John Wiley & Sons, 1993.

[45] *Heat & Mass Transfer: A Practical Approach.* McGraw-Hill Education (India) Pvt Limited, 2007.

[46] Thomas Blomberg. *Heat conduction in two and three dimensions: Computer modelling of building physics applications*, volume 1008. Byggnadsfysik LTH, Lunds Tekniska Högskola, 1996.

[47] E Chapelle, B Garnier, and B Bourouga. Interfacial thermal resistance measurement between metallic wire and polymer in polymer matrix composites. *International Journal of Thermal Sciences*, 48(12):2221–2227, 2009.

[48] *Q-Cel 5028 Hollow Microspheres Typical Properties.* Potters Europe – Engineered Glass Materials (EGM) Division. 3-04-244-1-02.

[49] *Material Safety Data Sheet: Expancel Microspheres 920 DU 80.* AkzoNobel, 2009. URL `http://doc.ccc-group.com/msds/english/505559.pdf`. 505559.

[50] *Material Safety Data Sheet: Expancel Microspheres 920 DE 80 d30.* AkzoNobel, 2010. URL `https://www.b2bcomposites.ca/msds/ecc/589137.pdf`. 589137.

[51] *Material Safety Data Sheet: Expancel 031 DU 40.* AkzoNobel, 2015. URL `http://doc.ccc-group.com/msds/english/505563.pdf`. 505563.

[52] D Mishra and A Satapathy. *A study on thermal and dielectric characteristics of solid glass microsphere filled epoxy composites.* PhD thesis, National Institute of Technology, Rourkela, 2014.

[53] Bruno Van Mele, G Van Assche, A Hemelrick, and H Rahier. Modulated dsc evaluation of isothermal cure and vitrification for thermosetting systems. *Thermochim. Acta*, 268:121, 1995.

[54] Jarlath McHugh, P Fideu, A Herrmann, and Wolfgang Stark. Determination and review of specific heat capacity measurements during isothermal cure of an epoxy using tm-dsc and standard dsc techniques. *Polymer Testing*, 29(6):759–765, 2010.

[55] Bruno Van Mele, Hubert Rahier, Guy Van Assche, and Steven Swier. The application of modulated temperature differential scanning calorimetry for the characterisation of curing systems. In *Modulated Temperature Differential Scanning Calorimetry*, pages 83–160. Springer, 2006.

[56] Cambridge Glassblowing. Glass properties: Borosilicate glass. `http://www.camglassblowing.co.uk/glass-properties/`. Accessed: 1-5-2017.

[57] Isidoro Martinez. Properties of gases. `http://webserver.dmt.upm.es/~isidoro/dat1/eGAS.pdf`. Accessed: 3-5-2017.

[58] *Acrylonitrile: Safe Storage and Handling Guide.* INEOS, 2007. URL `http://www.ineos.com/globalassets/ineos-group/businesses/ineos-nitriles/she/2007_acrylonitrile_brochure.pdf`.

[59] CHEMnetBASE. Poly(acrylonitrile). `http://polymerdatabase.com/polymers/polyacrylonitrile.html`, . Accessed: 1-5-2017.

[60] CHEMnetBASE. Poly(acrylonitrile). `http://polymerdatabase.com/polymers/polyacrylonitrile.html`, . Accessed: 4-6-2017.

[61] Ye P Mamunya, VV Davydenko, P Pissis, and EV Lebedev. Electrical and thermal conductivity of polymers filled with metal powders. *European polymer journal*, 38:1887–1897, 2002. 9.

[62] Karol Pietrak and Tomasz S Wisniewski. A review of models for effective thermal conductivity of composite materials. *Journal of Power Technologies*, 95(1):14, 2015.

[63] B SUNDÉN and J YUAN. Evaluation of models of the effective thermal conductivity of porous materials relevant to fuel cell electrodes. *International Journal of Computational Methods and Experimental Measurements*, 1(4):440–455, 2013.

[64] Bailin Zhu, Jing Ma, Jian Wang, Jun Wu, and Dongsheng Peng. Thermal, dielectric and compressive properties of hollow glass microsphere filled epoxy-matrix composites. *Journal of Reinforced Plastics and Composites*, 31(19):1311–1326, 2012.

[65] VS Shabde, KA Hoo, and GM Gladysz. Experimental determination of the thermal conductivity of three-phase syntactic foams. *Journal of materials science*, 41(13):4061–4073, 2006.

[66] *Q-Cel Hollow Microspheres Typical Properties.* Potters Europe – Engineered Glass Materials (EGM) Division, 2007. URL `http://www.potterseurope.org/Portals/14/lit/Q-Cel%20Hollow%20Microspheres%20Range%20Typical%20Properties.pdf`. 3-03-042-1-07.

[67] *Product Specification for Expancel microspheres.* AkzoNobel, 2016. URL `https://www.akzonobel.com/expancel/system/Images/AkzoNobel_Expancel_DE_product_specification_tcm65-49451.pdf`. 2016.08.

[68] Kunal H Kate, Ravi K Enneti, Seong-Jin Park, Randall M German, and Sundar V Atre. Predicting powder-polymer mixture properties for pim design. *Critical Reviews in Solid State and Materials Sciences*, 39(3): 197–214, 2014.

[69] ASTM E1269-11. Standard method for determining specific heat capacity by differential scanning calorimetry. Standard, ASTM International, West Conshohocken, USA, 2011.

[70] José M Kenny. Determination of autocatalytic kinetic model parameters describing thermoset cure. *Journal of Applied Polymer Science*, 51(4):761–764, 1994.

[71] Panagiotis I Karkanas and Ivana K Partridge. Cure modeling and monitoring of epoxy/amine resin systems. i. cure kinetics modeling. *Journal of applied polymer science*, 77(7):1419–1431, 2000.

[72] Bryan Bilyeu, Witold Brostow, and Kevin P Menard. Epoxy thermosets and their applications. iii. kinetic equations and models. *Journal of Materials Education*, 23(4-6):189–204, 2001.

[73] M Ghaemy, M Barghamadi, and H Behmadi. Cure kinetics of epoxy resin and aromatic diamines. *Journal of Applied Polymer Science*, 94(3):1049–1056, 2004.

[74] ASTM E2070-13. Standard test method for kinetic parameters by differential scanning calorimetry using isothermal methods. Standard, ASTM International, West Conshohocken, USA, September 2013.

[75] TA Instruments. A review of dsc kinetics methods (white paper). TA073.

[76] Daniel J O'Brien and Scott R White. Cure kinetics, gelation, and glass transition of a bisphenol f epoxide. *Polymer Engineering & Science*, 43(4):863–874, 2003.

[77] Jae-Do Nam and James C Seferis. Application of the kinetic composite methodology to autocatalytic-type thermoset prepreg cures. *Journal of applied polymer science*, 50(9):1555–1564, 1993.

[78] Frank P Incropera and David P Dewitt. *Introduction to Heat Transfer.* John WHey & Sons. New York. NY, 1996.

[79] Michael A Stubblefield, Su-Seng Pang, and Vic A Cundy. Heat loss in insulated pipe the influence of thermal contact resistance: a case study. *Composites Part B: Engineering*, 27(1):85–93, 1996.

[80] ASTM D1225-13. Standard Test Method for Thermal Conductivity of Solids Using the Guarded-Comparative-Longitudinal Heat Flow Technique. Standard, ASTM International, West Conshohocken, USA, 2013.

[81] ASTM E1461-13. Standard Test Method for Thermal Diffusivity by the Flash Method. Standard, ASTM International, West Conshohocken, USA, 2013.

[82] Robert N Jarrett, CK Merritt, JP Ross, and J Hisert. Comparison of test methods for high performance thermal interface materials. In *Semiconductor Thermal Measurement and Management Symposium, 2007. SEMI-THERM 2007. Twenty Third Annual IEEE*, pages 83–86. IEEE, 2007.

[83] ASTM E537-12. Standard test method for the thermal stability of chemicals by differential scanning calorimetry. Standard, ASTM International, West Conshohocken, USA, December 2012.

A

Method of X-Core Sample Manufacturing

The current appendix describes the manufacturing process used for the production of all X-Core samples made in this report.

Considerations when Weighing and Metering Constituents

X-Core consists of four individual constituents, being an epoxy/amine resin and three different microsphere types. The resin, Q-Cel and DU components are weighed on a scale with $0.1g$ accuracy. Due to its low density, DE microspheres are better metered using a suitable measuring cylinder with $2ml$ accuracy. The epoxy resin (Ancarez®) and amine hardener (Ancamide™ 3399) have to be mixed in a 100:60 weight ratio.

Required Equipment

The equipment required for the weighing, metering and mixing of X-Core are listed below:

- Plastic mixing cup ranging from 250 to $5L$ depending on the volume to be mixed
- Wooden stirring sticks
- Weighing scale with $0.1g$ accuracy
- Measuring cylinder with $2ml$ grading divisions

Safety Equipment

It is advised to wear protective rubber gloves when handling X-Core and its non-solid precursors. Using a dust mask is also recommended for all steps involving the preparation and mixing of X-Core as the lightweight microspheres tend to get airborne and gases can escape from the resin.

Procedure for manufacturing X-Core

A step-wise guide to the mixing procedure used for the manufacturing of X-Core is listed below:

1. Determine desired volume fraction of constituents
2. Determine volume of X-Core required for the sample or product
3. Calculate required weights for resin, Q-Cel and DU and required volume for DE
4. Very carefully meter the required volume of DE microspheres into the measuring cylinder and tap the cylinder with a wooden mixing stick. DE microspheres will start packing together, visible as a decrease in total volume. Continue tapping until no further volume decrease is visible within about $30s$ of tapping. Add extra DE to attain the required total volume and repeat the tapping procedure. Continue until desired amount of DE is reached. Cover the measuring cylinder to prevent loss of DE and continue with mixing of the other constituents
5. Place an adequately sized mixing cup on the scale
6. Pour in the required weight of epoxy (Ancarez®) to within $0.1g$

7. Pour in the required weight of amine hardener (Ancamide™ 3399) to within $0.1g$
8. Thoroughly mix the epoxy and hardener for around 2-$5min$ with a wooden mixing stick depending on the total volume until a uniform coloured substance in attained
9. Slowly add the required amount of DU microspheres to the mix in small ($\pm 0.3g$) steps as removing it from the cup after overfilling is not easily achieved. Weight to the nearest $0.1g$
10. Start by stirring slowly to evenly disperse the DU into the resin. Continue mixing at a higher speed until all DU is evenly dispersed and no lumps or clusters of DU are visible
11. Weight the required amount of Q-Cel directly into the mixing cup to the nearest $0.1g$
12. Again, start mixing with the wooden mixing stick slowly to prevent spilling of Q-Cel. After roughly $1min$ of stirring most (>80%) of the Q-Cel will adhere to the resin/DU mix, forming a white, viscous paste. Continue thoroughly mixing at a higher pace until no white powder is visible any more and all Q-Cel is evenly dispersed forming a uniform coloured viscous paste
13. Carefully add the pre-metered DE to the mixing cup. Start by stirring very slowly as DE tends to get airborne easily. Continue the slow stirring until no batches of DE are present in the mixing cup any more Again, mixing should be continued until DE is evenly dispersed inside the mix. The X-Core compositions can become either paste like or powder like depending on the composition.
14. Place X-Core inside the mould cavity

B

NTC Calibration Data

The NTC thermistors were calibrated using a pre-calibrated PT-100 sensor connected to *eltherm* ELTC-14 unit with a $1K$ accuracy. The NTC sensor was attached to the PT-100 sensor using aluminium tape to assure equal temperature of both sensors. Both sensor were placed inside a small *Tefal* oven. Temperature was increased stepwise and allowed to level for at least $10min$ after which the temperature was read from the ELTC-14 and the corresponding signal from the NTC was read using Arduino$_{®}$ software. Temperature was increased to the PT100 rated limit of 200°C. Resulting calibration data is shown in figure B.1 with the used third order polynomial to attain a data fit with an R^2=0.998 assuring an accurate fit to the data. This calibration equation was then implemented into the Arduino$^{®}$ sketch used for the reading out of the data. Note: This calibration curve is only valid with the used resistors of $10k\Omega$ which were selected to give a linear behaviour of the NTC output around ±100-170°C.

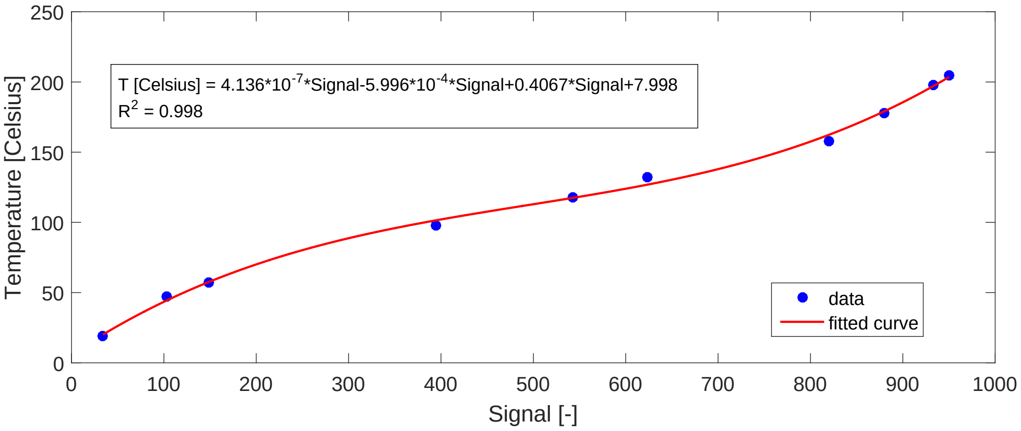

Figure B.1: NTC caliration data relating the signal read from the Arduino$_{®}$ to the Temperature from a pre-calibrated PT100 sensor

C

Calibration of FlexiForce® HT201 FSRs

Calibration of the FlexiForce® HT201 sensors was performed using a puck and weights setup as schematically shown in figure C.1. A zero-weight initial point was collected after which six step-wise increasing weights were placed on the sensors. The weights were selected to represent between 1 and 11bar of pressure in line of the expected pressures generated by X-Core. Live-data readout was performed on a PC to determine when a constant signal was attained for every weight, this took around 30s per calibration step. A load break-in was performed before every calibration step through placing the to be used weight on the sensor and adding around 1kg of extra manual pressure. The weights were then removed and re-positioned on the sensor. Calibration was performed under a temperature of 19.5°C. A second order polynomial provided the best fit to the attained calibration data due to the non-linearity observed above 4bar of pressure. The fitted functions are shown in parallel to the calibration curves in figure C.2.

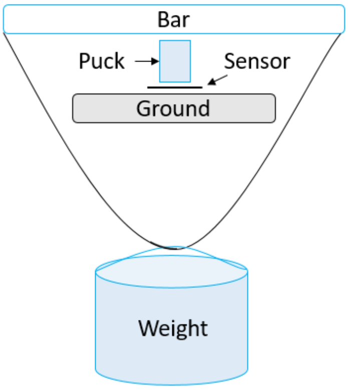

Figure C.1: Schematic representation of the used calibration setup [22]

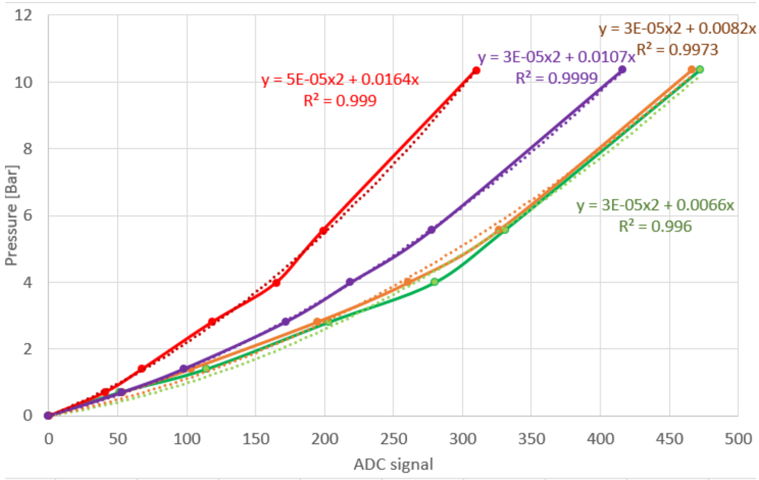

Figure C.2: NTC calibration data and functions

D

Overview of Design Choices of Oil Based X-Core Pressure Setup and Calibration

D.1. Design Choices and Justification

This section lists the different parts present in the designed pressure setup and a reason or justification for the specific design choices. Figure D.1 present a visual representation of the treated parts.

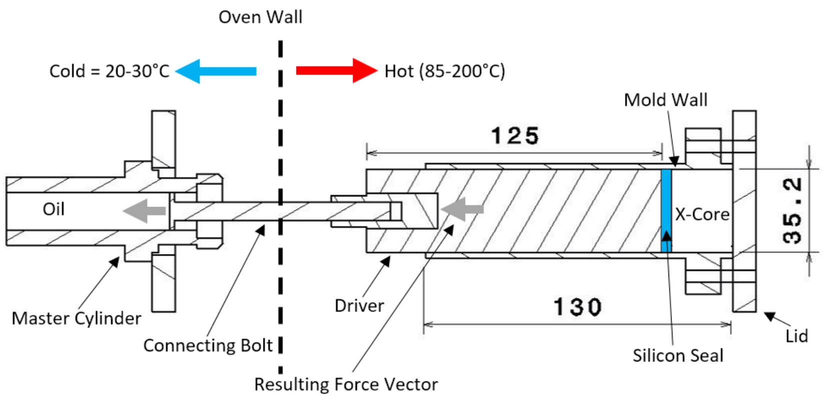

Figure D.1: Side view and cut-through of the pressure setup

1. Variable height X-Core chamber (20-80mm)
   Adjustable X-Core chamber height allows extra variable of X-Core height/volume to be tested on pressure differences
2. Oil pressure sensor attached to a master brake oil cylinder (*Girling 625*)
   Incompressible oil at room-temperature provides a highly stable medium to read pressure from
3. Close fitting driver inside X-Core chamber
   Low friction with mould walls and close sealing to eliminate X-Core leakage
4. Silicon seal
   High temperature stable (<200°C) two-component room temperature curing silicon. Poured in place to create close fitting seal. Seal improves under compression due to Poisson ratio of the material. No friction created in actuation direction as central region is flexible enough to allow slight («1mm) lateral displacement.
5. Large 35.2mm diameter X-Core chamber
   1:4.7 area ratio of X-Core pressure chamber (A_{X-Core}=929.41mm^2) to master cylinder chamber (A_{Oil}=197.93mm^2) to amplify X-Core pressure generating a greater measurement sensitivity
6. Aluminium oven wall plate
   Replaces the glass oven wall of the *Tefal* oven. Master cylinder is fixed to the aluminium wall using four threaded M8 ends and bolts. Insulation material is applied to the aluminium wall inside to limit

heat losses.

7. Connecting Bolt

   M8 driver bolt from master cylinder screwed into driver to transfer resultant force from X-Core pressure to the oil in the master cylinder.

D.2. Oil Pressure Sensor Calibration

The calibration of the sensor signal received by the Arduino® is calibrated through placing the master cylinder inside a pressure jack as shown in figure D.2. The master cylinder actuation bold is inserted into a hole in a steel block acting as pre-load for the load cell with $1lbs$ accuracy. Starting at 0 the sensor output is recorded. $20lbs$ increments are then used to increase the total load to $400lbs$, corresponding to $20bar$ of X-Core chamber pressure in the eventual setup. A highly linear ($R^2 = 0.999$) and repeatable behaviour was determined between a load of 0-400$[lbs]$. Two more calibration were run with $50lbs$ increments to check the repeatability of the setup. Results of the calibration procedure are shown in figure D.3. The readout of te pressure sensor with the 12-bit Arduino® results in a $1.4lbs$ resolution, correlating to a $0.067bar$ X-Core pressure resolution. The root mean square error of the calibration is $2.38lbs$. This translates to an X-Core pressure uncertainty in the calibration of:

$$P_{Oil} = \frac{F_{Oil}}{A_{Oil}} = \frac{2.38 * 0.453 * 9.81}{197.93} = 0.535bar \tag{D.1}$$

$$P_{X-Core} = P_{Oil} * \frac{A_{Oil}}{A_{X-Core}} = 0.535\frac{197.93}{929.41} = 0.11bar \tag{D.2}$$

Combined with the sensor accuracy of 1% of the total force, at $10bar$ of pressure, the uncertainty of the pressure measurement is 0.11+10*0.01 = $0.21bar$. Up to $5bar$ the uncertainty is 0.11+5*0.01=$0.16bar$.

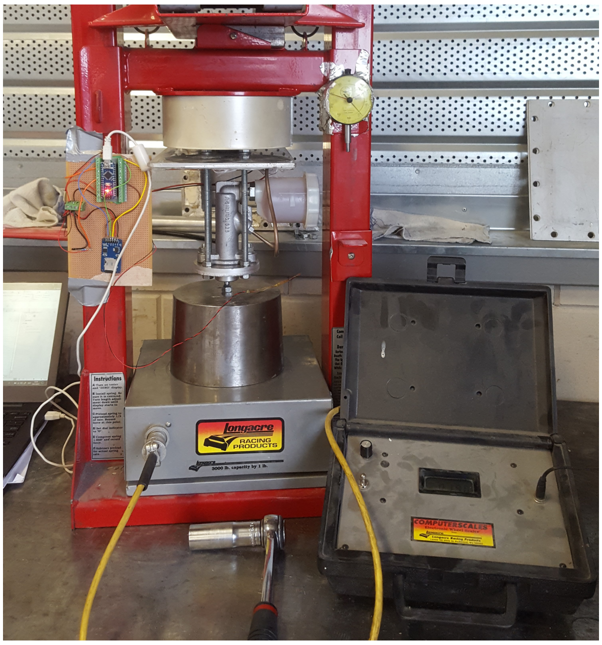

Figure D.2: Master cylinder placed inside the Donkervoort pressure jack with $1lbs$ accurate load cell underneath.

D.3. Test Procedure

The test procedure for testing the pressure generated of a certain X-Core mixture is as follows:

1. Pre-heat the oven to 70°C
2. Insert the driver into the mould wall and place the silicon seal on top of the driver inside the mould. Position the driver + seal such that $55mm$ is measured from the mould wall top edge to the silicon seal.
3. Place the X-Core mix into the chamber in ±$10ml$ portions to prevent air inclusion. Firmly press X-Core into the chamber and displace the driver with several mm

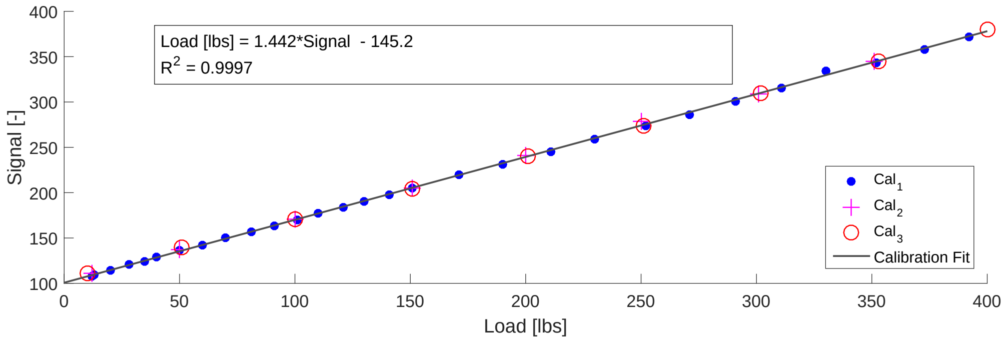

Figure D.3: Calibration data from the oil pressure sensor calibration

4. Push the driver back to the original position. Slice away the excess X-Core from the mould
5. Place a piece of vacuum foil on top of the cylindrical mould wall to assure a good seal with the lid
6. Place the lid on the mould and tightly screw it tight against the flange
7. Slide the lid over the four M8 thread ends and attach the driver to the master cylinder extending bolt
8. Screw four M8 nuts onto the thread ends up to the lid
9. Start the Arduino® and read out the pressure. Apply between 1 and $4 lbs$ of pre-load by tightening the four nuts contacting the lid to assure no empty room is present between the driver and X-Core
10. Place the pressure setup into the oven and set it to $70°C$.
11. Initiate data logging of the pressure using the Arduino®

E

Experimental Data for Density Determinations Using Archimedes Method

This Appendix lists the experimental data acquired during density determination according to ASTM standard D792[42]. Data include; water temperature and density measured during the density determination, dry sample weight (W_{dry}) and submerged wet sample weight/flotation (W_{wet}). Equation E.1 is applied to determine the density based on the attained data where ρ_{air}=0.0012g/cm^3 is used.

$$\rho = \frac{W_{dry}}{W_{dry} - W_{wet}}(\rho_{water} - \rho_{air}) + \rho_{air} \tag{E.1}$$

E.1. Density Determination of X-Ray Calibration Samples

Table E.1: Gathered data of X-Ray calibration samples for density determination according to ASTM standard D792[42]

Tw	21.4	C°C
rho water	0.88793	[g/cm3]
rho air	0.0012	[g/cm3]

Sample	Dry weight [g]	Wet weight [g]	Density [kg/m3]
150	0.624	-3.3871	139.1471
250	1.0758	-2.9737	236.7708
310	1.5559	-3.1803	292.5017

E.2. Density Determination for Density Gradient Tests

The orientation of the slices made in horizontal and vertical direction and the location from which they were attained from the 130x60x30mm blocks is shown in figure E.1. The following tables present the dry and wet weights of each slice along with the water temperature and according density attained for each experiment.

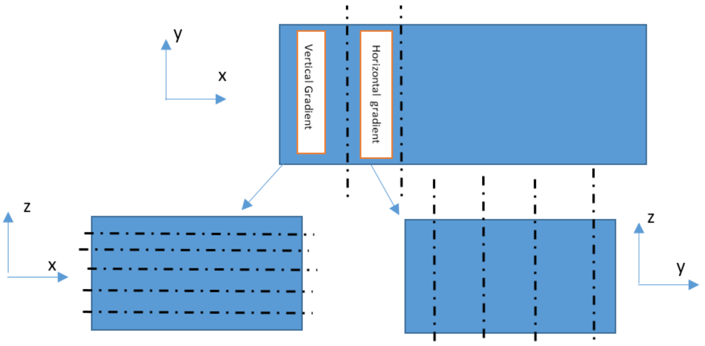

Figure E.1: Schematic representation of the sectioning method used for attaining thin slices in both vertical and horizontal direction

Table E.2: Gathered data of sample SR8 for density determination according to ASTM standard D792 [42]

Density Profile SR8			**Component**	**% Vol**
Avg. Estimated Density SR8	150	[kg/m3]	Resin	4.9%
Tw	21.8	$^\circ C$	DU	2.0%
rho water	0.99784	[g/cm3]	DE	46.6%
rho air	0.0012	[g/cm3]	Q-cel	46.6%

SR8	**Horizontal direction**			
Location [mm]	**Dry weight [g]**	**Wet weight [g]**	**Density [kg/m3]**	**Diff from avg.**
1.5	0.376	-2.111	151.93	-2%
4.5	0.381	-2.045	157.68	1%
12	0.854	-4.673	155.25	0%
24	0.875	-4.676	158.23	2%
36	0.842	-4.474	159.10	2%
48	0.825	-4.439	157.37	1%
55.5	0.424	-2.273	157.82	2%
58.5	0.391	-2.296	146.28	-6%
		Avg. Density	**155.460**	**-6%**

SR8	**Vertical direction**			
Location [mm]	**Dry weight**	**Wet weight**	**Density [kg/m3]**	**Diff from avg.**
2.5	0.907	-5.259	147.85	-6%
7.5	0.891	-4.717	159.55	1%
12.5	0.786	-4.020	164.20	4%
17.5	0.764	-3.949	162.80	3%
22.5	0.761	-3.998	160.56	2%
27.5	0.808	-4.626	149.42	-5%
		Avg. Density	**157.403**	**-6%**

Table E.3: Gathered data of sample SR9 for density determination according to ASTM standard D792 [42]

Density Profile SR9			**Component**	**% Vol**
Avg. Estimated Density SR9	250	[kg/m3]	Resin	20%
Tw	21.65	°C	DU	2%
rho water	0.99789	[g/cm3]	DE	20%
rho air	0.0012	[g/cm3]	Q-cel	58%

SR9 **Location**	**Horizontal direction** **Dry weight [g]**	**Wet weight [g]**	**Density [kg/m3]**	**Diff from avg.**
1.5	0.5773	-1.7939	243.85	-7%
4.5	0.6842	-1.7972	276.00	6%
12	1.5070	-4.0473	271.61	4%
24	1.2743	-3.4588	269.53	3%
36	1.4266	-3.9219	267.03	2%
48	1.4801	-4.1030	265.41	2%
55.5	0.7615	-2.1251	264.12	1%
58.5	0.6143	-2.0122	234.30	-10%
		Avg. Density	**261.48**	

SR9 **Location**	**Vertical direction** **Dry weight**	**Wet weight**	**Density [kg/m3]**	**Diff from avg.**
2.5	1.5328	-4.7435	244.60	-9%
7.5	1.4211	-3.6087	282.79	5%
12.5	1.393	-3.498	285.05	6%
17.5	1.5261	-3.9255	280.20	4%
22.5	1.8651	-4.8792	276.82	3%
27.5	0.9748	-3.094	239.97	-11%
		Avg. Density	**268.24**	

Table E.4: Gathered data of sample SR5 for density determination according to ASTM standard D792 [42]

Density Profile SR5			**Component**	**% Vol**
Avg. Estimated Density SR5	320	[kg/m3]	Resin	14.3%
Tw	22.3	°*C*	DU	2.0%
rho water	0.99775	[g/cm3]	DE	0.0%
rho air	0.0012	[g/cm3]	Q-cel	83.7%

SR5 **Location**	**Horizontal direction** **Dry weight [g]**	**Wet weight [g]**	**Density [kg/m3]**	**Diff from avg.**
1.5	0.8012	-1.764	312.46	-4%
4.5	0.8205	-1.6794	328.28	1%
12	1.8014	-3.6142	332.68	3%
24	1.7728	-3.4781	337.65	4%
36	1.9655	-4.0208	328.40	1%
48	1.6136	-3.3836	322.99	0%
55.5	0.9094	-1.884	325.63	0%
58.5	0.9163	-2.0596	308.04	-5%
		Avg. Density	**324.52**	

SR5 **Location**	**Vertical direction** **Dry weight**	**Wet weight**	**Density [kg/m3]**	**Diff from avg.**
2.5	1.9896	-4.3142	315.73	-6%
7.5	1.8676	-3.6045	341.32	2%
12.5	1.6164	-3.0125	349.19	4%
17.5	1.4888	-2.8196	345.57	3%
22.5	1.9582	-3.7519	342.95	2%
27.5	1.3286	-2.8438	318.53	-5%
		Avg. Density	**335.55**	

Table E.5: Gathered data of sample S5 for density determination according to ASTM standard D792 [42]

Density Profile S5			**Component**	**% Vol**
Avg. Density S5	370	[kg/m3]	Resin	24.5%
Tw	22.15	°C	DU	2.0%
rho water	0.99777	[g/cm3]	DE	36.8%
rho air	0.0012	[g/cm3]	Q-cel	36.8%

S5 **Location**	**Horizontal direction** **Dry weight [g]**	**Wet weight [g]**	**Density [kg/m3]**	**Diff from avg.**
1.5	0.9337	-1.4222	396.19	7%
4.5	1.3017	-2.2277	368.78	0%
12	2.0331	-3.5748	362.52	-2%
24	2.0497	-3.8042	350.17	-5%
36	1.8851	-3.4882	350.85	-5%
48	1.6912	-3.0124	359.55	-3%
55.5	1.0067	-1.6825	374.29	1%
58.5	1.3137	-2.0564	389.70	6%
		Avg. Density	**369.01**	

S5 **Location**	**Vertical direction** **Dry weight**	**Wet weight**	**Density [kg/m3]**	**Diff from avg.**
2.5	2.0298	-2.8078	419.38	15%
7.5	2.1993	-3.7389	370.32	1%
12.5	2.0294	-3.8017	348.06	-5%
17.5	1.8115	-3.4723	342.89	-6%
22.5	1.7299	-3.2436	347.85	-5%
27.5	2.2358	-3.8258	368.81	1%
		Avg. Density	**366.22**	

F

X-Ray Sample Preparation and Nanotom Calibration

F.1. X-Ray Sample Preparation

It is important to limit the variation in thickness in one slab as well as to limit the thickness variations over all the slabs to be tested as the variation in thickness will directly be related to the attenuation of the X-Rays. This was achieved by fabricating a simple sawing guide (figure F.1b) and sanding block (figure F.1c). Sample thickness variation could be limited to $\pm 1mm$ in this way.

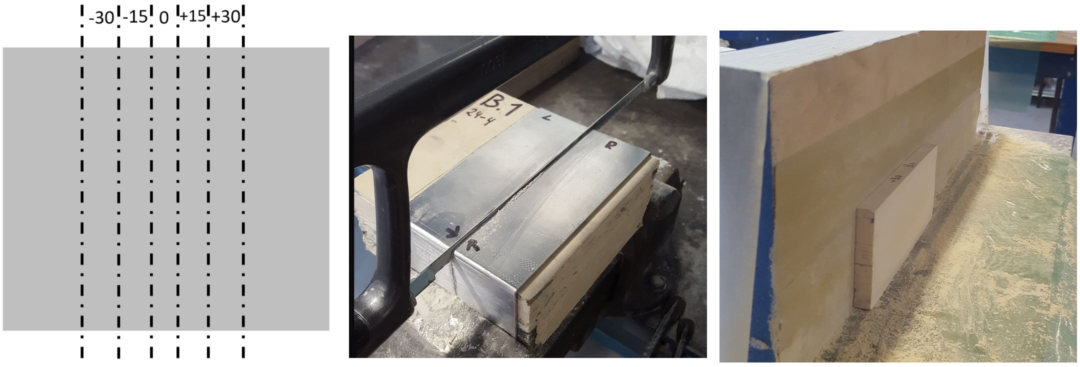

(a) Schematic representation of the location of the slabs cut from the X-Core blocks

(b) Sawing the blocks into evenly spaced slabs

(c) Sanding of X-Core blocks to constant thickness

Figure F.1: Preparation of the X-Ray samples through sawing (b) and sanding (c) the samples into constant thickness slabs at locations -30, -15, 0, +15 and +30mm away from the midplane of the main block (a)

Slabs of 12mm thickness were cut from the mid plane of the sample in the manner shown in figure F.1a. The midplane of each slab corresponds with a distance away from the sample mid plane of -30, -15, 0, +15 or +30mm. The limit was set at 30mm as this corresponds with the outer perimeter of the compression tests samples created in section 7.2.5 and because edge effects of the aluminium mould are expected to be present close to the mould edges. These edge effects are too specific to this mould type and are therefore not of interest.

Absolute Density Calibration Specimens

In order to attain knowledge of the absolute densities of the specimens from the X-Ray greyscale images three calibration specimens are used. First, the absolute density of these specimens are attained through using ASTM standard D792 [42]. This results in the densities listed in table F.1.

The calibration specimens were attached to the side of the slabs together with a small piece of wood to indicate the centre of the specimen. This is depicted in figure F.2a. The resulting calibration curves are

Table F.1: Densities of the calibration specimens attained through ASTM standard D792 [42]

Specimen	**Density [$kg/m3$]**
150	139.15
250	236.77
310	292.50

presented in figure F.2b for four arbitrary samples. The relation between the absolute density and grey value is linear for all samples. Some variation between samples occurs possibly due to slight differences in the positioning of the sample in the X-Ray scanner. A separate calibration was therefore performed for every sample that was tested.

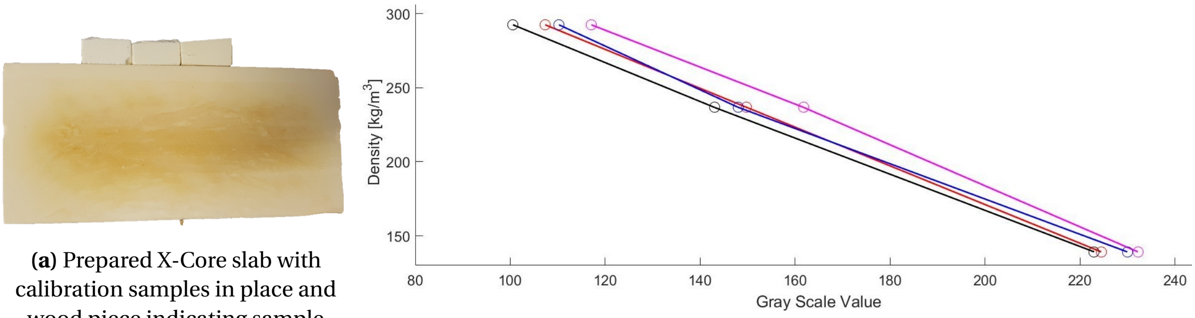

(a) Prepared X-Core slab with calibration samples in place and wood piece indicating sample centre

(b) Density calibration data for a sample

Figure F.2: Calibration specimens attached to a slab (a) and resulting calibration curve relating grey scale value to absolute density (b)

X-Ray Apparatus

A *Phoenix Nanotom* micro CT scanner was used for the X-Ray scanning. The machine is depicted in figure F.3.

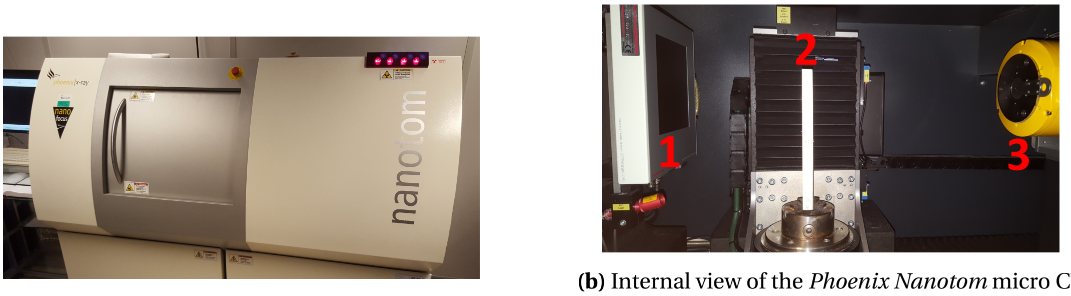

(a) *Phoenix Nanotom* micro CT scanner

(b) Internal view of the *Phoenix Nanotom* micro CT scanner with indicated: 1. Detector, 2. X-Core slab, 3. X-Ray transmitter

Figure F.3: *Phoenix Nanotom* micro CT scanner

G

Isothermal DSC Methodology

The isothermal cure kinetic analyses using a differential scanning calorimeter (DSC) were performed in accordance with ASTM standard E2070 [74]. A *Seiko Instruments Exstar 6000* DSC apparatus was used for these experiments. The followed experimental procedure is listed below:

1. Pre-heat the DSC chamber to the isothermal test temperature required

   Several experiments using a $20K/min$ ramp from $30C°$ were first executed. This resulted in unusable data as the reaction exotherm occurred during the heatup-phase of the DSC. The ramp to e.g. $100C°$ takes $3.5min$, typical exothermic peaks occurred after only 1-$2min$. Therefore, it was opted to pre-heat the DSC to be able to start data-collection at the isothermic temperature after a typical time of 15-$20s$ after inserting the sample in the DSC.

2. Use a needle to insert a small (50-$100\mu m$) pinhole in the lid of the specimen

   To prevent differences in pressure inside the sample pan during elevated temperatures and equilibrate the pressure in the sample pan to the ambient pressure in the DSC apparatus [83].

3. Weigh the aluminium sample holder (pan) and lid combined to the nearest $0.1mg$

   ASTM E2070 prescribes using a scale with $1\mu g$ accuracy [74]. Available scales for this research have a maximal accuracy of $0.1mg$ and are therefore applied.

4. Weigh approximately $15\pm0.01g$ op 4010 epoxy resin in a plastic mixing cup

5. Add required amount of 3399 hardener to the resin in the prescribed ratio of 4010:3399 = 100:60. Weigh to the nearest $0.01g$

6. Mix the resin and hardener thoroughly using a wood mixing stick for $3min$. Assure all resin is mixed with the hardener and none is left on the edges or bottom of the cup

7. Let the mixture rest for ± one minute to degas slightly

8. Use a glass capillary pipette to extract a small amount of mixed resin from the centre of the plastic cup and carefully place approx. $10mg$ of resin on the bottom of the aluminium pan. Assure the resin is not sticking to the edges of the pan. Weigh the weight of the resin sample to the nearest $0.1mg$

9. Place the aluminium lid on the pan and press very lightly. Do not hermetically seal the pan as the pressure exerted on the lid will cause the viscous resin to flow out

   A thermogravimetric analysis (TGA) was carried out on the resin to verify that <2% of weight loss occured over the used temperature range (80-$110C°$).

10. Quickly open the DSC chamber and insert the sample pan next to the reference empty pan. Close the DSC and wait until the isothermal set-temperature is achieved again within $\pm1K$.

    A typical temperature drop of around $10K$ was observed after inserting the sample pan. This typically took around 15-$20s$ to correct.

11. When the DSC chamber is within $1K$ of the isothermal temperature the data collection is initiated. The DSC is held at the isothermal temperature until complete conversion of the resin is reached, indicated by a leveling-of of the heat flow. Typical measurement times ranged from 100 to $180min$.

12. After the measurement is complete the DSC is cooled back to ambient temperature and the sample is collected from the chamber.

13. Re-weight the sample to the nearest $0.1mg$

    If any changes in mass greater than $0.1mg$ are detected the measurement has to be critically assessed as weight loss can affect the data

14. Repeat steps 1-12 for all isothermal measurements required

The used *Seiko Instruments Exstar 6000* heat flux DSC is depicted in figure G.1.

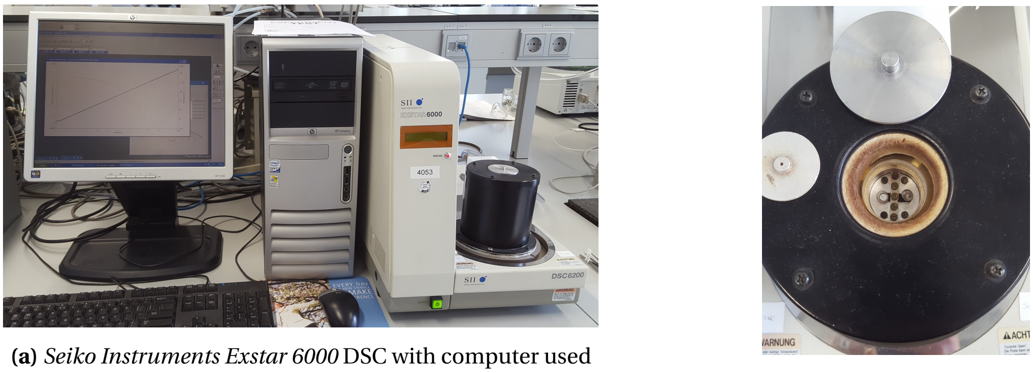

(a) *Seiko Instruments Exstar 6000* DSC with computer used for data collection

(b) DSC chamber of the *Seiko Instruments Exstar 6000* DSC

Figure G.1: Depictions of the DSC apparatus used for collecting the isothermal heat flow data

H

Specific Heat Capacity DSC Methodology

The experimental determination of the specific heat capacity of cured X-Core samples using a differential scanning calorimeter (DSC) were performed in accordance with ASTM standard E1269 [69]. A *Perkin Elmer, Sapphire DSC Standard 115V model* DSC apparatus was used for these experiments. The procedure is listed below:

1. Place an empty crucible (the sample crucible) in the DSC chamber next to the reference crucible
2. Start an isothermal hold of $30min$ at $0°C$ to equilibrate the sample and crucible temperature and initiate data collection
3. Using a heat up rate of $10K/min$ heat the DSC to $200°C$
4. Start an isothermal hold at $200°C$ for $30min$
5. Cool the DSC back to room temperature at any desired rate
6. Weight the sapphire standard calibration disk to the nearest $0.1mg$
7. Remove the lid from the sample crucible and place the sapphire standard disk inside. Place the lid on top of the sapphire disk
8. Place the sapphire containing crucible inside the DSC chamber nex to the reference crucible
9. Repeat steps 2-4
10. Remove the sapphire standard disk from the crucible
11. Weight $\pm 5mg$ of well mixed X-Core powder scraped from the center of a cured X-Core sample into the sample crucible. Weigh to the nearest $1mg$
12. Place the lid on the sample crucible
13. Insert the sample crucible into the DSC chamber next tot the reference crucible
14. Repeat steps 2-4
15. Remove the sample crucible from the DSC chamber and remove the X-Core powder by tapping on the back of the crucible gently until all powder is removed
16. Repeat steps 11-15 for the remaining X-Core samples while using the exact same crucible for every test

I

Flow Chart of Numerical Model

I.1. Numerical Model Flow Chart

Figure I.1 shows the flow chart of the numerical model, where user inputs are shown in red/italic text.

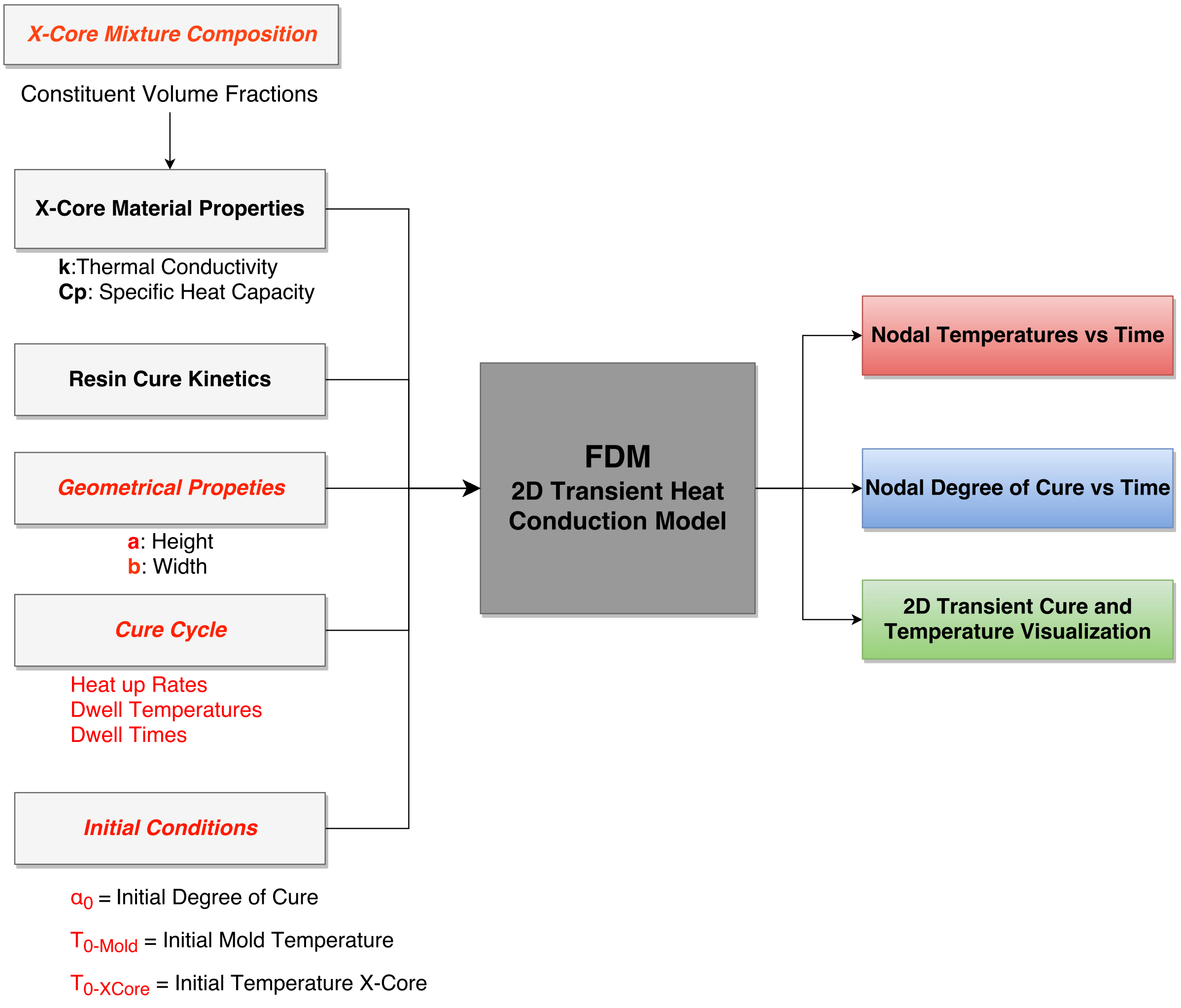
X-Core Mixture Composition
Constituent Volume Fractions
X-Core Material Properties
k:Thermal Conductivity
Cp: Specific Heat Capacity
Resin Cure Kinetics
Geometrical Propeties
a: Height
b: Width
Cure Cycle
Heat up Rates
Dwell Temperatures
Dwell Times
Initial Conditions
α0 = Initial Degree of Cure
T0-Mold = Initial Mold Temperature
T0-XCore = Initial Temperature X-Core
FDM
2D Transient Heat Conduction Model
Nodal Temperatures vs Time
Nodal Degree of Cure vs Time
2D Transient Cure and Temperature Visualization

Figure I.1: Flow chart of the numerical model with required used inputs in red/italic

J

Heisler Charts

The charts displayed here represent the analytical solution to a one-dimensional, transient conduction problem in a plane wall of thickness 2L used for the verification of the numerical model in chapter 8.

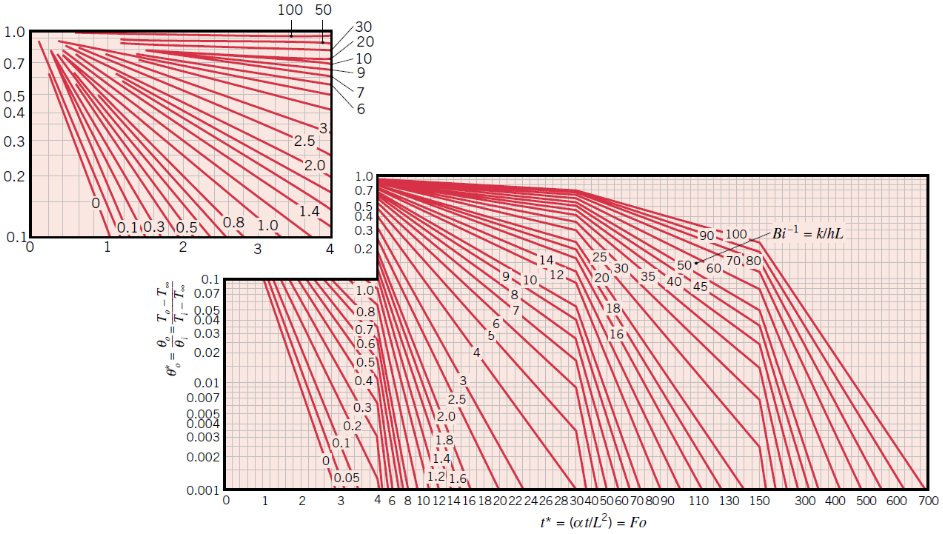

Figure J.1: Midplane temperature as function of time for plane wall of thickness 2L [78]

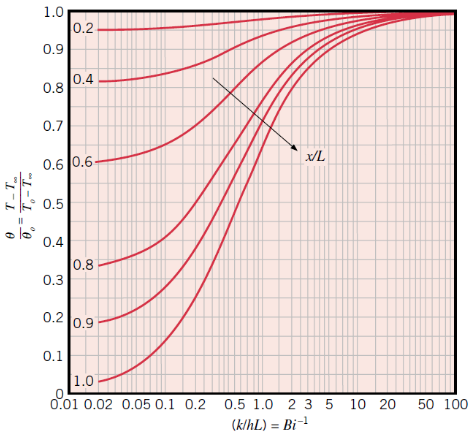

Figure J.2: Temperature distribution through the thickness in a plane wall of thickness 2L [78]